

## Oxygen evolution on NiCo<sub>2</sub>O<sub>4</sub> electrodes

**Citation for published version (APA):**

Haenen, J. G. D. (1985). *Oxygen evolution on NiCo<sub>2</sub>O<sub>4</sub> electrodes*. [Phd Thesis 1 (Research TU/e / Graduation TU/e), Chemical Engineering and Chemistry]. Technische Hogeschool Eindhoven.  
<https://doi.org/10.6100/IR189138>

**DOI:**

[10.6100/IR189138](https://doi.org/10.6100/IR189138)

**Document status and date:**

Published: 01/01/1985

**Document Version:**

Publisher's PDF, also known as Version of Record (includes final page, issue and volume numbers)

**Please check the document version of this publication:**

- A submitted manuscript is the version of the article upon submission and before peer-review. There can be important differences between the submitted version and the official published version of record. People interested in the research are advised to contact the author for the final version of the publication, or visit the DOI to the publisher's website.
- The final author version and the galley proof are versions of the publication after peer review.
- The final published version features the final layout of the paper including the volume, issue and page numbers.

[Link to publication](#)

**General rights**

Copyright and moral rights for the publications made accessible in the public portal are retained by the authors and/or other copyright owners and it is a condition of accessing publications that users recognise and abide by the legal requirements associated with these rights.

- Users may download and print one copy of any publication from the public portal for the purpose of private study or research.
- You may not further distribute the material or use it for any profit-making activity or commercial gain
- You may freely distribute the URL identifying the publication in the public portal.

If the publication is distributed under the terms of Article 25fa of the Dutch Copyright Act, indicated by the "Taverne" license above, please follow below link for the End User Agreement:

[www.tue.nl/taverne](http://www.tue.nl/taverne)

**Take down policy**

If you believe that this document breaches copyright please contact us at:

[openaccess@tue.nl](mailto:openaccess@tue.nl)

providing details and we will investigate your claim.

OXYGEN EVOLUTION ON  
 $\text{NiCo}_2\text{O}_4$  ELECTRODES

JOHAN HAENEN

OXYGEN EVOLUTION ON  
 $\text{NiCo}_2\text{O}_4$  ELECTRODES

# OXYGEN EVOLUTION ON $\text{NiCo}_2\text{O}_4$ ELECTRODES

PROEFSCHRIFT

TER VERKRIJGING VAN DE GRAAD VAN DOCTOR IN DE  
TECHNISCHE WETENSCHAPPEN AAN DE TECHNISCHE  
HOGESCHOOL EINDHOVEN, OP GEZAG VAN DE RECTOR  
MAGNIFICUS, PROF. DR. S.T.M. ACKERMANS, VOOR EEN  
COMMISSIE AANGEWEZEN DOOR HET COLLEGE VAN  
DEKANEN IN HET OPENBAAR TE VERDEDIGEN OP  
VRIJDAG 28 JUNI 1985 TE 14.00 UUR

DOOR

JOHAN GODELIEVE DANIEL HAENEN

GEBOREN TE HASSELT



Dit proefschrift is goedgekeurd door  
de promotoren Prof. E. Barendrecht  
en Prof. J. Schoonman  
co-promotor Dr. W. Visscher

Voor Inge

## CONTENTS

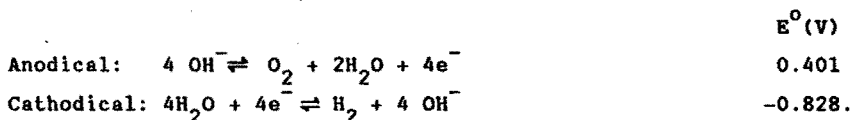
1. INTRODUCTION	1
2. LITERATURE REVIEW	2
2.1. Introduction	2
2.2. The metal oxides	2
2.3. Perovskite oxides $ABO_3$	8
2.4. Spinel oxides $AB_2O_4$	10
2.4.1. Crystal structure of spinel compounds	13
2.4.2. Electrophysical parameters of $NiCo_2O_4$	15
2.5. Literature	17
3. PREPARATION	23
3.1. Introduction	23
3.2. Experimental	24
3.2.1. Electrode preparation	24
3.2.2. Physical characterization	25
3.2.3. Electrochemical characterization	26
3.3. Results and discussion	26
3.3.1. Preparation parameters	26
3.3.1.1. Influence of the decomposition temperature and duration of the heat treatment	27
3.3.1.2. Influence of the number of coatings and catalyst loading	30
3.3.1.3. Influence of the anion in the metal salts and the solvent	35
3.3.1.4. Ageing phenomena and long-term performance	36
3.3.2. Comparison of Teflon-bonded and non Teflon-bonded electrode structures	39
3.4. Literature	44
4. OXYGEN EVOLUTION REACTION KINETICS	45
4.1. Introduction	45
4.2. Experimental	46
4.2.1. Electrode preparation	46
4.2.2. Electrochemical characterization	46

4.3. Results	47
4.3.1. Tafel lines	52
4.3.2. Temperature dependence	57
4.3.3. Effect of the electrolyte concentration	60
4.4. Discussion	69
4.5. Literature	69
5. ELECTROCHEMICAL CHARACTERIZATION	71
5.1. Introduction	71
5.2. Experimental	72
5.3. Freshly prepared $\text{NiCo}_2\text{O}_4$ electrodes	76
Results and discussion	
5.3.1. General features of the cyclic voltammogram	76
5.3.2. Rest potential of $\text{NiCo}_2\text{O}_4$	77
5.3.3. Effect of the potential scan rate	79
5.3.4. Effect of the catalyst loading	84
5.3.5. Effect of the heat treatment	87
5.3.6. Galvanostatic charging curves	94
5.3.7. Aprotic medium	95
5.3.8. Rotating ring-disc electrodes	97
5.3.9. Correlation between the anodic and cathodic processes	104
5.3.10. Cyclic voltammetric behaviour of $\text{Co}_3\text{O}_4$	112
5.3.11. Correlation of the observed peak potentials with standard potentials	113
5.4. Ageing phenomena: Influence of the limit potentials on the cyclic voltammetric behaviour	115
5.4.1. Introduction	115
5.4.2. Results	116
5.4.3. Discussion	128
5.5. Literature	131
6. NON-ELECTROCHEMICAL CHARACTERIZATION	134
6.1. Introduction	134
6.2. Thermogravimetric analysis	134
6.3. BET surface area determination	137
6.4. X-ray diffraction	140

6.5. Temperature programmed reduction	144
6.5.1. Introduction	
6.5.2. Experimental	145
6.5.3. Results and discussion	
6.6. X-ray and Auger photoelectron spectroscopy	152
6.6.1. Introduction	
6.6.2. Experimental	153
6.6.3. Results and discussion	154
6.6.4. Conclusions	162
6.7. Literature	163
7. NICKEL COBALT ALLOYS	165
7.1. Introduction	165
7.2. Experimental	
7.2.1. Electrode preparation	
7.2.2. Electrochemical characterization	
7.2.3. Ellipsometry	166
7.3. Results and discussion	166
7.3.1. Electrochemical characterization	166
7.3.2. Ellipsometry	175
7.4. Literature	188
8. GENERAL CONCLUSIONS	189
8.1. Literature	194
ACKNOWLEDGEMENTS	195
LIST OF SYMBOLS	196
SUMMARY	198
SAMENVATTING	200
CURRICULUM VITAE	202
DANKWOORD	203

## 1. INTRODUCTION

In recent years a growing interest in the electrolysis of water can be noticed, particularly after the energy crisis of 1973. The expected shortage of fossil fuels, i.e. petroleum, natural gas and coal, and the increasing load imposed on the environment by the production of carbon dioxide (green house effect) make an energy system relying on hydrogen, a proposition worth to be considered. This fuel can be produced from the abundant source water. The pertinent reactions in the electrolysis of water, with their electrochemical equivalent of free enthalpy change, the standard potential, are in alkaline medium:



Moreover, there is a necessity for an energy storage medium. Both, daily and seasonally, the consumption of energy varies considerably, while an increasing use of nuclear, solar, and wind energy can be expected. Since, nuclear, and, particularly, solar and wind energy are difficult to adapt to a varying demand, an efficient conversion of these forms of energy into an energy carrier that can be stored more easily, is desirable. Utilization of this off-peak energy for the production of hydrogen, and oxygen must be envisaged.

Hydrogen may become economically viable as a general purpose fuel. Water electrolysis is a suitable alternative to other hydrogen production methods, because it can make use of a variety of non-fossil energy sources, ranging from nuclear to wind energy. In this context, hydrogen is a good, even the only candidate for a universal energy carrier, also because it can be transmitted in pipelines, and thus can be delivered to users in a conventional way.

However, the economic constraints, and the significant technological breakthroughs needed to launch the "Age of Hydrogen", have not yet been overcome, respectively realized. One of the major problems in this conversion of electrical into chemical energy refers to the oxygen evolving anode; the high anodic overpotential is the main cause of efficiency loss in water electrolyzers. These kinetic overpotentials find their origin in the low value of the rate constants for the pertinent reactions of oxygen evolution, i.e. the high activation

enthalpy, which is strongly influenced by the substrate on which the heterogeneous reaction takes place, i.e. the anode material. Furthermore, the anodic overpotential increases due to the ohmic potential drop over the electrode-electrolyte interfase, in the electrolyte and as a result of gas bubble formation during oxygen evolution. Summarizing, it can be stated that search for a good oxygen anode must be concentrated on the selection of an anode material which should satisfy the following requirements:

1. a high electrocatalytic activity, expressed by a high exchange current density  $i_0$ , and a low Tafel slope  $b$ .
2. a high electrical conductivity.
3. be stable against chemical influences.
4. a rapid and easy way of preparing, which provides a high mechanical stability of the active layer.
5. a cheap and easily available material.

One of the most promising anode materials is  $\text{NiCo}_2\text{O}_4$ .

Though numerous articles have been published on the anodic performance of  $\text{NiCo}_2\text{O}_4$  electrodes, investigation of the influence of the preparation technique, and conditions on the anodic performance, the kinetics and mechanism of the electrocatalytic reaction, and the characterization of the  $\text{NiCo}_2\text{O}_4$  surface features are questions which have been answered to a lesser extent. A study of these problems will give, at least partly, insight into the complicated process of oxygen evolution, but also may help in developing better oxygen evolution electrocatalysts.

#### Outline of the thesis.

In this thesis an extensive investigation of  $\text{NiCo}_2\text{O}_4$ , prepared by thermal decomposition, was carried out. A brief literature review of the electrocatalysis of oxygen evolution, and possible electrocatalysts, is given in chapter 2. A systematic study of the preparation parameters such as the decomposition temperature, catalyst loading, etc., was carried out in chapter 3 in order to establish the optimum deposition conditions with respect to its electrocatalytic activity. The kinetics of the oxygen evolution reaction were examined in chapter 4 with galvanostatic steady-state measurements as function of the

temperature, and concentration of the electrolyte. The  $\text{NiCo}_2\text{O}_4$  catalyst was characterized in chapter 5, using electrochemical techniques such as cyclic voltammetry, the galvanostatic charging method, and the rotating ring-disc electrode, and in chapter 6, using non-electrochemical techniques such as X-ray diffraction, temperature programmed reduction, ESCA and Auger. Chapter 7 reports a comparison of the thermally prepared  $\text{NiCo}_2\text{O}_4$  electrodes with the electrochemically formed oxides on nickel-cobalt alloys, using cyclic voltammetry, kinetic analysis, and ellipsometry. This thesis is concluded with a general discussion in chapter 8.



## 2. LITERATURE REVIEW

### 2.1. Introduction

The study of the oxygen evolution reaction goes back to the early days of electrode kinetics [1,2], particularly with the work of Bowden [3] and Hoar [4].

From a general evaluation of metals as electrocatalysts for oxygen evolution, Miles reported that in alkaline solution [5] a good electrocatalytic activity is exhibited by Ni, Fe, and the noble metals, whereas in acid solution [6] the following sequence of activity was found  $\text{Ir} \approx \text{Ru} > \text{Pd} > \text{Rh} > \text{Pt} > \text{Au}$ ; nearly all other metals either dissolved, or passivated. The most serious problem faced in the use of metal anodes is the progressive, slow increase of the potential with time.

Nickel has for long been known as a very suitable anode material for oxygen evolution [7-10], and is used in most commercial water electrolyzers, which usually operate at 70 to 90°C in 30 to 50% KOH. The voltage efficiency amounts to 60-70% at current densities of  $2 \text{ kA m}^{-2}$ , with a current efficiency of 100% [11]. The metal is stable under anodic polarization in alkaline solution, and the overpotential is reasonable [8,12-15]. However, the potential drifts unavoidably towards more anodic values with long-term anodic performance [15,16]. Oxygen evolution occurs on an oxide surface, where the average oxidation state of the Ni-ions is 3+ [17]. It has been suggested that  $\text{Ni}^{3+}$  presumably converts to  $\text{Ni}^{4+}$  at higher potentials [12,18]. This valence state is inactive for oxygen evolution, and, therefore, causes the progressive deactivation of the anode.

### 2.2. The metal oxides.

There is evidence that thermally prepared nickel oxide [19], and thermally oxidized nickel [20] are electrocatalytically more active than the electrocatalytically grown oxide. Alloys of nickel with a number of other metals, especially, Ir and Ru have been explored for use [21]. However, after prolonged oxygen evolution the

oxide layer on the Ni-Ir, and Ni-Ru alloys predominantly comprises nickel oxide, and thus behave as a Ni 'metal' electrode.

A large number of exhaustive reviews have been written on oxide growth and oxygen evolution on metals and metal alloys [22-33]. Mostly, gas evolving anodic reactions are implicitly related to oxide electrodes, in that the case of oxygen evolution on 'bare metal' electrodes is practically unknown [22]. Since the oxygen evolution reaction takes place at an oxide layer on the metal, it can be concluded that the properties of the metal oxide determine the electrocatalytic activity. Hence, it is logically to investigate the oxides as candidate materials. Therefore, this review will be mainly confined to the work on bulk oxide electrodes.

A comparative investigation of the anodic performance of a number of thermally prepared metal oxides in alkaline solution was carried out by Srinivasan et al. [34], who found the following activity sequence for oxygen evolution:  $Ru > Ir \approx Pt \approx Rh \approx Pd \approx Ni \approx Os \gg Lo \gg Fe$ . The much poorer performance of Co and Fe oxides might be due to their instability during prolonged anodic polarization. The increase in the electrocatalytic activity of thermally prepared oxides is partly due to the increase of roughness. Among the metal oxides the anodic performance of Ru and Ir oxide was generally found to be superior, as illustrated by figure 2.1 which shows the E-log i relationships for oxygen evolution on various thermally prepared oxides.

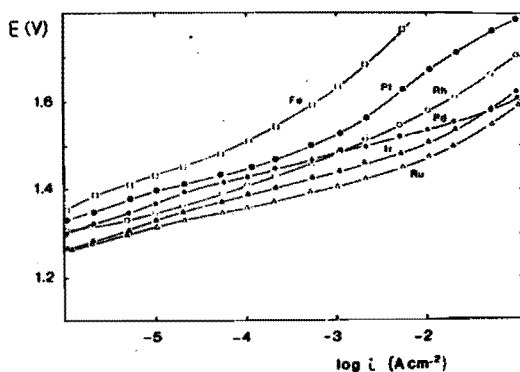


Fig. 2.1. Tafel lines for oxygen evolution in alkaline medium on various thermally prepared oxides. Data from ref. [41].

An extensive review of  $\text{RuO}_2$ -based electrodes was given by Trasatti and Lodi [35]. These electrodes are known for their use as anodes in the chlor-alkali cells [36-38], where these so-called Dimensionally Stable Anodes (DSA) as invented by Beer [39], with high corrosion resistance, and electrocatalytic activity, have replaced the graphite electrodes.

The oxygen evolution on  $\text{RuO}_2$ -based electrodes proceeds in acidic [40,41] as well as in alkaline solution [19,40,42]. Ru oxide, prepared by thermal decomposition on an inert substrate like Pt or Ti, has the highest known initial electrocatalytic activity for oxygen evolution in acid electrolyte [34,41,43-46], but this oxide is not stable in an acidic environment; also the oxygen overpotential increases with time [47,48]. The stability exhibits by such electrodes in alkaline medium is even less satisfactory [41,49]. The kinetic parameters have been studied in detail, both in strongly acidic [40,41] as well as in strongly alkaline solution [19,42,50], and they do not vary substantially going from pH 0 to 2 or, from pH 11 to 14. The Tafel slope at moderate current densities [19,40,47-50] is around 0.040 V, and seems to increase at higher current densities [46,47,49].

An interesting aspect is that oxygen evolution takes place at even lower overpotentials on Ru 'metal' [41,51] which, however, undergoes marked dissolution irrespective of the solution pH [52,53]. In the E-range where oxygen is evolved, Ru metal is covered with a thick layer of hydrous  $\text{RuO}_2$  [54-57].

$\text{IrO}_2$  is a relatively good electrocatalyst, but not as good as  $\text{RuO}_2$ , as follows from the Tafel line behaviour in figure 2.1 [42].

It has been reported that enhanced oxygen evolution takes place at Ir [18,58-60], Rh [61,62], and Ru [63], covered with a thick hydrous oxide, grown by a potential multicycling procedure. These electrocatalytically formed oxides are expected to behave as the corresponding thermal oxides. However, these thick hydrous oxide layers are unstable toward dissolution and are totally destroyed at higher potentials. Summarizing, it can be concluded that the noble metal oxides Ru and Ir are electrocatalytically good anode materials for oxygen evolution. However, these materials are too expensive for technological applications.

Recent research into developing new anodic materials is directed towards the utilization of transition metal oxides. These mixed oxides can be divided into two classes, i.e. the perovskite oxides (the mineral  $\text{CaTiO}_3$ ), presented by the formula  $\text{ABO}_3$ , and the spinel oxides, presented by the formula  $\text{AB}_2\text{O}_4$  with a crystal structure identical to the compound  $\text{MgAl}_2\text{O}_4$ . Both mixed oxides exhibit interesting features for the oxygen evolution reaction.

No satisfactory explanation has yet been given for the different overpotential values on different substrates at particular current densities. So, there is no answer to the question "Which are the factors governing the choice of oxides for the evolution of oxygen?"

Up to now, electrocatalysis is still mainly an experimental branch of electrochemistry, although its ultimate goal is to predict the electrocatalytic properties of materials on the basis of fundamental structural and electronic parameters. The most useful and reasonable guides are still correlations, where electrocatalytic properties are assessed on a relative scale by way of comparison with other physico-chemical properties of materials. Therefore, as a rule, data from experiments in the gas phase on oxidic catalysts are employed. A review of the possible factors on which a predictive basis for the choice (design and optimization) of electrocatalysts may be established, was given by Trasatti and Lodi [35].

Matsumoto et al. [65-71,80] have advanced an electronic theory to explain the behaviour of perovskite oxides both in the reduction, and the evolution of oxygen. According to these authors, the first step of the oxidation of water or  $\text{OH}^-$  to adsorbed OH takes place through the  $\sigma^*$  band, which is considered to extend up to the surface where  $e_g$  orbitals of the metal ion overlap with the  $sp_\sigma$  orbital of the adsorbing oxygenated intermediates. Thus, the degree of the orbital overlap at the surface may be predicted by the degree of the orbital overlap in the bulk. This concept predicts the catalytic activity of the oxide having the  $\sigma^*$  band to be high. This theory is an attempt to place electrocatalysis on a predictive basis which involves the intrinsic properties of the solids.

Tseung and Jasem [16,88,89] have put forward a guideline for the choice of semiconducting oxides for the evolution of oxygen in alkaline media. They emphasized the role of the metal/metal oxide or the

lower metal oxide/higher metal oxide couple in determining the minimum potential for oxygen evolution. This consideration, and other essential requirements such as electrical resistivity and corrosion resistance, led to the choice of  $\text{NiCo}_2\text{O}_4$  and Li-doped  $\text{Co}_3\text{O}_4$  spinel oxides as active electrocatalysts.

### 2.3. Perovskite oxides $\text{ABO}_3$ .

A detailed review of the physicochemical, and electrochemical properties of perovskite oxides was given by Tamura et al. [64]. Not all these oxides are suitable for use as electrocatalysts in strong caustic solutions, because of their excessively high resistivity or their lack of corrosion resistance with respect to the electrolyte. The evolution of oxygen has been studied essentially in alkaline medium on  $\text{SrFeO}_3$  [65],  $\text{SrFe}_{0.9}\text{M}_{0.1}\text{O}_3$  (with M = Ni, Co, Ti or Mn) [66],  $\text{La}_{1-x}\text{Sr}_x\text{MnO}_3$  [67],  $\text{La}_{0.7}\text{Pb}_{0.3}\text{MnO}_3$  [68],  $\text{LaCoO}_3$  [72,78],  $\text{La}_{1-x}\text{Sr}_x\text{CoO}_3$  [69],  $\text{La}_{1-x}\text{Ba}_x\text{CoO}_3$  [72-76],  $\text{La}_{1-x}\text{Sr}_x\text{Fe}_{1-y}\text{Co}_y\text{O}_3$  [70],  $\text{La}_{1-x}\text{Sr}_x\text{Fe}_{1-y}\text{Ni}_y\text{O}_3$  [71],  $\text{NiLn}_2\text{O}_4$  (with Ln = La, Pr or Nd) [77],  $\text{Ni}_{0.2}\text{Co}_{0.8}\text{LaO}_3$  [78], and  $\text{Nd}_{1-x}\text{Sr}_x\text{CoO}_3$  [79]. In figure 2.2 the Tafel lines for the oxygen evolution reaction on various perovskite-type oxides in alkaline solution are compared. Table 2.1 summarizes the kinetic parameters like, if available, the exchange current densities,  $i_0$ , and Tafel slopes, b, and gives the values of the overpotential at the apparent current density of  $10 \text{ mA cm}^{-2}$ . The parameter  $a (= b \log i_0)$  is a better comparison for various materials, since the best electrocatalyst is one with a high  $i_0$  and low b value. The activity for oxygen evolution at  $\text{La}_{1-x}\text{Sr}_x\text{MnO}_3$  ( $0 \leq x \leq 0.4$ ) [67] increases with the value of x up to a maximum of 0.4, as seen in figure 2.2. Fairly good electrocatalytic properties were observed on  $\text{SrFeO}_3$  electrodes [65] (Fig. 2.2). However, dissolution of the electrode was observed above 1.60 V vs. RHE. Matsumoto et al. [66] reported that the anodic dissolution is substantially suppressed by the substitution of Fe with M = Ni or Co in  $\text{SrFe}_{0.9}\text{M}_{0.1}\text{O}_3$ , and that the catalytic activity increased ( $\text{SrFe}_{0.9}\text{Ni}_{0.1}\text{O}_3$  in figure 2.2).  $\text{La}_{1-x}\text{Sr}_x\text{CoO}_3$  electrodes appeared to be suitable in alkaline medium [69], because anodic dissolution scarcely occurred, and the activity of the electrode with  $x = 0.4$  was higher than that of  $x = 0.2$ .

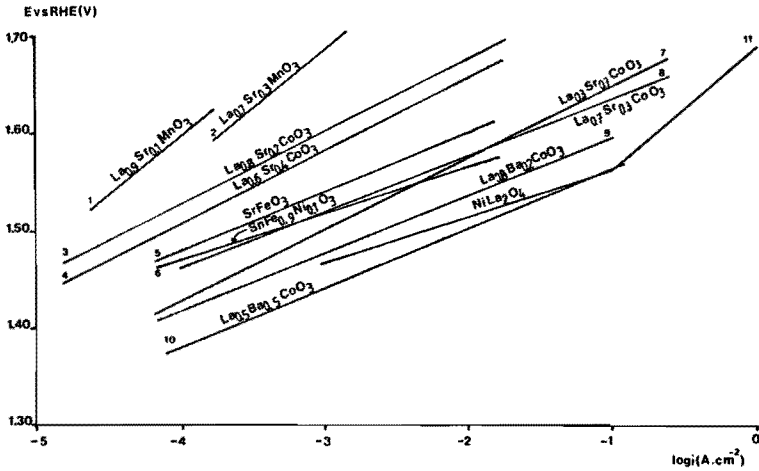


Fig. 2.2. Tafel lines for oxygen evolution in alkaline medium on various perovskite oxides. References: 1,2 [67]; 3,4 [69]; 5 [65]; 6 [66]; 7,8,9,10 [72]; 11 [77].

Table 2.1: Kinetic parameters of oxygen evolution on perovskites.

Electrode; medium <sup>1)</sup>	b(V)	$i_0$ (A cm <sup>-2</sup> )	a(V) <sup>2)</sup>	$\eta$ (V) at 10 mA cm <sup>-2</sup>	Ref.
SrFeO <sub>3</sub> I	0.062	$1.2 \cdot 10^{-8}$	0.49	0.39	65
SrFe <sub>0.9</sub> Ni <sub>0.1</sub> O <sub>3</sub> I	0.040	$6.6 \cdot 10^{-11}$	0.40	0.30	66
SrFe <sub>0.9</sub> Co <sub>0.1</sub> O <sub>3</sub> I	0.045	$3.2 \cdot 10^{-11}$	0.43	0.35	66
La <sub>0.7</sub> Pb <sub>0.3</sub> MnO <sub>3</sub> I	0.095	$1 \cdot 10^{-9}$	0.86		68
La <sub>0.8</sub> Sr <sub>0.2</sub> CoO <sub>3</sub> I	0.065	$3 \cdot 10^{-9}$	0.55	0.44	69
La <sub>0.6</sub> Sr <sub>0.4</sub> CoO <sub>3</sub> I	0.065	$7.4 \cdot 10^{-9}$	0.53	0.41	69
La <sub>0.8</sub> Ba <sub>0.2</sub> CoO <sub>3-y</sub> III	0.057	$4.8 \cdot 10^{-4}$	0.19	0.30	72
La <sub>0.5</sub> Ba <sub>0.5</sub> CoO <sub>3-y</sub> III	0.059	$2.6 \cdot 10^{-3}$	0.15	0.27	72
La <sub>0.7</sub> Sr <sub>0.3</sub> CoO <sub>3-y</sub> III	0.059	$1.1 \cdot 10^{-4}$	0.23	0.34	72
La <sub>0.3</sub> Sr <sub>0.7</sub> CoO <sub>3-y</sub> III	0.074	$2.3 \cdot 10^{-3}$	0.20	0.34	72
NiLa <sub>2</sub> O <sub>4</sub> II	0.040	$2.4 \cdot 10^{-5}$	0.19	0.29	77

1) I : 1 M KOH; 25°C

II : 6 M KOH; 25°C

III : 6 M KOH; room temperature

2)  $a = b \log i_0$

Kobussen et al. [72-76] found that Ba doping is more effective than Sr doping of  $\text{LaCoO}_3$ , and that within each set of electrodes the activity increased with doping, as seen in figure 2.2. Oxides with perovskite type structure like  $\text{La}_{1-x}\text{Sr}_x\text{Fe}_{1-y}\text{Co}_y\text{O}_3$  [70], and  $\text{La}_{1-x}\text{Sr}_x\text{Fe}_{1-y}\text{Ni}_y\text{O}_3$  [71] have been synthesized, and it was found that the catalytic activity for the oxygen evolution reaction increased with increasing x and y values in the composition range of the perovskite single phase, whereas the resistivity decreased. No appreciable difference in the electrocatalytic behaviour was observed for the perovskite-like oxides  $\text{NiLn}_2\text{O}_4$  with Ln = La, Nd or Pr [77], which are very promising anode materials, as illustrated by  $\text{NiLa}_2\text{O}_4$  in figure 2.2. The oxygen evolution reaction on perovskite oxides [70-77] has been explained by applying the theory of  $\sigma^*$  band formation [72], which is the same as that proposed for oxygen reduction on perovskite oxides [86].

#### 2.4. Spinel oxides $\text{AB}_2\text{O}_4$ .

The spinel oxides, especially  $\text{NiCo}_2\text{O}_4$ , are also very promising anode materials. A review of the properties of the spinel oxides was given by Tarasevich and Efremov [81]. The use of  $\text{NiCo}_2\text{O}_4$  as an electrocatalyst for oxygen evolution in alkaline solution was suggested by Tseung and Jasem [16]. A maximum in the electrocatalytic properties for  $\text{Ni}_x\text{Co}_y\text{O}_4$ , both for reduction [34,82], and evolution [81], is observed when the Ni:Co mole ratio corresponds to the spinel  $\text{NiCo}_2\text{O}_4$ . The performance of  $\text{NiCo}_2\text{O}_4$  electrodes is better than that of lithiated NiO and Ni screens [83]. The activation energy is reported to be close to [19], or possibly slightly higher [84] than that of  $\text{RuO}_2$  based electrodes. The oxygen evolution reaction on  $\text{NiCo}_2\text{O}_4$  is controlled by two Tafel slope regions, i.e. at low  $\eta$  a slope of about 0.040 V [16,19,81, 85,86] or 0.060 V [87] increasing to a slope in the range of 0.070 to 0.120 V [30,16,81,85-87] at high  $\eta$ . The results may be complicated [88] by the formation of higher oxides, gas bubbles and emptying of the electrocatalyst pores. Problems related to the structure of the electrode have been discussed by Tseung et al. [16,83], who strongly favoured Teflon-bonded active layers.

However, Singh et al. [33] reported that  $\text{NiCo}_2\text{O}_4$  layers prepared by thermal decomposition are more active than Teflon-bonded electrodes. Tseung et al. [89] carried out long-term endurance tests on Teflon-bonded  $\text{NiCo}_2\text{O}_4$  electrodes, prepared by the cryochemical synthesis [82], by evolving oxygen at a current density of  $1 \text{ A cm}^{-2}$  at  $85^\circ\text{C}$  in 45% KOH for 3000 h with less than 50 mV increase in overpotential. Vandenborre and Leysen [90] found that the performance of  $\text{NiCo}_2\text{O}_4$ , prepared via thermal decomposition, was the best of four electrocatalysts studied, and, exhibited a stable potential for over 2000 h of operation at a current density of  $1 \text{ A cm}^{-2}$  at  $85^\circ\text{C}$  in 50% KOH.

Shub et al. [91] reported that oxygen evolution at  $\text{Co}_3\text{O}_4$  in acidic medium takes place together with corrosion and dissolution of the layer. A linear Tafel line is observed in a narrow potential range (1.45 to 1.55 V), with a slope of about 0.06 V.  $\text{Co}_3\text{O}_4$  is anodically more stable as the pH of the solution increases [84,88,92-97]. Shalaginov et al. [98] have investigated a series of  $\text{Co}_3\text{O}_4$  electrodes in alkaline solution, prepared at different temperatures between 300 and  $450^\circ\text{C}$ , and observed a decrease in activity with increasing preparation temperature. Belova et al. [93] have related this effect to a decrease in excess oxygen in the film as the firing temperature is increased. Tamura et al. [94,95] have prepared  $\text{Co}_3\text{O}_4$  film anodes by thermal decomposition of an aqueous solution of  $\text{Co}(\text{NO}_3)_2 \cdot 6\text{H}_2\text{O}$ . The anodic polarization characteristics in 1 M KOH were found to be greatly affected by the kind of metal substrate (Ni, Co, Fe, Ti, Nb, Ta or Pt) used. Among them, the  $\text{Co}_3\text{O}_4/\text{Fe}$  electrode has the lowest oxygen overpotential, being comparable to those of  $\text{RuO}_2/\text{Ti}$ ,  $\text{IrO}_2/\text{Ti}$  or  $\text{RhO}_2/\text{Ti}$  [99], i.e. about 0.04 V at  $100 \text{ mA cm}^{-2}$ . A mechanistic study of the oxygen evolution was carried out on preanodized Teflon-bonded  $\text{Co}_3\text{O}_4$ , and Li-doped  $\text{Co}_3\text{O}_4$  electrodes [99,105] in 5 M KOH. The anodic performance was found to increase with increase in Li-doping. A Tafel slope of 0.060 V was observed on all the oxides, and it was suggested that the  $\text{Co}^{3+}$ -ions are the major active sites.



Cast magnetite has long been used [100,101] as an anode in technological applications like the chlorine and chlorate production. However, this material is not a good anode for oxygen evolution because of its relatively high overpotentials [102]. The activation energy for oxygen evolution in alkaline solution is  $109 \text{ kJ mol}^{-1}$  [103], which can be compared with  $59 \text{ kJ mol}^{-1}$  for Pt 'metal'. Mixed oxides of Fe and Ti, Ta and Co have been tested [104] for oxygen evolution in acidic solution. The overvoltage is approximately the same on all these oxides, and compared to  $\text{Fe}_3\text{O}_4$ , a decrease in the corrosion rate has been noticed.  $\text{M}_x\text{Fe}_{3-x}\text{O}_4$  ferrites with  $\text{M} = \text{Mg}, \text{Zn}, \text{Mn}, \text{Co}$  and  $\text{Ni}$  have found [105] to be much more corrosion resistant than  $\text{Fe}_3\text{O}_4$ , with a maximum for  $\text{M} = \text{Ni}$ . The spinel ferrites  $\text{Ni}_x\text{Fe}_{3-x}\text{O}_4$  [106],  $\text{Co}_{3-x}\text{Fe}_x\text{O}_4$ , and  $\text{Mn}_{3-x}\text{Fe}_x\text{O}_4$  [107] have been investigated for oxygen evolution with the purpose of establishing a relationship between the magnetic and the electrocatalytic properties. The oxygen evolution occurs at an appreciable rate on  $\text{NiFe}_2\text{O}_4$  and  $\text{CoFe}_2\text{O}_4$  with a common slope of about 0.04 V.

Figure 2.3 presents a summary of the better anode electrocatalysts in alkaline medium. It must be noted that in this figure the work of different authors has been compared based on, consequently, different physical forms of the catalyst, different roughness factors and porosities of the active layers, different concentration and temperatures of the electrolytes, different conditioning of the electrodes prior to the kinetic study, etc.

From this set of data, it follows that the best electrocatalysts for oxygen evolution presently are  $\text{NiCo}_2\text{O}_4$ ,  $\text{NiLa}_2\text{O}_4$ ,  $\text{La}_{0.5}\text{Ba}_{0.5}\text{CoO}_3$  and  $\text{RuO}_2$ . In particular oxides containing Co and Ni ions in the lattice are excellent. The presence of Co in these compounds is certainly important. Co as a metal (substrate) has been shown to exhibit a lower  $\eta$  for the oxygen evolution reaction in alkaline medium than the commonly used Ni electrodes [16].

Therefore, one of the most promising anode materials in alkaline solution is the spinel oxide  $\text{NiCo}_2\text{O}_4$ . From a fundamental point of view, a lowering of the large  $\eta$  is the most important challenge. However, on practical basis, the long-term stability is an even relevant parameter on which a possible choice is made.  $\text{NiCo}_2\text{O}_4$  has shown to be stable in alkaline water electrolysis [89,90] for over 3000 h.

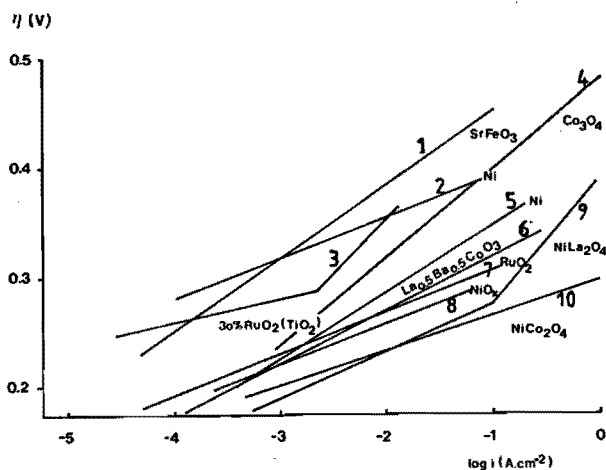


Fig. 2.3. Summary of the Tafel lines of anode electrocatalyst in alkaline medium. References: 1[65]; 2[12]; 3[46]; 4[97]; 5[21]; 6[72]; 7[50]; 8[19]; 9[77]; 10[88].

#### 2.4.1. Crystal structure of spinel compounds.

The unit cell of the ideal spinel structure, named for the mineral spinel  $MgAl_2O_4$ , is face centered cubic, with a large unit cell containing eight formula units [108]. In this ideal structure the anions form a cubic close packing, in which the cations partly occupy the tetrahedral and octahedral interstices as shown in figure 2.4.a. The unit cell contains 32 anions forming 64 tetrahedral interstices, and 32 octahedral interstices; of these 8 tetrahedral and 16 octahedral interstices are occupied by cations. The general formula of compounds with spinel structure is  $A[B_2]X_4$ . [Octahedrally coordinated ions are by convention placed within square brackets]. Here A is a tetrahedrally surrounded cation, B an octahedrally surrounded one and X an anion. There are twice as many B cations as A cations. A and B are transition elements and X = O, S, Se or Te.

The non-ideal structure is derived from the ideal one by moving the anions from their ideal positions in a [111] direction away from the nearest tetrahedral ion. The deviation of ideal structure  $u = 0.375$ , which corresponds to perfect close packing of the anions. In reality,  $u$  is often slightly larger, this implies larger A-sites and B-sites.

The position of the metal ions is fixed by the symmetry of the structure. Each anion in the spinel structure is surrounded by one A and three B cations. The B-B distance is considerably shorter than the A-A distance, for the anion octahedra surrounding the B cations share edges, whereas the anion tetrahedra surrounding the A cations do not have any contact.

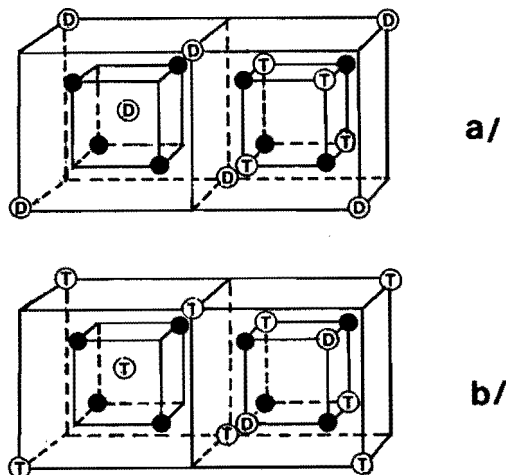


Fig. 2.4. (a) Two octants of the normal spinel structure. Open circles with D and T refer to di- and trivalent cations, respectively. Solid circles to oxygen anions (b). Same for inverted spinel.

The oxide spinels ( $X = 0$ ) are ionic crystals. In the oxide spinels, two main combinations of valence states of the cations occur: the 2-3 spinels, where  $\text{NiCo}_2\text{O}_4$  belongs to, and the 4-2 spinels. The oxide spinels will also tolerate a large number of metal ion vacancies. The existence of these metal ion vacancies frequently makes it difficult to prepare spinels with the stoichiometric metal: oxygen ratio.

An interesting property of compounds with the spinel structure is the so-called cation distribution, i.e. the distribution of the cations present among the tetrahedral and octahedral sites. In principle, the following cation distributions can be distinguished, with the 2-3 spinels (i.e.  $\text{Me}^{2+}[\text{Me}^{3+}]_2\text{O}_4$ ) as an example.

(i) Normal spinel or regular spinel:  $A[B_2]O_4$ . (Fig. 2.4a)

If the tetrahedral sites are occupied by A-ions and the octahedral sites by B-ions, e.g.  $Me^{2+}[Me^{3+}]_2O_4$ , then the divalent metal ions are on tetrahedral sites.

(ii) Inverse spinel:  $B[AB]O_4$ . (Fig. 2.4b)

If the tetrahedral sites are occupied by B-ions and the octahedral sites by a random arrangement of A and B-ions, e.g.

$Me^{3+}[Me^{2+}Me^{3+}]O_4$ , then the divalent metal ions are on octahedral sites.

(iii) Intermediate spinel: between normal and inverse spinel.

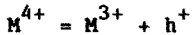
#### 2.4.2. Electrophysical parameters of $NiCo_2O_4$ .

The relevant electrophysical parameters of the oxide, within the framework of the bandmodel, are the electrical conductivity, electron work function, concentration and mobility of current carriers, and the forbidden band gap. These parameters are highly sensitive to the chemical, and structural composition of the oxide system, and therefore depend on the method and the conditions of the oxide synthesis. The reported electrophysical characteristics [81] of the Ni-Co-O system are listed in table 2.2. An increase in the conductivity, carrier mobility, and carrier concentration was found, going from simple to spinel oxides.

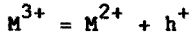
Table 2.2: Electrophysical characteristics of Ni-Co-O system [81]

Co content (atom %)	Conductivity ( $S\ m^{-1}$ )	Hole concentration ( $m^{-3}$ )	Carrier mobility ( $m^2\ V\ s^{-1}$ )
0	$8 \cdot 10^{-3}$	$3 \cdot 10^{27}$	$4.6 \cdot 10^{-3}$
25	$3 \cdot 10^{-1}$	-	-
67	60	$9 \cdot 10^{27}$	$1.4 \cdot 10^1$
82	20	$8 \cdot 10^{27}$	6.4
100	$2 \cdot 10^{-2}$	$9.5 \cdot 10^{26}$	$5.6 \cdot 10^{-2}$

$\text{NiCo}_2\text{O}_4$  and  $\text{Co}_3\text{O}_4$  are p-type semiconductors. In addition p-type conductivity varies considerably with deviations from stoichiometry. The electrical conductivity is expected to increase with increasing stoichiometric excess of oxygen. The conductivity of  $\text{NiCo}_2\text{O}_4$  has been reported to be  $10 \text{ S m}^{-1}$  [82], and that of  $\text{Co}_3\text{O}_4$   $10^{-2} \text{ S m}^{-1}$  [109]. The appearance of ions of different valencies in spinels is mainly determined by the structural defects. The excess oxygen in cobalt is thought [91] to determine the defect structure, in which a part of the  $\text{M}^{3+}$  ions is converted into  $\text{M}^{4+}$ ,



where  $\text{h}^+$  stands for an electron. Another type of defect structure may arise when part of the  $\text{M}^{3+}$ -ions in the octahedral sites are converted into  $\text{M}^{2+}$  [110],



In both situations the electron holes are assumed to migrate via a hopping mechanism.

The other electrophysical parameters have been scarcely investigated in the literature. The electron work function of Ni-Co oxides, when the Ni:Co ratio changes, has been determined [110]. The ratio of 1 to 2, i.e.  $\text{NiCo}_2\text{O}_4$ , showed the highest value, 6.23 eV.

The forbidden band gap for  $\text{NiCo}_2\text{O}_4$  is about 0.1 to 0.4 eV [111]. No data are available regarding a correlation between the forbidden band gap, and the activity of complex oxides in redox reactions.

## 2.5. Literature

- [1] A. Coehn and Y. Osaka, *Z. Anorg. Chem.* 34, 86 (1903).
- [2] F. Foerster and A. Piquet, *Z. Electrochem.* 10, 714 (1904).
- [3] P. Bowden, *Proc. Roy. Soc., A* 126, 107 (1929).
- [4] T.P. Hoar, *Proc. Roy. Soc., A* 142, 628 (1933).
- [5] M.H. Miles, *J. Electroanal. Chem.* 60, 89 (1975).
- [6] M.H. Miles and M.A. Thomason, *J. Electrochem. Soc.* 123, 1459 (1976).
- [7] P.W.T. Lu and S. Srinivasan, *J. Appl. Electrochem.* 9, 269 (1979).
- [8] M.H. Miles, G. Kissel, P.W.T. Lu and S. Srinivasan, *J. Electrochem. Soc.* 123, 332 (1976).
- [9] E.A. Chapman, *Chem. Process Eng.* 46, 387 (1965).
- [10] S. Srinivasan, F.J. Salzano and A.R. Landgrebe (Eds.), *Industrial Water Electrolysis*, The Electrochemical Society, Princeton (1978).
- [11] D.H. Smith in A.T. Kuhn (Ed.), *Industrial Electrochemical Processes*, Elsevier, Amsterdam, 127 (1971).
- [12] P.W.T. Lu and S. Srinivasan, *J. Electrochem. Soc.* 125, 1416 (1978).
- [13] B.E. Conway and P.L. Bourgault, *Can. J. Chem.* 40, 1690 (1962).
- [14] B.E. Conway, M.A. Sattar and D. Gilroy, *Electrochim. Acta* 14, 677 (1969).
- [15] R.F. Scarr, *J. Electrochem. Soc.* 116, 1526 (1969).
- [16] A.C.C. Tseung and S. Jasem, *Electrochim. Acta* 22, 31 (1977).
- [17] J.P. Hoare, *Nature* 241, 44 (1973).
- [18] S. Gottesfeld and S. Srinivasan, *J. Electroanal. Chem.* 86, 89 (1978).
- [19] G. Singh, M.H. Miles and S. Srinivasan in A.D. Franklin (Ed.), *Electrocatalysis on Non-metallic Surfaces*, NBS Spec. Publ. No. 455, U.S. Government Printing Office, Washington, 289 (1976).
- [20] V.S. Bagotskii, N.A. Shumilova and E.I. Khrushcheva, *Electrochim. Acta* 21, 919 (1976).
- [21] P.W.T. Lu and S. Srinivasan, *J. Electrochem. Soc.* 125, 265 (1978).

- [22] J.P. Hoare, *The Electrochemistry of oxygen*, Interscience, New York (1968).
- [23] M. Breitner in P. Delahay (Ed.), *Advances in Electrochemistry and Electrochemical Engineering*, Interscience, New York 1, 123 (1961).
- [24] J.P. Hoare in P. Delahay (Ed.), *ibid.* 6, 201 (1967).
- [25] J.P. Hoare in A.J. Bard (Ed.), *Encyclopedia of electrochemistry of the elements*, Marcel Dekker, New York 2, 191 (1974).
- [26] A. Damjanovic in J.O'M. Bockris and B.E. Conway (Eds.), *Modern Aspects of Electrochemistry*, Butterworths, London 5, 369 (1969).
- [27] A. Damjanovic and A.T. Ward in H. Bloom and F. Gutmann (Eds.), *Electrochemistry of the Past Thirty and Next Thirty Years*, Plenum, New York, 89 (1977).
- [28] A.J. Appleby in J.O'M. Bockris and B.E. Conway (Eds.), *ibid.* 9, 369 (1974).
- [29] J.O'M. Bockris in J.O'M. Bockris and B.E. Conway, *ibid.* 1, 180 (1954).
- [30] T. Erdey-Gruz. *Kinetics of Electrode Processes*, Wiley-Interscience, New York (1972).
- [31] A.J. Appleby, *Catal. Rev.* 4, 221 (1970).
- [32] L.D. Burke in S. Trasatti (Ed.), *Electrodes of Conductive metallic oxides*, Elsevier, Amsterdam, Part A, 3, 141 (1980).
- [33] B.E. Conway in *ibid.*, Part B, 9, 433 (1981).
- [34] M.H. Miles, Y.H. Huang and S. Srinivasan, *J. Electrochem. Soc.* 125, 1931 (1978).
- [35] S. Trasatti and G. Lodi in S. Trasatti (Ed.), *Electrodes of conductive metallic oxides*, Elsevier, Amsterdam, Part B, 10, 521 (1981).
- [36] J. Horacek and S. Puscharer, *Chem. Eng. Progr.* 67, 71 (1971).
- [37] O. De Nora, *Chem. Ing. Tech.* 42, 222 (1970); 43, 182 (1971).
- [38] A. Nidola, *Metall. Ital.* 66, 55 (1974).
- [39] H.B. Beer, *Britt* 855107 (1958); *CA* 55 (1961) 12115; 925080 (1960); *CA* 56 (1962).
- [40] G. Lodi, E. Sivieri, A. De Battisti and S. Trasatti, *J. Appl. Electrochem.* 8, 135 (1978).

- [41] C. Iwakura, K. Hirao and H. Tamura, *Electrochim. Acta* 22, 329, 335 (1977).
- [42] E. Yeager in A.D. Franklin (Ed.), *Electrocatalysis on Non-metallic Surfaces*, NBS Spec. Publ. No. 455, U.S. Government Printing Office, Washington, 203 (1976).
- [43] S. Trasatti and G. Buzzanca, *J. Electroanal. Chem.* 29, A1 (1971).
- [44] P. Ruetschi and P. Delahay, *J. Chem. Phys.* 23, 556 (1955).
- [45] D. Galizzioli, F. Tantardini and S. Trasatti, *J. Appl. Electrochem.* 4, 57 (1974); 5, 203 (1975).
- [46] D.V. Kokoulina, Y.I. Krasovitskaya and T.V. Iranova, *Sov. Electrochem.* 14, 398 (1978).
- [47] L.D. Burke, O. Murphy, J. O'Neill and S. Venkatesan, *J. Chem. Soc., Faraday Trans, I*, 73, 1659 (1977).
- [48] T. Laveka, *J. Appl. Electrochem.* 7, 221 (1977).
- [49] R.U. Bondar and E.A. Kalinovskii, *Sov. Electrochem.* 14, 633 (1978).
- [50] W. O'Grady, C. Iwakura, J. Huang and E. Yeager in M.W. Breiter (Ed.), *Electrocatalysis*, The Electrochemical society, Princeton, 286 (1974).
- [51] R.T. Atanasoski, B.Z. Nicolic, M.M. Jaksic, A. R. Despic, *J. Appl. Electrochem.* 5, 159 (1975).
- [52] L.D. Burke and T.O. O'Meara, *J.C.S. Faraday I* 68, 839 (1972).
- [53] L.D. Burke and D.P. Whelan, *J. Electroanal. Chem.* 103, 179 (1979).
- [54] D. Mitchell, D.A.J. Rand and R. Woods, *ibid.* 89, 11 (1979).
- [55] L.D. Burke and J.K. Mulcahy, *ibid.* 73, 207 (1976).
- [56] L.D. Burke, J.K. Mulcahy and S. Venkatesan, *ibid.* 81, 339 (1977).
- [57] S. Hadzi-Jordanov, H. Angerstein-Kozlowska, M. Vukovic and B.E. Conway, *J. Electrochem. Soc.* 125, 1471 (1978).
- [58] D.N. Buckley and L.D. Burke, *J. Chem. Soc. Faraday 1*, 71, 1447 (1975).
- [59] D.N. Buckley, L.D. Burke and J.K. Mulcahy, *ibid.* 1, 71, 1896 (1976).
- [60] E.J. Frazer and R. Woods, *ibid.* 102, 127 (1979).



- [61] L.D. Burke and E.J.M. O'Sullivan, *J. Electroanal. Chem.* 93, 11 (1978).
- [62] L.D. Burke and E.J.M. O'Sullivan, *ibid.* 97, 123 (1979).
- [63] R. Woods, *Isr. J. Chem.* 18, 118 (1979).
- [64] H. Tamura, H. Yoneyama and Y. Matsumoto in S. Trasatti (Ed.), *Electrodes of conductive metallic oxides*, Elsevier, Amsterdam, Part A, 6, 261 (1980).
- [65] Y. Matsumoto, J. Kurimoto and E. Sato, *J. Electroanal. Chem.* 102, 77 (1979).
- [66] Y. Matsumoto, J. Kurimoto and E. Sato, *ibid.* 25, 539 (1980).
- [67] Y. Matsumoto and E. Sato, *Electrochim. Acta* 24, 421 (1979).
- [68] Y. Matsumoto and E. Sato, *ibid.* 25, 585 (1980).
- [69] Y. Matsumoto, M. Manabe and E. Sato, *J. Electrochem. Soc.* 127, 811 (1980).
- [70] Y. Matsumoto, S. Yamada, T. Nishida and E. Sato, *ibid.* 127, 2360 (1980).
- [71] S. Yamada, Y. Matsumoto and E. Sato, *Denki Kagaku* 49, 269 (1981).
- [72] A.G.C. Kobussen, F.R. van Buren, T.G.M. Belt and H.J.A. Van Wees, *J. Electroanal. Chem.* 96, 123 (1979).
- [73] A.G.C. Kobussen and C.M.A. Mesters, *ibid.* 115, 131 (1980).
- [74] A.G.C. Kobussen, *ibid.* 126, 199 (1981).
- [75] A.G.C. Kobussen and G.H.J. Broers, *ibid.* 126, 221 (1981).
- [76] A.G.C. Kobussen, H. Willems and G.H.J. Broers, *ibid.* 142, 67 (1982); 142, 85 (1982).
- [77] G. Fiori, C. Mandelli, C.M. Mari and P.V. Scolari in T.N. Veziroglu and W. Seifritz (Eds.), *Hydrogen Energy System* 1, 193 (1978).
- [78] G. Fiori and C.M. Mari, *Electrocatalysis in the oxygen evolution*, Proceedings of the Third World Energy Conference, Tokyo Japan, 165 (1980).
- [79] T. Kudo, H. Obayashi and M. Yoshida, *J. Electrochem. Soc.* 124, 321 (1977).
- [80] Y. Matsumoto, H. Yoneyama and H. Tamura, *J. Electroanal. Chem.* 83, 237 (1977); 83, 245 (1977).

- [81] M.R. Tarasevich and B.N. Efremov in S. Trasatti (Ed.), *Electrodes of conductive metallic oxides*, Elsevier, Amsterdam, part A, 5, 221 (1980).
- [82] W.J. King and A.C.C. Tseung, *J. Electrochem. Soc.* 126, 1353 (1979).
- [83] A.C.C. Tseung, S. Jasem and M.N. Mahmood in T.N. Veziroglu and W. Seifritz (Eds.), *Hydrogen Energy Systems*, Pergamon Press, Oxford, vol. I, 215 (1976).
- [84] N. Sato and T. Ohtsuka, *J. Electrochem. Soc.* 125, 1735 (1978).
- [85] P. Rasiyah and A.C.C. Tseung, *ibid.* 130, 2384 (1983).
- [86] B.N. Efremov and M.R. Tarasevich, *Sov. Electrochem.* 17, 1392 (1981).
- [87] C.R. Davidson, G. Kissel and S. Srinivasan, *J. Electroanal. Chem.* 132, 129 (1982).
- [88] S.M. Jasem and A.C.C. Tseung, *J. Electrochem. Soc.* 126, 1353 (1979).
- [89] A.C.C. Tseung, P. Rasiyah, M.C.M. Manu and K.L.K. Yeung, *Hydrogen as an Energy Vector*, Commission of European Communities, 199 (1978).
- [90] H. Vandenborre and R. Leysen in E. Vecchi (Ed.), *International Society of Electrochemistry 31st Meeting*, 319 (1980).
- [91] D.M. Shub, A.N. Chemodanov and V.V. Shalaginov, *Sov. Electrochem.* 14, 507 (1978).
- [92] M.B. Konovalov, V.I. Bystrov and V.L. Kubasov, *Sov. Electrochem.* 12, 1160 (1976).
- [93] I.D. Belova, V.V. Shalaginov, B.Sh. Galyamov, Yu.E. Roginskaya and D.M. Shub, *Russ. J. Inorg. Chem.* 23, 161 (1978).
- [94] A. Honji, C. Iwakura and H. Tamura, *Chemistry Letters*, 1153 (1979).
- [95] C. Iwakura, C. Henji and H. Tamura, *Electrochim. Acta* 26, 1319 (1981).
- [96] M.R. Tarasevich, A.M. Khutornoi, F.Z. Sabirov, G.I. Zakharkin and V.N. Storozhenko, *Sov. Electrochem.* 12, 259 (1976).
- [97] P. Rasiyah and A.C.C. Tseung, *J. Electrochem. Soc.* 130, 365 (1983).

- [98] V.V. Shalaginov, I.D. Belova, Yu.E. Roginskaya and D.M. Shub, *ibid.* 14, 1485 (1978).
- [99] H. Tamura and C. Iwakura, *Denki Kagaku* 43, 674 (1975).
- [100] M. Hayes and A.T. Kuhn, *J. Appl. Electrochem.* 8, 327 (1978).
- [101] A.T. Kuhn and P.M. Wright in A.T. Kuhn (Ed.), *Industrial Electrochemical Processes*, Elsevier, Amsterdam, 525 (1971).
- [102] P.D. Allen, N.A. Hampson and G.J. Bignold, *J. Electroanal. Chem.* 99, 299 (1979).
- [103] Y. Yoneda, *Bull. Chem. Society Japan* 22, 266 (1949).
- [104] G.N. Trusov and E.P. Gochaliera, *Sov. Electrochem.* 15, 333 (1979).
- [105] S. Wakabayashi and T. Aoki, *J. Phys. Colloq.*, 271 (1977).
- [106] J. Orehotsky, H. Huang, C.R. Davidson and S. Srinivasan, *J. Electroanal. Chem.* 95, 233 (1979).
- [107] C. Iwakura, M. Nishioka and H. Tamura, *The Chem. Soc. of Japan* 1, 1136 (1982); 8, 1294 (1982).
- [108] G. Blasse, *Philips Res. Reports* 18, 383 (1963).
- [109] G. Feuillade, R. Coffre and G. Outhier, *Ann. Radio-electr.* 21, 105 (1966).
- [110] A.M. Trunov, V.A. Presnov, M.V. Uminskii, O.F. Rakityanskaya, T.S. Bakutina and A.N. Kotseruba, *Sov. Electrochem.* 11, 552 (1975).
- [111] M.V. Uminskii, N.N. Verenikina, A.M. Trunov and V.A. Presnov, *Sov. Electrochem.* 7, 554 (1971).

### 3. PREPARATION

#### Abstract<sup>1</sup>

$\text{NiCo}_2\text{O}_4$  was investigated as anode material for alkaline water electrolysis. This catalyst was prepared by thermal decomposition of metal salts and this rapid and simple technique gives reproducible results. A study of the preparation parameters shows that factors, such as decomposition temperature, duration of the heat treatment and catalyst loading, determine the morphology of the oxide layer and so influence the performance of the catalyst. The conductivity of the oxide layer was found to change markedly with the final heat treatment. It is shown that alternative Teflon-bonded  $\text{NiCo}_2\text{O}_4$  electrode structures give approximately the same activity.

#### 3.1. Introduction

The oxygen evolution reaction during water electrolysis is of special interest, because of its high anodic overvoltage. The main cause of efficiency losses is the bad electrocatalytic properties of the present anode materials. A good anode material should have a high exchange current density ( $i_0$ ) and a low Tafel slope ( $b$ ).

Recent research into developing new anode materials has been mainly directed to the use of transition metal oxides. One of the most promising materials in an alkaline electrolyte is the p-type, spinel oxide  $\text{NiCo}_2\text{O}_4$ , which is, moreover, a cheap electrode material. A review at  $\text{NiCo}_2\text{O}_4$  and other spinels was given by Trasatti and Lodi [1]. Many papers have been devoted to a study of the kinetics of these materials [2-7] and different preparation techniques have been used, e.g.: thermal decomposition [5,8], cryochemical synthesis [3,4,8] and coprecipitation [4,8]. Sometimes an effect of the substrate (Pt or Ni) has been noticed [2]. Tseung et al. [3] have investigated the use of Teflon-bonded  $\text{NiCo}_2\text{O}_4$  electrodes

---

<sup>1</sup> Publication: J.G.D. Haenen, W. Visscher, E. Barendrecht  
J. Appl. Electrochem. 15, 29 (1985).

and found an increased electrochemical activity. Singh et al. [5], on the other hand, noticed that non Teflon-bonded electrodes have higher activity and stability than Teflon-bonded systems; moreover, the Teflon incorporation influences the gas bubble evolution and this also affects the anodic behaviour.

Comparison of the results of various authors is difficult because of different preparation techniques, which result in differences in porosity and hence surface area. Furthermore, the various conditions for the deposition of the  $\text{NiCo}_2\text{O}_4$  layer on the substrate appear to have a large influence on its activity and, moreover, discrepancies are evident in the way the  $iR$ -drop is corrected. Therefore a systematic study was carried out to establish the kinetic parameters of the oxygen evolution reaction at  $\text{NiCo}_2\text{O}_4$  electrodes with emphasis on the preparation technique. The thermal decomposition method was chosen because it results in electrodes with a high mechanical stability, and this preparation technique is an easy and rapid one. Furthermore with this technique, both Teflon and non Teflon-bonded electrodes can be prepared, whereas with  $\text{NiCo}_2\text{O}_4$  prepared via cryochemical synthesis (freeze drying followed by decomposition in vacuum) or coprecipitation, only Teflon-bonded electrodes can be made. In this work the optimum deposition conditions for thermal decomposition were determined, and the anodic performance of Teflon bonded and non-Teflon bonded  $\text{NiCo}_2\text{O}_4$  electrodes were compared.

### 3.2. Experimental

#### 3.2.1. Electrode preparation

##### Preparation of porous $\text{NiCo}_2\text{O}_4$ electrodes

All porous  $\text{NiCo}_2\text{O}_4$  electrodes used in this study were prepared by thermal decomposition on a substrate. In principle, the preparation method was as follows.  $\text{Ni}(\text{NO}_3)_2 \cdot 6 \text{H}_2\text{O}$  and  $\text{Co}(\text{NO}_3)_2 \cdot 6 \text{H}_2\text{O}$ , mixed in stoichiometric amounts, were dissolved in water or in alcohol. A nickel screen of 30 mesh ( $1 \text{ cm}^2$ ) was spot-welded to a nickel wire.

After cleaning it was preheated for 3-5 minutes in an oven at  $T_F$  °C ( $T_F$  = temperature of the final heat treatment). The nickel screen was dipped into the solution of the nitrates, dried in hot air to remove the solvent before decomposition, and heated in the furnace in air at  $T_F$  °C for 3 to 5 minutes to decompose the nitrates. This process was repeated until the desired loading had been reached. The electrode was then finally cured at  $T_F$  °C for  $t_F$  hours ( $t_F$  = duration of the final heat treatment) to complete the thermal decomposition.

#### Preparation of Teflon-bonded $NiCo_2O_4$ electrodes.

In order to compare the Teflon-bonded and non Teflon-bonded electrode structure, the same preparation method of the  $NiCo_2O_4$  catalyst, namely thermal decomposition, was used for both electrode structures.

The Teflon-bonded electrodes were prepared by mixing the appropriate amounts of Teflon (Teflon 30 N Dupont or Teflon powder 0.3 - 0.5  $\mu$ ) and  $NiCo_2O_4$  catalyst in a small bottle, and dispersing it in an ultrasonic bath. The resulting mixture was then painted onto the nickel gauze. The electrode was then dried in hot air and finally cured in air in a furnace at 300°C for 1 hour.

The  $NiCo_2O_4$  catalyst was prepared according to two variants. In the first [9,10], the two nitrates,  $Ni(NO_3)_2 \cdot 6H_2O$  and  $Co(NO_3)_2 \cdot 6H_2O$  were weighted in the exact proportion Ni:Co = 1:2 and dissolved in water. The solution was evaporated to dryness until there were no more  $NO_2$  fumes. The black powder was heated in an electric furnace in air for  $t_F$  hours at temperature  $T_F$ . In the second variant, the  $NiCo_2O_4$  catalyst material was scraped from the nickel carrier of porous  $NiCo_2O_4$  electrodes, prepared as described before.

#### 3.2.2. Physical characterization

An X-ray pattern of the samples was obtained using MoK $\alpha$  or FeK $\alpha$  radiation and compared with ASTM data for nickel cobalt oxide.

Thermogravimetric analysis was applied to study the course of the decomposition as a function of temperature with a Mettler thermoanalyzer 2.

### 3.2.3. Electrochemical characterization

All experiments were performed in a thermostatted, (25°C) three compartment Pyrex glass cell containing 5 M KOH, prepared from Merck potassium hydroxide p.a. and double distilled H<sub>2</sub>O. A piece of 7 x 2.5 cm platinum foil was used as the counter electrode and the potential of the working electrode was measured against the reversible hydrogen electrode (RHE) or the mercury(II)-oxide electrode (Hg/HgO, 5 M KOH; 0.926 V vs. RHE, 25°C), via a Luggin capillary close to the working electrode.

To determine the electrocatalytic activity steady-state galvanostatic measurements were carried out. The electrodes were firstly subjected to anodic polarization for 30 minutes to 2 hours at the highest current densities to be studied, to ensure the presence of higher oxides on the surface (see chapter 5). The potentials were measured with decreasing current densities. The time between each reading was 5 minutes. The time required to reach steady-state was in all cases within 2 minutes, and usually within 1 minute.

The ohmic potential drop between the tip of the Luggin capillary and the working electrode was measured by the current interruptor technique [11].

## 3.3. Results and Discussion

### 3.3.1. Preparation parameters

The following parameters were investigated: temperature of the thermal decomposition, duration of the final heat treatment, catalyst loading, number of coatings, type of anion in the metal salts, solvent and support material.

### 3.3.1.1. Influence of the decomposition temperature and duration of the heat treatment.

In order to investigate the effect of the heat treatment on both the electrocatalytic activity and the mechanical stability of the deposit, the temperature and duration of heat treatment was studied. The temperature range between 250°C and 600°C was examined whilst the time of heat treatment was varied between 15 minutes and 100 hours.

Although there is a possibility of segregation of the individual oxides, NiO and CoO, during decomposition, the spinel structure could be confirmed for all the electrodes by X-ray analysis in the temperature range 250° - 400°C. With temperatures above 400°C and longer time of heat treatment, lines corresponding to another cubic phase, presumably NiO appeared. The thermogravimetric diagram for  $\text{NiCo}_2\text{O}_4$  is in agreement with X-ray analysis for  $\text{NiCo}_2\text{O}_4$  and reveals furthermore that the decomposition of the  $\text{NiCo}_2\text{O}_4$  spinel sets in at temperatures above 400°C. These results are in agreement with those obtained by other authors [8,12,13].

#### Decomposition temperature.

Figure 3.1 shows the effect of the temperature of the heat treatment on the anodic performance of  $\text{NiCo}_2\text{O}_4$  for oxygen evolution at  $200 \text{ mA.cm}^{-2}$  (iR-corrected). Lowering the temperature of the final heat treatment leads to an increase in the electrochemical activity of the catalyst. Actually, the figure can be divided into two parts. In the spinel-only area (Part A: below 400°C), the oxygen overvoltage decreases with decreasing temperature of heat treatment. In part B (above 400°C), where the decomposition in binary oxides of the spinel structure starts, the oxygen overvoltage increases faster with increasing temperature  $T_F$ . It was suggested [8,12,13,20] that the  $\text{NiCo}_2\text{O}_4$  decomposition takes place as follows:  $3 \text{ NiCo}_2\text{O}_4 \rightarrow 3 \text{ NiO} + 2 \text{ Co}_3\text{O}_4 + [\text{O}]$ . From the data without iR-drop correction and with iR-correction it appears that the resistance of the oxide layer increases because of the decomposition of the  $\text{NiCo}_2\text{O}_4$  spinel structure.



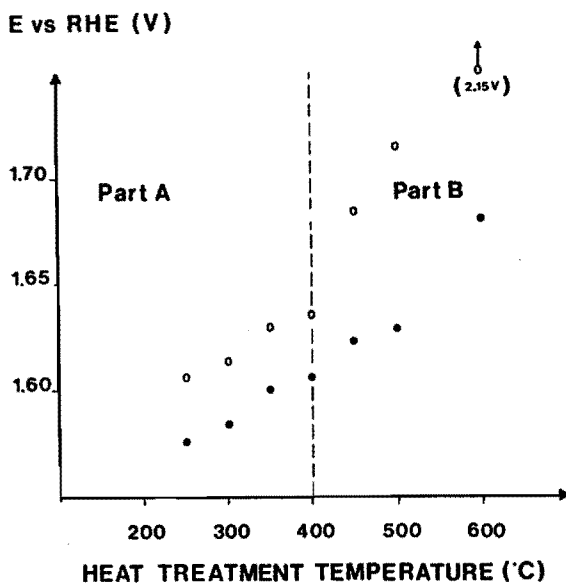


Fig. 3.1: Effect of the temperature of the final heat treatment on the anodic performance of  $\text{NiCo}_2\text{O}_4$  electrodes for oxygen evolution at  $200 \text{ mA cm}^{-2}$  in 5 M KOH,  $25^\circ\text{C}$ .

[●] :  $200 \text{ mA cm}^{-2}$ . (iR-corrected)

[○] :  $200 \text{ mA cm}^{-2}$  (not iR-corrected)

Heat treatment			Catalyst loading
$T_F$ (°C)	$t_F$ (h)		( $\text{mg cm}^{-2}$ )
250	-	1	20.85
300	-	1	18.65
350	-	1	20.40
400	-	1	17.70
450	-	1	14.20
500	-	1	18.95
600	-	5	17.35

However, the heat treatment temperature of 250°C at a duration of 1 hour appears insufficient to complete the decomposition and, consequently, the mechanical stability was not satisfactory since the electrode tends to shed the  $\text{NiCo}_2\text{O}_4$  oxide layer: nearly half of the catalyst loading was lost. The stability of the other electrodes was good. No visible damage was observed.

The surface morphology of the  $\text{NiCo}_2\text{O}_4$  layer was found to be dependent on the preparation temperature. Visual and microscopic observation of the  $\text{NiCo}_2\text{O}_4$  electrodes indicate that the roughness factor increases with decreasing temperature. Our results are in agreement with the work of Tamura et al. [14,15], who observed the same tendency for  $\text{Co}_3\text{O}_4$  electrodes, also prepared by thermal decomposition. The difference in oxygen overvoltage can be ascribed partly to the change in the roughness factor. Many authors suggest the existence of a relation between high surface area and low oxygen overvoltage. This is in contradiction with the observation of Tseung et al. [4,8] who concludes that there is no correlation between the surface area and the electrochemical performance and who suggests that for maximum activity the formation of a metastable spinel on the point of losing its oxygen is required.

Duration of the heat treatment.

The duration of the heat treatment,  $t_p$ , which was varied between 15 minutes and 100 hours, gives no significant changes in activity or iR-corrected results in the temperature range up to 400°C.

However, the conductivity changes with the final heat treatment, as is shown in table 3.1, for all temperatures from 400°C on. Because the conductivity of the oxide layer seems to decrease with increasing duration of the heat treatment, it is advisable to restrict the duration. It has been established [8,12,13] that with increase in temperature and duration of the heat treatment, above 400°C a cubic phase, presumably high resistance NiO appears, due to the decomposition of the spinel structure; consequently, we might expect a decrease in conductivity. It is, however, noted here that at the same Luggin

TABLE 3.1

EFFECT OF THE DURATION OF THE FINAL HEAT TREATMENT ON THE MAGNITUDE OF THE  $iR$ -DROP  
(AT THE SAME LUGGIN CAPILLARY TO WORKING ELECTRODE DISTANCE) GIVEN AS

$iR$  (TEMP.  $T_F(^{\circ}C)$ , DURATION  $t_F$  (h)).

$iR$  (300 $^{\circ}C$ , 1h)

TEMPERATURE OF THE HEAT TREATMENT ( $^{\circ}C$ )	DURATION OF THE HEAT TREATMENT $t_F$ (h)				
	1	5	10	24	100
250	1	-	1	-	-
300	1	1	1	1	1
400	1	1.5-2	2	2	> 2
450	2	-	2-3	-	-
500	> 3	-	-	-	-
600	-	20	-	-	-

capillary to working electrode distance the measured  $iR$ -drop increases for prolonged 400 $^{\circ}C$  heat treatment; the powder X-ray patterns, however, confirmed the spinel structure. The  $iR$ -drop for the 400 $^{\circ}C$  - 1 hour heat treatment is nearly the same as for the  $NiCo_2O_4$  electrodes prepared in the temperature range 250 $^{\circ}C$  - 350 $^{\circ}C$ , which did not change with increasing duration of heat treatment. The lower limit of detection with the D.S. powder X-ray diffraction method is about 5%, so some NiO might be present in the layer after treatment at 400 $^{\circ}C$ . However, the magnitude of the  $iR$ -drop for the 450 $^{\circ}C$  treatment is not larger (in which case a cubic phase is definitely detected).

The lack of knowledge of the magnitude of the ohmic drop can give rise to misleading conclusions. The  $iR$ -corrected results show nearly the same electrocatalytic activity for the 400 $^{\circ}C$  series, but the electrode resistance increases when the duration increases.

### 3.3.1.2. Influence of the number of coatings and catalyst loading.

Concentration of the dipping solution.

Firstly, the concentrations of the mixed nitrates in water was varied,

in a constant stoichiometric ratio of Ni:Co = 1:2. Table 3.2 shows for the same catalyst loading the effect of the concentrations of the nickel and cobalt nitrates, the number of coatings and the percentage of the holes per  $\text{cm}^2$  gauze which are completely filled up with  $\text{NiCo}_2\text{O}_4$ .

As the number of coatings increases, the electrocatalytic activity for oxygen evolution decreases. The  $\text{NiCo}_2\text{O}_4$  layers are prepared by repeated immersion in the mixed nitrate solution. With decreasing concentration of the dipping solution the number of coating layers must be increased, in order to obtain the same catalyst loading. If in that case the number of coatings (i.e. immersions) increases, a denser and smoother structure of the  $\text{NiCo}_2\text{O}_4$  layer is obtained with mostly open holes of the gauze substrate. If at constant catalyst loading the number of coatings decreases, the resulting  $\text{NiCo}_2\text{O}_4$  layer is rougher and the holes nearly all completely filled. In all cases the

TABLE 3.2

INFLUENCE OF THE NUMBER OF COATINGS AND CONCENTRATION RATIO OF THE MIXED NITRATES ON THE ANODIC PERFORMANCE OF  $\text{NiCo}_2\text{O}_4$  IN 5 N KOH, 25°C (iR-CORRECTED)

$\text{Ni}(\text{NO}_3)_2 \cdot 6\text{H}_2\text{O} : \text{Co}(\text{NO}_3)_2 \cdot 6\text{H}_2\text{O}$ (M)	1.0:2.0	$5 \cdot 10^{-1} : 1.0$	$2.5 \cdot 10^{-1} : 5 \cdot 10^{-1}$	$1 \cdot 10^{-1} : 2 \cdot 10^{-1}$	$5 \cdot 10^{-2} : 1 \cdot 10^{-1}$
NUMBER OF COATINGS	2	4	8	20	50
CATALYST LOADING (MG $\text{CM}^{-2}$ )	11.80	10.00	10.15	11.35	10.15
% OF THE HOLES WHICH ARE COMPLETELY FILLED UP (%)	85	40	0	0	0
POTENTIAL (mV) AT C.D.: (iR-CORRECTED)					
200 MA. $\text{CM}^{-2}$	1615	1633	1651	1672	1674
100 MA. $\text{CM}^{-2}$	1592	1616	1629	1652	1646

nickel wires of the screen were completely covered with  $\text{NiCo}_2\text{O}_4$  and the gauze profile was maintained.

The morphology of the nickel cobalt oxide layer is influenced by the rate of deposition of the layer. A gradual formation of the  $\text{NiCo}_2\text{O}_4$  electrode leads to a smoother structure in contrast to a faster deposition which gives a rougher  $\text{NiCo}_2\text{O}_4$  surface. Hence, we conclude that the total top surface area of the  $\text{NiCo}_2\text{O}_4$  layer is greater in the case of a highly concentrated solution. The difference in oxygen overpotential is a consequence of the difference in roughness of the electrode surface: the lower the overpotential, the rougher the surface. This is in contrast with the earlier mentioned observation of Tseung et al. [4,8].

#### Catalyst loading.

The variation in anodic performance with the catalyst loading can give an answer to the degree of utilization of the electrocatalyst surface. A visual observation of the course of the catalyst loading process shows that at lower loadings, up to  $5 \text{ mg cm}^{-2}$ , the nickel wires are not completely covered by the  $\text{NiCo}_2\text{O}_4$ . As the loading is increased further, the wires become completely covered and subsequently the holes at the centre of each mesh opening become filled, probably reaching then the maximum surface area. Finally, at higher loadings, the coating becomes much denser. The electrode surface is flattened and consequently the roughness decreases.

In the previous section, it has been shown that the number of coatings influences the morphology of the porous layer and hence the electrocatalytic activity.

In the stepwise deposition, which occurs from a more diluted dipping solution, (see figure 3.2), the catalyst loading has virtually no influence on the anodic performance, while the percentages of the holes per  $\text{cm}^2$  gauze which are filled increase slightly. This indicates that the utilization of the porous  $\text{NiCo}_2\text{O}_4$  electrode is limited to the top surface. The same effect was observed more clearly for a nickel plate as substrate.

## E vs RHE (V)

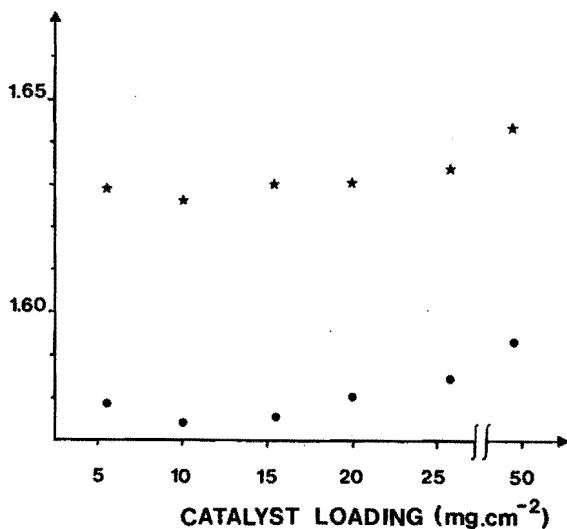


Fig. 3.2 : Influence of the catalyst loading on the anodic performance of  $\text{NiCo}_2\text{O}_4$  electrodes in 5 M KOH, 25°C at two current densities (iR-corrected).

Stepwise deposition (occurs from a more diluted dipping solution): 0.5 M  $\text{Ni}(\text{NO}_3)_2 \cdot 6 \text{ aq}$  : 1.0 M  $\text{Co}(\text{NO}_3)_2 \cdot 6 \text{ aq}$ .

Heat treatment: 300°C - 1 h.

[●] : 100 mA cm<sup>-2</sup>

[★] : 500 mA cm<sup>-2</sup>

Catalyst loading (mg cm <sup>-2</sup> )	5.50	10.00	15.50	20.00	25.75	49.50
Number of coatings	3	5	7	9	11	19
% of holes per cm <sup>-2</sup> which are completely filled up (%)	10	20	20	30	35	70

Figure 3.3 shows the result when the deposition proceeds from a more concentrated solution: the catalyst now seems to influence the performance. These differences in oxygen overpotentials are due to differen-

ces in roughness: in the range  $15\text{--}20 \text{ mg.cm}^{-2} \text{ NiCo}_2\text{O}_4$  maximum activity coincides with maximum roughness.

At extremely high loadings, the electrode resistance increases as a consequence of the denser structure.

E vs RHE (V)

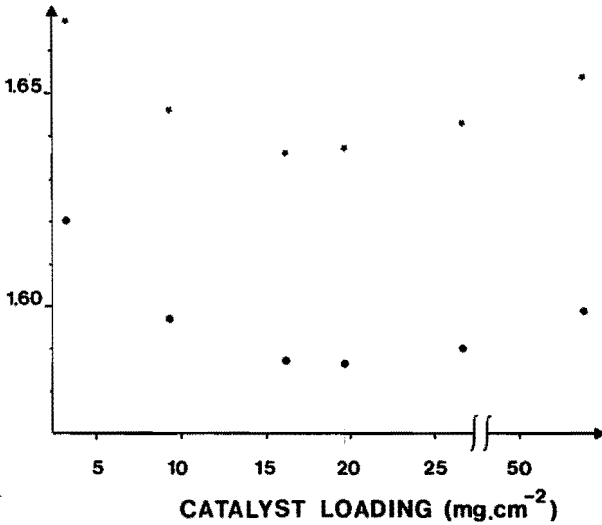


Fig. 3.3 : Influence of the catalyst loading on the anodic performance of  $\text{NiCo}_2\text{O}_4$  electrodes in 5 M KOH, 25°C at two current densities (iR-corrected).

Faster deposition (proceeds from a more concentrated solution):

1.0 M  $\text{Ni}(\text{NO}_3)_2 \cdot 6 \text{ aq}$  : 2.0 M  $\text{Co}(\text{NO}_3)_2 \cdot 6 \text{ aq}$ .

Heat treatment: 400°C - 1 h.

[●] : 100 mA cm<sup>-2</sup>

[★] : 500 mA cm<sup>-2</sup>

Catalyst loading (mg cm <sup>-2</sup> )	3.30	9.25	16.15	19.50	26.50	53.50
Number of coatings	1	2	3	4	5	9
% of holes per cm <sup>-2</sup> which are completely filled up (%)	40	85	85	85	95	100

### 3.3.1.3. Influence of the anion in the metal salts and the solvent.

#### Effect of the anion of the metal salts.

Anions of metal salts other than  $\text{NO}_3^-$ , such as  $\text{CH}_3\text{COO}^-$  and  $\text{Cl}^-$  have been examined for possible effects on the catalytic activity. The metal salt should be able to decompose in about the same temperature range and produce the  $\text{NiCo}_2\text{O}_4$  spinel only.

The experimental results for electrodes prepared under identical conditions did not show any difference in activity. In the previous section, it has been shown that the concentration of the mixed salt solution influences the morphology of the deposited layer and hence the anodic performance. The solubility of the mixed nitrates in water is the greatest of the various anions investigated; it was therefore decided to use the nitrates in the further study.

#### Solvent effect.

Different solvents, i.e. water and alcohols, were examined for the best deposition conditions. Non-aqueous solvents spread out better on the surface, and evaporate at lower temperatures. The  $\text{NiCo}_2\text{O}_4$  layer deposited from an alcohol solution has a lower oxygen overvoltage than the same electrode obtained from an aqueous solution (see figure 3.4). [The other preparation parameters were the same]. The percentage of the holes per  $\text{cm}^2$  gauze which are filled, shows the influence on the surface morphology.

Though there is a decrease in oxygen overpotential as a result of the use of an alcohol as solvent which spreads out better, there is a negative aspect: because of the smaller solubility of the mixed nitrates in alcohol as compared with water, a greater number of dips is required to obtain the same loading. This also affects the morphology. Under similar preparation conditions, the more interesting solvent appears to be 1-butanol (see figure 3.4). But there are no significant differences in overpotential, if for each solvent the more concentrated dipping solution is used for both water and BuOH.



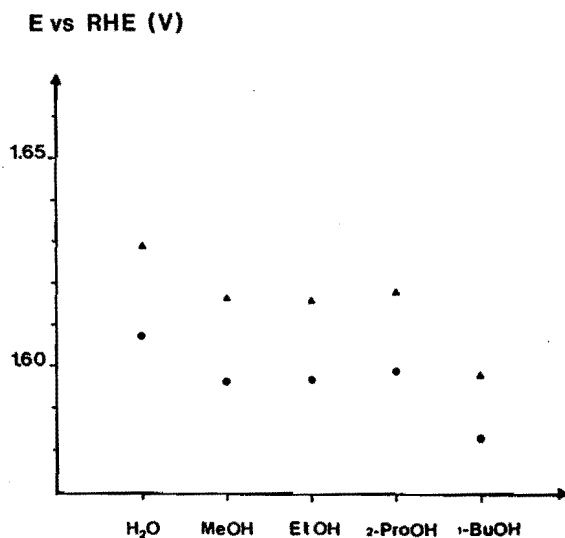


Fig. 3.4: Influence of the solvents of the dipping solution on the anodic performance of  $\text{NiCo}_2\text{O}_4$  electrodes in 5 M KOH, 25°C (iR-corrected).

[•] :  $100 \text{ mA cm}^{-2}$

[▲] :  $200 \text{ mA cm}^{-2}$

Heat treatment: 400°C - 1 h.

Concentration of the mixed nitrates:  $0.4 \text{ M Ni}^{2+} : 0.8 \text{ M Co}^{2+}$ .

Solvents	H <sub>2</sub> O	MeOH	EtOH	2-ProOH	1-BuOH
Catalyst loading ( $\text{mg cm}^{-2}$ )	13.60	12.40	13.45	15.90	14.75
% of holes per $\text{cm}^{-2}$ which are filled up (%)	25	70	45	45	70

#### 3.3.1.4. Ageing phenomena and long-term performance.

The effect of ageing was studied in order to compare our results with these of Tseung [16] and Davidson [17]. An initial decrease in performance of freshly prepared  $\text{NiCo}_2\text{O}_4$  electrodes at constant

current density can mostly be observed, see figure 3.5. After 1 hour, the anodic behaviour remains almost constant. Figure 3.6 shows the performance of  $\text{NiCo}_2\text{O}_4$  electrodes prepared at different temperatures and durations of heat treatment at  $500 \text{ mA cm}^{-2}$  during a 24 h run in 5 M KOH. The rate and magnitude of ageing is not always the same and varies with different parameters, like the electrode preparation and the applied current density. The increase in overpotential takes place only if the electrode is submerged in the electrolyte. If a porous  $\text{NiCo}_2\text{O}_4$  electrode is kept in air, even for several months, no change in the activity occurs. Study of the ageing phenomenon is continuing. The decline in performance may be ascribed to a surface modification, resulting in a decrease of the roughness of the electrode surface or to a chemical transformation by a change in valency states. Other authors [16] have mentioned partial charge compensation in the oxide surface by hydroxyl ions from the electrolyte.

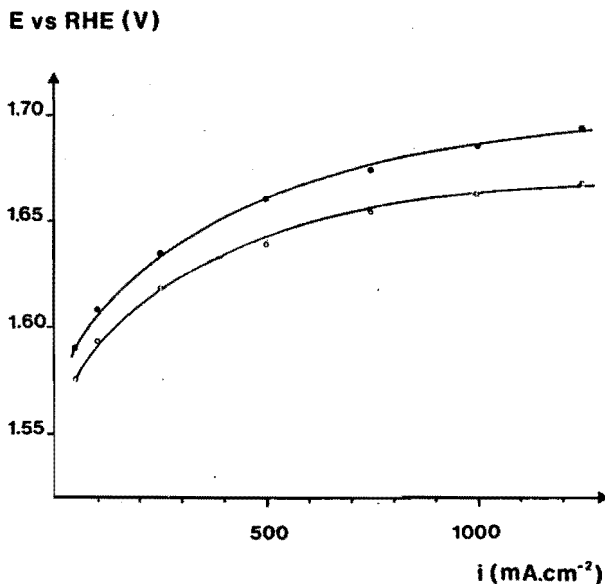


Fig. 3.5: Initial decrease in performance of a  $\text{NiCo}_2\text{O}_4$  electrode for oxygen evolution in 5 M KOH,  $25^\circ\text{C}$  ( $iR$ -corrected).

[o] : measurements taken immediately at freshly prepared electrode

[•] : after 1 h polarization at the highest current density.

## E vs RHE (V)

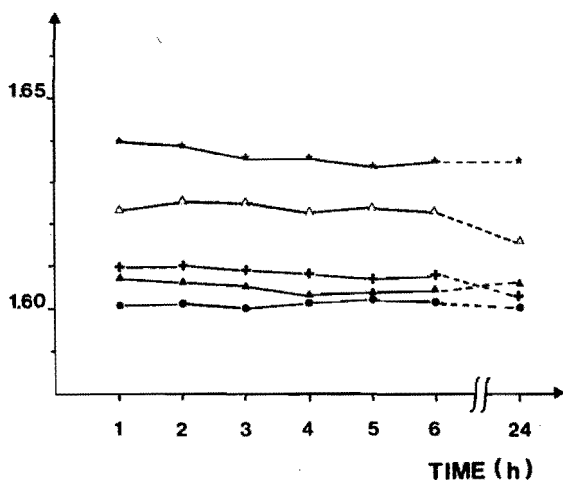


Fig. 3.6: Performance at  $500 \text{ mA cm}^{-2}$  (iR-corrected) during a 24 h run of  $\text{NiCo}_2\text{O}_4$  electrodes in 5 M KOH,  $25^\circ\text{C}$  prepared at different decomposition temperatures and durations of heat treatment.

Symbol	Heat treatment		Catalyst loading ( $\text{mg cm}^{-2}$ )
	$T_F$ ( $^\circ\text{C}$ )	$t_F$ (h)	
[★]	400	1	18.15
[Δ]	350	1	19.45
[+]	300	10	17.30
[▲]	300	1	20.60
[•]	250	10	19.70

In view of possible practical applications long-term stability tests were carried out for up to 350 hours continuous operation. It was noticed that after the earlier mentioned initial rapid decrease in anodic performance, only a small increase in oxygen overpotential was found. Table 3.3 shows data at 1, 250 or 350 hours (2nd column). At

the end of this long-term performance, the KOH solution was renewed and the potential was measured again, as shown in table 3.3 (see 3rd column), the values were found to be only slightly higher than the 1 hour data. The change of electrolyte is necessary because of the excessive water loss by evaporation and possible  $\text{CO}_2$  uptake. The porous electrodes were mechanical stable. This was checked by determining the loss of  $\text{NiCo}_2\text{O}_4$  particles by weighing before and after the long-term performance and was less than 3% after 300-600 h.

TABLE 3.3

LONG-TERM PERFORMANCE OF  $\text{NiCo}_2\text{O}_4$ -ELECTRODES FOR OXYGEN EVOLUTION IN 5 M KOH, 25°C (iR-CORRECTED)

CURRENT DENSITY ( $\text{mA}\cdot\text{cm}^{-2}$ )	POTENTIAL vs RHE, AFTER x HOURS (h) : (mV)	1 h AFTER CHANGING ELECTROLYTE (mV)	CATALYST LOADING ( $\text{MG}\cdot\text{CM}^{-2}$ )	$\text{Ni}^{2+} : \text{Co}^{2+}$ (M)	HEAT TREATMENT $T_F(^{\circ}\text{C})$ $t_F(\text{h})$
200	1 : 1615 250 : 1630	1620	17.75	$5\cdot 10^{-1} : 1.0$	400 - 1
200	1 : 1590 350 : 1635	1600	18.90	1.0 : 2.0	400 - 1
500	1 : 1605 250 : 1630	1620	23.00	1.0 : 2.0	320 - 1

### 3.3.2. Comparison of Teflon-bonded and non Teflon-bonded electrode structures.

Some authors [3,4,5] have observed differences in anodic performance as a consequence of the incorporation of Teflon in the catalyst. Therefore, the Teflon-bonded and non Teflon-bonded electrode structure were compared, with the  $\text{NiCo}_2\text{O}_4$  catalyst prepared by thermal decomposition for both electrode structures. The Teflon bonded electrodes were made as described earlier and the ratio of catalyst: Teflon was varied.

The measured R-values for Teflon-bonded  $\text{NiCo}_2\text{O}_4$  electrodes as a function of the Teflon content is shown in figure 3.7 for the same

Luggin capillary to working electrode distance. It is interesting to note that in the range 0-30% Teflon content the measured  $iR$ -drop is nearly the same and that beyond 30% there appears a sharp increase in the electrode resistance (30-40% is a transition range). It is evident that, as long as the volume of the Teflon aggregates is smaller than the volume of the catalyst aggregates, the latter will be in contact with each other.

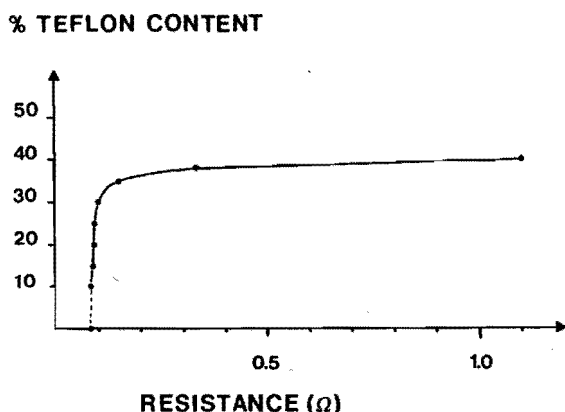


Fig. 3.7: Influence of the Teflon content (% w) on the electrode resistance of Teflon bonded  $\text{NiCo}_2\text{O}_4$  electrodes in 5 M KOH, 25°C.  
Catalyst loading:  $\pm 20 \text{ mg cm}^{-2}$ .

Figure 3.8 demonstrates the effect of the catalyst: Teflon ratio on the anodic behaviour of the Teflon-bonded  $\text{NiCo}_2\text{O}_4$  electrodes by applying the current interruptor technique. The  $iR$ -corrected curve also shows a decrease in performance with decreasing catalyst: Teflon ratio.

E vs RHE (V)

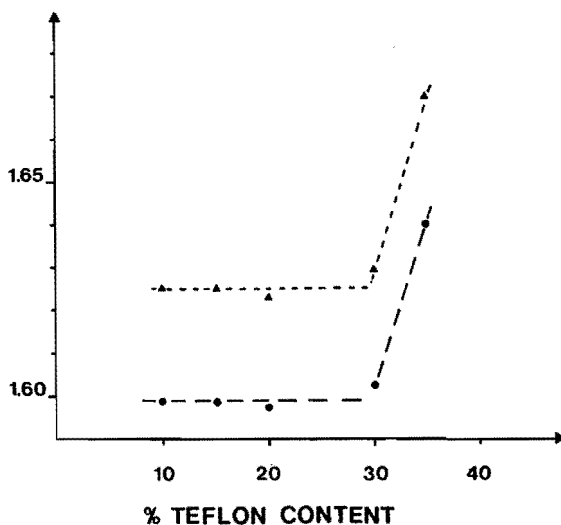


Fig. 3.8: Influence of the Teflon: catalyst ratio on the anodic behaviour of Teflon bonded  $\text{NiCo}_2\text{O}_4$  electrodes in 5 M KOH, 25°C (iR-corrected).

[●] : 100 mA cm<sup>-2</sup>

[▲] : 200 mA cm<sup>-2</sup>.

Oxygen bubbles formed on Teflon-bonded electrodes are larger than those formed on porous non Teflon-electrode surfaces. The bubble size increases, and the bubbles detach with greater difficulty with increasing Teflon content due to the increasing hydrophobicity of the catalyst surface. The larger bubble formation on the Teflon-bonded electrode surface leads to an increased resistance at higher current densities, and also reduces the electrochemically active surface available for oxygen evolution. The irregular detaching of larger bubbles hinders accurate measurements at high current densities during steady-state oxygen evolution.

TABLE 3.4

COMPARISON OF THE ANODIC PERFORMANCE OF TEFLON BONDED AND NON-TEFLON BONDED  $\text{NiCo}_2\text{O}_4$ -ELECTRODES IN 5 M KOH, 25°C (iR-CORRECTED). HEAT TREATMENT: 400°C - 1 TO 2 h.

RATIO $\text{NiCo}_2\text{O}_4$ : TEFLON	100 : 0	90 : 10	90 : 10	85 : 15	80 : 20
PREPARATION METHOD					
(1) BY EVAPORATION	(2)	(1)	(2)	(1)	(1)
(2) BY DIPPING					
CATALYST LOADING ( $\text{MG CM}^{-2}$ )	23.25	~ 24	~ 13	~ 24	~ 24
POTENTIAL (MV) AT C.D.:					
250 $\text{MA CM}^{-2}$	1615	1612	1625	1620	1613
100 $\text{MA CM}^{-2}$	1590	1585	1600	1593	1583

Table 3.4 shows a comparison of the anodic performance for Teflon-bonded and non Teflon-bonded  $\text{NiCo}_2\text{O}_4$  electrodes in which the  $\text{NiCo}_2\text{O}_4$  catalyst material was prepared by thermal decomposition with the same thermal treatment (duration  $t_F$  and temperature  $T_F$ ) and the same catalyst loading. The Teflon content was limited to a maximum of 20%. Beyond 10% Teflon content the structure was friable, and the  $\text{NiCo}_2\text{O}_4$  layer tended to fall off during oxygen evolution. It is seen that the alternative Teflon-bonded electrode structure gives about the same activity and ohmic potential drop as the porous electrode. Thermal decomposition by evaporation (first method) or by dipping (second method) did not significantly change the anodic performance. The influence of the catalyst loading on the anodic behaviour in case of the alternative electrode structure shows the same activity for loadings in the range 15-25  $\text{mg.cm}^{-2}$   $\text{NiCo}_2\text{O}_4$ , indicating that only the top surface is active. With respect to the substrate the same tendency was observed with the alternative and the porous electrode: at lower loadings a nickel gauze support material was more favourable than a nickel plate support. At higher loadings the electrode surface was flattened and, consequently, the electrocatalytic activity was the same. After careful examination of the data, we conclude that the catalytic activity of porous electrodes is at least comparable with the Teflon-bonded  $\text{NiCo}_2\text{O}_4$  electrodes. In no case was a superior behaviour of the Teflon-bonded electrodes observed.

In the literature, contradictory results have been reported about the effect of Teflon incorporation: according to Tseung et al. [3,4,17], the far better performance of the Teflon-bonded electrode structure is a result of the incorporation of Teflon in the catalyst ensuring greater utilization of the available catalyst surface, because the interior of the electrode is not completely denuded of electrolyte. This alternative structure is presented as a hydrophobic porous Teflon phase, intertwined with a porous hydrophylic catalyst phase. The comparison of Teflon-bonded with non Teflon-bonded electrode structure has been made with electrodes in which the  $\text{NiCo}_2\text{O}_4$  catalyst is prepared in the former structure by cryochemical synthesis (freeze drying followed by decomposition in vacuum) and in the latter by thermal decomposition. Results of Singh et al. [5] have shown that  $\text{NiCo}_2\text{O}_4$  layers prepared by the thermal decomposition method are more active than Teflon-bonded electrodes.

The results of our study indicate that mainly the top surface of the  $\text{NiCo}_2\text{O}_4$  electrode is electrochemically active, independently of the electrode structure. It has also been shown that the alternative Teflon-bonded  $\text{NiCo}_2\text{O}_4$  electrode gives about the same activity and no drastic changes with the catalyst loading have been observed for both structures. According to the criterion for the choice of semiconducting oxides for oxygen evolution reaction, presented by Tseung and Jasem [2,6], the potential of the metal/metal oxide or the lower metal oxide/higher metal oxide couple must be reached before oxygen evolution takes place. This hypothesis implies that the final step in the irreversible reaction of the oxygen evolution on a metal or metal-oxide surface takes place by the breakdown of a species in a high oxidation state, which is formed on the active site. Since our results show that only the top layer is active, it can be said that these active sites must be limited to the surface only. This is in agreement with the work of Rasiyah et al. [18], on Teflon-bonded electrodes, and of Hibbert [19], on porous  $\text{NiCo}_2\text{O}_4$  electrodes.



## 3.4. Literature

- [1] S. Trasatti and G. Lodi in S. Trasatti (Ed.), *Electrodes of conductive metallic oxides Part B*, Elsevier scientific publishing company, Amsterdam, 521 (1980).
- [2] A.C.C. Tseung and S. Jasem, *Electrochim. Acta* 22, 31 (1977).
- [3] A.C.C. Tseung, S. Jasem and M.N. Mahmood in T.N. Veziroglu and W. Seifritz (Eds.), *Hydrogen Energy systems*, Pergamon Press, Vol. I, 215 (1978).
- [4] M.C.M. Man, S. Jasem, K.L.K. Yeung and A.C.C. Tseung, *Hydrogen as an Energy vector*, Commission of the European Communities, Brussels, 255 (1978).
- [5] G. Singh, M.H. Miles and S. Srinivasan in A.D. Fromkin (Ed.), *Electrocatalysis on Non-metallic Surfaces*, N.B.S. Spec. Publ. 455, V.S. Government Printing Office, Washington, 289 (1976).
- [6] S. Jasem and A.C.C. Tseung, *J. Electrochem. Soc.* 126, 1353 (1979).
- [7] C.R. Davidson, G. Kissel and S. Srinivasan, *J. Electroanal. Chem.* 132, 129 (1982).
- [8] W.J. King and A.C.C. Tseung, *Electrochim. Acta* 19, 485 (1974).
- [9] S. Holgersson and A. Karlsson, *Z. Anorg. Chem.* 183, 384 (1929).
- [10] F.K. Lotgering, *Philips Res. Rep.* 11, 337 (1956).
- [11] K.R. Williams, *An introduction to fuel cells*, Elsevier, Amsterdam, 58 (1966).
- [12] J. Robin and C. Bénard, *C.R. Acad. Sci. Paris* 235, 1301 (1952), (*Annls. Chim.* 10, 389 (1955)).
- [13] O. Knop, K.I.G. Reid, Saturno and Yasuaki Nakagawa, *Can. J. Chem.* 46, 3463 (1968).
- [14] A. Honji, C. Iwakura and H. Tamura, *Chem. Letters* 1153 (1979).
- [15] C. Iwakura, A. Honji and H. Tamura, *Electrochim. Acta* 26, 1319 (1981).
- [16] W.J. King and A.C.C. Tseung, *Electrochim. Acta* 19, 493 (1974).
- [17] A.D. Tantram and A.C.C. Tseung, *Nature* 221, 167 (1969).
- [18] P. Rasiyah and A.C.C. Tseung, *J. Electrochim. Soc.* 129, 1724 (1982).
- [19] D.B. Hibbert, *J. Chem. Soc. Chem. Comm.* 202 (1980).
- [20] A.A. Domnikov, G.I. Reznikov and F.R. Yuppets, *Sov. Electrochem.* 12, 1694 (1976).

## 4. OXYGEN EVOLUTION REACTION KINETICS

### 4.1. Introduction

In this chapter, the electrode kinetics of the oxygen evolution reaction on  $\text{NiCo}_2\text{O}_4$  spinel oxide as a function of the temperature, i.e. from 10 to 80°C, and the electrolyte concentration, i.e. from 0.1 to 7.0 M KOH, will be investigated. In the previous chapter, it was shown that the anodic performance is influenced by the temperature  $T_F$  of the final heat treatment. Therefore, the determination of the kinetic parameters has been studied as function of  $T_F$ . Furthermore, the kinetic behaviour of Teflon-bonded and non Teflon-bonded  $\text{NiCo}_2\text{O}_4$  electrodes is compared.

Since, sometimes an effect of the substrate [8], on the anodic behaviour has been noticed with respect to the nature or to the mesh size of the support material, also experiments were carried out with different substrates.

Several workers [1-7] have also investigated the kinetics of the anodic oxygen evolution reaction. It was reported that the oxygen evolution reaction on  $\text{NiCo}_2\text{O}_4$  is controlled by two Tafel slope regions, i.e.  $2RT/3F$  [1-5] or  $RT/F$  [6] at low  $\eta$  increasing to a slope of  $2RT/F$  [1-6] at high  $\eta$ . There is some disagreement about the observation of the lower Tafel slope with decreasing electrolyte concentration: Rasiyah et al. [4,5] reported that in KOH electrolytes of concentration less than 1.2 M KOH the slope of 40 mV is not observed, whereas Efremov et al. [3] reported that the first segment with the lower slope is not observed in solutions less than 0.03 M KOH. Moreover, at higher  $\eta$ , a range of Tafel slopes was observed ranging from 70 to 120 mV, which was assumed to be  $2RT/F$  [2-6]. Hibbert [7] showed from measurements with incorporation of  $^{18}\text{O}$  in a  $\text{NiCo}_2\text{O}_4$  electrode that during the evolution in KOH solution an unstable oxide is formed. Thus, the irreversible process of oxygen evolution on the transition metal oxide anode in alkaline solution may proceed via unstable, higher oxidation states of the metal cations. The appearance of two Tafel slopes has been discussed

in relation to the nature of the active site, i.e. the di- or trivalent cation sites of  $\text{NiCo}_2\text{O}_4$ , by several authors [3-5] in a different way.

No definite mechanism has yet been put forward that involves the identification of the active sites of the mixed spinel. Therefore, it is tried to elucidate the oxygen evolution mechanism on  $\text{NiCo}_2\text{O}_4$  and to postulate a role for the different surface sites on  $\text{NiCo}_2\text{O}_4$  during the reaction.

## 4.2. Experimental

### 4.2.1. Electrode preparation

All porous  $\text{NiCo}_2\text{O}_4$  electrodes used in this study were prepared by thermal decomposition onto a 30 mesh nickel screen (1 x 1 cm geometrical surface area), as described in section 3.2.1. A mixture of 1 M  $\text{Ni}(\text{NO}_3)_2 \cdot 6\text{H}_2\text{O}$  : 2 M  $\text{Co}(\text{NO}_3)_2 \cdot 6\text{H}_2\text{O}$  dissolved in water was used as dipping solution. The temperature  $T_F$  was varied between 300 and 400°C and the duration  $t_F$  was kept equal to 1 h.

The Teflon-bonded  $\text{NiCo}_2\text{O}_4$  electrodes were made as reported in section 3.2.1.

Before actual measurements were done, the  $\text{NiCo}_2\text{O}_4$  electrodes under study were subjected to prolonged oxygen evolution in order to obtain 'aged' electrodes (see chapter 5). For Teflon-bonded  $\text{NiCo}_2\text{O}_4$  electrodes the preanodization gave rise to smaller oxygen bubbles.

### 4.2.2. Electrochemical characterization

The experiments were performed in a thermostatted, three-compartment Pyrex glass cell. The potential of the working electrode was measured against the reversible hydrogen electrode (RHE) via a Luggin capillary close to the working electrode. A piece of 7 x 2.5 cm platinum foil was used as counter electrode. All experiments, except for the study of the temperature, were made at 25°C. Electrolyte solutions of different concentration were prepared from KOH pa (Merck) and double distilled water. The solutions were freshly prepared prior to each set

of experiments. The temperature dependency of the oxygen evolution was measured in 5 M KOH.

Steady-state galvanostatic measurements were carried out as follows: the  $\text{NiCo}_2\text{O}_4$  electrodes were first subjected to anodic polarization for 1 h at the highest current density (upper limit  $1.5 \text{ A cm}^{-2}$ ), thereafter, the potentials were measured with progressively decreasing current densities, down to  $10^{-4} \text{ A cm}^{-2}$ ; by doing so the electrode potential was always maintained above the potential of the higher oxide formation, i.e.  $> 1.40 \text{ V}$ . The time between each reading was 5 minutes. The time required to reach steady-state was in all cases less than 2 minutes, and usually within 1 min. The ohmic potential drop between the tip of the Luggin capillary and the working electrode was measured with the current interruptor technique [9]. The current densities are calculated on the basis of the apparent geometrical surface area and are IR-corrected.

#### 4.3. Results

##### 4.3.1. Tafel lines

Steady-state polarization measurements on Teflon-bonded and non Teflon-bonded  $\text{NiCo}_2\text{O}_4$  electrodes in 5 M KOH at  $25^\circ\text{C}$  are shown in figure 4.1.

The E-log i curves illustrate the increase in the electrochemical activity of the non Teflon-bonded  $\text{NiCo}_2\text{O}_4$  electrode with lowering of the temperature of the final heat treatment  $T_F$ , as seen by comparison of the curves indicated with the symbols [o], i.e.  $T_F = 300$  and [•], i.e.  $T_F = 400^\circ\text{C}$ .

Figure 4.1 also shows a comparison of the anodic performance of Teflon-bonded, i.e. the curves indicated with the symbols [ $\blacktriangle$ , \*], and non Teflon-bonded, [•],  $\text{NiCo}_2\text{O}_4$  electrodes. The data clearly show that the Teflon-bonded  $\text{NiCo}_2\text{O}_4$  electrodes give about the same activity, if for both electrode structures, the  $\text{NiCo}_2\text{O}_4$  catalyst is prepared by the same preparation technique (thermal decomposition) and -conditions, as is the case in figure 4.1.

The anodic behaviour of these  $\text{NiCo}_2\text{O}_4$  electrodes is also compared

with that of a Teflon-bonded electrode, as received from A.C.C. Tseung, prepared by freeze drying followed by decomposition in vacuum, as described in [12]. This Teflon-bonded electrode indicated with the symbol [+] in figure 4.1, is comparable in activity with that of the non Teflon-bonded electrode, prepared by thermal decomposition with  $T_F = 300^\circ\text{C}$ , i.e. [o].

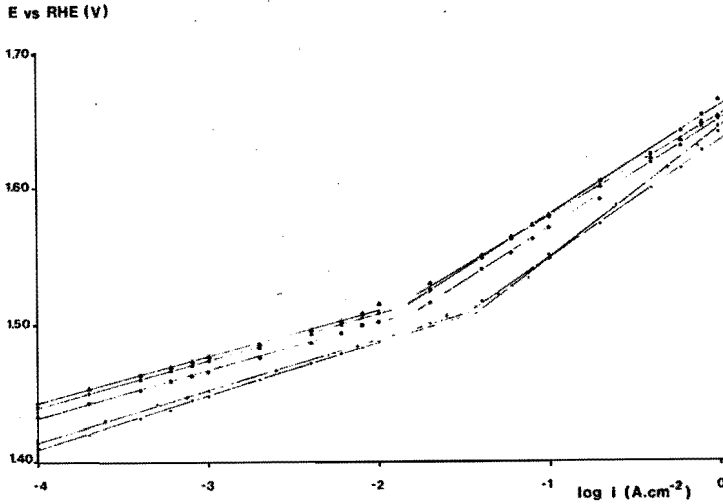


Figure 4.1: Tafel plots for oxygen evolution on Teflon-bonded and non Teflon-bonded  $\text{NiCo}_2\text{O}_4$  electrodes in 5 M KOH,  $25^\circ\text{C}$  (iR-corrected).

Symbol	Teflon content (wt %)	Support material	$T_F$ - $t_h$ ( $^\circ\text{C}$ ) (h)	Catalyst loading ( $\text{mg cm}^{-2}$ )
[o]	0	30 mesh Ni	300 - 1	26.1
[•]	0	30 mesh Ni	400 - 1	24.0
[▲]	10	Ni-plate	400 - 2	15.0
[x]	15	30 mesh Ni	400 - 2	24.0
[+]	26	100 mesh Ni	(1)	29.0

1: as received from A.C.C. Tseung.  $\text{NiCo}_2\text{O}_4$  catalyst was prepared by the cryochemical synthesis. BET-surface area =  $122 \text{ m}^2 \text{ g}^{-1}$ .

The apparent exchange current densities  $i_0$  and the Tafel slopes  $b$ , calculated from the Tafel lines in figure 4.1, are summarized in table 4.1. It is seen that the Teflon-bonded and non Teflon-bonded  $\text{NiCo}_2\text{O}_4$  electrodes have the same Tafel behaviour. The Tafel plots, as given in figure 4.1, can be divided in two regions, one with a slope of about 40 mV for an overpotential  $\eta < 280$  mV and one with a slope of 75 to 95 mV for  $\eta > 280$  mV.

Table 4.1: Kinetic parameters for oxygen evolution on Teflon-bonded and non Teflon-bonded  $\text{NiCo}_2\text{O}_4$  electrodes in 5 M KOH, 25°C.

Symbol <sup>1</sup>	b(mV)		$i_0$ (A.cm <sup>-2</sup> ) <sup>2</sup>	
	low $\eta$	high $\eta$	low $\eta$	high $\eta$
Non Teflon-bonded				
[o]	40	85	$3.6 \cdot 10^{-9}$	$1.8 \cdot 10^{-6}$
[•]	37	81	$1.1 \cdot 10^{-10}$	$5.0 \cdot 10^{-6}$
Teflon-bonded				
[▲]	35	74	$8.0 \cdot 10^{-11}$	$2.0 \cdot 10^{-6}$
[*]	36	80	$1.6 \cdot 10^{-10}$	$5.3 \cdot 10^{-6}$
[+]	38	94	$1.4 \cdot 10^{-9}$	$4.0 \cdot 10^{-5}$

<sup>1</sup>: for explanation see figure 4.1.

<sup>2</sup>: based on the geometrical surface area.

Figure 4.2 shows the E-log  $i$  curves of Teflon-bonded  $\text{NiCo}_2\text{O}_4$  electrodes with different  $\text{NiCo}_2\text{O}_4$ :Teflon ratios. As mentioned in chapter 3.3.2, it appears that below 30% Teflon content the anodic performance is similar.

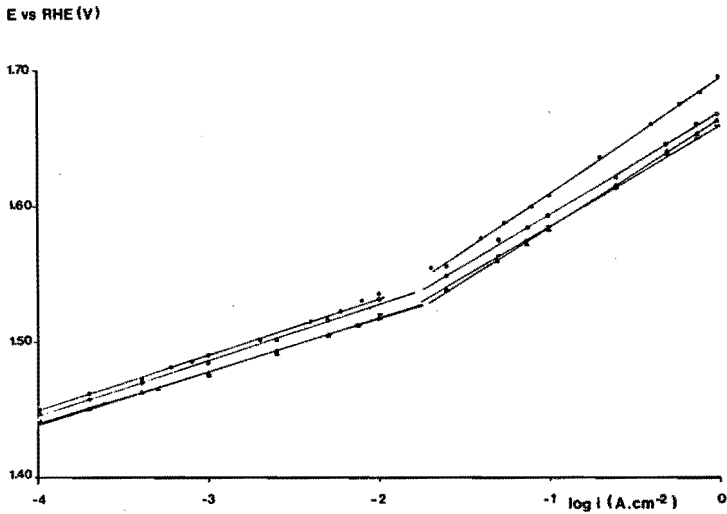


Figure 4.2: Tafel plots for oxygen evolution on Teflon-bonded  $\text{NiCo}_2\text{O}_4$  electrodes as function of the Teflon content in 5 M KOH, 25°C (iR-corrected).

All other preparation parameters were the same.

[—] = 10 wt %; [o] = 15 wt %; [▲] = 20 wt %;

[\*] = 30 wt %.

Figure 4.3 shows the Tafel lines of non Teflon-bonded  $\text{NiCo}_2\text{O}_4$  electrodes on different supporting materials, i.e. Pt-plate [o], Ni-plate [\*] and 30 mesh Ni-gauze [x] with the same high catalyst loading (see section 3.3.1.2). All other preparation parameters were the same. Virtually no influence of the nature (Pt or Ni) or mesh size (plate or gauze) of the substrate on the anodic performance was found. From the SEM photographs of the above mentioned  $\text{NiCo}_2\text{O}_4$  electrodes on different substrates, as shown in figure 4.4 on Ni-plate (picture a) and Pt-plate (b) and in figure 6.3 on 30 mesh Ni-gauze, it appears that the surface morphology was not influenced by the substrates. All  $\text{NiCo}_2\text{O}_4$  electrodes show circular, scaly surfaces and exhibit cracks.

Also, no difference in anodic performance was observed between Teflon-bonded  $\text{NiCo}_2\text{O}_4$  electrodes on nickel plate or on 30 mesh nickel screen.

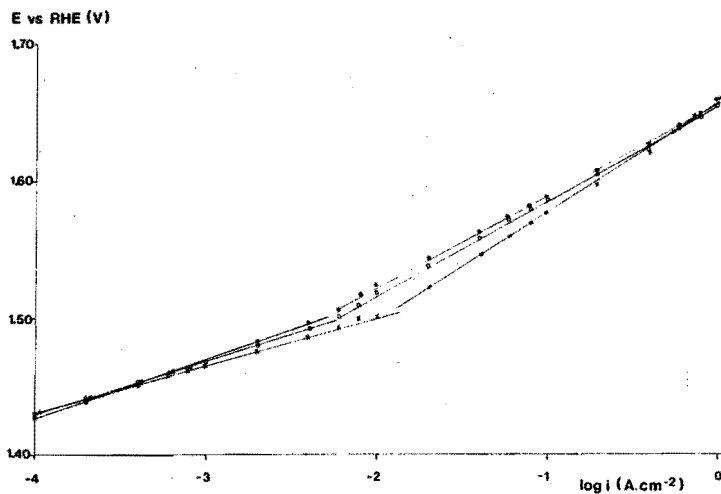


Figure 4.3: Tafel plots for oxygen evolution on non Teflon-bonded  $\text{NiCo}_2\text{O}_4$  electrodes deposited on different substrates in 5 M KOH, 25°C (iR-corrected).

$T_F = 400^\circ\text{C}$  and  $t_F = 1$  h; catalyst loading  $\sim 25 \text{ mg cm}^{-2}$ ;  
 [o] = Pt-plate; [•] = Ni-plate; [x] = 30 mesh Ni-gauze.

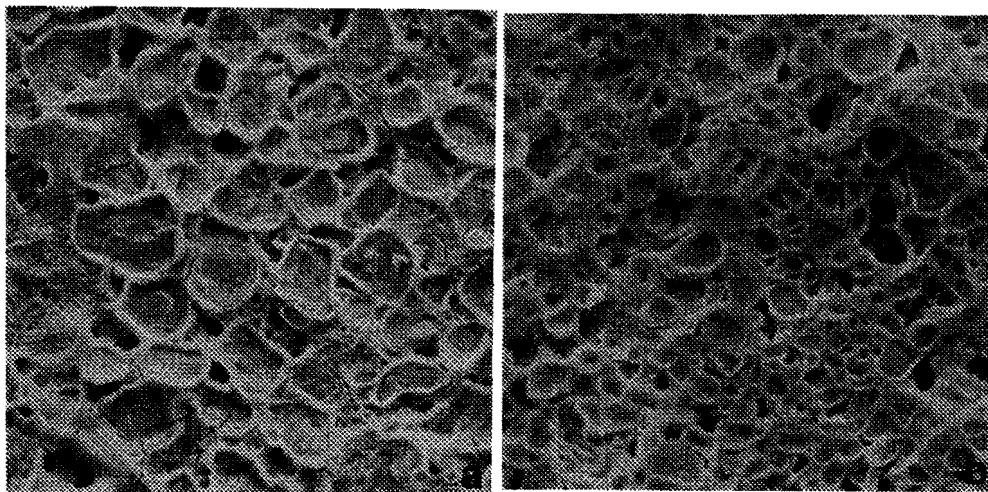


Figure 4.4: SEM Micrographs of the surfaces of non Teflon-bonded  $\text{NiCo}_2\text{O}_4$  electrodes deposited on different substrates. Magnification factor 208 x.

a = on Pt-plate; b = on Ni-plate.



## 4.3.2. Temperature dependence

The temperature dependence of the current density was studied on  $\text{NiCo}_2\text{O}_4$  electrodes, prepared by thermal decomposition at different  $T_F$ , i.e. 300, 350 and 400°C. The duration  $t_F$  was in all cases 1 h. The resulting Tafel lines for oxygen evolution at four temperatures are shown in figure 4.5 for  $\text{NiCo}_2\text{O}_4$  prepared at  $T_F = 300^\circ\text{C}$ . A break in the Tafel slopes with increasing overpotential is observed at all temperatures. The Tafel slopes  $b$  and the exchange current densities  $i_0$  are presented in the tables 4.2 to 4.4. The value of the overpotential  $\eta_c$ , where the change in Tafel slope takes place, is also given in the tables. The  $\eta_c$ -values were determined by extrapolating the potential of the change in the Tafel slope to the reversible potential of oxygen evolution at the respective temperature.

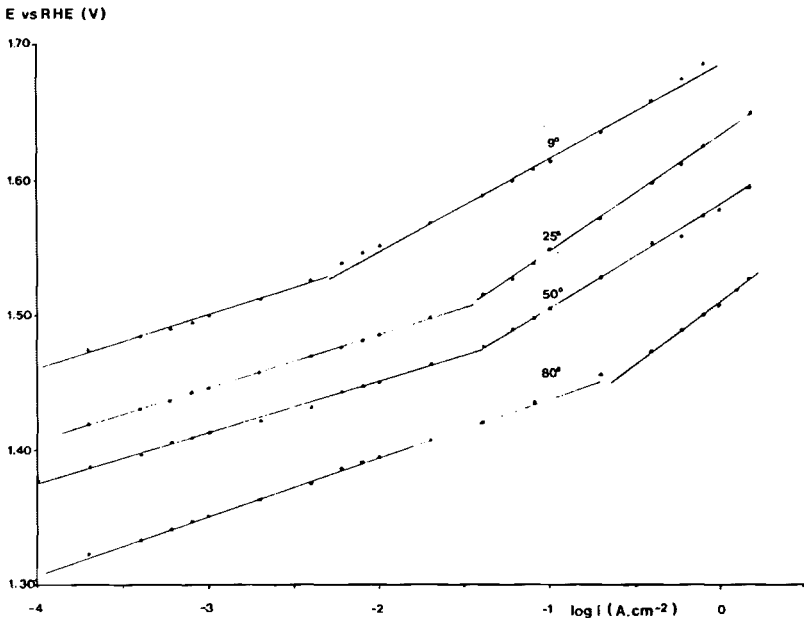


Figure 4.5: Tafel plots for oxygen evolution on  $\text{NiCo}_2\text{O}_4$  electrode as a function of the temperature in 5 M KOH (iR-corrected).  $T_F = 300^\circ\text{C}$  and  $t_F = 1$  h; catalyst loading  $26.05 \text{ mg cm}^{-2}$ .

Table 4.2: Kinetic parameters for oxygen evolution on  $\text{NiCo}_2\text{O}_4$  electrode in 5 M KOH.  $T_F = 300^\circ\text{C}$  and  $t_F = 1$  h; catalyst  $26.1 \text{ mg cm}^{-2}$ .

T (°C)	b (mV)		$i_o$ ( $\text{A cm}^{-2}$ )		$\eta_c$ (mV)
	low $\eta$	high $\eta$	low $\eta$	high $\eta$	
8	40	69	$4.3 \cdot 10^{-10}$	$3.7 \cdot 10^{-7}$	285
25	40	85	$3.6 \cdot 10^{-9}$	$1.8 \cdot 10^{-6}$	280
50	37	76	$4.5 \cdot 10^{-9}$	$1.5 \cdot 10^{-5}$	270
80	44	94	$1.2 \cdot 10^{-7}$	$2.8 \cdot 10^{-4}$	275

Table 4.3: Kinetic parameters for oxygen evolution on  $\text{NiCo}_2\text{O}_4$  electrode in 5 M KOH.  $T_F = 350^\circ\text{C}$  and  $t_F = 1$  h; catalyst loading:  $21.1 \text{ mg cm}^{-2}$ .

T (°C)	b (mV)		$i_o$ ( $\text{A cm}^{-2}$ )		$\eta_c$ (mV)
	low $\eta$	high $\eta$	low $\eta$	high $\eta$	
11	41	90	$9.5 \cdot 10^{-10}$	$1.5 \cdot 10^{-5}$	290
25	42	70	$1.4 \cdot 10^{-9}$	$8.0 \cdot 10^{-7}$	290
50	35	73	$7.0 \cdot 10^{-10}$	$1.0 \cdot 10^{-5}$	280
80	40	74	$1.6 \cdot 10^{-8}$	$3.5 \cdot 10^{-5}$	280

Table 4.4: Kinetic parameters for oxygen evolution on  $\text{NiCo}_2\text{O}_4$  electrode in 5 M KOH.  $T_F = 400^\circ\text{C}$  and  $t_F = 1$  h; catalyst loading =  $24.6 \text{ mg cm}^{-2}$ .

T (°C)	b (mV)		$i_o$ ( $\text{A cm}^{-2}$ )		$\eta_c$ (mV)
	low $\eta$	high $\eta$	low $\eta$	high $\eta$	
11	41	88	$7.5 \cdot 10^{-11}$	$2.7 \cdot 10^{-6}$	280
25	37	81	$1.0 \cdot 10^{-10}$	$5.0 \cdot 10^{-6}$	270
50	37	79	$3.0 \cdot 10^{-10}$	$1.8 \cdot 10^{-6}$	260
80	37	--	$1.0 \cdot 10^{-9}$	--	260

A Tafel slope  $b$  of about 40 mV is found at lower overvoltage over 2 to 3 decades of the current density and at higher overpotentials the Tafel slope increases and varies between 70 and 95 mV. Thus, a linear dependence of the Tafel slopes on the temperature is not observed, as theoretically expected when the overall transfer coefficient  $\beta$  is assumed to be constant. The observed Tafel slopes as function of the temperature  $T$  suggest that  $\beta$  is a function of  $T$ , i.e.  $\beta$  generally increases with increasing  $T$ .

The accuracy of the determination of the Tafel slope at higher overvoltages decreases with increasing temperature, because the region in which the second Tafel slope is measured, is smaller at higher temperatures.

It can be inferred from the Tafel plots that no major change in reaction mechanism or electrocatalytic activity takes place over the temperature under investigation: the oxygen evolution reaction is still controlled by two Tafel slopes.

The apparent exchange current densities  $i_0$ , determined by extrapolation of the Tafel lines in the lower overvoltage region to the equilibrium oxygen potential at the respective temperature show an increase with increasing temperature as seen in tables 4.2 to 4.4. The temperature dependence of the  $i_0$  in the higher overvoltage region is less evident, because of the earlier mentioned discrepancy in the second Tafel slope.

The break in the Tafel slope, indicated by the  $\eta_c$ -value, does not appear to depend on the temperature.

The apparent activation energy at constant overpotential  $\Delta H(\eta)$  can be calculated from the observed current densities as function of the temperature, using the equation 4.1 [13],

$$\Delta H(\eta) = -2.303 R \left( \frac{\partial \log i}{\partial T^{-1}} \right)_{\eta} \quad (4.1)$$

where  $R$  is the gas constant equal to  $8.314 \text{ J mol}^{-1} \text{ K}^{-1}$  and  $T$  is the temperature in Kelvin. Sets of current density-temperature data for three values of the overpotential, i.e. 230, 250 and 350 mV were determined. An overvoltage of 230 or 250 mV was chosen in order to obtain current density data for the lower Tafel region and a  $\eta$  of 350 mV for these of the second Tafel region. A plot of the  $\log i$  versus  $T^{-1}$  shows reasonable straight lines, as given in figure 4.6

for  $\text{NiCo}_2\text{O}_4$  prepared at  $400^\circ\text{C}$  for 1 h. From the data in the temperature range of 10 to  $80^\circ\text{C}$ , in 5 M KOH, the apparent activation energies were calculated with Eq. 4.1 and summarized in table 4.5.

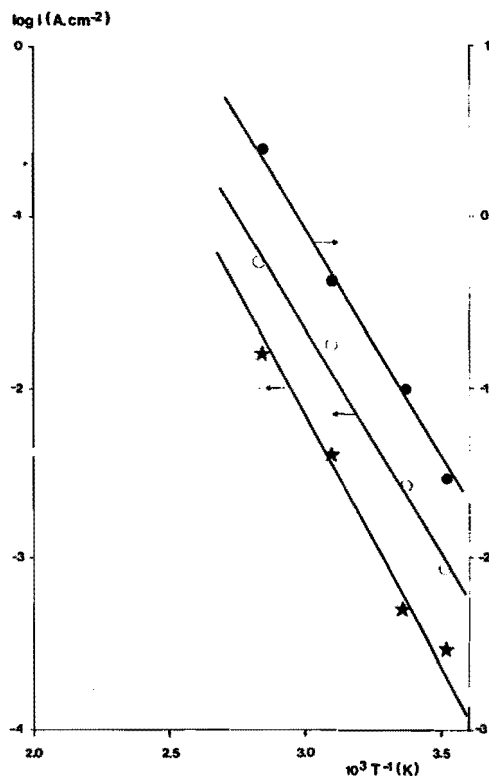


Figure 4.6: Temperature dependence of the current density for oxygen evolution on  $\text{NiCo}_2\text{O}_4$  at different overpotentials in 5 M KOH.  $T_F = 400^\circ\text{C}$  and  $t_F = 1$  h.  
 $\eta = 230$  mV [ $\star$ ];  $\eta = 250$  mV [ $\circ$ ];  $\eta = 350$  mV [ $\bullet$ ].

Table 4.5: Apparent activation energy at constant overpotential  $\Delta H(\eta)$  of  $\text{NiCo}_2\text{O}_4$  electrode prepared at different  $T_F$  and  $t_F = 1$  h.

Overpotential (mV)	$\Delta H(\eta)$ ( $\text{kJ mol}^{-1}$ )		
	$T_F = 300^\circ\text{C}$	$T_F = 350^\circ\text{C}$	$T_F = 400^\circ\text{C}$
230	47	46	56
250	45	48	50
350	37	48	50

Theoretically,  $\Delta H(\eta)$  is a function of the overpotential  $\eta$  and decreases with increasing  $\eta$  according to the equation 4.2 [13]

$$\Delta H(\eta) = \Delta H(\eta = 0) - \beta F\eta \quad (4.2)$$

By using an average of the measured transfer coefficients  $\beta$ , the apparent activation energies  $\Delta H(\eta)$  of table 4.5 can be extrapolated to zero overpotential. Table 4.6 shows the apparent activation energies for  $\eta = 0$ , i.e.  $\Delta H(\eta = 0)$ , for the different  $\text{NiCo}_2\text{O}_4$  electrodes and for their different Tafel regions.

These activation energies are in general not very revealing for a specific mechanism. However, one expects the apparent activation energy to change if there would occur a change in mechanism when going to higher overvoltages. So support for a change in reaction mechanism or rate determining step could be extracted from temperature dependent measurements, as was done by Iwakura et al. [14] for oxygen evolution on  $\text{PtO}_2$ . The measured apparent activation energies  $\Delta H(\eta = 0)$  decrease going from the low  $\eta$  to the high  $\eta$  region, as seen in table 4.6, which therefore points to a change in the reaction mechanism or rate determining step.

Table 4.6: Extrapolation of apparent activation energies  $\Delta H(\eta = 0)$  using an averaged value  $\beta$  of the transfer coefficient.

$T_F$ (°C)	low $\eta$		high $\eta$	
	$\beta$	$\Delta H(\eta=0)$ (kJ mol <sup>-1</sup> )	$\beta$	$\Delta H(\eta=0)$ (kJ mol <sup>-1</sup> )
300	1.55	82	0.79	64
350	1.59	81	0.83	76
400	1.65	91	0.73	75

Furthermore, it is noticed that the  $\Delta H$  also reflects the influence of the temperature  $T_F$  on the electrocatalytic behaviour:  $\Delta H$  increases with increasing  $T_F$ . This is seen in table 4.5 and 4.6 by comparing the results of the 300 and 400°C heat treatment. The  $\Delta H(\eta)$  values in table 4.5 compare reasonably with the value of  $49 \text{ kJ mol}^{-1}$ , determined at 1.6 V vs. DHE in 5 M KOH from 25 to 70°C for Teflon-bonded  $\text{NiCo}_2\text{O}_4$ , prepared via cryochemical synthesis, as reported by Jasem et al. [3]. From a plot of the  $\log i_0$  versus  $T^{-1}$ , an activation energy of  $71 \text{ kJ mol}^{-1}$  was calculated for the lower  $\eta$  region by Davidson et al. [6], for similar Teflon-bonded electrodes in 30% KOH from 0 to 165°C. This value is slightly smaller than the  $\Delta H(\eta = 0)$  values in table 4.6, but differs from the activation energy of  $48.6 \text{ kJ mol}^{-1}$  found by Singh et al. [1] for oxygen evolution in the lower  $\eta$  region ( $\eta < 300 \text{ mV}$ ) on  $\text{NiCo}_2\text{O}_4$ , thermally deposited on Ni-plate, in the temperature range of 25 to 100°C in 30% KOH.

#### 4.3.3. Effect of the electrolyte concentration.

The current-potential curves for oxygen evolution were also measured in alkaline solutions with different concentrations in the range of 0.1 to 7.0 M KOH. Figure 4.7 shows some typical Tafel lines on  $\text{NiCo}_2\text{O}_4$ , prepared at  $T_F = 300^\circ\text{C}$  and  $t_F = 1 \text{ h}$ , in electrolytes of concentrations 0.1, 0.5, 1.0 and 5.0 M KOH. A change in the Tafel slope at higher overpotentials is discernible and the observed Tafel slopes are similar in all electrolyte concentrations: at low overpotentials the slopes vary between 36 and 40 mV and at high overvoltages between 85 and 105 mV.

Furthermore, it appears that the oxygen evolution performance remains nearly constant in electrolytes of KOH concentrations greater than 1 M. From this kind of measurements the reaction order can be calculated. A point which causes confusion in the literature is the difference between the reaction order measured at constant potential and those at constant overpotential. However, since the dependence of the equilibrium potential on the activity of the hydroxyl ion is the same for the theoretically reversible oxygen electrode (ROE) and the used reference electrode, i.e. the reversible hydrogen electrode (RHE), the

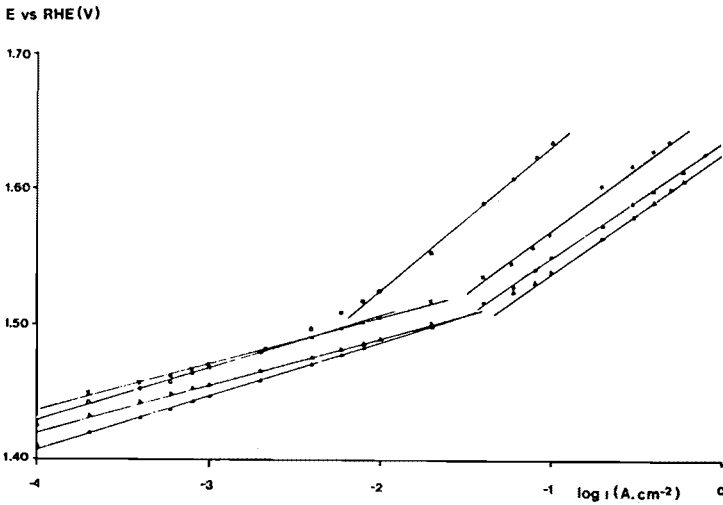


Figure 4.7: Tafel plots for oxygen evolution on  $\text{NiCo}_2\text{O}_4$  electrode in different KOH concentrations at  $25^\circ\text{C}$  (iR-corrected).  $T_F = 300^\circ\text{C}$  and  $t_F = 1$  h; catalyst loading =  $26.0 \text{ mg cm}^{-2}$ . [o] = 0.1; [\*] = 0.5; [ $\blacktriangle$ ] = 1.0 and [ $\bullet$ ] = 5.0 M KOH.

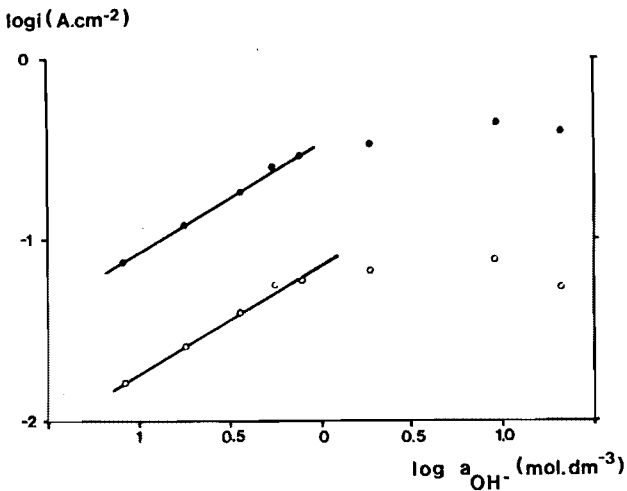


Figure 4.8: Dependency of the current density on the hydroxyl ion activity at  $25^\circ\text{C}$ . measured at  $\eta = 320$  [o] and  $370$  mV [ $\bullet$ ] for a  $\text{NiCo}_2\text{O}_4$  electrode, prepared at  $T_F = 400^\circ\text{C}$  and  $t_F = 1$  h; catalyst loading =  $23.3 \text{ mg cm}^{-2}$ .

measured potential differences are independent of the hydroxyl activity. This means that the reaction order can be measured at constant overpotential  $\eta$ . The reaction order  $p$ , with respect to the hydroxyl ion, is defined as given in equation 4.3,

$$p_{OH^-} = \left( \frac{\partial \log i}{\partial \log a_{OH^-}} \right)_{\eta, T} \quad (4.3)$$

The activities of the KOH solutions were calculated from the molalities and the appropriate activity coefficients as given by Akerlof and Bender [15]. The  $p_{OH^-}$  measured on  $NiCo_2O_4$  should be, like the Tafel slopes, different for the two overpotential regions. No reliable reaction order could be determined in the lower overpotential region, as indicated by figure 4.7.

In figure 4.8 a plot is shown of the  $\log i$  versus  $\log a_{OH^-}$  at constant overpotentials 320 and 370 mV, i.e. in the second Tafel region for a  $NiCo_2O_4$  electrode prepared at 400°C. The curves show a linear relationship in electrolyte concentration  $\leq 1$  M KOH. At higher KOH concentrations, it seems that there is nearly no dependence on the hydroxyl ion activity. This is in agreement with the results of Rasiyah et al. [4]. Table 4.7 shows the values of the reaction order  $p_{OH^-}$  at constant  $\eta$ , obtained in the concentration range  $\leq 1$  M KOH, for  $NiCo_2O_4$  electrodes prepared at different temperatures  $T_F$ .

Table 4.7: Reaction order at constant overpotential with respect to hydroxyl ion activity for  $NiCo_2O_4$  electrodes prepared at different  $T_F$ .

$T_F$ (°C)	$\eta$ (mV)	$p_{OH^-}$
300	320	0.61
	370	0.65
400	320	0.59
	370	0.61



#### 4.4. Discussion.

Summarizing, virtually no effect on the electrocatalytic behaviour of  $\text{NiCo}_2\text{O}_4$  electrodes is observed, as a result of the Teflon incorporation. The non Teflon-bonded  $\text{NiCo}_2\text{O}_4$  electrode, prepared by thermal decomposition (dipping method), is favored because it results in active electrodes and the preparation technique is an easy and rapid one. Lowering  $T_F$  leads to an increase in activity. Furthermore, nickel gauze was chosen for practical reasons in the dipping method, where it provides a better adherence and spread of the nitrate solution after dipping.

Generally, the Tafel slopes observed in the lower overvoltage region are nearly all equal to 40 mV, which points to a theoretical slope of  $2RT/3F$ , whereas the slopes in the higher overpotential region varied between 70 and 110 mV for various electrodes under similar conditions. The variation in Tafel slope is somewhat higher on Teflon-bonded than on non Teflon-bonded electrodes.

A similar range of the value of the Tafel slope in the higher  $\eta$ -region in steady-state measurements has also been noticed by other authors [2,3,6], although it is generally assumed in the literature that the oxygen evolution reaction on  $\text{NiCo}_2\text{O}_4$  electrodes is controlled by a slope of  $2RT/F$  at higher  $\eta$ .

Several explanations for the variation of the higher Tafel slope can be proposed:

1. Surface blockage by gas bubble formation.

In a first explanation, it was reported [3] that due to gas bubble formation, and continuous pore filling and expulsiing on  $\text{NiCo}_2\text{O}_4$ , the amount of surface available is continuously changing with the overpotential, making the measurement of the Tafel equation a difficult one. The author claimed to overcome these difficulties with potentiostatic pulse techniques, and so observed a Tafel slope of about 120 mV at higher  $\eta$ .

However, it is surprising to find a distinct linear relationship for the Tafel lines in the steady-state measurements. This implicates that in the  $E\text{-log } i$  curves, the decrease of the available electrochemical active surface area, due to the gas evolution process, should take

place logarithmically with increasing overvoltage in the second Tafel region.

Moreover, it is found that the Tafel slope in the lower  $\eta$ -region is not influenced by the gas bubble formation, however, this surface blockage model requires indirectly that the lower Tafel line is also affected, otherwise the observed deviation of the slope in the higher  $\eta$ -region (decrease in  $b$ ) would reflect an increase of the electrochemical activity, which is in contradiction with the supposition of a surface blocking process. Thus, in order to apply this model, it must be considered that the gas bubble formation would cause either a parallel shift of the lower Tafel line to higher  $\eta$  without a change of the slope (in other words a constant decrease in surface area over the lower  $\eta$ -region) or a decrease of the  $\eta_c$ -value and further a decrease of the second slope in the higher  $\eta$ -region.

## 2. Surface blockage by higher oxide formation.

Another approach to explain the deviation of the Tafel slope, as suggested by Willems [16] for the oxygen evolution on Co, is based on a potential dependent surface blocking by a higher oxide. A similar approach could be proposed for  $\text{NiCo}_2\text{O}_4$ , which also forms higher oxides, prior to oxygen evolution, as reported in chapter 5.

The main assumption of this model is that the oxidation of the surface and the oxygen evolution reaction are fully separated. However, this assumption that the higher oxide is not involved in the reaction is doubtful. No oxygen evolution is detected before the higher oxide formation is finished, i.e. about 1.45 V as shown in chapter 5, which points to a role of the higher oxides in the oxygen evolution reaction. Furthermore, from the galvanostatic RRDE experiments (see chapter 5), it appeared that no further oxidation reactions were observed in the oxygen evolution potential range up to 1.6 V. Also, according to Willems [16] the 120 mV Tafel slope will be found at very long stabilization times. However, no influence of the stabilization time on the value of the Tafel slope of  $\text{NiCo}_2\text{O}_4$  was observed in the steady-state polarization measurements.

## 3. Dual barrier model.

An unconventional transfer coefficient, i.e.  $0.6 \leq 1-\alpha \leq 0.8$  could

account for the anomalous behaviour of the Tafel slope at higher potentials on  $\text{NiCo}_2\text{O}_4$ . Unusual transfer coefficients have been explained in the literature with the assumption of an extra potential dependent process, i.e. a higher oxide on the surface which controls the conductivity of the oxide layer and thus behaves as a series process.

The effect of surface films on surface oxidation kinetics has been discussed by Meyer [17] using a dual barrier model. It was assumed that in the steady-state, two potential dependent reactions are occurring at equal rates. One reaction corresponds to the migration of charge carriers across a potential difference  $\Delta E_{\text{OX}}$  over the oxide layer and the other to an electrochemical oxidation reaction at the oxide surface across a potential difference  $\Delta E_s$  over the double layer. Accordingly the transfer coefficient is given by equation 4.4 [17].

$$(1-\alpha) = \frac{(1-\alpha_{\text{OX}}) (1-\alpha_s)}{(1-\alpha_{\text{OX}}) + (1-\alpha_s)} \quad (4.4)$$

where  $(1-\alpha_{\text{OX}})$  and  $(1-\alpha_s)$  are the transfer coefficients for the charge carrier transport and surface oxidation reactions, respectively. The concept of the dual barrier model has been applied by MacDonald and Conway [18] in the oxygen evolution at Au and Pd, by Willems [16] at Co and Co-Ni alloys, and by Smit [19] at Pt during the formation of the peroxodisulphate ion.

This concept can be applied to  $\text{NiCo}_2\text{O}_4$ , which also forms higher oxides as reported in chapter 5. Until now, we tacitly assumed that the experimental observed slope in the higher  $\eta$ -region on  $\text{NiCo}_2\text{O}_4$  points to a theoretical slope of  $2RT/F$  (i.e.  $\alpha = 0.5$ ). However, according to equation 4.4, it is not possible to find a  $(1-\alpha) > 0.5$  because the Tafel slope according to the dual-barrier model is in fact the sum of the individual slopes, i.e. the sum of the slope of the electrochemical oxidation reaction at the surface and the slope of the charge transfer in the oxide layer. Thus, the concept is only useful in order to account for lower transfer coefficients (or higher slopes).

Another possibility could then be that the slope for oxygen evolution at high  $\eta$  is equal in fact to 40 or 60 mV. The slope of the charge transfer over the oxide layer is then equal to the difference between the experimental observed slope and that of the oxidation reaction. However, the dual barrier concept involves a change in the semiconducting properties of the  $\text{NiCo}_2\text{O}_4$  electrode and this change apparently must take place above the overpotential value  $\eta_c$ . However, no further higher oxide formation was observed above 1.45 V (chapter 5). Consequently, the variation in the Tafel slope should already be noticeable at low  $\eta$ , which is not the case. Moreover, the  $iR$ -drop measurements did not indicate any change in the semiconducting properties of the  $\text{NiCo}_2\text{O}_4$  electrode with increasing  $\eta$ .

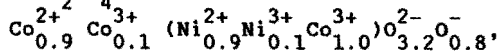
Summarizing, no definite explanation can be proposed to explain the variation in the Tafel slope in the higher  $\eta$ -region. For the further discussion it is arbitrarily assumed that the slope is 120 mV. From the experimental results, it can be concluded that the oxygen evolution reaction on  $\text{NiCo}_2\text{O}_4$  may be separated into two parts: a Tafel region with a slope of  $2RT/3F$  at low  $\eta$  and at higher  $\eta$  a range of Tafel slopes which points to a slope of  $2RT/F$ . Both potential regions will be discussed separately.

The cyclic voltammetric study of  $\text{NiCo}_2\text{O}_4$ , as reported in chapter 5, shows that the metal cation sites ( $\text{M}^{2+}$  and  $\text{M}^{3+}$ ) on the surface can undergo the oxidation state transitions  $\text{M}^{2+} \rightarrow \text{M}^{3+} \rightarrow \text{M}^{4+}$ , as derived from the observation of two anodic oxidation peaks before oxygen evolution starts, i.e. at about 1.45 V. The highest valence state before oxygen is evolved is 4+: no higher oxidation state was observed in the oxygen evolution potential range up to 1.55 V. This indicates that the higher oxides, up to 4+, may play a role in the oxygen evolution reaction. The two Tafel slopes will be discussed in relation to the activity of divalent or trivalent sites of  $\text{NiCo}_2\text{O}_4$  with respect to the reaction mechanism.

It has been suggested in the literature that the change in Tafel slope is due to a change in valence state of the oxide at the break potential  $\eta_c$  [3]. Rasiyah et al. [4,5] postulated a role for the different surface sites in the oxygen evolution reaction on

$\text{NiCo}_2\text{O}_4$ : the slope  $2RT/3F$  at low  $\eta$  was related to oxygen evolution taking place at trivalent cation sites via a bridge formed species, whereas the slope  $2RT/F$  at higher  $\eta$  was attributed to divalent cations being active, via the reaction sequence known as the electrochemical path. This remarkable change in the active site from trivalent cations at low  $\eta$  to divalent ones at high  $\eta$  is related to the cation distribution, as proposed by King and Tseung [12], of

$\text{NiCo}_2\text{O}_4$  at rest, i.e.

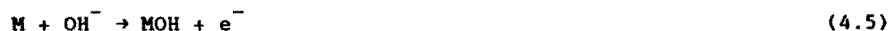


wherein trivalent sites are minority sites. However, it is more probable that with increase in  $\eta$  the divalent site becomes a minority site. Furthermore, Battle et al. [20] rejected such a complex cation distribution because it implies metallic conductivity associated with partially filled oxygen 2p bands as well as an easy electron transfer between A-site cobalt and B-site nickel. However, the conductivity measurements on polycrystalline materials do not appear compatible with broad band metallic conductivity [12,21]. Finally, a mean valence state of the metal ions of 2.4+ is suggested by the above mentioned cation distribution, which is not in agreement with the value of 2.67+ as determined by temperature programmed reduction in chapter 6.

Efremov and Tarasevich [2] reported a displacement of the predominant location of the reaction from divalent cation sites at low  $\eta$  to trivalent cations at higher  $\eta$ , the overall scheme of the process remaining unchanged. However, this includes the formation of valence state greater than 4+, which is in contradiction with the results of the voltammetric study in chapter 5.

For a proper kinetic formulation, the electrochemical evolution of oxygen requires at least three steps and indeed, a variety of mechanisms is given in the literature.

Taking into account the higher oxide formation, it can be suggested that oxygen evolution on  $\text{NiCo}_2\text{O}_4$  proceeds via the following path,



where M must represent a divalent metal cation. It is to be noted that the highest oxidation state of the species which can be formed in this reaction mechanism is 4+ in MO (equation 4.6) and is reached by a maximum of two electron transfers. No further transitions can take place before oxygen is evolved and consequently MO decomposes to form M, releasing oxygen (equation 4.7).

The Tafel slope of 40 mV at lower overpotentials can be related to equation 4.6 being rate determining (rd) at low coverages of the intermediates with Langmuir type adsorption, i.e.  $\Theta_{\text{MOH}} \rightarrow 0$ . Accordingly, the rate equation that will govern oxygen evolution, is given by equation 4.8,

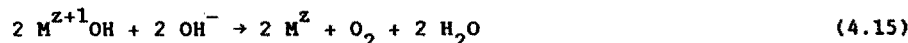
$$i = 4 F k a_{\text{OH}^-}^2 \cdot \exp [3FE/2RT] \quad (4.8)$$

where  $\alpha$  is supposed to be 1/2, k is a constant and  $a_{\text{OH}^-}$  is the activity of the hydroxyl ions in the electrolyte. The proposed reaction mechanism is supported by the results of the voltammetric study of  $\text{NiCo}_2\text{O}_4$  in aprotic medium (acetonitrile), as reported in section 5.3.7, where it is concluded that the hydroxyl ion plays an important role in the electrochemical reactions prior to oxygen evolution.

However, a further confirmation is not possible since no reliable reaction order could be determined in the lower  $\eta$ -region. The same line of reasoning applies to the Krasil'shchikov path, as given in equation 4.9 to 4.12,



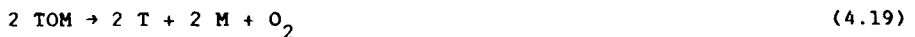
and to the path suggested by O'Grady [22], as shown in equations 4.13 to 4.15



which also take into account the formation of the higher oxides. For both mechanisms the Tafel slope of 40 mV at low overpotentials can be related to the second charge transfer step being rate determining, i.e. equation 4.10 and 4.14 respectively, at low coverages of the intermediates with Langmuir type adsorption.

However, it is not possible to evolve oxygen on trivalent sites in the reaction sequence 4.5 to 4.7 (neither in the two other reaction mechanisms) without forming pentavalent species, which is in contradiction with the results of the higher oxide formation. Therefore, the trivalent sites cannot be involved in this reaction mechanism. Thus the lower Tafel region must be related to oxygen evolution taking place at divalent sites of  $\text{NiCo}_2\text{O}_4$ .

If the higher Tafel slope is related to oxygen evolution on trivalent cation sites, T, which is more reasonable in the higher  $\eta$ -region, a possible mechanistic sequence [4,5] on trivalent is one, wherein the second electron transfer should involve an interaction with another di- or trivalent site, forming a bridge species as follows



where T is a trivalent and M is a di- or trivalent cation. The higher slope can be due to equation 4.16 being rate determining at low TOH coverages, i.e.  $\Theta_{\text{TOH}} \rightarrow 0$ , or to equation 4.18 taken as rds at high TOH coverages, i.e.  $\Theta_{\text{TOH}} \rightarrow 1$ .

A further confirmation of the rds from the reaction order at constant potential i.e.  $(d \log i / d \log a_{\text{OH}^-})_{E,T}$  is not possible, since both reactions when rate determining give similar reaction rate equations. With the first step (Eq. 4.16) or the third step (Eq. 4.18), respectively, taken as the rds, with respect to the above mentioned conditions, the current density can be described by a similar rate equation,

$$i_1 \approx i_3 \approx nFk a_{\text{OH}^-} \cdot \exp(FE/2RT) \quad (4.20)$$

where  $\alpha = 1/2$  and which gives in both cases a reaction order at con-

stant potential with respect to the hydroxyl ion activity of 1.0. The overpotential  $\eta$  can be defined in terms of the equilibrium potential  $E_{eq}$  and  $E$ , the potential of the electrode, as follows

$$\eta = E - E_{eq} = E - \left( E^0 - \frac{RT}{nF} \ln \frac{a_{OH^-}^4 a_{H_2O}^2}{P_{O_2}} \right) \quad (4.21)$$

Substituting equation (4.21) into equation (4.20) gives

$$i_1 \approx i_3 \approx nFk a_{OH^-}^{1/2} \exp(F/2RT \eta)$$

which gives in both cases a reaction order with respect to  $a_{OH^-}$  at constant overpotential ( $d \log i / d \log a_{OH^-}$ ) $_{\eta, T}$  of 0.5.

Until now, we have assumed that the activity of water is constant and independent of the hydroxyl activity  $a_{OH^-}$ . In strongly alkaline solutions however the influence of the changing water activity should also be taken into account. Then, a useful extra criterion is obtained to distinguish between different reaction paths or rate determining steps. From the data of Willems [23], the slope of the plot of  $\log a_{OH^-}$  versus  $a_{H_2O}$  of KOH solutions is estimated to be

$$(d \log a_{H_2O} / d \log a_{OH^-}) = -1/8 \quad (4.22)$$

in the concentration area of interest. The reaction order with respect to  $OH^-$  and  $H_2O$  can now be combined into an effective reaction order according to [23], by

$$(d \log i / d \log a_{OH^-})_{eff, \eta, T} = n + m (d \log a_{H_2O} / d \log a_{OH^-}) \quad (4.23)$$

where  $n$  and  $m$  are the reaction orders at constant  $\eta$  for the hydroxyl ion and water, respectively. If we take into account the activity of water in calculating the reaction order, we obtain for the first step (Eq. 4.16) being rate determining,

$$i_1 = nFk a_{OH^-}^{1/2} a_{H_2O}^{1/8} \exp(\eta F/2RT) \quad (4.24)$$

and for the third step (equation 4.18), respectively



$$i_3 = nFk a_{\text{OH}^-}^{1/2} \cdot a_{\text{H}_2\text{O}}^{-1/2} \exp(\eta F/2RT) \quad (4.25)$$

By applying equation 4.22, the effective reaction order with respect to  $a_{\text{OH}^-}$  at constant  $\eta$  is calculated to be 0.47 in the first case and for the latter 0.59.

Furthermore, the dependence of the equilibrium potential on the activity of water is not the same for the theoretically reversible oxygen electrode (ROE) and the reference electrode, i.e. RHE. According to the Nernst law

$$E_{\text{O}_2} - E_{\text{H}_2} = (E_{\text{O}_2}^{\circ} - E_{\text{H}_2}^{\circ}) + \frac{RT}{2F} \ln \frac{p_{\text{O}_2}^{1/2} p_{\text{H}_2}^{1/2}}{a_{\text{H}_2\text{O}}} \quad (4.26)$$

Thus the measured potential differences are dependent on the water activity. Correcting equation 4.24 and 4.25, the reaction rate equations are given by

$$i_1 = nFk a_{\text{OH}^-}^{1/2} \cdot \exp(\eta F/2RT) \quad (4.27)$$

for step 1 (Eq. 4.16) being rate determining, and by

$$i_3 = nFk a_{\text{OH}^-}^{1/2} \cdot a_{\text{H}_2\text{O}}^{-1} \exp(\eta F/2RT) \quad (4.28)$$

when step 3 (Eq. 4.18) is taken as rds.

The corrected reaction order at constant  $\eta$  with respect to  $a_{\text{OH}^-}$  is calculated by applying equation 4.22 and amounts in the former case (Eq. 4.27) to 0.5 and in the latter to 0.63 (Eq. 4.28). From the experimental observed reaction orders at constant  $\eta$ , as given in table 4.7, it appears that step 3 (Eq. 4.18) being rate determining at high TOH coverages explains more reasonably the results than step 1 (Eq. 4.16) when the activity of water is taken into consideration. Furthermore, a decrease in the concentration of a divalent at higher  $\eta$  is likely. Consequently, the M sites in equation 4.18 are mainly trivalent.

This reaction order is in fact related to the KOH concentration range

$\leq 1$  M, while the oxygen evolution was normally measured in 5 M KOH. Furthermore, it appears from the data of Willems [23] that no linear relationship was found for the plot of  $\log a_{\text{OH}^-}$  versus  $\log a_{\text{H}_2\text{O}}$  over the total concentration range. The value of  $(d \log a_{\text{H}_2\text{O}} / d \log a_{\text{OH}^-})$  is estimated to be  $-1/3$  in the concentration range 1 to 7 M KOH, in which case the corrected reaction order at constant  $\eta$  with respect to  $a_{\text{OH}^-}$ , for step 3 (Eq. 4.27) being rate determining, increases to 0.83. This is in contradiction with the experimental results, as given in figure 4.8, which shows nearly no dependence on the hydroxyl ion activity in KOH solutions  $\geq 1$  M KOH ( $p_{\text{OH}^-} \rightarrow 0$ ).

Summarizing, it can be concluded that at potentials exceeding the  $\eta_c$ -overpotential, a shift in active site takes place from divalent (Eq. 4.6) to trivalent sites (Eq. 4.18).

The Tafel slope of 40 mV in the lower  $\eta$ -region can also be related to equation 4.18 being rate determining at low TOH coverages, i.e.

$\Theta_{\text{TOH}} \rightarrow 0$ . In this case, the valence state of the active site does not change with exceeding  $\eta_c$ : a shift from low,

$\Theta_{\text{TOH}} \rightarrow 0$ , to high coverages,  $\Theta_{\text{TOH}} \rightarrow 1$ , occurs.

#### 4.4. Literature

- [1] G. Singh, M.H. Miles and S. Srinivasan in A.D. Franklin (Ed.), *Electrocatalysis on Non-metallic surfaces*, N.B.S. Spec. Publ. 455, V.S. Government Printing Office, Washington, 289 (1976).
- [2] B.N. Efremov and M.R. Tarasevich, *Sov. Electrochem.* 17, 1392 (1981).
- [3] S. Jasem and A.C.C. Tseung, *J. Electrochem. Soc.* 126, 1353 (1979).
- [4] P.C. Rasiyah and A.C. Tseung, *J. Electrochem. Soc.* 130, 365 (1983).
- [5] P. Rasiyah and A.C.C. Tseung, *Proc. of the 4th World Hydrogen Conference*, T.N. Veziroglu, W.D. van Vorst and J.H. Kelley (Ed.), California, 1, 383 (1982).
- [6] C.R. Davidson, G. Kissel and S. Srinivasan, *J. Electroanal. Chem.* 132, 129 (1982).

- [7] D.B. Hibbert, J.C.S. Chem. Comm., 202 (1980).
- [8] A.C.C. Tseung and S. Jasem, *Electrochim. Acta* 22, 31 (1977).
- [9] K.R. Williams, *An Introduction to fuel cells*, Elsevier, Amsterdam, 58 (1966).
- [10] A.C.C. Tseung, S. Jasem and M.N. Mahmood in T.N. Veziroglu and W. Seifritz (Eds.), *Hydrogen Energy systems*, Pergamon Press, Vol. I, 215 (1978).
- [11] M.C.M. Man, S. Jasem, K.L.K. Yeung and A.C.C. Tseung, *Hydrogen as an Energy vector*, Commission of the European Communities, Brussels, 255 (1978).
- [12] W.J. King and A.C.C. Tseung, *Electrochim. Acta* 19, 485 and 493 (1974).
- [13] E. Gileadi, E. Kirowa-Eisner and J. Penciner, *Interfacial Electrochemistry. An experimental approach*, Addison-Wesly, Reading, 74 (1975).
- [14] C. Iwakura, K. Fukuda and H. Tamura, *Electrochim. Acta* 21, 501 (1976).
- [15] G.C. Akerlof and P. Bender, *J. Am. Chem. Soc.* 70, 2366 (1948).
- [16] H. Willems, *Dissertation*, Utrecht (1984).
- [17] R.E. Meyer, *J. Electrochem. Soc.* 107, 847 (1960).
- [18] J.J. MacDonald and B.E. Conway, *Proc. Roy. Soc.* 269, 419 (1962).
- [19] W. Smit, *Dissertation*, Eindhoven (1969).
- [20] P.D. Battle, A.K. Cheetham and J.B. Goodenough, *Mat. Res. Bull.* 14, 1013 (1979).
- [21] G. Feuillade, R. Coffre and G. Outhier, *Annales de radioelectricite* 21, 105 (1966).
- [22] W. O'Grady, C. Iwakura, J. Huang and E. Yeager, *Proc. of Symposium on Electrocatalysis*, M. Breiter (Ed.), The Electrochemical Society, Princeton, New Jersey, 289 (1974).
- [23] H. Willems, A.G.C. Kobussen, J.H.W. de Wit and G.H.J. Broers, *J. Electroanal. Chem.* 170, 227 (1984).

## 5. ELECTROCHEMICAL CHARACTERIZATION

### 5.1. Introduction

The main aim of the work reported in this chapter is the characterization of the surface features of  $\text{NiCo}_2\text{O}_4$  electrodes by voltammetric and charging curves, and to elucidate the role of the surface state in the oxygen evolution reaction. These electrochemical techniques are particularly suited for in situ analysis of the electrode surface. The performance of a  $\text{NiCo}_2\text{O}_4$  oxide electrode depends on the state of the surface in the potential range where the desired reaction takes place. The irreversible process of oxygen evolution takes place by breakdown of a species in a high oxidation state, which is formed on an active site. Therefore, it is important to establish the valence state of the transition metal ions at rest, the highest oxidation state and the oxidation state transitions, which are possible at oxygen evolution potentials.

Also, the correlation between the electrocatalytic activity and the surface state will be investigated. The influence of the preparation conditions on the anodic performance is already reported in chapter 3. Therefore, the cyclic voltammetric behaviour will be investigated as a function of the temperature  $T_F$  and the duration  $t_F$  of the final heat treatment and catalyst loading.

Finally, the ageing phenomena in the oxygen reduction and -evolution potential range will be examined. Though numerous articles have been published on the performance of the  $\text{NiCo}_2\text{O}_4$  electrodes, the investigation of the voltammetric behaviour of  $\text{NiCo}_2\text{O}_4$  is still sparse. Previous studies were aimed at investigating the relationship between the electrocatalytic activity and the surface structure [1-3], the bulk composition [1,4,5], the preparation procedure [1,6-8] and other physicochemical properties [9,10]. However, the investigation of the surface properties under conditions of electrochemical work have been marginal and occasional. Trasatti et al. [11-13] reported the observation of one anodic peak before oxygen evolution starts in 1 M KOH. The peak position appeared to depend on temperature  $T_F$  of the thermal decomposition and increased from about 1.38 V at 350°C up to 1.48 V at 500°C. The most peculiar result was that the

voltammetric charge increased with increasing  $T_p$ . The state of the  $\text{NiCo}_2\text{O}_4$  surface has been found to change with the pH of the solution. The voltammogram became modified, as the pH became slightly acidic. The state of the surface of  $\text{NiCo}_2\text{O}_4$  prior to oxygen evolution was studied by Rasiyah [14] in 5 M KOH. The voltammogram of  $\text{NiCo}_2\text{O}_4$  cycled at a low sweep rate, i.e.  $18.3 \text{ mV s}^{-1}$ , showed only one broad oxide peak which resolved into two peaks at a sweep rate of  $100 \text{ mV s}^{-1}$ .

Based on coulometric studies, they proposed the formation of three oxides, at 1.25, 1.31 and 1.40 V vs. DHE (Dynamic Hydrogen Electrode) and suggested that the formation of higher oxides is limited to the surface of the  $\text{NiCo}_2\text{O}_4$  particles only.

### Cyclic voltammetry

The cyclic voltammetric behaviour of a  $\text{NiCo}_2\text{O}_4$  electrode must be treated as an electrochemical surface process. In section 5.3, the characteristic elements of the theory of cyclic voltammetry for a surface-immobilized redox system, as described by E. Laviron [15] will be applied with some caution to the  $\text{NiCo}_2\text{O}_4$  electrodes. The theory of linear potential sweep voltammetry for a simple redox system in case of a space distributed redox modified electrode, i.e. adsorption of an electroactive substance in several layers, was established on the basis of a multilayer model, as discussed in [15-18]. The theories elaborated for a simple redox reaction, when both O and R are strongly adsorbed [15,19,20], will be directly applicable to redox modified electrodes, which can be considered as representing the extreme limit of strong adsorption. A detailed discussion of this theory is given in [16,17,21]. The  $\text{NiCo}_2\text{O}_4$  catalyst can be treated as a surface immobilized species with 'specific' catalytic centers at an electron conducting material.

## 5.2. Experimental

### Electrode design and preparation

All porous  $\text{NiCo}_2\text{O}_4$  electrodes used in this section were prepared

by thermal decomposition on a nickel screen ( $1 \text{ cm}^2$  geometrical surface), as reported in detail in chapter 3. The porous  $\text{Co}_3\text{O}_4$  electrodes were prepared in a similar way, starting from a pure  $\text{Co}(\text{NO}_3)_2 \cdot 6\text{H}_2\text{O}$  solution.

Also, a rotating ring disc electrode was used. Figure 5.1 shows the construction of the demountable ring-disc electrode. The disc electrode was made of nickel, the ring electrode of platinum. The demountable nickel disc electrode was covered with  $\text{NiCo}_2\text{O}_4$  prepared by thermal decomposition. The preparation conditions were chosen such that a smooth  $\text{NiCo}_2\text{O}_4$  layer was obtained. The platinum ring was slightly platinized.

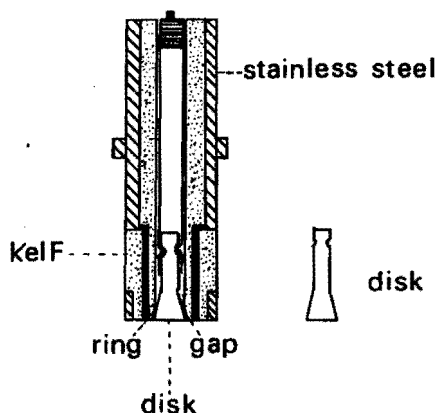


Figure 5.1: Construction of the demountable ring-disc electrode.

Construction parameters of the demountable ring-disc electrode.

Disc/Ring	$r_{10}$ (mm)	$r_{20}$ (mm)	$r_{30}$ (mm)
Ni/Pt	2.80	3.10	3.65

## Electrochemical characterization

### Cell Design

The electrochemical measurements with the porous electrodes were made in a thermostatted, conventional, three-compartment Pyrex glass cell, as shown in figure 5.2. A piece of 7 x 2.5 cm platinum foil was used as the counter electrode and the potential of the working electrode was measured against the reversible hydrogen electrode (RHE) in the same solution, or the mercury (II)-oxide electrode (Hg/HgO, 5 M KOH; 0.926 V vs. RHE, 25°C), via a Luggin capillary close to the working electrode. All potentials are given with respect to the RHE. The electrolyte solutions were freshly prepared prior to each set of experiments from analytical grade chemicals (Merck KOH p.a.) and double distilled water.

The rotating ring-disc experiments were performed in the cell given in figure 5.3 at room temperature, i.e. about 22°C. All other experimental conditions were the same as mentioned above.

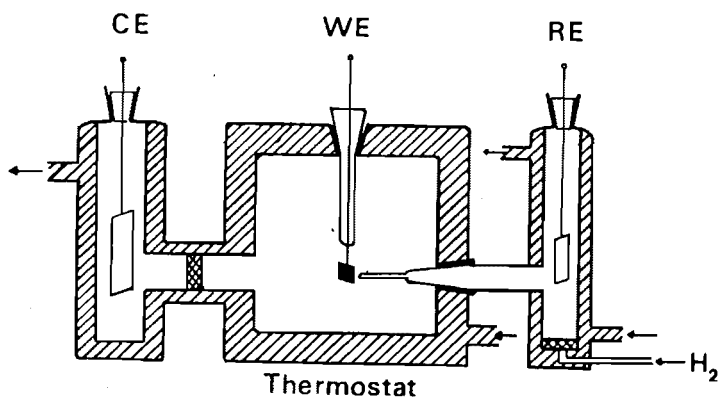


Figure 5.2: The cell: WE = working electrode, CE = counter electrode, RE = reference electrode.

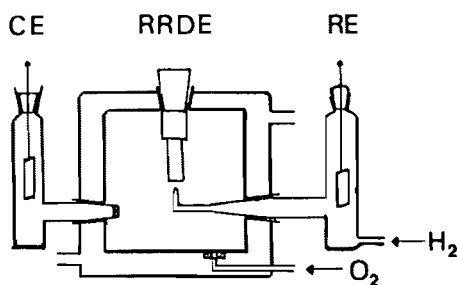


Figure 5.3: Measuring cell used in RRDE experiments.

#### Experimental set-up

The cyclic voltammetric measurements of the  $\text{NiCo}_2\text{O}_4$  gauze electrodes were carried out using a High Power Wenking Potentiostat (HP 72), a Universal programmer (PAR 175) or a Wenking Voltage Scan Generator (VSG 71) and a Data precision 2480 digital multimeter. The current-potential curves were recorded on a XY recorder (Philips PM 2041). The constant current charging was carried out with a Bruker Galvanostat (E 350) and the change in potential recorded with time on a Xt recorder (Kipp & Zonen BD 40).

All measurements with the demountable ring-disk electrodes were carried out using a Tacussel bipotentiostat (Bi-PAD) and an XYY'-recorder (HP 7046 A). No correction for the uncompensated solution resistance  $R_u$  was applied.

#### Aprotic medium

Some cyclic voltammetric measurements were carried out in Acetonitrile (Janssen Chimica),  $\text{CH}_3\text{CN}$ , with lithiumperchlorate (Fluka p.a.) as supporting electrolyte. All solutions were deoxygenated with nitrogen. The reported potentials are referred to the standard calomel electrode (SCE), connected to the electrochemical cell via an agar-agar/KCl bridge. A platinum plate served as counter electrode.



### 5.3. Freshly prepared $\text{NiCo}_2\text{O}_4$ electrodes.

#### Results and discussion

#### 5.3.1. General features of the cyclic voltammogram

The shape of the voltammetric curve of a 'freshly' prepared  $\text{NiCo}_2\text{O}_4$  electrode is remarkably different from that for 'aged ones'. Therefore, the set of electrodes presented in this section was used only for voltammetric measurements. The maximum applied potential scan range is the E-range of 0.9 to 1.5 V. The lower limit potential of 0.9 V was chosen in order to prevent spinel decomposition and the upper limit of 1.5 V for minimum oxygen evolution reaction. Before cycling the electrode was maintained at its rest potential, i.e. 1.1 V to reduce all surface compounds. The cyclic voltammogram, which was always started from the rest potential, was independent of the direction of the potential sweep (minimum two cycles). The number of cycles was limited to about 20. Prolonged cycling altered the potentiodynamic behaviour. The results of this will be discussed in section 5.4. The removal of dissolved oxygen by bubbling nitrogen through the cell did not alter the E-i characteristics.

Figure 5.4 shows the voltammetric behaviour of a freshly prepared  $\text{NiCo}_2\text{O}_4$  electrode cycled between 0.9 and 1.50 V at a sweep rate of  $25 \text{ mV s}^{-1}$  in 5 M KOH. A stable E-i profile is immediately obtained, and maintained as long as the anodic switching potential is kept below the vigorous oxygen evolution.

Anodically, the formation of at least two higher oxides before oxygen evolution starts, is indicated by cyclic voltammetry: the first anodic peak  $E_{a1}$  at 1.21 V, and a second anodic peak  $E_{a2}$  at 1.40 V. The cathodic profile is less sharp, and probably consists of a doublet peak: a sharp cathodic peak  $E_{c1}$  at 1.17 V, and a shoulder  $E_{c2}$ , at  $\sim 1.375 \text{ V}$ .

The ratio of the total anodic charge versus total cathodic charge approaches unity.

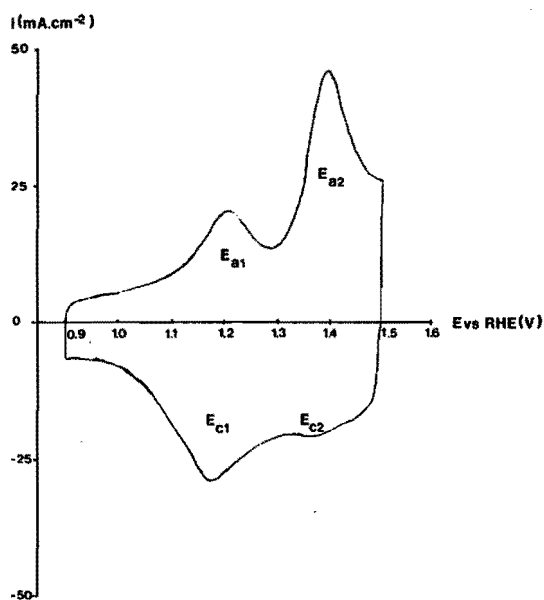


Figure 5.4: Cyclic voltammogram of a freshly prepared  $\text{NiCo}_2\text{O}_4$  electrode in 5 M KOH, 25°C at a sweep rate of  $25 \text{ mV s}^{-1}$ .  $T_F = 400^\circ\text{C}$  and  $t_F = 1 \text{ h}$ ; catalyst loading =  $12.30 \text{ mg cm}^{-2}$ .

### 5.3.2. Rest potential of $\text{NiCo}_2\text{O}_4$ .

Table 5.1 presents the rest potential of freshly prepared  $\text{NiCo}_2\text{O}_4$  electrodes as a function of the decomposition temperature  $T_F$  and duration  $t_F$  of the final heat treatment measured in 5 M KOH, oxygen free, 25°C. In the spinel-only range (below 400°C), the rest potential fluctuates around 1.1 V and above 400°C, where the decomposition of the spinel structure starts, the rest potential is slightly lower. When a potential of the oxygen evolution range, i.e. higher than 1.45 V, has been applied to a  $\text{NiCo}_2\text{O}_4$  electrode, the open circuit voltage is higher and appears to be determined by the lower metal oxide  $\text{NiCo}_2\text{O}_4$ /higher metal oxide  $\text{NiCo}_2\text{O}_4$  couple, i.e. 1.40-1.45 V [4,22].

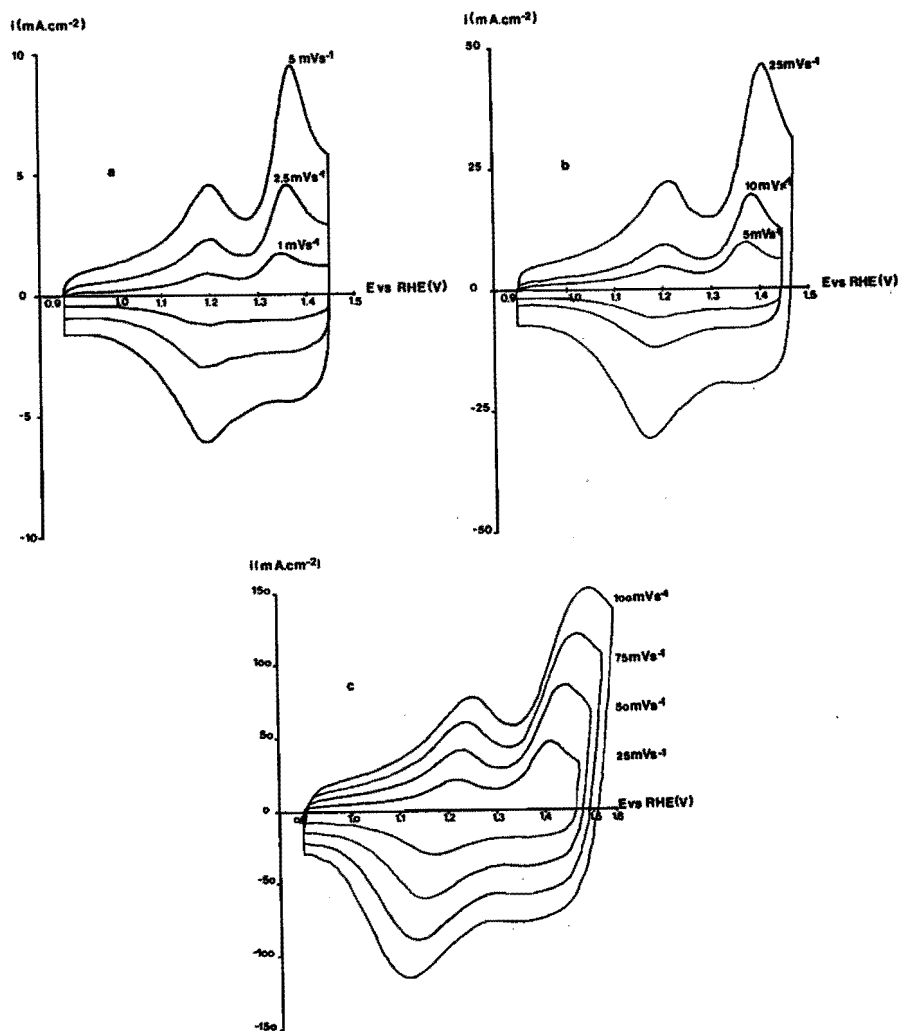


Figure 5.5: Cyclic voltammetric behaviour of a freshly prepared  $\text{NiCo}_2\text{O}_4$  electrode as a function of the potential sweep rate  $v$  in 5 M KOH, 25°C.  $T_{\text{F}} = 400^\circ\text{C}$  and  $t_{\text{F}} = 1$  h; catalyst loading =  $15.30 \text{ mg cm}^{-2}$ .  
 a)  $v = 1.0\text{-}2.5\text{-}5.0 \text{ mV s}^{-1}$ ; b)  $v = 5\text{-}10\text{-}25 \text{ mV s}^{-1}$ ;  
 c)  $v = 25\text{-}75\text{-}100 \text{ mV s}^{-1}$ .

Table 5.1: Rest potential of freshly prepared  $\text{NiCo}_2\text{O}_4$  electrodes as a function of the temperature ( $T_F$ ) and duration ( $t_F$ ) of the final heat treatment in 5 M KOH, 25°C.

$T_F$ (°C)	$t_F$ (h)	Catalyst loading (mg.cm <sup>-2</sup> )	$E_{\text{OCV}}$ (V)
250	10	21.35	1.134
300	1	19.05	1.117
300	10	20.70	1.114
350	1	21.05	1.099
400	1	20.95	1.120
400	10	15.90	1.135
500	1	20.00	1.051
600	1	17.75	1.055

### 5.3.3. Effect of the potential scan rate

The E-i characteristics were studied as a function of the potentials scan rate  $v$ , in the range 1 to 100  $\text{mV s}^{-1}$  for fresh  $\text{NiCo}_2\text{O}_4$  electrodes, prepared at different temperatures of final heat treatment  $T_F$ , i.e. 300 and 400°C. The position of the anodic peaks appears to depend on the potential scan rate  $v$ , as given in figure 5.5a and b for the sweep rates of 1 to 25  $\text{mV s}^{-1}$ . The second anodic peak  $E_{a2}$  is shifted more towards anodic potential values than the first anodic peak  $E_{a1}$ . The peak  $E_{a2}$  shows a less reversible character than peak  $E_{a1}$ . With further increasing the potential sweep rate, the anodic peaks shifted to more positive potentials whereas the cathodic peaks moved towards more negative values.

The voltammetric curves are not corrected for the ohmic drop ( $iR_{\text{drop}}$ ). However, the peak currents are relatively high in the case of  $\text{NiCo}_2\text{O}_4$  electrodes and the peak current  $i_p$  increases with the potential sweep rate  $v$ , so that, the larger the scan rate  $v$  the more

the peak potential  $E_p$  will be shifted on account of the uncompensated resistance  $R_u$ . This becomes evident for scan rates greater than  $25 \text{ mV s}^{-1}$ , as shown in figure 5.5c. The voltammetric curves become less symmetrical and flattened. Hence the upper limit of the sweep rate was limited to  $100 \text{ mV s}^{-1}$ .

The cyclic voltammogram of a freshly prepared  $\text{NiCo}_2\text{O}_4$  electrode shows two anodic oxidation peaks prior to oxygen evolution in the studied potential sweep rate range of 1 to  $100 \text{ mV s}^{-1}$ . This is in contradiction with the work of Rasiyah [14]. According to these authors, at low sweep rates, only one broad oxide peak is seen before oxygen evolution takes place, which resolved into two peaks at a sweep rate of  $100 \text{ mV s}^{-1}$ .

In earlier reported work of the same authors [4], the sweep rate  $v$  was varied between 20 and  $90 \text{ mV s}^{-1}$  and only one peak was observed. No indication of a doublet peak was observed. Moreover, in their study, Rasiyah et al. [14] observed two peaks, i.e. at 1.3 and 1.5 V, but in a peak current ratio of 2 to 1, whereas in this study and in the work of Yeager et al. [2] an inversed ratio of 1 to 2 is observed. The difference in the surface state of the  $\text{NiCo}_2\text{O}_4$  electrode is probably a result of the difference in preparation techniques, i.e. thermal decomposition and cryochemical synthesis.

Figure 5.6 shows the total anodic peak currents,  $i_{pa1,t}$  and  $i_{pa2,t}$  versus the potential sweep rate  $v$ , recorded in the E-range 0.9–1.5 V for  $\text{NiCo}_2\text{O}_4$  electrodes prepared at different temperature of heat treatment  $T_p$ , i.e. 300 and  $400^\circ\text{C}$ .

The difference on the potential scan rate  $v$  makes it possible to distinguish between a surface- and a solution redox reaction. In the former, the peak current  $i_p$  is directly proportional to the potential scan rate  $v$  and in the latter, the peak current is proportional to its square root,  $\sqrt{v}$ .

A linear relationship is found for both anodic peaks, pointing to a surface redox reaction. A slight deviation in the linear relationship between  $i_p$  and  $v$  is noted, as a result of the flattening of the cyclic voltammogram for earlier reported reasons. This is more pronounced for the second anodic peak  $E_{a2}$ , because of the higher peak currents.

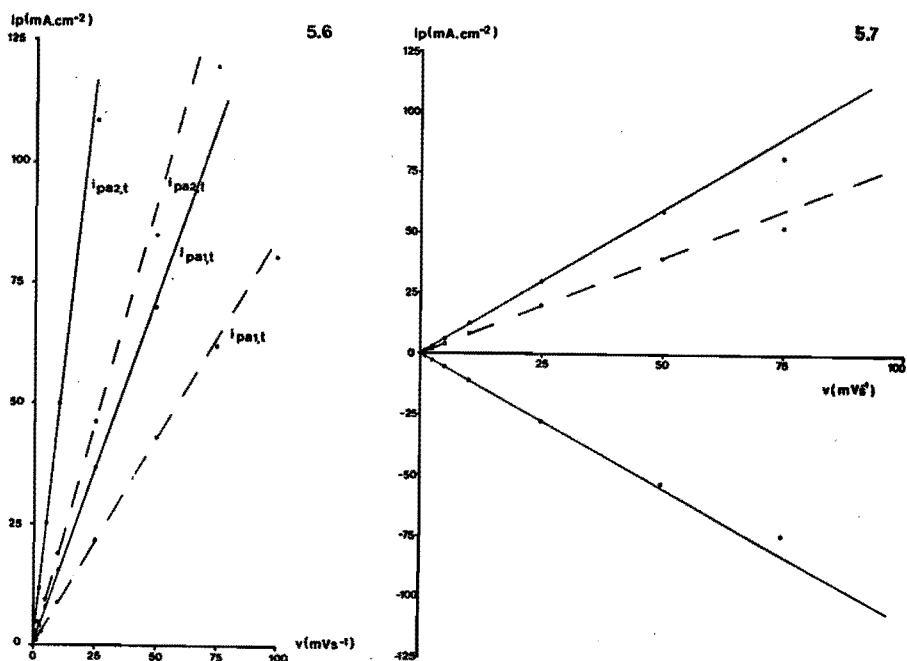


Figure 5.6: The dependence of the anodic peak currents  $i_{pa}$  on the potential sweep rate  $v$  in 5 M KOH, 25°C.

	$T_F$ (°C)	$t_F$ (h)	Catalyst loading (mg cm <sup>-2</sup> )
—————	300	1	19.05
-----	400	1	15.30

Figure 5.7: Plot of the first anodic and cathodic  $i_p$  versus  $v$  relation in 5 M KOH, 25°C.

$T_F = 400^\circ\text{C}$  and  $t_F = 1$  h; catalyst loading = 18.20 mg cm<sup>-2</sup>.

————— : total peak current  $i_{pt}$   
 ----- : peak current  $i_{pf}$  corrected for charging current  $i_c$ .

Figure 5.7 shows the first anodic and cathodic  $i_p$  versus  $v$  relation for NiCo<sub>2</sub>O<sub>4</sub> electrodes, prepared at the temperature of final heat treatment  $T_F$ , equal to 400°C. The peak currents were recorded in the potential range 0.9 to 1.3 V, as shown in figure 5.8a and in presence of the second anodic peak  $E_{a2}$ , at ~ 1.4 V, in the earlier mentioned potential range 0.9 to 1.5 V, figure 5.8b, both for different

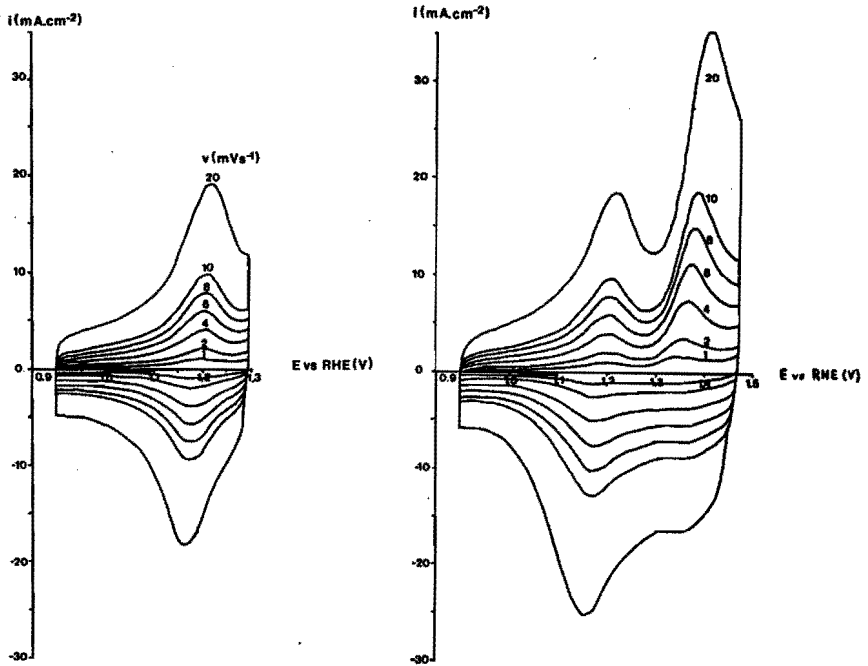


Figure 5.8: Cyclic voltammetric behaviour of a freshly prepared  $\text{NiCo}_2\text{O}_4$  electrode as function of the potential sweep rate  $v$  in 5 M KOH, 25°C.  $T_F = 400^\circ\text{C}$  and  $t_F = 1$  h; catalyst loading =  $16.20 \text{ mg cm}^{-2}$ .  
 a) Potential scan range 0.9 to 1.3 V; b) 0.9 to 1.475 V.

potential sweep rates. Increasing the upper limit potential to 1.5 V did not change the anodic peak current  $i_{\text{pal}}$  versus  $v$  relation. This indicates that an upper limit potential of 1.3 V is sufficient to complete the first anodic oxidation process.

The  $i_{\text{pal}}$  versus  $v$  relation was presented with and without charging current correction in figure 5.7. Since the potential is continuously changing in a potential sweep experiment, a charging current  $i_c$  always flows and the faradaic current  $i_f$  must always be measured from a baseline of charging current. The capacitive current  $i_c$  in the voltammogram is given by the expression (5.1),

$$i_c = A C_d v \quad (5.1)$$

where  $A$  is the surface area and  $C_d$  is the double layer capacitance.

The precision of the baseline subtraction depends on the choice of the lower switching potential, as shown in figure 5.9. Accurate baseline subtraction demands scanning in the lower potential range, where the spinel decomposition takes place. As demonstrated in the figure 5.9 the charging current correction line becomes more and more parallel with the current axis, when the lower limit potential decreases. The reproducibility of the  $\text{NiCo}_2\text{O}_4$  electrodes in the different potential ranges allows to take account of this fact during the capacitive current correction in the studied potential range. Note that while for a solution redox reaction  $i_p$  varies with  $\sqrt{v}$ ,  $i_c$  becomes relatively more important at faster scan rates. On the other hand, both the surface redox reaction and the charging current  $i_c$  applies to a linear relationship with the potential sweep rate  $v$ . Therefore, the results are shown with and without baseline subtraction in figure 5.7.

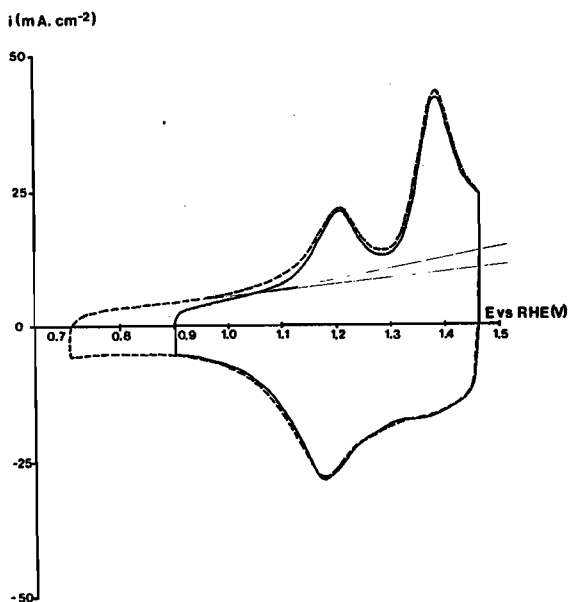


Figure 5.9: Influence of the lower switching potential on the precision of the base line subtraction.

Experimental conditions: 5 M KOH, 25°C;  $v = 25 \text{ mV s}^{-1}$ ;  
 $T_F = 400^\circ\text{C}$  and  $t_F = 1 \text{ h}$ ; catalyst loading =  $12.70 \text{ mg cm}^{-2}$ .



The peak width at mid-height  $W_{1/2}$  for a reversible surface redox reaction is equal to  $90.6/n$  mV at  $25^\circ\text{C}$ , where  $n$  is the number of electrons [15]. As shown in table 5.2, the measured width of both the current peaks at mid-height are only slightly higher than the theoretical  $W_{1/2}$  for an one-electron process. A small increase in the  $W_{1/2}$  for both anodic peaks with decreasing  $T_F$  is noted.

Table 5.2: The peak width at mid-height  $W_{1/2}$  of the anodic current peaks of fresh  $\text{NiCo}_2\text{O}_4$  electrodes prepared at different temperatures  $T_F$ .

Experimental conditions: 5 M KOH,  $25^\circ\text{C}$ ,  $t_F = 1$  h.

$T_F$ ( $^\circ\text{C}$ )	Catalyst loading ( $\text{mg cm}^{-2}$ )	Potential scan range (V)	Peak	$W_{1/2}^*$ (mV)
300	17.80	0.9 to 1.3	$E_{a1}$	100-120
300	19.05	0.9 to 1.5	$E_{a2}$	100-120
400	18.20	0.7 to 1.3	$E_{a1}$	105-110
400	12.30	0.9 to 1.3	$E_{a1}$	90-100
400	47.60	0.7 to 1.475	$E_{a1}$	110-115
			$E_{a2}$	110-115

\*: Measured  $W_{1/2}$  in the potential sweep rate range of 1 to  $100 \text{ mV s}^{-1}$  with base line subtraction.

#### 5.3.4. Effect of the catalyst loading

Figure 5.10 shows the anodic voltammetric charge for a set of freshly prepared  $\text{NiCo}_2\text{O}_4$  electrodes as a function of the catalyst loading ( $\text{mg cm}^{-2}$ ). It demonstrates that the voltammetric charge is independent of the amount of the  $\text{NiCo}_2\text{O}_4$  catalyst loading, from about  $20 \text{ mg cm}^{-2}$ . This agrees well with the results reported in section 3.1.2 where it was found that the catalyst loading has virtually no influence on the anodic performance, as shown in figures 3.2 and 3.3. These

results already indicated that mainly the top surface of the  $\text{NiCo}_2\text{O}_4$  electrode is active for oxygen evolution. The formation of higher oxides is limited to the surface of the  $\text{NiCo}_2\text{O}_4$  catalyst layer. The discrepancy in voltammetric charge at lower catalyst loadings, i.e. below  $20 \text{ mg cm}^{-2}$  can be explained by the influence of the deposition rate or the number of coatings on the morphology of the  $\text{NiCo}_2\text{O}_4$  layer, as reported in section 3.3.2.1.

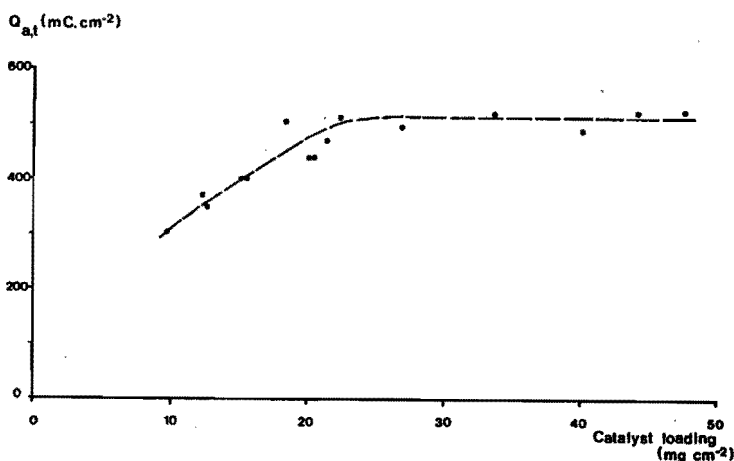


Figure 5.10: Plot of the anodic voltammetric charge  $Q_{a,t}$  as function of the catalyst loading for freshly prepared  $\text{NiCo}_2\text{O}_4$  electrodes.

Experimental conditions: 5 M KOH,  $25^\circ\text{C}$ ;  $v = 25 \text{ mV s}^{-1}$ ;  $T_F = 400^\circ\text{C}$  and  $t_F = 1 \text{ h}$ .

Figure 5.11 which exhibits the anodic peak currents,  $i_{pa1}$  and  $i_{pa2}$ , for a set of  $\text{NiCo}_2\text{O}_4$  electrodes, prepared at  $400^\circ\text{C}$ , as a function of the catalyst loading, shows that also the oxidation peaks are independent of the catalyst loading from  $20 \text{ mg cm}^{-2}$ .

The good reproducibility of the preparation method, as earlier reported in chapter 3, is confirmed by the excellent reproducibility of the voltammetric behaviour of freshly prepared  $\text{NiCo}_2\text{O}_4$  electrodes in relation to the values of the peak potentials  $E_p$ , peak currents  $I_p$  and voltammetric charges  $Q$ .

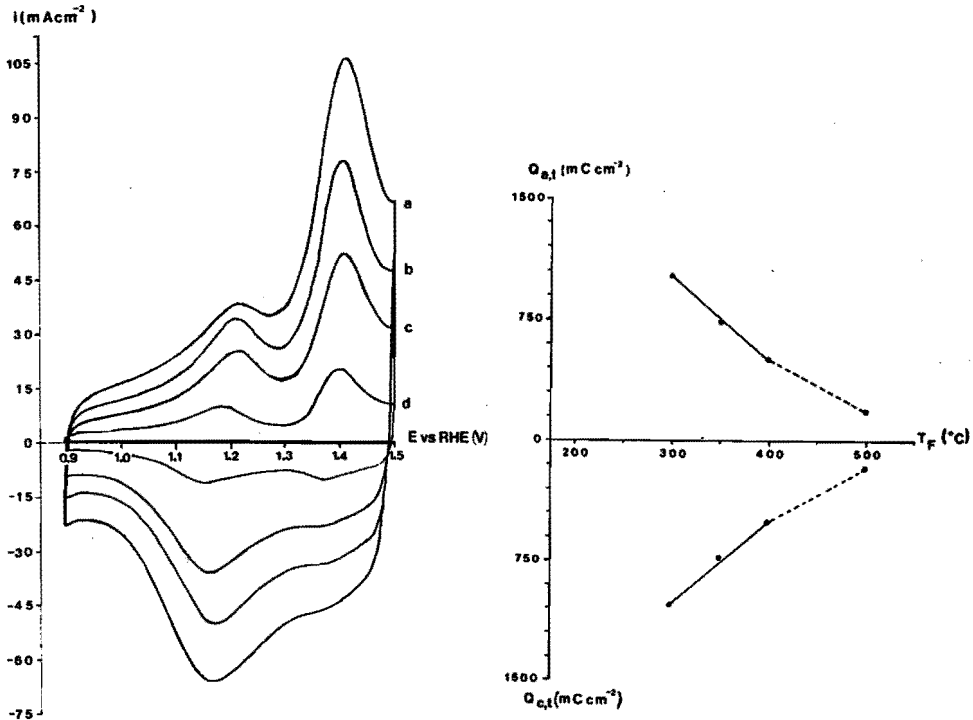


Figure 5.12: Cyclic voltammograms of fresh  $\text{NiCo}_2\text{O}_4$  electrodes prepared at different temperatures  $T_F$  of the final heat treatment.

Experimental conditions: 5 M KOH, 25°C;  $v = 25 \text{ mV s}^{-1}$ ;  $t_F = 1 \text{ h}$ .

curve	$T_F$ (°C)	Catalyst loading ( $\text{mg cm}^{-2}$ )
a	300	19.05
b	350	21.05
c	400	20.95
d	500	20.00

Figure 5.13: Plot of the voltammetric charge  $Q_{e,t}$  as a function of  $T_F$ .

Experimental conditions: see figure 5.13.

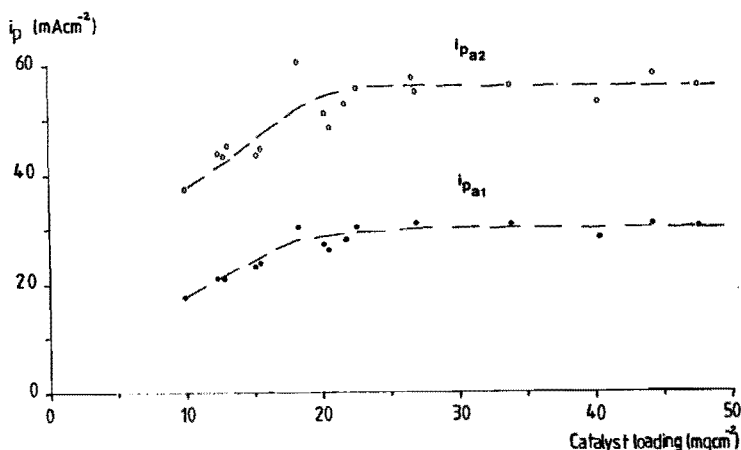


Figure 5.11: Plot of the anodic peak currents  $i_{pa}$  as function of the catalyst loading.

Experimental conditions: 5 M KOH, 25°C;  $v = 25 \text{ mV s}^{-1}$ ;

$T_F = 400^\circ\text{C}$  and  $t_F = 1 \text{ h}$ .

[•] =  $i_{pa1}$ ; [o] =  $i_{pa2}$

### 5.3.5. Effect of the heat treatment

The temperature range  $T_F$  between 250 and 600°C was examined, whilst the duration of the heat treatment  $t_F$  was varied between 1 and 10 h. Figure 5.12 shows the cyclic voltammograms of fresh  $\text{NiCo}_2\text{O}_4$  electrodes prepared at different temperatures of the final heat treatment. All other preparation parameters were the same, including the duration of the heat treatment of 1 h. In the spinel-only range, i.e.

$T_F \leq 400^\circ\text{C}$ , the anodic and cathodic peak potentials do not depend on the temperature  $T_F$  of the decomposition. With increasing  $T_F$  the peak profile becomes sharper and more symmetrical. In figure 5.13 the voltammetric charges as function of the decomposition temperature  $T_F$  are given. The voltammetric charge decreases monotonically as the temperature of the heat treatment  $T_F$  increases. This could indicate that the surface area decreases with increasing  $T_F$ . The ratio of the total anodic to the total cathodic charge is about unity for all  $T_F$ -values.

The peak currents, from the cyclic voltammograms recorded at  $25 \text{ mV s}^{-1}$ , as function of the final heat treatment temperature are given in figure 5.14. Anodically, it appears that the second anodic peak current  $i_{pa2}$  increases faster with decreasing temperature  $T_F$  than the first anodic peak current  $i_{pa1}$ . This indicates that the surface composition depends on the temperature  $T_F$ .

Figure 5.15 presents the ratio  $i_{pa2}$  vs.  $i_{pa1}$  as a function of the final heat treatment, i.e.  $T_F$  and  $t_F$ . The ratio  $i_{pa2}$  versus  $i_{pa1}$  depends on the temperature  $T_F$ , it increases with decreasing  $T_F$ , with the duration  $t_F$  held constant. A most peculiar result was the change in the voltammetric charge ratio of the anodic oxidation peaks as a function of  $T_F$ . This implies that the effect of the heat treatment does not only involve the extension of the surface area. On the other hand, the ratio  $i_{pa2}$  versus  $i_{pa1}$  does not change with the duration of the heat treatment  $t_F$ , as given in figure 5.15 for  $t_F = 1 \text{ h}$  and  $t_F = 10 \text{ h}$ , with the temperature  $T_F$  held constant. Above  $400^\circ\text{C}$ , the ratio of the anodic peak currents remains nearly constant.

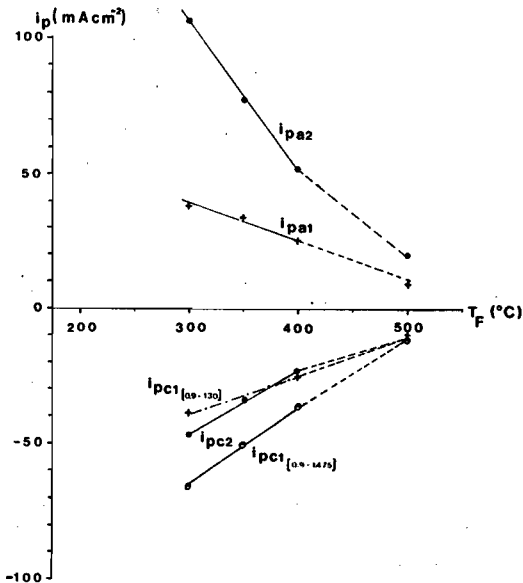


Figure 5.14: Plot of the peak currents  $i_p$  as a function of  $T_F$ .  
Experimental conditions: see figure 5.13.

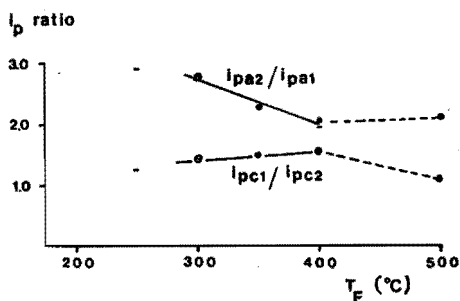


Figure 5.15: Plot of the ratio of the anodic, i.e.  $i_{pa2}/i_{pa1}$ , and cathodic, i.e.  $i_{pc1}/i_{pc2}$ , peak currents as a function of  $T_F$  and  $t_F$ .

Experimental conditions: 5 M KOH, 25°C; catalyst loading  $\sim 20 \text{ mg cm}^{-2}$ .

[●] =  $t_F = 1 \text{ h}$ ; [■] =  $t_F = 10 \text{ h}$ ; [⊗] = overlapping points.

On the cathodic side in figure 5.14, the first cathodic peak current  $i_{pc1}$  is plotted twice, once recorded in the potential scan range 0.9 to 1.3 V, as mentioned earlier, directly correlated to  $E_{a1}$ , and in the potential range 0.9 to 1.475 V, with the reduction contribution of  $E_{a2}$ . The  $i_{pa1}$ -curve, independently of being recorded in the E-range 0.9 to 1.3 V or 0.9 to 1.475 V is perfectly reflected in the  $i_{pc1}$ -curve recorded in the E-range 0.9 to 1.3 V. The increase of  $i_{pc1}$  and  $i_{pc2}$  with decreasing  $T_F$ , is nearly equal. The same fact is also observed from the ratio of the cathodic peak currents, as given in figure 5.15 which is not strongly influenced by  $T_F$  in the spinel only temperature range, i.e. below 400°C. Above 400°C, there is a strong deviation in the tendency of the peak current ratios, especially in the cathodic ratios, probably due to the start of the breakdown of the spinel structure.

Figure 5.16 presents the voltammetric behaviour of an electrode treated at 500°C ( $T_F$ ) for 1 h ( $t_F$ ). In the temperature range where the spinel decomposition takes place, a sharp doublet of cathodic peaks and a clear shift of the peak potential  $E_a$  is observed. Further increasing of  $T_F$  results in a cyclic voltammogram which is strongly

disturbed by the increased resistance as a consequence of the decomposition of  $\text{NiCo}_2\text{O}_4$  into individual oxides with higher resistances. In figure 5.17 the potentiodynamic respons of an electrode treated at  $600^\circ\text{C}$  ( $T_F$ ) for 1 h ( $t_F$ ), recorded at  $2.5 \text{ mV s}^{-1}$ , is shown. The anodic and cathodic peak potentials, however, do not depend on the temperature  $T_F$  of the decomposition in the spinel-only range, while the voltammetric charge decreases monotonically as the temperature  $T_F$  increases. These results are contradictory to those of Trasatti et al. [11-13], who reported that the peak position and the voltammetric charge increased with increasing  $T_F$ . This disagreement is probably due to the ageing process, as will be discussed in section 5.4, which was not recognized by Trasatti as indicated by the observation of only one anodic peak.

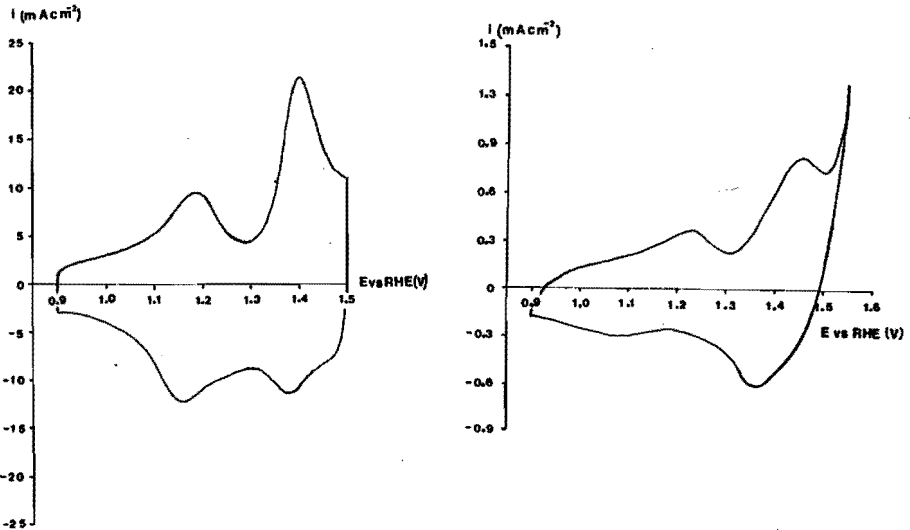


Figure 5.16: Cyclic voltammogram of a fresh electrode prepared  $500^\circ\text{C}$  ( $T_F$ ) for 1 h ( $t_F$ ).

Experimental conditions: 5 M KOH,  $25^\circ\text{C}$ ;  $v = 25 \text{ mV s}^{-1}$ ; catalyst loading =  $20 \text{ mg cm}^{-2}$ .

Figure 5.17: Cyclic voltammogram of a nickel cobalt oxide electrode prepared at  $600^\circ\text{C}$  ( $T_F$ ) for 1 h ( $t_F$ ).

Experimental conditions: 5 M KOH,  $25^\circ\text{C}$ ;  $v = 2.5 \text{ mV s}^{-1}$ ; catalyst loading =  $17.75 \text{ mg cm}^{-2}$ .

Our results are in agreement with the work of Tamura [23,24], who observed the same tendency for  $\text{Co}_3\text{O}_4$  electrodes, also prepared by thermal decomposition, but are in contradiction with the observation of Tseung [6,25], who concludes that there is no correlation between the surface area and the electrochemical performance.

In section 3.3.1.1, it was reported that lowering the temperature  $T_F$  of the final heat treatment leads to an increase in electrochemical activity for oxygen evolution, as given in figure 3.1. It was also found that the voltammetric charge increases with decreasing  $T_F$ , as shown in figure 5.13. It appears that the voltammetric charge is halved in going from 300°C to 400°C. The correlation between the increase in activity and the increase in voltammetric charge with decreasing  $T_F$ , indicates that it can be attributed to a change in the surface area.

Table 5.3 shows the correlation between the anodic performance and the voltammetric charge for  $\text{NiCo}_2\text{O}_4$  electrodes prepared at 300 and 400°C. It appears that the current density at high overpotentials increases with a factor 2 in going from 400 to 300°C, while the voltammetric charge increases similarly.

Therefore, the voltammetric charge of freshly prepared  $\text{NiCo}_2\text{O}_4$  electrodes can be taken as a measure for the surface area. This is in agreement with the BET-results, where the surface area increases with decreasing  $T_F$ , as will be reported in chapter 6.

However, the surface composition is also influenced by  $T_F$ , as is indicated by the change in the anodic peak currents ratio  $i_{pa2}/i_{pa1}$ , as shown in figure 5.15. So it is possible that the difference in anodic performance is not only a result of the difference in surface area, but also of the difference in surface composition.

On the other hand, the duration  $t_F$  of the heat treatment gives no significant changes in activity, as also reported in chapter 3. Likewise the voltammetric charge as function of  $t_F$  at constant  $T_F$  changes only slightly (maximal 15%). It appears that there is virtually no further change in surface area after a 1 h heat treatment. Summarizing, it can be concluded that in the spinel-only range the surface composition is influenced by the temperature  $T_F$ , but not by the duration  $t_F$  of the final heat treatment.



Table 5.3: Correlation between the anodic performance and the voltammetric charge of  $\text{NiCo}_2\text{O}_4$  electrodes as a function  $T_F$ . Experimental conditions: 5 M KOH, 25°C.

E (V)	$T_F$ (°C) - $t_F$ (h)	
	300 - 1 h	400 - 1 h
	$i$ (mA cm <sup>-2</sup> )	
1.44	0.65	0.20
1.45	1.10	0.36
1.50	20	10
1.55	100	45
1.60	400	200

$Q_{a,t}$ (mC cm <sup>-2</sup> )	
1020	502

Table 5.4: Weight percentage (wt %), apparent electrochemical roughness factor (ARF) and -surface area (ASA) of the  $\text{NiCo}_2\text{O}_4$  electrodes as a function of  $T_F$  and  $t_F$ , based on the cyclic voltammetric charge. Experimental conditions: 5 M KOH, 25°C;  $v = 25$  mV s<sup>-1</sup>.

$T_F$ (°C)	$t_F$ (h)	Cat. loading (mg cm <sup>-2</sup> )	$Q_{a,t}$ (mC cm <sup>-2</sup> )	wt% in 4+ state (wt %)	ARF	ASA (m <sup>2</sup> g <sup>-1</sup> )
250	1	21.35	1175	5.18	2284	10.7
300	1	19.05	1020	3.33	1306	6.9
300	10	20.70	1155	3.48	1479	5.9
350	1	21.05	740	2.19	949	4.5
400	1	20.95	507	1.51	650	3.1
400	10	15.90	405	1.59	519	3.3
500	1	20.70	182	0.57	233	1.2

The voltammetric charge can be taken as a measure of the surface concentration of metal ions participating in the electrochemical processes, From the charge passed to form the higher oxides before oxygen evolution commences, and assuming that all metal ions are oxidized to the 4+ valence state, the percentage of the oxidized catalyst material can be estimated, as shown in tabel 5.4 for freshly prepared  $\text{NiCo}_2\text{O}_4$  electrodes with about the same catalyst loading, i.e.  $20 \text{ mg cm}^{-2}$ , as function of  $T_F$ . Since the voltammetric charge was not influenced by the catalyst loading, the percentage will decrease with further increasing catalyst loading. The values strongly indicate that the change in valence state is limited to the surface  $\text{NiCo}_2\text{O}_4$  layer. The weight of an unit area monolayer  $\text{NiCo}_2\text{O}_4$  ( $4.86 \cdot 10^{-7} \text{ g cm}^{-2}$ ) can be calculated, assuming that the unit cell edge or lattice parameter  $a_0$  is equal to  $8.11 \text{ \AA}$  [26,27]. Hence, from the voltammetric charge (which is proportional to weight per unit area  $\text{NiCo}_2\text{O}_4$  oxidized to the 4+ state) the number of monolayer ( $\text{cm}^{-2}$ ) can be calculated. This apparent electrochemical roughness factor ARF is a magnitude for the product of the electrochemical surface roughness and the depth. From this number of monolayers ( $\text{cm}^{-2}$ ) and the catalyst loading ( $\text{g cm}^{-2}$ ) an apparent electrochemical surface area ASA ( $\text{m}^2 \text{ g}^{-1}$ ) can be calculated, as tabulated in 5.4. The apparent electrochemical roughness factor and -surface area decrease with the temperature  $T_F$ ; nearly no influence of  $t_F$  is observed.

It was reported in section 3.2.1 that the magnitude of the  $\text{NiCo}_2\text{O}_4$  catalyst loading had virtually no influence on the anodic performance and on the voltammetric charge (section 5.3.4). Table 5.5 shows the weight percentage of the  $\text{NiCo}_2\text{O}_4$  catalyst loading oxidized to the 4+ state, the apparent electrochemical roughness factor and -surface area for a set of freshly prepared  $\text{NiCo}_2\text{O}_4$  electrodes ( $T_F = 400^\circ\text{C}$  and  $t_F = 1 \text{ h}$ ) as function of the catalyst loading. It appears that the weight  $\text{NiCo}_2\text{O}_4$  in the 4+ valence state and the roughness factor are virtually constant above  $20 \text{ mg cm}^{-2}$  catalyst loading. It is evident that the weight percentage and the surface area changes with the catalyst loading, because they were defined as function of the catalyst loading.

Table 5.5: Weight percentage (wt %), apparent electrochemical roughness factor (ARF) and -surface area (ASA) for a set of freshly prepared  $\text{NiCo}_2\text{O}_4$  electrodes as a function of the catalyst loading.

Experimental conditions: 5 M KOH, 25°C;  $v = 25 \text{ mV s}^{-1}$ ;  
 $T_F = 400^\circ\text{C}$  and  $t_F = 1 \text{ h}$ .

Cat. loading ( $\text{mg cm}^{-2}$ )	$Q_{a,t_2}$ ( $\text{mC cm}^{-2}$ )	weight in 4+ ( $\text{mg cm}^{-2}$ )	wt % in 4+ (wt %)	ARF	ASA ( $\text{m}^2 \text{ g}^{-1}$ )
12.30	350	0.22	1.77	448	3.6
15.15	401	0.25	1.65	514	3.4
18.20	505	0.32	1.73	647	3.6
20.10	439	0.27	1.36	562	2.8
21.40	470	0.29	1.37	603	2.8
22.50	515	0.32	1.43	660	2.9
26.50	495	0.31	1.16	634	2.4
34.00	520	0.32	0.95	667	1.9
47.60	526	0.33	0.69	673	1.4

### 5.3.6. Galvanostatic charging curves

The appearance of oxidation state transitions before oxygen evolution starts is evident from cyclic voltammetry, however not, how many oxidation state transitions take place. Therefore, the galvanostatic charging method was tried to split up the anodic current peaks. Figure 5.18 shows the constant current charging curve for a  $\text{NiCo}_2\text{O}_4$  electrode, prepared at  $300^\circ\text{C}$  ( $T_F$ ). An anodic charging current of  $0.125 \text{ mA cm}^{-2}$  (curve I) was applied to the electrode from its rest potential, i.e. 1.1 V, and the change in potential was recorded with time (or charge). No definite plateaus and areas could be observed, it is possible to distinguish four regions, which are not clearly separated: first a fast increase of the potential versus char-

ge (Q), due to the double layer charging, then three intermediate regions, where the potential increases slowly, two of which can be ascribed to the two earlier observed anodic processes, i.e.  $E_{a1}$  and  $E_{a2}$ , and finally the last region where the potential doesn't change anymore with time and oxygen evolution takes place.

A cathodic charging current of  $-0.5 \text{ mA cm}^{-2}$  was applied to the electrode after the anodic charging curve was finished, as given in figure 5.18, curve II. The charging curve profile is even less distinct and only one broad reduction area is observed.

Varying the magnitude of the charging current did not change the charging curve profiles.

No further information was obtained from charging curves.

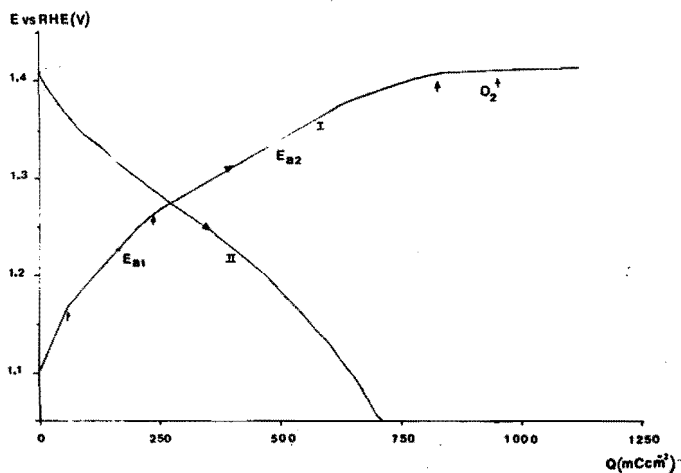


Figure 5.18: Galvanostatic charging curve for a  $\text{NiCo}_2\text{O}_4$  electrode, prepared at  $300^\circ\text{C}$  ( $T_F$ ) for 1 h ( $t_F$ ).

Experimental conditions: 5 M KOH,  $25^\circ\text{C}$

curve I: anodic charging current =  $+0.125 \text{ mA cm}^{-2}$ ;

curve II: cathodic charging current =  $0.5 \text{ mA cm}^{-2}$ .

### 5.3.7. Aprotic medium

The use of an aprotic solvent for cyclic voltammetry makes it possible to investigate the role of the hydroxyl ion in the electrochemical

reaction before oxygen evolution takes place. Acetonitrile,  $\text{CH}_3\text{CN}$ , serves as an excellent solvent because it is quite difficultly oxidized and reduced; both anodic and cathodic limiting currents apparently are caused by discharge of the supporting electrolyte  $\text{LiClO}_4$  [28]. The voltammogram recorded from 0 to 1.5 V vs. SCE is shown in figure 5.19, curve I. No sign of the valency state transitions is observed. The anodic scan range is limited to 1.5 V vs. SCE, due to the discharge of the lithium perchlorate. Prolonged oxidation at 1.5 V vs. SCE resulted in a turbid solution as a consequence of this oxidation of the supporting electrolyte. In order to examine whether the oxide peaks were shifted to higher potentials in the aprotic solvent, water was added to the  $\text{CH}_3\text{CN-LiClO}_4$  solution. Now, the oxide peaks and the  $\text{H}_2\text{O}$  oxidation are observed indeed before the discharge starts, as shown in figure 5.19, curve II. Anodically, it is not possible to distinguish clearly between the oxide reactions, the oxygen evolution reaction and further the oxidizing of the electrolyte. However, the reduction peaks show clearly the existence of the anodic oxide reactions.

These results indicate that the hydroxyl ion plays an important role in the electrochemical reactions before the oxygen evolution reaction.

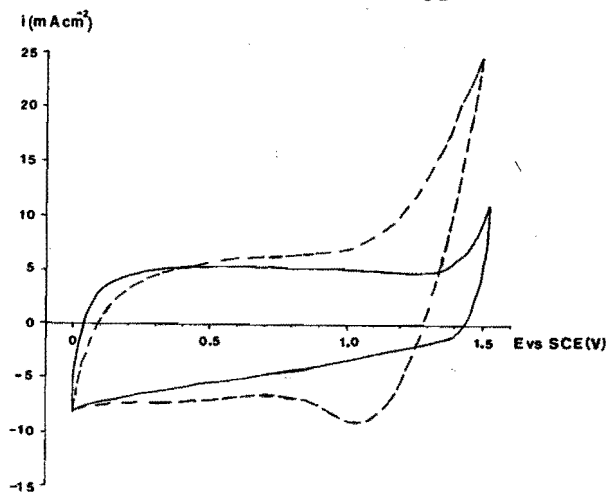


Figure 5.19: Cyclic voltammogram of a  $\text{NiCo}_2\text{O}_4$  electrode in aprotic medium.

Experimental conditions:  $\text{CH}_3\text{CN} + 0.1 \text{ M LiClO}_4$ ,  $25^\circ\text{C}$ ;  
 $v = 50 \text{ mV s}^{-1}$ ;  $T_{\text{F}} = 400^\circ\text{C}$  and  $t_{\text{F}} = 1 \text{ h}$ ; catalyst  
 loading =  $15.45 \text{ mg cm}^{-2}$ .

### 5.3.8. Rotating ring-disc electrodes

A demountable rotating ring-disc electrode was used in order to investigate the possibility of further oxidation steps in the oxygen evolution range. The nickel disc was covered with a  $\text{NiCo}_2\text{O}_4$  layer via thermal decomposition. The platinum ring was slightly platinized.

#### Testing of the ring-disc system

The solid curve in figure 5.20 shows the theoretical oxygen reduction limiting current at the ring  $I_{R,L}^o$  as function of the square root of the rotation frequency  $\sqrt{\omega}$ . The limiting ring current  $I_{R,L}^o$  was calculated using the Levich equation [29-31],

$$I_{D,L} = 0.62 nFA D_O^{2/3} \nu^{-1/6} C_O^* \omega^{1/2} \quad (5.2)$$

$$I_{R,L}^o = \beta^{2/3} I_{D,L} \quad (5.3)$$

with the number of electrons,  $n$  equal to 4.

The influence of the deposited  $\text{NiCo}_2\text{O}_4$  layer on the hydrodynamics of the rotating ring-disc electrode was examined in a 1 M KOH oxygen saturated solution. A less concentrated potassium hydroxide solution was chosen in order to increase the solubility for oxygen. The relevant physical properties of 1 M KOH solutions was obtained from [32] and are summarized in table 5.6.

The  $I_{R,L}$  versus  $\omega^{1/2}$  relation was measured on the demountable rotating ring-disc electrode, once in which the nickel disc was covered with a  $\text{NiCo}_2\text{O}_4$  layer and once without this layer. The experimental limiting oxygen reduction curves measured on the platinum ring, held at 0.2 V versus RHE, in an oxygen saturated 1 M KOH solution, at room temperature, are given in figure 5.20. The linear relationship of the experimental  $I_{R,L}$  versus  $\omega^{1/2}$  relation indicates that the hydrodynamics of the rotating ring-disc electrode is not influenced by the construction, nor by the coverage with a  $\text{NiCo}_2\text{O}_4$  layer.

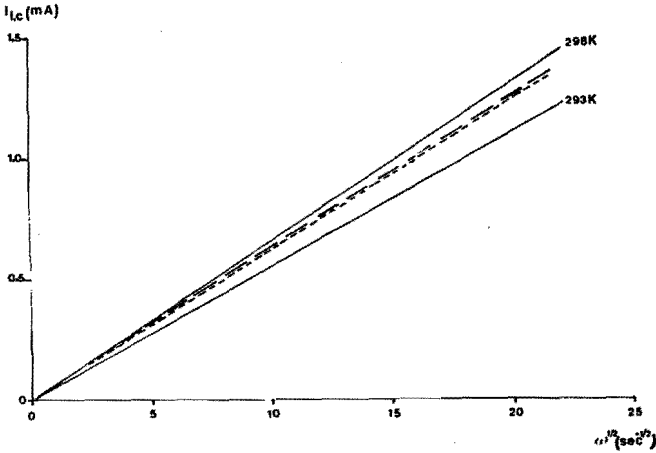


Figure 5.20: Plot of the  $I_{R,1}$  versus  $\sqrt{\omega}$  for oxygen reduction at the demountable RRDE in  $O_2$ -saturated 1 M KOH.  $E_R = 0.2$  V.

————— : theoretical  $I_{R,1}$  at  $T = 293$  and  $298$  K.  
 — — — : uncovered nickel disc  
 - - - - - :  $NiCo_2O_4$  covered disc.

Table 5.6: Relevant physical properties of 1 M KOH solutions.

T (K)	$D_{O_2}$ ( $cm^2 s^{-1}$ )	$\nu$ ( $cm^2 s^{-1}$ )	$c_{O_2}$ ( $mole\ cm^{-3}$ )
293	$1.36 \cdot 10^{-5}$	0.01063	$0.84 \cdot 10^{-6}$
298	$1.59 \cdot 10^{-5}$	0.00950	$0.89 \cdot 10^{-6}$

### Collection efficiency N

In the potential range, where the anodic galvanostatic disc current is only used for oxygen evolution, i.e. when the higher oxide formation is finished, the ratio  $-I_R/I_D$  is an experimental measure for the collection efficiency  $N$  of the evolved oxygen.

The  $-I_R/I_D$  ratio was measured at the pure nickel disc and at the nickel disc covered with a  $\text{NiCo}_2\text{O}_4$  layer. Different galvanostatic anodic currents were applied to the disc electrode and the evolved oxygen was detected on the platinized platinum ring. Before each measurement, nitrogen was bubbled through the cell to remove dissolved oxygen. Figure 5.22 shows the experimental  $-I_R/I_D$  ratios ( $N_{\text{exp}}$ ) measured in an 1 M KOH solution at room temperature.

The collection efficiency theoretically depends only on the geometry. However, it was found that the experimental  $N_{\text{exp}}$  is smaller than the calculated  $N_{\text{calc}}$  and is a function of the rotation frequency  $\omega$  and the disc current  $I_D$ . The major difference between the calculated  $N_{\text{calc}}$ , i.e. 0.308 and the experimental collection efficiency  $N_{\text{exp}}$ , approximately 0.20, during anodic oxygen evolution, is a consequence of the gas bubble formation. When gas is evolved initially at low current densities, the gas diffuses into the solution. At higher current densities oxygen bubbles are formed. In fact oxygen evolution starts to evolve as bubbles when the solution is supersaturated with oxygen. So, the oxygen bubble formation at the disc takes place in the supersaturated diffusion layer. The fraction of oxygen which evolves as bubbles is probably not detected at the platinum ring. The detection of the dissolved disc oxygen at the ring will be disturbed by the oxygen bubble stream.

The similar results for  $N_{\text{exp}}$  on the nickel disc with and without a  $\text{NiCo}_2\text{O}_4$  layer confirms that it was not an oxide layer effect. However, the surface roughness can also give rise to disturbance of the Levich behaviour of the rotating ring-disc electrode. The Levich behaviour will no longer be valid when the thickness of the diffusion layer becomes comparable with the surface roughness. Therefore, a very smooth  $\text{NiCo}_2\text{O}_4$  layer was applied to the nickel disc, deposited from a diluted nickel cobalt nitrate solution.

The similar results for the experimental collection efficiency  $N_{\text{exp}}$  on the nickel disc with and without a  $\text{NiCo}_2\text{O}_4$  layer, confirms that it was mainly a gas bubble effect.

It is also noted that the experimental  $-I_R/I_D$  ratios vary with the magnitude of the anodic disc current  $I_D$ , as shown in figure 5.21 at very high disc currents. This effect is clearly a consequence of the vigorous gas bubble evolution. The insufficient removal of the



bubbles, disturbs the oxygen detection. A gas bubble ring, which was visually observed, sticks to the gap ring and blocks a part of the platinum ring, thus hindering the supply of dissolved oxygen.

Therefore the detection of any further oxidation steps in the oxygen evolution potential range must experimentally be restricted to a maximum potential  $E_{Dmax}$ , which is determined by the maximum galvanostatic disc current  $I_{Dmax}$ . The value of  $I_{Dmax}$ , and therefore  $E_{Dmax}$ , also depends on the rotation frequency, as will be discussed in the next paragraph.

At the given rotation frequency  $\omega = 33 \text{ s}^{-1}$  in figure 5.21, the ratio  $-I_R/I_D$  can be considered as nearly constant in the galvanostatic disc current range of 0.125 to 5 mA.

The experimental collection efficiency  $N_{exp}$  is also influenced by the rotation frequency  $\omega$ . Figure 5.22 presents the experimental  $-I_R/I_D$  ratio as a function of  $\sqrt{\omega}$ , for different anodic galvanostatic currents applied to the disc.

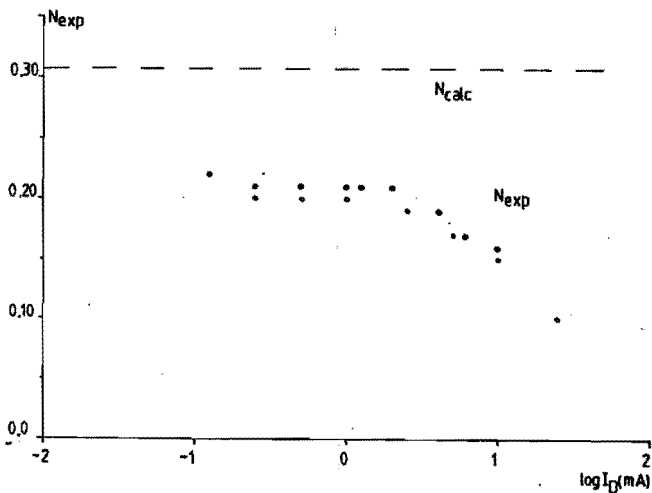


Figure 5.21: Plot of the experimental  $-I_R/I_D$  ratio as a function of the anodic galvanostatic disc current  $I_D$ .  
 Experimental conditions:  $O_2$ -free 1 M KOH;  $E_R = 0.2 \text{ V}$ ;  
 $\omega = 33.3 \text{ s}^{-1}$ ; [\*] =  $N_{exp}$  of the uncovered nickel disc; [o] =  $N_{exp}$  of the  $NiCo_2O_4$  disc.

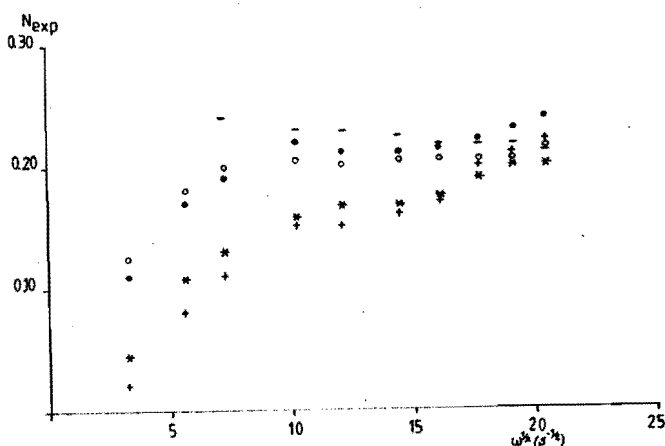


Figure 5.22: Plot of the experimental  $-I_R/I_D$  ratio versus  $\sqrt{\omega}$  for different anodic galvanostatic currents  $I_D$ . Experimental conditions:  $O_2$ -free 1 M KOH;  $E_R = 0.2$  V;  $I_D = 0.125$  mA [-]; 1 mA [o]; 2 mA [•]; 6 mA [\*]; 10 mA [+].

At lower rotation frequency, i.e. below  $15 s^{-1}$ , there is a sharp decrease in  $N_{exp}$ . This can be explained in a similar way, as mentioned before. The rotation of the ring-disc electrode introduces a solution flow and as a result the bubbles will be carried away more quickly with increasing  $\omega$ .

However, the purpose of the rotating ring-disc experiments here is to establish to what extent the anodic galvanostatic current is used for oxygen evolution and for higher oxide formation. With increasing galvanostatic disc current, the recorded limiting ring current must increase, according to the experimentally determined collection factor  $N_{exp}$ . A decrease in the limiting ring current  $I_{R,l}$  should indicate the presence of a disc charging current consuming process, i.e. a further oxidation step. The reproducibility of the  $-I_R/I_D$  ratios for the different ring-disc electrode under stipulated conditions, allows to execute the earlier stated experiments with the demountable RRDE.

Investigation of further oxidation steps in the oxygen evolution potential range.

A constant anodic charging current was applied to the disc, covered with  $\text{NiCo}_2\text{O}_4$  layer, starting from its rest potential, i.e. about 1.1 V, and the change in disc potential  $E_D$  versus time was recorded. The platinized Pt ring was held at 0.2 V in order to detect the evolved oxygen, by recording the ring current  $I_R$  versus time. The experiments were carried out in a 1 M KOH solution at room temperature from which the dissolved oxygen was removed by bubbling nitrogen through the cell. The ring current as a result of rest oxygen in the solution was taken into account.

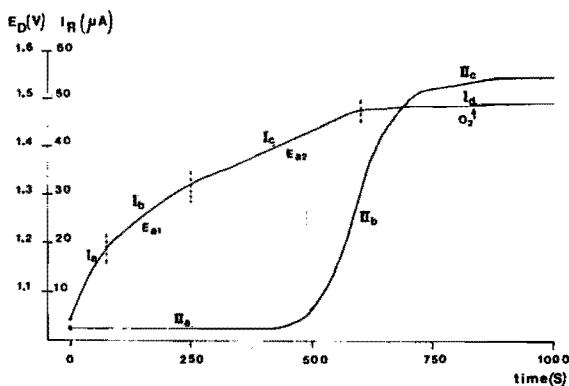


Figure 5.23: Constant anodic charging curve at demountable RRDE.

Experimental conditions:  $\text{O}_2$ -free 1 M KOH;  $\omega = 33.3 \text{ s}^{-1}$ ;  
 $D = \text{NiCo}_2\text{O}_4$  covered disc,  $T_F = 400^\circ\text{C}$  and  $t_F = 1 \text{ h}$ ;  
 catalyst loading =  $12 \text{ mg cm}^{-2}$ ; R = platinized platinum.  
 curve I :  $I_D = 0.25 \text{ mA} \rightarrow E_D \text{ vs. time}$   
 curve II:  $E_R = 0.2 \text{ V} \rightarrow I_R \text{ vs. time.}$

Figure 5.23 presents the two curves i.e. the disc potential  $E_D$  versus time (curve I) and the ring current  $I_R$  versus time (curve II). After the anodic charging current was finished, the current was switched to a cathode current of equal magnitude. The resulting disc potential  $E_D$  versus time, as given in figure 5.24 gave only a broad reduction peak, as earlier mentioned in section 5.3.6. The  $I_R$  versus time curve decreased immediately. The galvanostatic anodic charging

current  $I_D$  was systematically increased. This always resulted in a  $I_R$  versus time curve with the same profile.

The deposited  $\text{NiCo}_2\text{O}_4$  layer was also submitted to a potentiodynamic experiment. A potential scan rate  $v$  of  $1 \text{ mV s}^{-1}$  was applied to a  $\text{NiCo}_2\text{O}_4$  disc electrode, initially kept at  $1.0 \text{ V}$ , and then scanned up to  $1.5 \text{ V}$ , where it was kept constant for 5 minutes. The potentiodynamic behaviour of the disc electrode is given in figure 5.25, curve I. The corresponding ring current versus the disc potential is given in curve II.

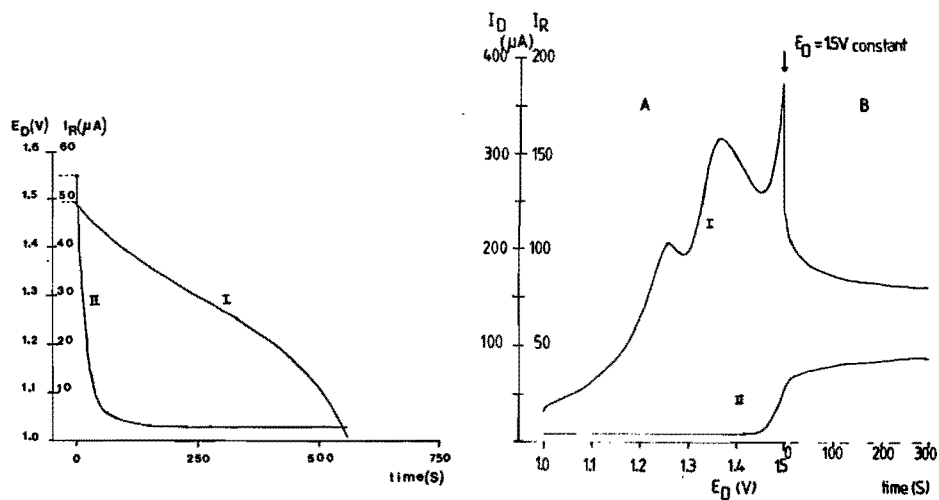


Figure 5.24: Constant cathodic charging curve at the demountable RRDE.

Experimental conditions: see figure 5.24.

curve I :  $I_D = -0.25 \text{ mA} \rightarrow E_D$  vs. time.

curve II:  $E_R = 0.2 \text{ V} \rightarrow I_R$  vs. time.

Figure 5.25: Potentiodynamic behaviour of a freshly prepared  $\text{NiCo}_2\text{O}_4$  covered disc in  $1 \text{ M KOH}$ , oxygen-free,  $\omega = 33.3 \text{ s}^{-1}$ .

Part A:  $E_D = 1.0 \text{ V}$ ,  $v = 1 \text{ mV s}^{-1}$ ;  $E_R = 0.2 \text{ V}$ .

curve I =  $I_D$  vs.  $E_D$ ; curve II =  $I_R$  vs.  $t \sim E_D$

Part B: at  $E_D = 1.5 \text{ V}$  for 5 min.

In the disc potential versus time, (curve I in figure 5.23), four areas can be distinguished, as found earlier in section 5.3.6.

- I<sub>a</sub> Double layer charging area
- I<sub>b</sub> First anodic peak E<sub>a1</sub>
- I<sub>c</sub> Second anodic peak E<sub>a2</sub>, both indicated by a slow increase in the disc potential E<sub>D</sub>.
- I<sub>d</sub> Oxygen evolving area, in which the disc potential E<sub>D</sub> becomes constant.

The corresponding ring current I<sub>R</sub> versus time curve consists of three parts:

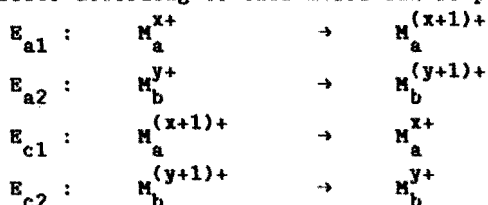
- II<sub>a</sub> No oxygen reduction current is detected up to 1.40 V. This shows that the charging current I<sub>D</sub> is only used to complete the higher oxide formation. II<sub>a</sub> can be correlated with the areas I<sub>a</sub> to I<sub>c</sub>.
- II<sub>b</sub> A transition area in the potential range of 1.40 to 1.45 V. The oxide formation is nearly finished and the oxygen evolution starts, which corresponds to the I<sub>c</sub> to I<sub>d</sub> transition.
- II<sub>c</sub> Only oxygen detection. The oxygen reduction current approaches a constant level, indicating that there is no higher oxide reaction participating, which corresponds with I<sub>d</sub>. The experimental  $-I_R/I_D$  ratio is about 0.20.

The recorded ring currents I<sub>R</sub>, at higher anodic charging curves I<sub>D</sub>, exceed the theoretical limiting oxygen reduction for an oxygen saturated 1 M KOH solution with a factor 2 to 3, in spite of the decrease of the collection efficiency N, as a result of the gas bubble formation. This clearly indicates that supersaturation takes place. On the other hand, figure 5.25 also illustrates the role of the oxide formation prior to the oxygen evolution reaction. No oxygen evolution is observed before this oxide formation is nearly finished. From the galvanostatic charging curves, it can be concluded that there was no indication of any further oxidation reactions, up to 1.55-1.60 V.

### 5.3.9. Correlation between the anodic and cathodic processes.

The cyclic voltammogram of NiCo<sub>2</sub>O<sub>4</sub> indicates anodically the formation of two higher oxides before oxygen evolution starts. Any further

oxidation steps, i.e. above 1.45 V, could be hidden by the oxygen evolution current. As shown in section 5.3.8, there is no further anodic formation of higher valency oxides of nickel and cobalt on  $\text{NiCo}_2\text{O}_4$  in the oxygen evolution range up to 1.55–1.60 V. Therefore we can assume that the corresponding cathodic reduction profile consists of only two reduction steps. The correlated anodic and cathodic processes according to this model can be presented as follows:



where  $M_a$  and  $M_b$  represent the cations in the  $\text{NiCo}_2\text{O}_4$  spinel oxide. As mentioned before, the study of the E-i characteristics, as a function of the potential scan rate for freshly prepared  $\text{NiCo}_2\text{O}_4$  electrodes showed that the second oxidation-reduction process was less reversible than the first oxidation-reduction reaction. The cathodic profile is less sharp and cannot be separated in different peaks by varying the potential sweep rate  $v$ . As a consequence of this, the anodic oxidation peaks will be more separated with increasing potential sweep rate  $v$ , as given in figure 5.26. This figure shows the potentiodynamic respons of  $\text{NiCo}_2\text{O}_4$ , at two different potential sweep rates, i.e. 2.5 and 25  $\text{mV s}^{-1}$ . It can be seen that the anodic peaks remain separated and no variation in peak charge (indicated by the peak current) is noted. However, no distinct separation of the cathodic profile could be obtained.

In some additional experiments, the potential scan is interrupted in the reduction sweep at certain potentials and kept constant, in order to complete the reduction process of the second anodic peak  $E_{a2}$ . The interruption potentials were chosen such that the two anodic respectively cathodic peaks, were split up.

Figure 5.27 shows the potentiodynamic respons of a  $\text{NiCo}_2\text{O}_4$  electrode, recorded at 25  $\text{mV s}^{-1}$ , which is interrupted at 1.25 and 1.30 V for 10 minutes, after which the potential scan was continued.

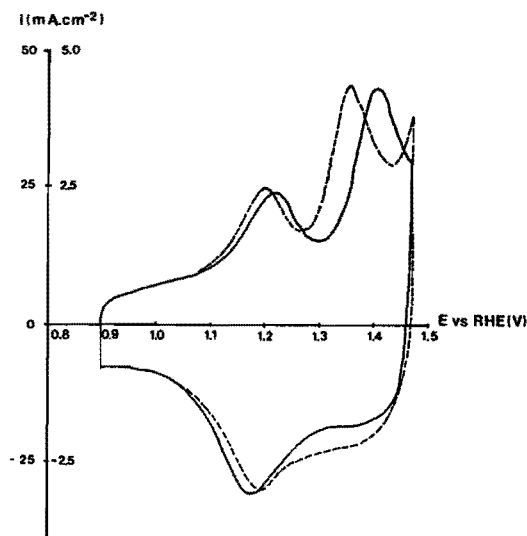


Figure 5.26: Cyclic voltammetric behaviour of a fresh  $\text{NiCo}_2\text{O}_4$  electrode at two different potential sweep rates in 5 M KOH, 25°C.  $T_F = 400^\circ\text{C}$  and  $t_F = 1$  h; catalyst loading:  $15.30 \text{ mg cm}^{-2}$ ;  $v = 2.5 \text{ mV s}^{-1}$  (dashed curve);  $v = 25 \text{ mV s}^{-1}$  (solid curve).

It follows from this voltammogram that during the arrest at 1.30 V the second reduction is not complete. There is still a contribution in cathodic charge on top of the first reduction peak, as can be seen by comparing the scan, started at 1.3 V, i.e. curve I, with the reduction part of the linear potential sweep in the potential range 0.9 to 1.3 V (curve III), i.e. the  $E_{a1}/E_{c1}$  couple.

Interrupting the potential sweep at 1.25 V for 10 minutes, i.e. curve II, leads to a complete reduction of the second anodic process. The ratio anodic versus the cathodic charge of curve II approaches unity, because after holding at 1.25 V, the first anodic oxidation is still complete, so that the reduction charge of the continued sweep belongs exclusively to the reduction of the first anodic oxidation.

This is also shown, more pronounced in figure 5.28, recorded at  $v = 2.5 \text{ mV s}^{-1}$ , where the reduction sweep was interrupted at 1.275 V for 10 (curve I), and at 1.25 for 10 (curve II) and 30 minutes (curve III). The interruption at 1.275 V does not complete the reduction of the second anodic process.

Fixing the potential at 1.25 V the second reduction process, related to the second oxidation process, can be regarded as finished, for with increasing the time of arrest at 1.25 V, no further change in the potentiodynamic response was observed.

It can thus be concluded that the reduction of the second anodic peak is not complete above 1.25 V. However, these experiments do not exclude the possibility that the second reduction process exists of two steps.

In order to establish the relationships between the different oxidation and reduction peaks, the cyclic voltammograms were run to different potentials at the same scan rate, i.e.  $v$  is  $25 \text{ mV s}^{-1}$ .

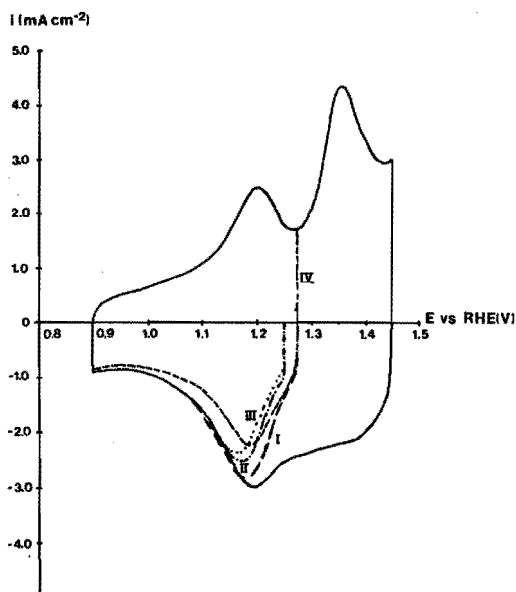


Figure 5.27: Cyclic voltammogram of fresh  $\text{NiCo}_2\text{O}_4$ , which is interrupted in the reduction sweep at 1.25 V and at 1.30 V for 10 minutes, after which the linear potential scan was continued.

Experimental conditions: 5 M KOH,  $25^\circ\text{C}$ ;  $v = 25 \text{ mV s}^{-1}$ ;  $T_F = 400^\circ\text{C}$  and  $t_F = 1 \text{ h}$ ; catalyst loading =  $15.30 \text{ mg cm}^{-2}$ .  
 Curve I = continued sweep after arrest at 1.30 V for 10 minutes; curve II = after arrest at 1.25 V for 10 minutes; curve III = voltammogram in the E-range 0.9 to 1.3 V.



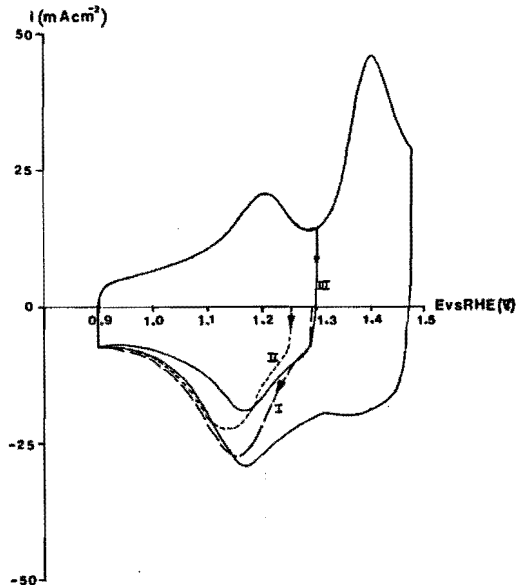


Figure 5.28: Cyclic voltammogram of a  $\text{NiCo}_2\text{O}_4$  electrode, which is interrupted in the reduction sweep at 1.275 V for 10 minutes and at 1.25 V for 10 and 30 minutes.

Experimental conditions:  $v = 2.5 \text{ mV s}^{-1}$ ; others see fig. 5.28.

Curve I = continued sweep after arrest at 1.275 V for 10 minutes; curve II = idem at 1.25 V for 10 minutes; curve III = idem for 30 minutes; curve IV = voltammogram recorded in the E-range 0.9 to 1.275 V.

Figure 5.29 shows that the first anodic peak  $E_{a1}$ , at 1.21 V, corresponds with the first cathodic peak  $E_{c1}$ , at 1.175 V. The ratio of anodic charge  $Q_{a1}$  versus the cathodic charge  $Q_{c1}$  is equal to unity. There is no further increase in the cathodic peak height of  $E_{c1}$ , when the anodic switching potential is 1.25 or 1.30 V.

As seen in figure 5.29, it appears that the second anodic peak  $E_{a2}$  is reduced in two steps, at two different cathodic potentials. With increasing anodic switching potential ( $1.30 < E_s < 1.40$ ) it is noticed that the first part of the second anodic peak  $E_{a2}$ , at about 1.39

V, is reduced on top of the first cathodic peak  $E_{c1}$ , at about 1.175 V, and the remaining part of  $E_{a2}$  ( $E_{a,s} \geq 1.40$  V) is reduced at higher potentials, i.e. the shoulder  $E_{c2}$  at about 1.375 V. The ratio of the total anodic charge  $Q_{a,t}$  versus total cathodic charge  $Q_{c,t}$  approaches unity.

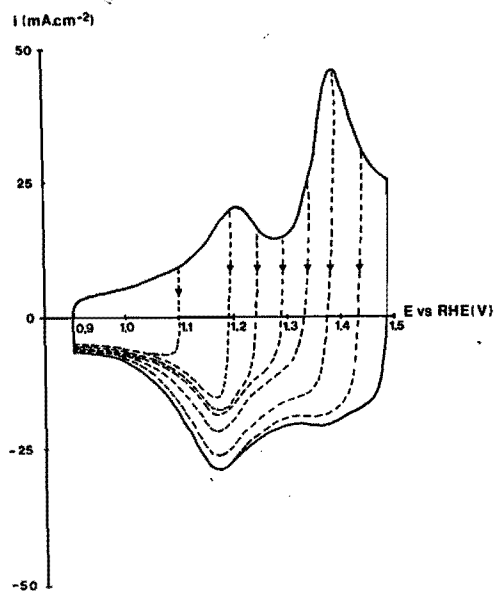


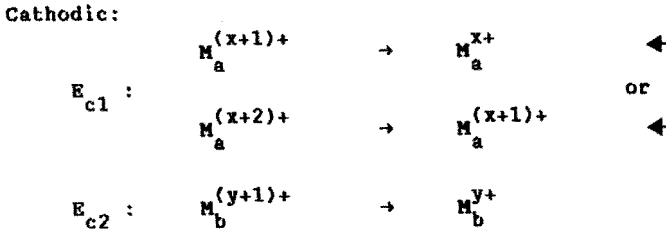
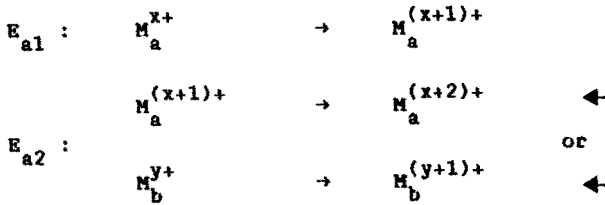
Figure 5.29: Cyclic voltammetric behaviour of a fresh  $\text{NiCo}_2\text{O}_4$  electrode, run to different anodic switching potentials. Experimental conditions: 5 M KOH, 25°C;  $v = 25 \text{ mV s}^{-1}$ ;  $T_F = 400^\circ\text{C}$  and  $t_F = 1 \text{ h}$ ; catalyst loading =  $12.30 \text{ mg cm}^{-2}$ .

This is investigated further with the perturbation program, as shown in Figure 5.30, which confirms the correlation of the different anodic and cathodic processes, as mentioned before.

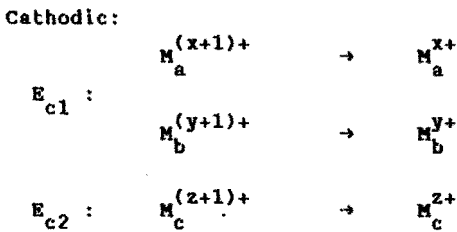
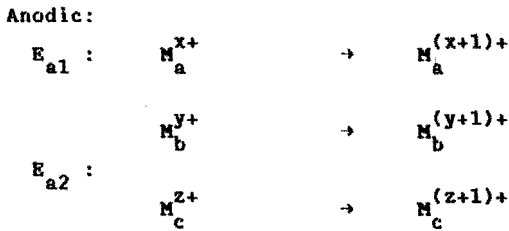
On the basis of these data, we can suggest three different models for the conjugated electrochemical processes, before oxygen evolution takes place on the freshly prepared  $\text{NiCo}_2\text{O}_4$  electrode.

1. The second anodic peak is made up of two different metal cations which oxidize at nearly the same potential, one of them are metal ions involved in the further oxidation of  $E_{a1}$

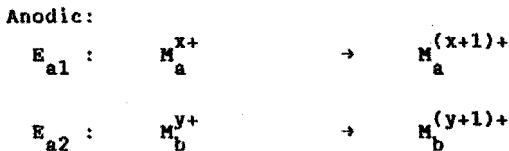
Anodic:



2. The same as in the first model, but without further oxidation of metal ions involved in  $E_{a1}$ .



3. One metal cation which is reduced at different potentials e.g. because of a difference in coordination in the crystal structure, i.e. tetrahedrally or octahedrally.



Cathodic:

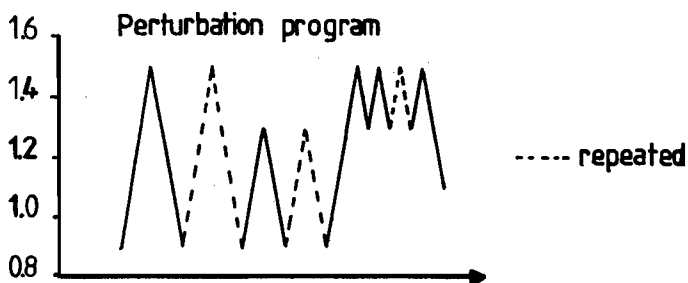
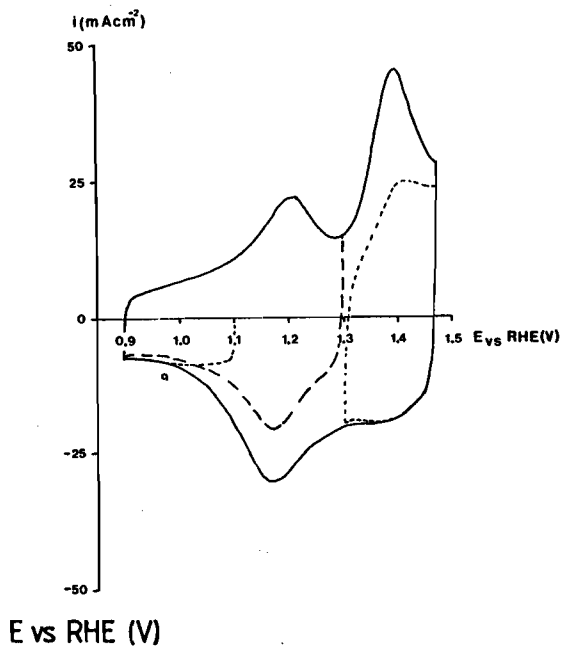
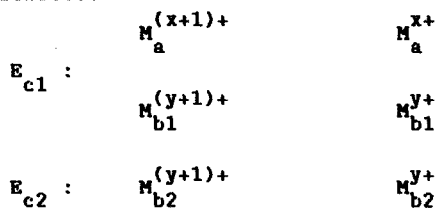


Figure 5.30: Cyclic voltammetric responses of a fresh  $\text{NiCo}_2\text{O}_4$  electrode subjected to the perturbation program.

Experimental conditions: 5 M KOH, 25°C;  $v = 25 \text{ mV s}^{-1}$ ;

$T_F = 400^\circ\text{C}$  and  $t_F = 1 \text{ h}$ ; catalyst loading =  $15.15 \text{ mg cm}^{-2}$ .

5.3.10. Cyclic voltammetric behaviour of  $\text{Co}_3\text{O}_4$ 

Figure 5.31 shows the cyclic voltammogram of a  $\text{Co}_3\text{O}_4$  electrode, run to different anodic switching potentials  $E_{a,s}$ , at the same scan rate  $v = 25 \text{ mV s}^{-1}$  in the E-range 0.9 to 1.5 V. The potentiodynamic behaviour of  $\text{Co}_3\text{O}_4$  spinel is very similar to that of  $\text{NiCo}_2\text{O}_4$ . Only the reduction of the second anodic peak  $E_{a2}$  is more clearly separated into two processes. The first anodic peak  $E_{a1}$ , at 1.17 V, is reduced at the first cathodic peak  $E_{c1}$ , at 1.15 V. The first part of the second anodic peak  $E_{a2}$ , at 1.46 V, is reduced at the second cathodic peak  $E_{c2}$ , at 1.25 V. And the following part is reduced at  $E_{c3}$ , at 1.375 V. Sometimes a shoulder has been observed on the left part of  $E_{a2}$ .

Thus, the potentiodynamic behaviour of  $\text{Co}_3\text{O}_4$  can be described by the same models as presented earlier for  $\text{NiCo}_2\text{O}_4$ .

Table 5.7 shows the observed anodic and cathodic potentials on the  $\text{Co}_3\text{O}_4$  electrodes in 5 M KOH, 25°C for two different potential sweep rates, i.e. 25 and 2.5  $\text{mV s}^{-1}$ . There are no further shifts in potential values with decreasing  $v$ .

Figure 5.31 shows also that in the E-range 0.7–1.5 V, an extra weak anodic peak, at 0.875 V, and the corresponding cathodic peak, at 0.875 V, appears. These faradaic current peaks probable correspond to the  $2+/2.67+$  transition (i.e.  $\text{Co}(\text{OH})_2/\text{Co}_3\text{O}_4$  or  $\text{CoO}/\text{Co}_3\text{O}_4$ ) [33,34].

Table 5.7: Observed potentials on  $\text{Co}_3\text{O}_4$  electrodes in 5 M KOH, 25°C.

$v$ ( $\text{mV s}^{-1}$ )	$E_{a1}$ (V)	$E_{a2}$ (V)	$E_{c1}$ (V)	$E_{c2}$ (V)	$E_{c3}$ (V)
25	1.160	1.450	1.140	1.250	1.370
2.5	1.150	1.410	1.140	1.255	1.400

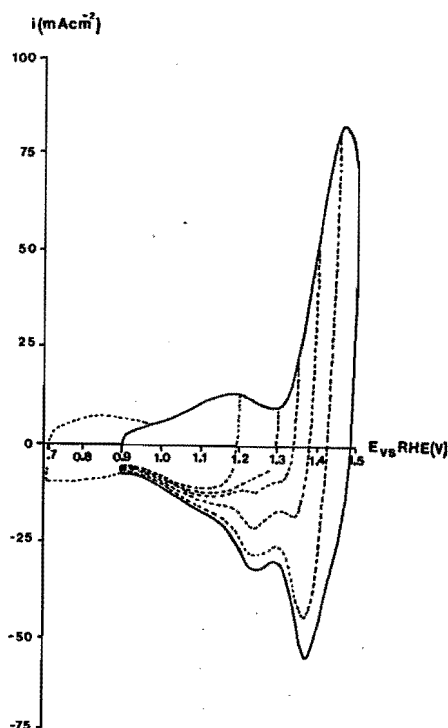


Figure 5.31: Cyclic voltammogram of a fresh  $\text{Co}_3\text{O}_4$  electrode, run to different anodic switching potentials.

Experimental conditions: 5 M KOH,  $25^\circ\text{C}$ ;  $v = 25 \text{ mV s}^{-1}$ ;  
 $T_{\text{F}} = 400^\circ\text{C}$  and  $t_{\text{F}} = 1 \text{ h}$ ; catalyst loading =  $20.15 \text{ mg cm}^{-2}$ .

### 5.3.11. Correlation of the observed peak potentials with standard potentials

The cyclic voltammogram of  $\text{NiCo}_2\text{O}_4$  represents a surface layer of an electrochemically formed oxide(s), leading locally to higher valence states of the  $\text{NiCo}_2\text{O}_4$  catalyst.

On the basis of the observed potentials at which the oxidation and reduction takes place, we have tried to identify the ions involved by comparing them with the standard potentials. Any assignment of the current peaks to a specific surface reaction is difficult because there are no definite thermodynamic data for the  $\text{NiCo}_2\text{O}_4$  spinel helping to identify the redox couples involved. However, we can

attempt to correlate the redox behaviour of  $\text{NiCo}_2\text{O}_4$  with the thermodynamic data of the individual oxides, as shown in [33,34]. From the general cation distribution of the spinel structure ( $\text{NiCo}_2\text{O}_4$  belongs to 2-3 spinels; see introduction) and the observed peaks, it seems reasonable to assume that the possible transitions to higher valence states before oxygen evolution are limited to  $\text{Co}^{2+} \rightarrow \text{Co}^{3+}$ ;  $\text{Ni}^{2+} \rightarrow \text{Ni}^{3+}$ ;  $\text{Ni}^{3+} \rightarrow \text{Ni}^{4+}$  and  $\text{Co}^{3+} \rightarrow \text{Co}^{4+}$ .

From [33] it follows that transition between 2+/3+ oxidation states of cobalt occur at lower potentials than the corresponding transitions of nickel. An assignment of the first transition as  $\text{Co}^{2+/3+}$  or  $\text{Ni}^{2+/3+}$  cannot be made from the observed peak potentials alone.

Cobalt forms an oxide with the spinel structure i.e.  $\text{Co}_3\text{O}_4$ .

However there does exist a nickel spinel 'Ni<sub>3</sub>O<sub>4</sub>' like  $\text{Co}_3\text{O}_4$ .

$\text{Co}_2\text{O}_4$  is a normal spinel with a well-known cation distribution  $\text{Co}^{2+}[\text{Co}_2^{3+}]_2\text{O}_4$ . From the published standard potentials of the cobalt

oxidation state transitions [33,34], it is obvious that the first anodic peak  $E_{a1}$ , reduced at  $E_{c1}$ , is a  $\text{Co}^{2+/3+}$  transition (i.e.

$\text{Co}_3\text{O}_4/\text{CoOOH}$  or  $\text{Co}_3\text{O}_4/\text{Co}_2\text{O}_3$ ) and the second current peak

$E_{a2}$ , reduced at  $E_{c2}$  and  $E_{c3}$ , a  $\text{Co}^{3+/4+}$  transition (i.e.

$\text{CoOOH}/\text{CoO}_2$  or  $\text{Co}_2\text{O}_3/\text{CoO}_2$ ) or  $\text{Co}^{2,67+/4+}$  ( $\text{Co}_3\text{O}_4/\text{CoO}_2$ ).

From the similarity of the voltammetric behaviour of the  $\text{NiCo}_2\text{O}_4$

and  $\text{Co}_3\text{O}_4$  electrodes, the assignment of the first transition to

$\text{Co}^{2+/3+}$  may therefore be justified.  $\text{NiCo}_2\text{O}_4$  is a 2-3 spinel. If

the first anodic peak is a  $\text{M}^{2+} \rightarrow \text{M}^{3+}$  transition, the second

anodic peak  $E_{a2}$  should be a  $\text{M}^{3+} \rightarrow \text{M}^{4+}$  transition. The reported

higher couples of  $\text{Ni}^{3+/4+}$  and  $\text{Co}^{3+/4+}$  are resp. 1.43 V [34] and

1.45 to 1.47 V [14,34], which are close to the experimental value

for the highest oxidation state transition. From the difference in the published equilibrium potentials of  $\text{Co}^{3+/4+}$  and  $\text{Ni}^{3+/4+}$

transitions, there is no sufficient evidence why one of them should be favored for the second anodic peak.

#### 5.4. Ageing phenomena: Influence of the limit potentials on the cyclic voltammetric behaviour.

##### 5.4.1. Introduction

Electrochemical polarization conditions have a significant influence on the stability of oxide systems. Only a few investigations have been carried out on the voltammetric behaviour of nickel cobalt systems [1,6,7,35-37].

Bagotzky [35] found that the reduction of the spinel oxides formed on nickel cobalt alloys started at 0.6 V. Likewise, Singh et al. [7] reported that porous  $\text{NiCo}_2\text{O}_4$  electrodes appear to be unstable in the region of potential where oxygen reduction occurs at appreciable rates.  $\text{NiCo}_2\text{O}_4$  has been shown to undergo complete decomposition at potentials below 0.1 V [36,37]. However, the influence of the lower limit potential and the anodic polarization on the cyclic voltammetric behaviour was not reported.

The dependence of the stability of the  $\text{Co}_3\text{O}_4$  spinel structure on the potential has been studied in detail in [1, 38-41]. It has been shown that the  $\text{Co}_3\text{O}_4$  spinel structure on the catalyst surface undergoes decomposition in the potential range of 0.9 to 0.0 V with the formation of various simple compounds [38-41]. In the potential range from 0.8 to 0.7 V the hydroxide  $\text{Co}(\text{OH})_2$  appears on the electrode, which loosens on further cathodic polarization. In the E-range 0.2 to 0.0 V large amounts of simple oxides are found on the electrode surface,  $\text{Co}^{2+}$  ions going into the solution.

In section 5.3.1, it was reported that the voltammetric behaviour of a freshly prepared  $\text{NiCo}_2\text{O}_4$  electrode was found to differ remarkably from that of an aged one. The ageing process introduces an irreversible transformation in the potentiodynamic respons.

It will be shown in this section that the voltammetric behaviour of a fresh  $\text{NiCo}_2\text{O}_4$  electrode is not only influenced by the lower and upper switching potentials of the scan range, but that the voltammetric respons is also influenced, in a different way, by potentiostatic or potentiodynamic treatment.



## 5.4.2. Results

Influence of the lower limit potential

The time of residence of the freshly prepared electrode at the rest potential, i.e. 1.1 V, in alkaline solution was varied between 5 minutes and 65 hours and did not influence the voltammetric responses. Also, keeping the  $\text{NiCo}_2\text{O}_4$  electrode in air for 6 to 12 months before the measurements were started, did not affect the results.

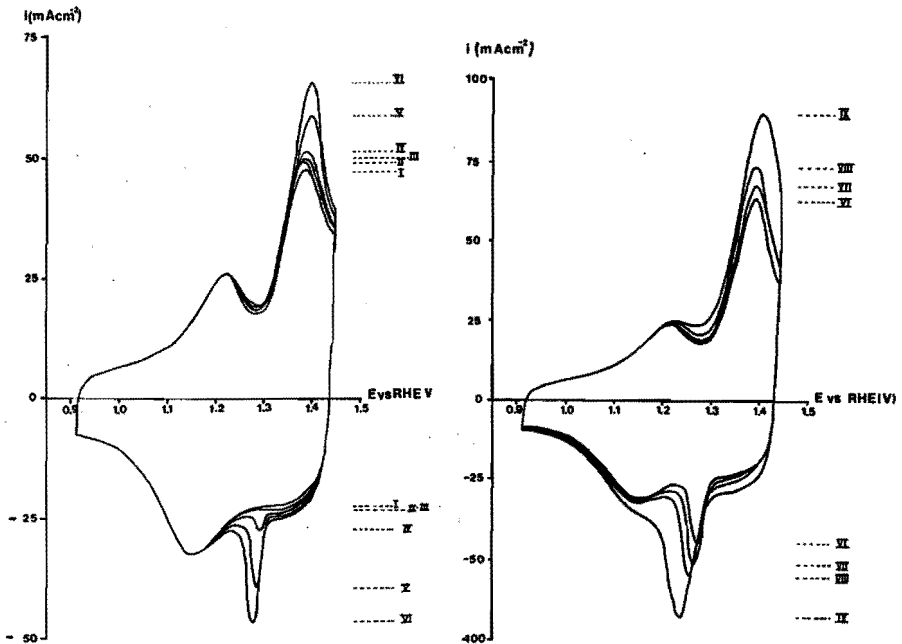


Figure 5.32: Cyclic voltammetric behaviour of a freshly prepared  $\text{NiCo}_2\text{O}_4$  electrode, previously cathodically polarized in the E-range 0.9 to 0.7 V.

Experimental conditions: oxygen-free 5 M KOH, 25°C;  $v = 25 \text{ mV s}^{-1}$ ;  $T_F = 400^\circ\text{C}$  and  $t_F = 1 \text{ h}$ ; catalyst loading =  $22.60 \text{ mg cm}^{-2}$ .  $E_{\text{pol}} = 1.1 \text{ V} - 15 \text{ min}$  (curve I); 0.9 V 15 min (II) - 1 h (III); 0.8 V - 15 min (IV) - 1 h (V) - 2 h (VI) - 3 h (VII); 0.7 V - 15 min (VIII) - 4 h (IX).

Figure 5.32 presents the potentiodynamic response of a freshly prepared  $\text{NiCo}_2\text{O}_4$  electrode, which was previously subjected to a potential in the range 0.9 to 0.7 V. The voltammogram was recorded, starting from the rest potential, in the E-range 0.9 to 1.45 V at a sweep rate of  $25 \text{ mV s}^{-1}$ . Curve I presents the cyclic voltammogram of the fresh  $\text{NiCo}_2\text{O}_4$  electrode. Previously holding the fresh  $\text{NiCo}_2\text{O}_4$  electrode at a potential of 0.9 V for different periods did not influence the voltammetric response, as shown by curve II, 15 minutes at 0.9 V, and curve III, 60 minutes. Thereafter the electrode was held at a potential of 0.8 V for different periods. The voltammetric behaviour started to change as presented in curves IV and VI: a sharp new cathodic peak, at about 1.3 V, and an increase in the second anodic peak  $E_{a2}$  is observed; both continuously increasing with increasing time of arrest at 0.8 V. The increase in the second anodic peak  $E_{a2}$  is correlated with the new cathodic peak as is indicated by the ratio of the respective charges which approaches unity. Further lowering of the arrest potential to 0.7 V did not give rise to new peaks, as demonstrated by curve VIII. With longer keeping at 0.7 V, the increase in both peaks will finally dominate the voltammetric curve, cf. curve IX. From the voltammetric charge of the new cathodic peak, the net mean potentiostatic reduction current at 0.8 V was calculated, as a function of the polarization time; this is shown in figure 5.33. It indicates that the decomposition process in the E-range 0.9 to 0.7 V is slow and probably limited to the surface of the catalyst. This is also illustrated in the next experiment.

The current due to the reduction of the spinel  $\text{NiCo}_2\text{O}_4$  was measured in 1 M KOH, oxygen free, at room temperature, as shown in figure 5.34. A fresh  $\text{NiCo}_2\text{O}_4$  electrode was cathodically polarized in the potential region of 1.1 V to 0.6 V, with stepwise decrease of the potential ( $-50 \text{ mV}$ ). The current starts to increase below 0.9 V, but this increase fades with time.

Decreasing the lower limit potential accelerates the irreversible breakdown of  $\text{NiCo}_2\text{O}_4$ . Below 0.5 V the cathodic current increases fast. The  $\text{NiCo}_2\text{O}_4$  oxide desintegrates rapidly and fine flakes of oxide can be seen to fall off the electrode. At 0 V the catalyst loading is nearly completely lost.

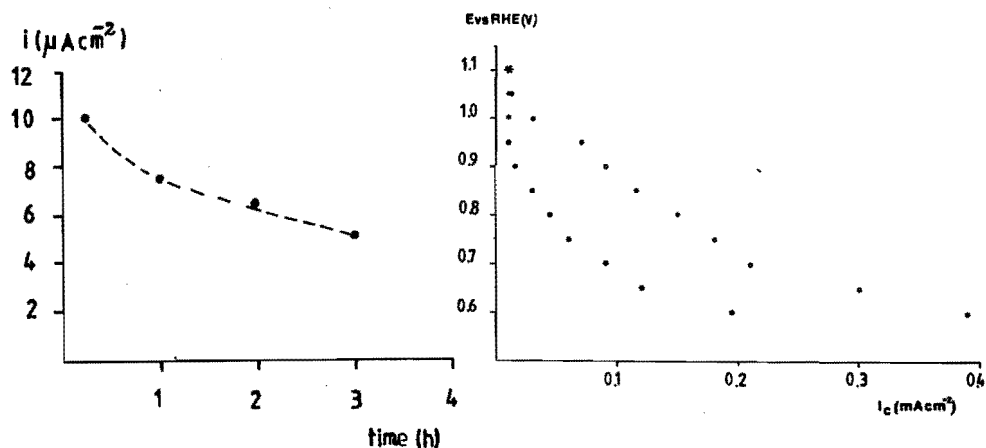


Figure 5.33: Plot of the net mean potentiostatic reduction current as a function of the polarization time at 0.8 V. Experimental conditions: oxygen-free 1 M KOH, 25°C.

Figure 5.34: Potential-current density relation on  $\text{NiCo}_2\text{O}_4$  cathodically polarized in the E-range 1.1 to 0.6 V, with stepwise decreasing cathodic potential of -50 mV. [o]: after 1 minute; [•]: after 5 minutes.

It appears that the 'breakdown' of the  $\text{NiCo}_2\text{O}_4$  spinel already starts below 0.9 V. The decomposition of the  $\text{NiCo}_2\text{O}_4$  spinel in the E-range 0.9 to 0.7 V, as shown in figure 5.32 resembles that of  $\text{Co}_3\text{O}_4$  in which the hydroxide  $\text{Co}(\text{OH})_2$  appears on the electrode in the same potential region [38,41]. On the basis of the observed potentials at which the decomposition takes place and the standard potential of the individual nickel and cobalt oxides, as given in [33,34], it can be suggested that the  $\text{NiCo}_2\text{O}_4$  structure initially decomposes with the formation of  $\text{Ni}(\text{OH})_2$  and that the change in the voltammetric response is due to the appearance of the  $\text{Ni}(\text{OH})_2/\text{NiOOH}$  couple. Prolonged cathodic polarization in the E-range below 0.9 V leads to a breakdown of the spinel structure. Thus, a lower limit potential of 0.9 V was chosen in order to prevent spinel decomposition.

### Influence of the upper limit potential

The  $\text{NiCo}_2\text{O}_4$  electrode was subjected to stepwise increased anodic potentials in order to investigate the dependence of the cyclic voltammetric behaviour on the magnitude of the upper potential limit. Figure 5.35 presents the voltammetric curves of a fresh  $\text{NiCo}_2\text{O}_4$  electrode, which was each time first polarized at different potentials in the oxygen evolution range for 15 minutes. The voltammograms were recorded in the potential region 0.9 to 1.475 V, at a sweep rate of  $25 \text{ mV s}^{-1}$ . Curve I presents the voltammogram of the fresh  $\text{NiCo}_2\text{O}_4$  electrode. It was found that previously holding  $\text{NiCo}_2\text{O}_4$  at anodic potentials below 1.4 V did not influence the voltammetric response of curve I. Further polarizing the  $\text{NiCo}_2\text{O}_4$  electrode at potentials higher than 1.4 V, resulted in a change in the potentiodynamic response, as given in curves II to VI. The figure shows that the first anodic peak  $E_{a1}$  decreases, while the second  $E_{a2}$  increases. The reduction of the increased peak  $E_{a2}$  results in an extra cathodic peak. It thus appears that the change in the voltammetric behaviour starts in the oxygen evolution range. Therefore, the influence of the polarization potential and time in the oxygen evolution range was investigated.

Figure 5.36 shows the progressive change of the voltammetric response of a freshly prepared  $\text{NiCo}_2\text{O}_4$  electrode which was previously held at 1.5 V, i.e. just after the oxide formation is completed, before the cyclic voltammogram was recorded. This process was repeated and resulted in the same changes as observed in figure 5.35. Increasing the polarization time at 1.5 V has no effect on the magnitude of the voltammetric change, as shown by comparing the different curves. It was also noticed that the anodic current at 1.5 V initially decreases rapidly with 50%, in going from curve I to IV, after which it remains nearly constant. Finally, it appears that anodically and cathodically a single peak voltammogram is obtained. The first anodic oxidation peak  $E_{a1}$  has virtually disappeared, while the peak  $E_{a2}$  is practically doubled. The cyclic voltammetric response of a fresh  $\text{NiCo}_2\text{O}_4$  electrode which was previously subjected to galvanostatic ageing at appreciable oxygen evolution is given in figure 5.37. The voltammograms were recorded in the E-range 0.925 to 1.475 V at a scan rate  $v$

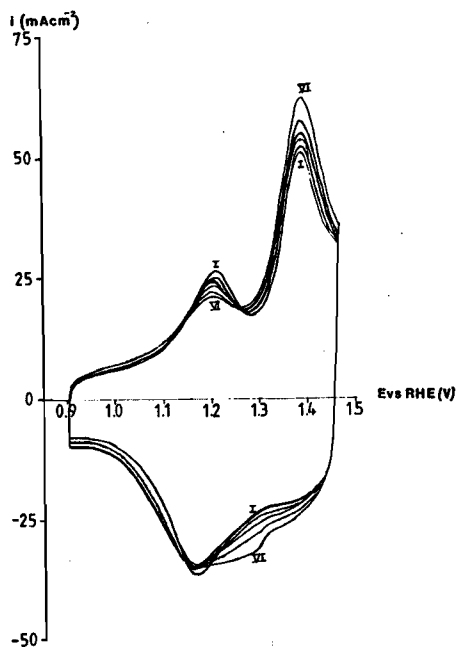


Figure 5.35: The cyclic voltammetric behaviour of a freshly prepared  $\text{NiCo}_2\text{O}_4$  electrode, previously anodically polarized in the E-range 1.40 to 1.55 V.

Experimental conditions: 5 M KOH, 25°C;  $v = 25 \text{ mV s}^{-1}$ ;  $T_{\text{F}} = 400^\circ\text{C}$  and  $t_{\text{F}} = 1 \text{ h}$ ; catalyst loading =  $20.10 \text{ mg cm}^{-2}$ . Polarization time is 15 min at  $E_{\text{pol}} = 1.10 \text{ V}$  (curve I); 1.40 V (II); 1.45 V (III); 1.475 V (IV); 1.50 V (V); 1.55 V (VI).

of  $25 \text{ mV s}^{-1}$  in 5 M KOH, 25°C. Curve I presents the cyclic voltammogram of the fresh  $\text{NiCo}_2\text{O}_4$ . The voltammetric response is changed into curve II, after oxygen evolution at  $250 \text{ mA cm}^{-2}$  for 1 h. Curve III presents the potentiodynamic response after oxygen evolution overnight at  $500 \text{ mA cm}^{-2}$  (14 h). It appears that increasing the polarization potential in the oxygen evolution range only initially accelerates the ageing process, i.e. the change in the voltammetric response. This follows by comparing the increase in the voltammetric charge (expressed by  $i_{\text{p}}$ ) of curve IV in figure 5.36, i.e. after preanodization at 1.5 V for 1 h, and of curve II in figure 5.37, i.e. after 1 h oxygen evolving at about 1.62 V. It is found to be nearly equal. After

prolonged polarization in the oxygen evolution range, the  $\text{NiCo}_2\text{O}_4$  electrode exhibits a more or less constant voltammogram. No correlation was found between the time or potential of the polarization and the change in the voltammetric behaviour.

Also galvanostatic rotating ring-disc experiments were performed, as earlier described in section 5.3.8. An anodic charging current  $I_D$  of 0.250 mA was applied to the freshly deposited  $\text{NiCo}_2\text{O}_4$  layer, until steady-state oxygen evolution is reached for 10 minutes. Curve  $I_1$  and  $II_1$  in figure 5.38 represent, respectively, the change in disc potential and ring current versus time. Thereafter, the  $\text{NiCo}_2\text{O}_4$

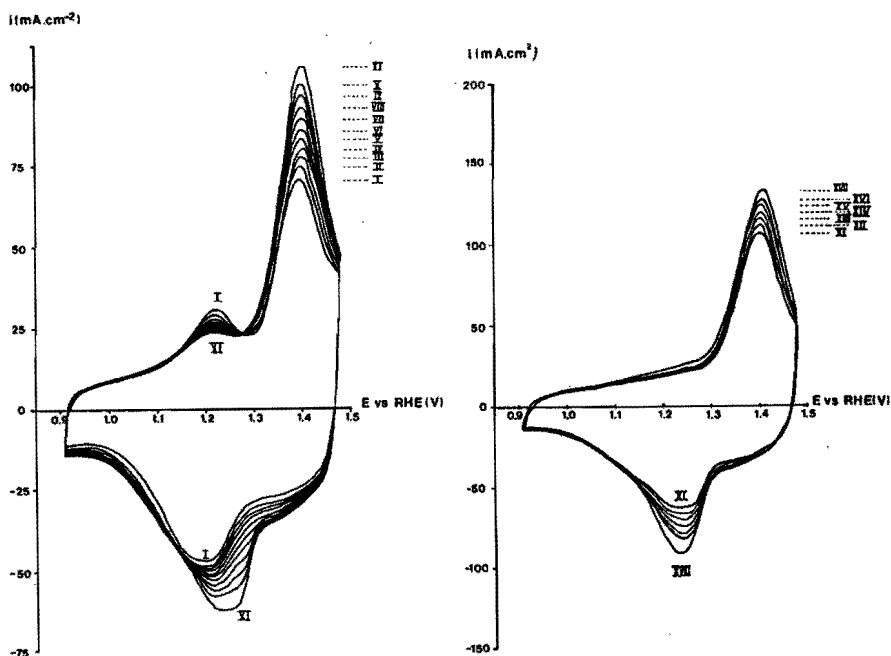


Figure 5.36: The cyclic voltammetric behaviour of a  $\text{NiCo}_2\text{O}_4$  electrode which is repeatedly subjected to anodic polarization at 1.5 V.

Experimental conditions: 5 M KOH, 25°C;  $v = 25 \text{ mV s}^{-1}$ ;

$T_F = 400^\circ\text{C}$  and  $t_F = 1 \text{ h}$ ; catalyst loading =  $26.50 \text{ mg cm}^{-2}$ .

Curve I = voltammogram of fresh  $\text{NiCo}_2\text{O}_4$ . Time at

$E_{\text{pol}} = 1.5 \text{ V}$ : 5 min (curve II); 10 min (III); each time 15 minutes (IV to X); each time 30 minutes (XI to XVI); 15 h (XVII).

electrode was brought back to the rest potential and the charging experiment was started again. Curve  $I_2$  and  $II_2$  present the respectively repeated curves. It shows that repeating the galvanostatic anodic charging process leads to an increase in overpotential. The difference in overpotential as oxygen evolution is reached, is about 30 mV, as seen in figure 5.38 by comparing curve  $I_1$  and  $I_2$ . Next, the disc electrode was subjected to prolonged anodic oxygen evolution at a current density of  $10 \text{ mA cm}^{-2}$  for 16 h. Then the galvanostatic charging experiment was repeated and resulted in curves  $I_3$  and  $II_3$ . No further increase in overpotential was observed. The results clearly show that the upper limit potential influences the voltammetric behaviour of  $\text{NiCo}_2\text{O}_4$ .

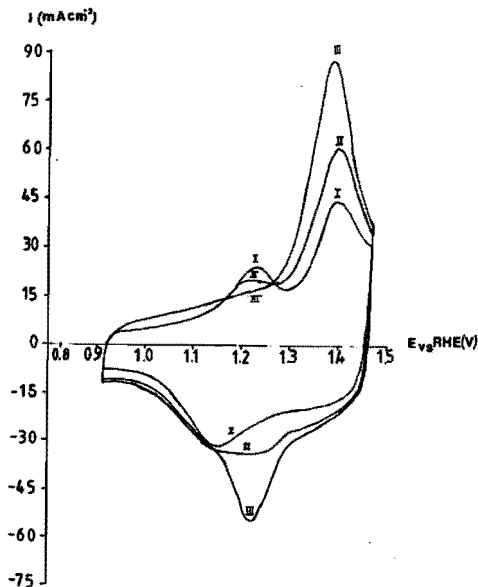


Figure 5.37: Cyclic voltammogram of a fresh  $\text{NiCo}_2\text{O}_4$  electrode subjected to oxygen evolution.

Experimental conditions: 5 M KOH,  $25^\circ\text{C}$ ;  $v = 25 \text{ mV s}^{-1}$ ;

$T_F = 400^\circ\text{C}$  and  $t_F = 1 \text{ h}$ ; catalyst loading =  $20.40 \text{ mg cm}^{-2}$ .

Curve I = fresh  $\text{NiCo}_2\text{O}_4$ ; after 1 h  $250 \text{ mA cm}^{-2}$  (II);

after 2 h  $250 \text{ mA cm}^{-2}$  (III); after 15 h  $500 \text{ mA cm}^{-2}$  (IV).

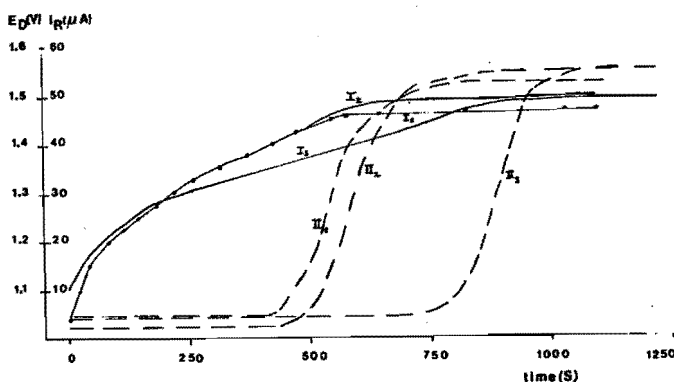


Figure 5.38: Plot of the galvanostatic charging curves on a demountable RRDE.

Experimental conditions:  $O_2$ -free 1 M KOH,  $20^\circ C$ ;  $\omega = 33.3 \text{ s}^{-1}$ . Disc:  $NiCo_2O_4$  covered nickel disc;  $I_D = 0.250 \text{ mA} \rightarrow E_D$  vs. time (curve I). Ring: platinized platinum;  $E_R = 0.2 \text{ V} \rightarrow I_D$  vs. time (curve II); curve  $I_1$  and  $II_1$ : respons of fresh  $NiCo_2O_4$ ;  $I_2$  and  $II_2$ : repeated charging process;  $I_3$  and  $II_3$ : previously subjecting to oxygen evolution at  $10 \text{ mA cm}^{-2}$  for 16 h.

In chapter 3, we have reported the phenomenon of ageing in the oxygen evolution range. An initial decrease in anodic performance of freshly prepared  $NiCo_2O_4$  was observed and it was mentioned that the rate and extent of ageing varied with different parameters, like the electrode preparation and the applied current density. It was found that the anodic behaviour remains nearly constant after 1 hour preanodization. However, it must be noted that the electrocatalytic activity for oxygen evolution was determined at electrodes which were firstly subjected to anodic polarization at the highest current densities to be studied, i.e.  $1000$  to  $1500 \text{ mA cm}^{-2}$ .

A correlation of the anodic performance with the progressive change in voltammetric behaviour is complicated by the fact that determining the change in activity demands subjecting the electrode to higher anodic potentials, where ageing takes place. In fact, only the anodic performance of a freshly prepared and completely aged electrode can be com-



pared. However, the galvanostatic rotating ring-disc experiment showed that already after one charging experiment, an increase in overpotential is observed. When the electrode was subjected to prolonged oxygen evolution, it appears that there is no further increase in the disc potential  $E_D$ , although the  $E_D$  versus time curve is significantly changed. The voltammetric charge before oxygen evolution starts, is nearly doubled. It also shows that no oxygen evolution is detected before the oxide formation is nearly finished and that the start of it is shifted from 1.40 to 1.44 V, as seen from curves  $II_1$  and  $II_3$ . The results also show that in case of the ageing process no further oxidation steps take place above 1.55-1.60 V.

#### Influence of cycling

The cyclic voltammetric behaviour of  $NiCo_2O_4$  is also influenced by continuous potentiodynamic scanning.

A freshly prepared  $NiCo_2O_4$  electrode was continuously cycled in the potential range of 0.7 to 1.5 V for about 1500 cycles at a sweep rate of  $25 \text{ mV s}^{-1}$  in 5 M KOH,  $25^\circ\text{C}$ , as shown in figure 5.39. Both the switching potentials exceed the limit potentials, which were earlier determined. A fast change of the cyclic voltammogram of the  $NiCo_2O_4$  electrode is obtained. At first, the second anodic peak  $E_{a2}$ , at 1.40 V, increases and a shoulder on the cathodic peak  $E_{c1}$ , at 1.175 V, is observed. No decrease in the first anodic peak  $E_{a1}$ , at 1.225 V, takes place. After 50 scans a shoulder at  $E_{a2}$  is clearly observed. With further increasing cycle number a new anodic peak, at 1.35 V, increases fast and dominates  $E_{a2}$ . At the same time, a new cathodic peak grows and shifts to more cathodic potentials. Finally, after 1500 scans, the voltammogram results in one broad anodic peak, at 1.39 V and a cathodic peak, at 1.04 V. The total voltammetric charge increased with a factor 3.0, and the ratio of the anodic versus cathodic charge approaches unity.

The electrode was then subjected to oxygen evolution at a current density of  $500 \text{ mA cm}^{-2}$  for 24 h. Thereafter the voltammogram exhibited the same features and the charge increase was less than 5%.

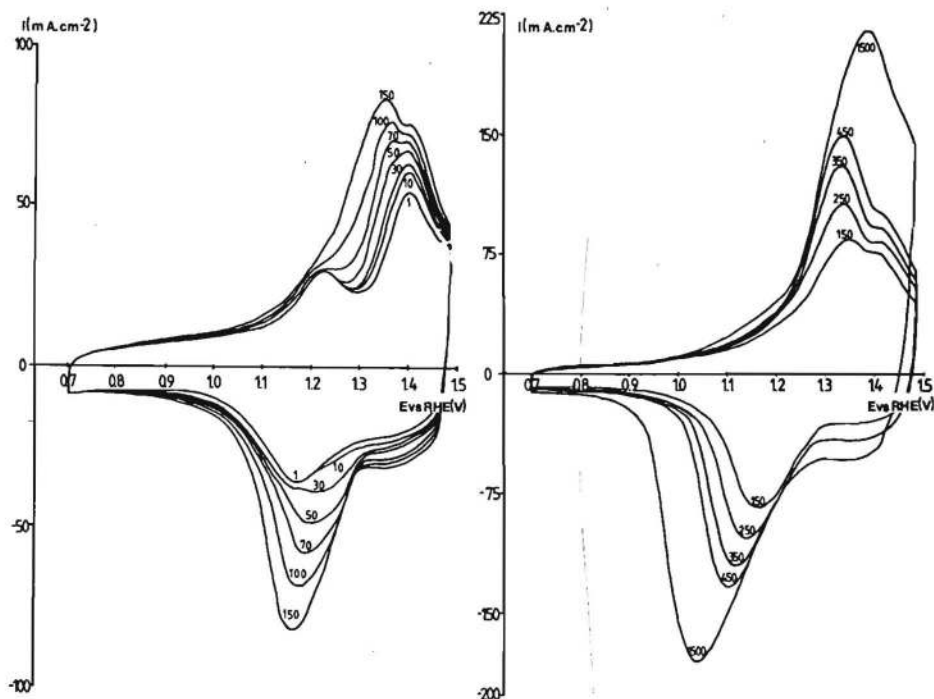


Figure 5.39: Cyclic voltammetric behaviour of a fresh  $\text{NiCo}_2\text{O}_4$  electrode continuously cycled in the E-range 0.7 to 1.5 V. Experimental conditions: 5 M KOH, 25°C;  $v = 25 \text{ mV s}^{-1}$ ;  $T_F = 400^\circ\text{C}$  and  $t_F = 1 \text{ h}$ ; catalyst loading =  $22.50 \text{ mg cm}^{-2}$ . a/ cycles 1 to 150; b/ cycles 150 to 1500.

The voltammogram of the cycled  $\text{NiCo}_2\text{O}_4$  electrode recorded at a sweep rate of  $2.5 \text{ mV s}^{-1}$ , is given in figure 5.40. Lowering the scan rate results in a deconvolution of the broad peaks an anodic peak at 1.275 V, with a shoulder at 1.355 V corresponding to  $E_{a2}^*$ . The  $E_{a1}$  peak cannot be distinguished anymore. Cathodically, the new anodic peak is reduced at 1.115 V. The shoulders at higher potentials correspond to the reduction of  $E_{a2}$ .

This experiment was repeated with switching potentials which did not exceed the (lower) limit potential, i.e. in the potential range 0.9 to 1.45 V, as shown in figure 5.41. In contrast with figure 5.40, the

\* Foot-note: The observed peak potentials for the fresh  $\text{NiCo}_2\text{O}_4$  electrode at a scan rate of  $2.5 \text{ mV s}^{-1}$  were  $E_{a1}$  at 1.20 V;  $E_{a2}$  at 1.35 V and  $E_{c1}$  at 1.19 V.

cyclic voltammetric behaviour of the fresh  $\text{NiCo}_2\text{O}_4$  electrode is much more stable. The voltammetric charge increase was less than 5% in the first 100 scans. The changing profile in the first 500 cycles resembles that of potentiostatic or galvanostatic ageing in the oxygen evolution range. Anodically, only an increase in the second anodic peak  $E_{a2}$  is observed, which is reduced in the shoulder at about 1.25 V. Also, a slight decrease in the first anodic peak  $E_{a1}$  is noticed. Between scan number 500–1725 as presented in figure 5.41b, a similar behaviour is observed, as seen before in figure 5.39. The new anodic peak is distinctly observed as a shoulder of  $E_{a2}$  and its increase is high compared to that of  $E_{a2}$ . However, the change in the voltammetric charge over 1800 cycles is only a factor 0.5 and the observed peaks are  $E_{a1}$  at 1.22 V, the new anodic peak at 1.325 V and  $E_{a2}$  at 1.39 V. Cathodically, a broad peak is observed at 1.17 V with a shoulder at 1.35 V. Thereafter, the electrode was subjected to oxygen evolution potentials, and again one broad peak was obtained, (the dashed curve in figure 5.41a).

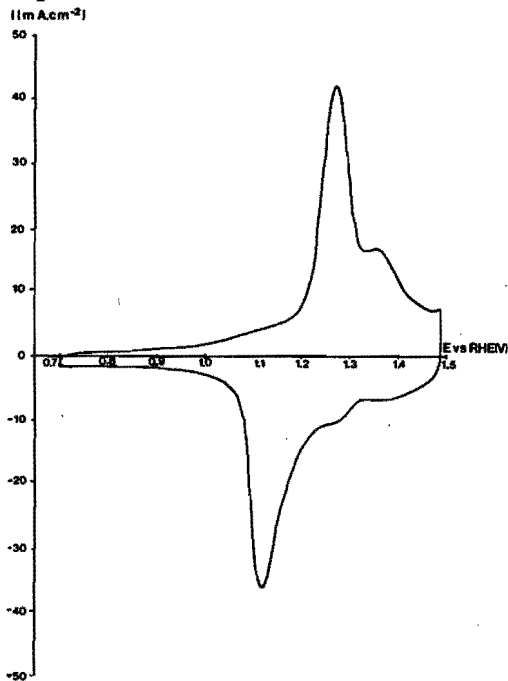


Figure 5.40: Voltammogram of the cycled  $\text{NiCo}_2\text{O}_4$  electrode at a sweep rate  $v$  of  $2.5 \text{ mV s}^{-1}$ .

Experimental conditions: see figure 5.40.

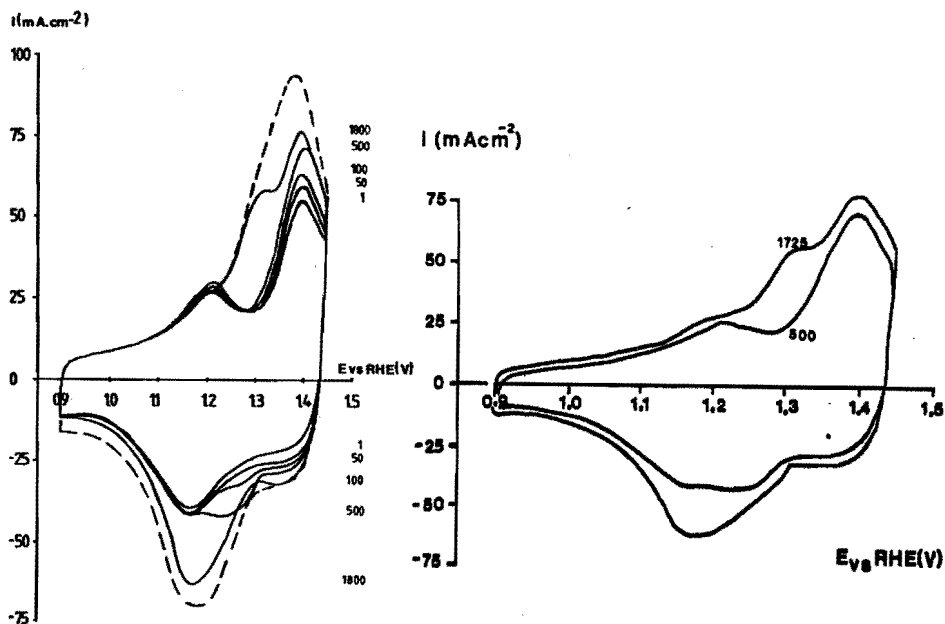


Figure 5.41: Cyclic voltammetric behaviour of a fresh  $\text{NiCo}_2\text{O}_4$  electrode continuously cycled in the E-range 0.9 to 1.45 V.

Experimental conditions: 5 M KOH,  $25^\circ\text{C}$ ;  $v = 25 \text{ mV s}^{-1}$ ;  $T_F = 400^\circ\text{C}$  and  $t_F = 1 \text{ h}$ ; catalyst loading =  $26.85 \text{ mg cm}^{-2}$ .  
 a/ cycles 1 to 1800 (dashed curve = after oxygen evolution); b/ cycles 500 to 1725.

Table 5.8: Comparison of the anodic performance for oxygen evolution of the prolonged cycled electrodes and a fresh  $\text{NiCo}_2\text{O}_4$  electrode in 5 M KOH,  $25^\circ\text{C}$  (iR-corrected).

Electrode treatment <sup>1</sup>	E(V) at $200 \text{ mA cm}^{-2}$	E(V) at $500 \text{ mA cm}^{-2}$
Cycled from 0.9 to 1.45 V	1.60	1.63
Cycled from 0.7 to 1.5 V	1.63	1.66
Fresh <sup>2</sup>	1.60	1.635

1:  $T_F = 400^\circ\text{C}$  and  $t_F = 1 \text{ h}$  2: only preanodized at  $1.5 \text{ A cm}^{-2}$  for 1 h.

Table 5.8 gives the anodic performance for oxygen evolution at two current densities, i.e. 200 and 500 mA cm<sup>-2</sup>, for the prolonged scanned electrodes and for a fresh NiCo<sub>2</sub>O<sub>4</sub> electrode which was only preanodized at 1.5 A cm<sup>-2</sup> for 1 h, as reported in chapter 3. The voltammetric behaviour was differently influenced by potentiodynamic cycling or treatment at constant potential or current density. With cycling, a new anodic peak is observed and E<sub>al</sub> remains nearly constant. With subsequent cycling E<sub>al</sub> will be hidden gradually by the higher anodic peaks, while with potentiostatic or galvanostatic treatment, no similar new anodic peak is observed and E<sub>al</sub> in general decreases. It is evident that the switching potentials, i.e. the lower and upper limit potential, influence this kind of ageing. Comparison of figures 5.39 and 5.41 indicates that it is probably the lower limit potential which is responsible for the difference in the rate of changes in the voltammograms.

Table 5.8 also shows the effect of potentiodynamic cycling on the anodic performance. An increase in overpotential is found for the electrode at which both limit potentials were exceeded, i.e. for the E-range 0.7 to 1.5 V. This increase is not due to a change in surface area, because the voltammetric charge increases with a factor 3, which indicates that the surface area increases. The decrease in activity is probably a result of the spinel decomposition. On the other hand, the anodic performance of the NiCo<sub>2</sub>O<sub>4</sub> electrode scanned in the E-range 0.9 to 1.45 V is still comparable with that of a NiCo<sub>2</sub>O<sub>4</sub> electrode which was only preanodized. Apparently, the ageing here is just only started, compared to that in figure 5.39.

#### 5.4.3. Discussion

##### Correlation of the change in voltammetric behaviour and activity

It was attempted to correlate the change in voltammetric response with the electrocatalytic activity for oxygen evolution. A most striking observation was that the cyclic voltammetric behaviour of a freshly prepared NiCo<sub>2</sub>O<sub>4</sub> electrode differs remarkably from that of an aged one. The voltammogram of a freshly prepared NiCo<sub>2</sub>O<sub>4</sub> electrode exhibits two anodic oxidation peaks, while that of an aged one only

shows one single peak. The influence of both the limit potentials and of the cycling procedure on the cyclic voltammetric behaviour was considered to be an ageing phenomenon. The shifts in the peak potentials and -currents, and the appearance of new anodic and cathodic peaks indicate that it cannot be only an increase in surface area. In case of the lower limit potential, it is evident that finally, the decomposition leads to loss of activity. The decrease in the electrocatalytic activity is correlated with the rate of decomposition of the spinel  $\text{NiCo}_2\text{O}_4$  which depends on the lower limit potential. In case of the upper limit potential, the anodic performance remains nearly constant, after an initial decrease in activity, as earlier reported in chapter 3.

Continuously cycling leads also to a decrease in anodic performance. Although in all cases, the voltammetric charge increases significantly, which indicates an increase in surface area, no increase in anodic performance was observed.

If the voltammetric charge is a measure for the number of active sites for oxygen evolution, as concluded for fresh  $\text{NiCo}_2\text{O}_4$ , we should expect an increase in anodic performance with ageing. However, the anodic performance remains nearly constant after ageing in the oxygen evolution range. This implies that the number of active sites on the surface where oxygen evolution takes place is constant. Therefore, it must be concluded that the voltammetric charge of the aged electrodes is no longer a measure for the number of active sites for oxygen evolution. The increase in the voltammetric charge indicates that an increasing part of the  $\text{NiCo}_2\text{O}_4$  layer becomes involved in the oxidation-reduction process. However, the oxygen evolution takes only place on the top surface of the  $\text{NiCo}_2\text{O}_4$  electrode, as earlier reported in chapter 3, where the number of active sites is apparently constant.

#### Interpretation of the ageing phenomenon

The ageing phenomenon in this section was mainly a phenomenological description of the change in voltammetric behaviour of the freshly prepared  $\text{NiCo}_2\text{O}_4$  electrode. The ageing in the oxygen evolution potential range is of special importance in view of the practical

application in water electrolysis and will be discussed here. The contradiction of the observed increase in the voltammetric charge, which should indicate an increase in the surface area, and the observation that the anodic performance remains nearly constant, which in turn indicates that the number of active sites is constant, could be interpreted in terms of partial decomposition of the  $\text{NiCo}_2\text{O}_4$  surface layer. It seems that a part of the surface sites is unstable, probably as a result of the defective nature of  $\text{NiCo}_2\text{O}_4$ . A chemical decomposition step is not seen in the cyclic voltammogram. However,  $\text{NiCo}_2\text{O}_4$  was always under potential control in the alkaline solution. No change in voltammetric behaviour was observed at the rest potential. Thus, polarization is essential to start the ageing phenomenon. These unstable sites will also be oxidized and reduced and lead to the change in the voltammetric behaviour. The initial decrease in anodic performance must be attributed to the loss of a part of the active spinel sites, whereafter the number of active sites on the surface is constant. It appeared that the ageing process initially goes rather fast, so the defect sites at the surface are preferentially involved. It was also reported [38,39] that preliminary anodic oxidation markedly increases the stability of  $\text{Co}_3\text{O}_4$ . A similar effect can also explain the decrease in the rate of ageing with time for  $\text{NiCo}_2\text{O}_4$ .

It must be suggested that at least part of the unstable sites dissolves, resulting in a roughening of the  $\text{NiCo}_2\text{O}_4$  layer. So, the increasing voltammetric response can be explained by a penetration effect in the  $\text{NiCo}_2\text{O}_4$  layer as a result of the 'partial decomposition' and 'dissolving' process. Consequently, the total area increases i.e. the number of active and inactive sites. However, this is not expressed in an increase in anodic performance, because the oxygen evolution is limited to the surface. A dissolving or leaching process is essential for the roughening or penetration process, but it is also limited in depth. This follows from the observation that the increase in the voltammetric charge with ageing in the oxygen evolution range was maximum a factor 3 to 4.

A complete decomposition, which should result in the formation of individual oxides of nickel and cobalt must be excluded, because then a sharp decrease in anodic performance and an increase in the iR-drop

should be observed.

It was also found that the rate of ageing increases with lowering the temperature  $T_F$  of the heat treatment, while the magnitude of ageing was nearly equal.

### 5.5. Literature

- [1] M.R. Tarasevich and B.N. Efremov in S. Trasatti (Ed.), *Electrodes of Conductive metallic oxides, Part A*, Elsevier Scientific publishing company, Amsterdam, 221 (1980).
- [2] H. Takahashi, W. Aldred, P. Bindra and E. Yeager, Ext. Abstr. 31 ISE Meeting, Venice, 783 (1980).
- [3] D.B. Hibbert, J. Chem. Soc. Chem. Comm. 202 (1980).
- [4] S.M. Jasem and A.C.C. Tseung, J. Electrochem. Soc. 126, 1353 (1979).
- [5] V.S. Bagotzky, N.A. Shumilova and E.I. Krushcheva, *Electrochim. Acta* 21, 919 (1976).
- [6] W.J. King and A.C.C. Tseung, *Electrochim. Acta* 19, 485 (1974).
- [7] G. Singh, M.H. Miles and S. Srinivasan in A.D. Franklin (Ed.), *Electrocatalysis on Non-metallic surfaces*, N.B.S. Spec. Publ. 455, U.S. Government Printing Office, Washington, 289 (1976).
- [8] A.C.C. Tseung, S. Jasem and M.N. Mahmood in T.N. Veziroglu and W. Seifritz (Eds.), *Hydrogen Energy systems*, Pergamon Press, Vol. I, 215 (1978).
- [9] A.M. Trunov, V.A. Presnov, M.V. Uminskii, O.F. Rakityanskaya, T.S. Bakutina and A.I. Kotseruba. *Sov. Elektrochem.* 11, 509 (1975).
- [10] W.J. King and A.C.C. Tseung, *Electrochim. Acta* 19, 493 (1974).
- [11] C.M. Mari, G. Gilardoni, A. Carugati and S. Trasatti, *Extended Abstracts 32 ISE Meeting*, 96 (1981).
- [12] A. Carugati and S. Trasatti, *Extended Abstracts 33 ISE Meeting*, 118 (1982).
- [13] A. Carugati, G. Lodi and S. Trasatti, *J. Electroanal. Chem.* 143, 419 (1983).



- [14] P. Rasiyah, A.C.C. Tseung and D.B. Hibbert, *J. Electrochem. Soc.* 129, 1724 (1982).
- [15] E. Laviron in A.J. Bard (Ed.), *Electroanalytical Chemistry*, M. Dekker Inc. N.Y. 12, 53 (1982) and references.
- [16] E. Laviron, *J. Electroanal. Chem.* 112, 1 (1980).
- [17] E. Laviron, L. Roullier, C. Degrand, *J. Electroanal. Chem.* 112, 11 (1980).
- [18] E. Laviron, L. Roullier, *J. Electroanal. Chem.* 115, 65 (1980).
- [19] E. Laviron, *J. Electroanal. Chem.* 100, 263 (1979).
- [20] E. Laviron, *J. Electroanal. Chem.* 101, 19 (1979).
- [21] D.D. MacDonald, *Transient Techniques in Electrochemistry*, Plenum, New York (1977).
- [22] A.C.C. Tseung and S. Jasem, *Electrochim. Acta* 22, 31 (1977).
- [23] A.J. Honji, C. Iwakura and H. Tamura, *Chem. Letters* 1153 (1979).
- [24] A.J. Honji, C. Iwakura and H. Tamura, *Electrochim. Acta* 26, 1319 (1981).
- [25] M.C.M. Man, S. Jasem, K.L.K. Yeung and A.C.C. Tseung, Hydrogen as an energy vector, Commission of the European Communities, Brussels, 255 (1978).
- [26] W.B. Pearson, C.B. Shoemaker and V. Duckworth, *Structure Reports, Publ. Int. Union of crystallography.* 33A, 290 (1968).
- [27] D. Bonnenberg and H.P.J. Wijn in Landolt-Bornstein, *Numerical data and functional relationships in science and technology*, K.H. Hellwege (Ed.), III 4b, 481.
- [28] C.K. Mann in A.J. Bard (Ed.), *Electroanalytical Chemistry*, M. Dekker Inc. N.Y. 3, 57 (1969).
- [29] W.L. Albery, M.L. Hitchmann, 'Rotating Ring disc electrodes', Clarendon Press, Oxford (1971).
- [30] A.J. Bard and L.R. Faulkner, 'Electrochemical Methods', J. Wiley & Sons, Inc. (1980).
- [31] V.G. Levich, 'Physicochemical Hydrodynamics', Prentice Hall (1962).
- [32] F.T.B.J. van den Brink, Thesis, Eindhoven University of Technology, The Netherlands, 74 (1981).

- [33] A.J. Bard, Encyclopedia of electrochemistry of the elements, Publ. M. Dekker Vol. 3 (1975).
- [34] W.K. Behl and J.E. Toni, J. Electroanal. Chem. 31, 63 (1971).
- [35] V.S. Bagotzky, Electrochim. Acta 21, 919 (1976).
- [36] N.I. Ryasintseva, E.I. Khrusheva, A.M. Trunov, N.A. Shumilova and V.A. Presnov, Sov. Electrochem. 11, 339 (1975).
- [37] J. Brenet and J.F. Koenig, Z. Phys. Chem. N.F. 98, 351 (1975).
- [38] A.M. Khutornoi, G.I. Zakharkin and M.R. Tarasevich, Zh. Prikl. Khim. 50, 255 (1976).
- [39] B.N. Efremov, G.I. Zakharkin, M.R. Tarasevich and S.R. Zhukov, Russ. J. Phys. Chem. 52, 966 (1978).
- [40] B.N. Efremov, G.I. Zakharkin, M.R. Tarasevich and S.R. Zhukov, Sov. Electrochemistry 74, 1303 (1978).
- [41] V.V. Klepikov, V.V. Sysoeva and R.V. Boldin, Zh. Prikl. Khim. 51, 1904 (1978).

## 6. NON-ELECTROCHEMICAL CHARACTERIZATION

### 6.1. Introduction

The results reported in chapter 3 and 5 have shown that the preparation method, and so the conditions of oxides affect the textural characteristics. Besides the in-situ electrochemical analysis of  $\text{NiCo}_2\text{O}_4$  as reported in chapter 5, a number of ex-situ techniques were used to characterize the nickel cobalt spinel system. This chapter provides supplementary information about the surface features of  $\text{NiCo}_2\text{O}_4$ , in particular with reference to the heat treatment.

Thermogravimetric analysis was applied to study the course of the decomposition of cobalt nitrate as a function of the temperature. BET-measurements and scanning electron microscopy were used for the investigation of the surface morphology. X-ray diffraction, temperature programmed reduction and X-ray- and Auger photoelectron spectroscopy were employed to study the surface and bulk composition of  $\text{NiCo}_2\text{O}_4$ .

### 6.2. Thermogravimetric analysis

Thermogravimetric analysis (TGA) was carried out using a Mettler thermoanalyzer 2. The heating rate was  $3^\circ\text{C min}^{-1}$  in the temperature range of 25 to  $1000^\circ\text{C}$ .

Figure 6.1 shows the thermogravimetric diagram of the decomposition of  $\text{Co}(\text{NO}_3)_2 \cdot 6\text{H}_2\text{O}$  (Merck) and of  $\text{Ni}(\text{NO}_3)_2 \cdot 6\text{H}_2\text{O}$  (Merck) and  $\text{Co}(\text{NO}_3)_2 \cdot 6\text{H}_2\text{O}$  mixed in a stoichiometric ratio of 1:2. The TGA curves are plotted as a fraction of the initial weight  $(G_0 - G)/G_0$  versus the temperature ( $G_0$  is the initial weight and  $G$  is the weight loss of the sample). It appears that in either case decomposition occurs below  $300^\circ\text{C}$ . It is well known that both decomposition processes give rise to the formation of a spinel oxide, i.e. in the former  $\text{Co}_3\text{O}_4$ , and in the latter  $\text{NiCo}_2\text{O}_4$ . The TGA curve of cobalt nitrate can be distinguished into different regions: a major weight loss region below  $280^\circ\text{C}$  which can be divided into two parts, followed by a very small monotonic weight loss up to  $500^\circ\text{C}$ . Then no further weight loss takes place in the temperature range of 500 to  $900^\circ\text{C}$ . Finally, a sharp weight loss is observed at  $900^\circ\text{C}$ .

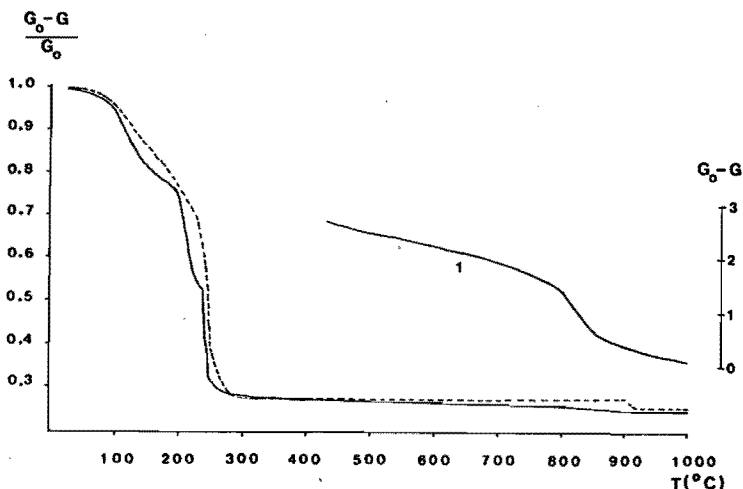


Fig. 6.1. Thermogravimetric curves plotted as the fraction of the initial weight vs. temperature.

[ - - - - ] =  $\text{Co}(\text{NO}_3)_2 \cdot 6\text{H}_2\text{O}$

[ ————— ] =  $\text{Ni}(\text{NO}_3)_2 \cdot 6\text{H}_2\text{O} : \text{Co}(\text{NO}_3)_2 \cdot 6\text{H}_2\text{O} = 1:2$

1 = part of the solid curve on an expanded real weight scale.

The hydration water molecules are removed in the temperature range below  $230^{\circ}\text{C}$  as confirmed by calculations of the weight loss curve. The decomposition of the nitrate, with the evolution of  $\text{NO}_x$ , apparently starts as soon as the dehydration is completed. It takes place over a short temperature interval of about  $50^{\circ}\text{C}$  and results in the spinel oxide  $\text{Co}_3\text{O}_4$ . The weight at  $280^{\circ}\text{C}$  does not correspond exactly to that of  $\text{Co}_3\text{O}_4$ . The presence of hydration water in excess over the nominal composition can disturb the calculations based on the TGA curve.  $\text{Co}(\text{NO}_3)_2 \cdot 6\text{H}_2\text{O}$  is known to be extremely deliquescent [1]. The temperature at which the spinel oxide is formed, changes with the heating rate. Pope et al. [2] observed that the decomposition was already completed at  $200^{\circ}\text{C}$  when lowering the heating rate, while Garavaglia [3] reported that at sufficient long times  $\text{Co}_3\text{O}_4$  is even formed at  $150^{\circ}\text{C}$  (24 h). The small monotonic weight loss observed in the temperature range of  $280$  to  $500^{\circ}\text{C}$  has been related to the progressive loss of excess oxygen in the initially non-stoichiometric oxide [3-6]. Further heating of the sample does not result in any

change in weight up to 900°C. This indicates that the oxide of the spinel type does not undergo further conversion in this temperature range. At about 900°C, a sharp decrease in the curve is noticed: the spinel oxide  $\text{Co}_3\text{O}_4$  decomposes to  $\text{CoO}$ , as indicated by the weight loss.

The TGA curve of the mixed nitrates is initially similar to that obtained for the cobalt nitrate: a sharp weight loss takes place immediately on heating, tapering off above 275°C, which consists of the earlier mentioned processes, i.e. fusion of the salt, dehydration, and decomposition of the mixed nitrates. Thereafter, a steady weight loss starting at 275°C up to 800°C is observed, followed by a more pronounced weight loss above 800°C (as shown by the curve on an expanded weight scale in figure 6.1).

It can be suggested that  $\text{NiCo}_2\text{O}_4$  is already formed after the nitrate decomposition is finished (at about 275°C). Further increasing in the temperature up to about 400°C causes a weight loss, which can be correlated with the loss of excess oxygen of  $\text{NiCo}_2\text{O}_{4+x}$ . The weight loss above 400°C can then be interpreted as the thermal decomposition of the spinel oxide  $\text{NiCo}_2\text{O}_4$ . The sharp decrease above 800°C has been attributed to the loss of all spinel phases [7].

From the weight loss in the range 300 to 400°C the excess oxygen, i.e. the value of  $x$  in  $\text{NiCo}_2\text{O}_{4+x}$ , can be calculated from the thermogram using the equation (6.1),

$$x = \frac{G_T - G_S}{G_S} \frac{240.56}{16} \quad (6.1)$$

where  $G_T$  is the weight of the sample at temperature  $T$ ,  $G_S$  is the weight expected for the formation of the stoichiometric compound and the constants in the nominator are the molecular mass of  $\text{NiCo}_2\text{O}_4$ , respectively, in the denominator the atomic mass of oxygen. The results are shown in table 6.1. It appears that the stoichiometric composition is reached at about 360°C. At 400°C a negative value of  $x$  is found, which indicates the decomposition of the spinel structure. This number has no physical meaning above 400°C, i.e. in the two-phase region.

Table 6.1.: Oxygen content in  $\text{NiCo}_2\text{O}_{4+x}$  obtained from the thermal analysis of the mixed nickel cobalt nitrate.

T (°C)	300	350	400
x	+0.40	+0.03	-0.14

However, the restrictions of the calculation based on a simple weight loss curve must be borne in mind. The values were derived from TGA, which gives non-equilibrium data. It was also found that when the TGA curve is interrupted and hold constant, the weight loss still considerably changes. The calcination time is important here, especially at lower temperatures ( $\leq 300^\circ\text{C}$ ). Further, the presence of excess hydration water can disturb the calculation. The thermogravimetric analysis of the cobalt nitrate, and the mixed cobalt nitrate is in agreement with those obtained by other authors [1-10].

The TGA experiments were carried out in the laboratory of Prof. R. Prins at the Department of Inorganic Chemistry, Eindhoven University of Technology.

### 6.3 BET surface area determination

Surface areas were measured using the Brunauer-Emmet-Teller method (BET). Also the pore size distribution was determined. The  $\text{NiCo}_2\text{O}_4$  powder samples were prepared by thermal decomposition as described in section 3.2.1.

These experiments were carried out by the group of Prof. J. Scholten at the Department of Chemical Technology, Delft University of Technology.

Figure 6.2 illustrates the effect of the temperature  $T_F$  and duration time  $t_F$  of the heat treatment on the BET surface area of the  $\text{NiCo}_2\text{O}_4$  powders. The specific surface areas decrease with increase of  $T_F$ , and with  $t_F$ . At each temperature  $T_F$  the surface area of

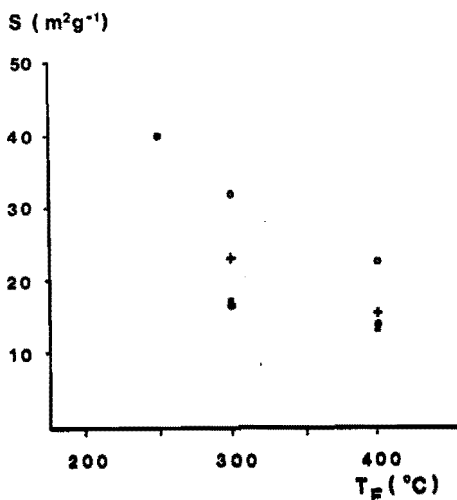


Fig. 6.2. BET-surface area of  $\text{NiCo}_2\text{O}_4$  powders as a function of the temperature  $T_F$ .

[o]:  $t_F = 1$  h; [+]:  $t_F = 5$  h; [\*]:  $t_F = 10$  h; [-]:  $t_F = 24$  h.

$\text{NiCo}_2\text{O}_4$  will reach a constant value as the duration time  $t_F$  is increased. So, at each temperature  $T_F$ , a duration time  $t_F$  exists beyond which no significant changes in surface area will be observed; this value is, of course, reached faster at higher  $T_F$ . The difference in surface area in this limit, i.e.  $t_F = 24$  h, between the heat treatment of 300 and 400°C is 25%. This differs from the results reported in chapter 5, where the cyclic voltammetric charge was proposed to be a measure for the surface area of the  $\text{NiCo}_2\text{O}_4$  electrode. The voltammetric charge strongly depends on  $T_F$ , but only slightly on  $t_F$ . Virtually no further change in surface area after a heat treatment of one hour was observed. It was found that the difference in surface area between the heat treatment at 300 and 400°C was about 100%.

The BET-surface area of the  $\text{NiCo}_2\text{O}_4$  powder materials and the apparent electrochemical surface area of the  $\text{NiCo}_2\text{O}_4$  electrodes are compared in table 6.2. They show the same dependence with respect to the temperature  $T_F$ : a decrease of the surface area with increasing  $T_F$ .

Table 6.2.: BET-surface area of  $\text{NiCo}_2\text{O}_4$  powders and apparent electrochemical surface area of  $\text{NiCo}_2\text{O}_4$  electrodes as function of  $T_F$  and  $t_F$ .

Heat treatment		BET-surface area	Apparent electrochemical
$T_F$	$t_F$	$\text{NiCo}_2\text{O}_4$ -powders	surface area of $\text{NiCo}_2\text{O}_4$
(°C)	(h)	( $\text{m}^2 \text{g}^{-1}$ )	electrodes ( $\text{m}^2 \text{g}^{-1}$ )
250	10	39.9	10.7
300	1	32.0	6.9
300	10	16.0	5.9
350	1	—	4.5
400	1	22.5	3.1
400	10	13.7	3.3

The dependence of the surface area on the duration time  $t_F$  shows that in the case of using a voltammetric technique, an approximately constant surface area is reached faster. Apparently, no further sintering takes place after a heat treatment of one hour, while in the case of powder material at least a thermal treatment of 10 hours at 300°C or 5 hours at 400°C is required. The discrepancies in the magnitude of the surface area as a function of  $T_F$  and  $t_F$  between the powder and electrodes can be explained by a difference in the morphology of the  $\text{NiCo}_2\text{O}_4$  oxide due to the slightly different preparation conditions. Unfortunately, it was not possible to subject the  $\text{NiCo}_2\text{O}_4$  electrodes as such to a BET examination.

A pore size distribution was carried out on  $\text{NiCo}_2\text{O}_4$  powder samples, prepared at a/ temperature  $T_F$  of 300°C and for a duration time of 1 hour, b/ at 400°C for 1 h and c/ at 400°C for 24 h. In describing pore size, the notation of Dubinin [11] is commonly adopted: micropores are pores with a diameter of less than 20 Å, mesopores have diameters in the range of 20 to 300 Å and macropores are those larger



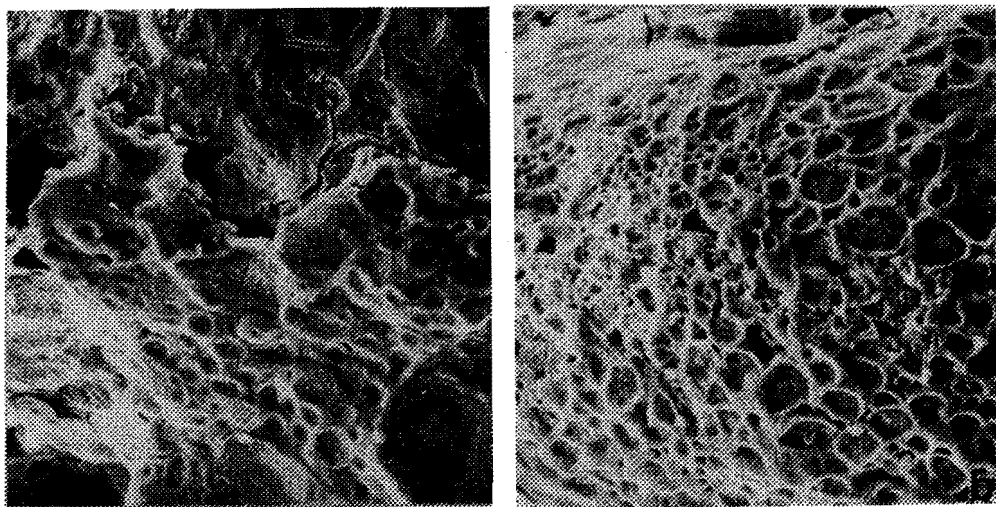


Fig. 6.3. SEM micrographs of the surfaces of  $\text{NiCo}_2\text{O}_4$  electrodes prepared at different  $T_F$ .

a.  $300^\circ\text{C} - 1 \text{ h}$  :

b.  $400^\circ\text{C} - 1 \text{ h}$  :

Magnification factor = 204.

than  $300 \text{ \AA}$ . The samples showed no distinct mean pore diameter; they are spread in the mesopore range. It appeared that there were no micropores. In sample a/ most pore diameters are situated in the range  $20$  to  $50 \text{ \AA}$ , in sample b/  $50$  to  $150 \text{ \AA}$ , and in sample c/ from  $70$  to  $200 \text{ \AA}$ .

The observation of the samples with scanning electron microscopy (SEM) gives additional evidence that the surface morphology is determined by the preparation temperature  $T_F$ . SEM micrographs of  $\text{NiCo}_2\text{O}_4$  electrodes are given in figure 6.3. The  $\text{NiCo}_2\text{O}_4$  electrode prepared at  $400^\circ\text{C}$  exhibits a smooth, circular scaly surface, while the electrode prepared at  $300^\circ\text{C}$  shows a rougher and more porous texture. All coatings exhibit some cracks.

#### 6.4 X-ray diffraction

The X-ray diffraction analysis of the  $\text{NiCo}_2\text{O}_4$  catalyst was carried out using a Philips model PW 1009 röntgen diffraction spectrometer. A  $\text{FeK}\alpha$  radiation with a Mn filter was used. All diffraction patterns

were recorded at room temperature. The Debye-Scherrer powder diffraction photographs were obtained using a camera with a diameter of 57.3 mm. X-ray diffraction patterns of the  $\text{NiCo}_2\text{O}_4$  electrodes were also obtained using the Philips diffractometer.

The phase composition was identified by comparison with the ASTM data [12].

The X-ray diffraction measurements were carried out in the laboratory of Prof. R. Metselaar at the Department of Physical Chemistry, Eindhoven University of Technology.

Table 6.3 shows the phase composition as derived from the Debye-Scherrer powder photographs of freshly prepared  $\text{NiCo}_2\text{O}_4$  as a function of  $T_F$  and  $t_F$ . With lowering  $T_F$  and  $t_F$ , the diffraction lines became broader and less well defined. However, there was little difficulty in identifying the phase present. The X-ray analysis confirmed the expectations, i.e. the detection of the single phase  $\text{NiCo}_2\text{O}_4$  spinel oxide in the  $T_F$ -range of 250 to 400°C. The visually estimated intensities of the Debye-Scherrer diffraction lines were in agreement with the ASTM data of  $\text{NiCo}_2\text{O}_4$  [12]. At higher temperatures lines, corresponding to another cubic phase were observed, presumably NiO.  $\text{NiCo}_2\text{O}_4$  electrodes at which oxygen had been evolved, were analyzed with the spectrometric diffraction method.

Table 6.4 presents the values of the interplanar d-spacings, the Miller indices (hkl), and the relative intensity (referred to the strongest line  $I_1$ , i.e.  $2\theta = 46.6^\circ$ ) of the  $\text{NiCo}_2\text{O}_4$  coatings as a function of  $T_F$  and  $t_F$ , together with the ASTM data of  $\text{NiCo}_2\text{O}_4$  and NiO. The X-ray diffraction patterns in the  $T_F$ -range below 400°C are characteristic for the  $\text{NiCo}_2\text{O}_4$  spinel. The deviation in the measured relative intensity, which seems to increase with decreasing temperature  $T_F$ , can be attributed to preferred orientations. The appearance of NiO at  $T_F$  greater than 400°C is confirmed by the detection of the additional reflections at  $2\theta$  equal to  $49.0^\circ$  ( $d = 2.41$ ),  $55.2^\circ$  ( $d = 2.09$ ) and  $81.8^\circ$  ( $d = 1.48$ ). The values between the brackets in table 6.4 give the relative intensity  $I/I_1$ , referred to the strongest line  $I_1$  of the additional lines, i.e.  $2\theta = 55.2^\circ$ .

Table 6.3.: Phase composition of the powders

Heat treatment			Phases
$T_F$ (°C)	$t_F$ (°C)		
250	1	(a)	$\text{NiCo}_2\text{O}_4$ spinel
250	10	(a)	"
300	1	(a)	"
300	10	(a)	"
300	24	(a,b)	"
350	1	(a)	"
400	1	(a,b)	"
400	10	(a)	"
400	24	(a,b)	"
450	1	(a)	$\text{NiCo}_2\text{O}_4$ + trace cubic phase
450	10	(a)	$\text{NiCo}_2\text{O}_4$ + " " "
500	1	(a,b)	$\text{NiCo}_2\text{O}_4$ + appreciable cubic phase

a.: catalyst scraped from electrode.

b.: evaporation method (see chapter 3)

The X-ray data analysis is in agreement with the TGA diagram (section 6.2), and reveals furthermore that the decomposition of the  $\text{NiCo}_2\text{O}_4$  spinel sets in at temperatures above 400°C, with the appearance of NiO. With Röntgen diffraction no influence of the oxygen evolution reaction on the  $\text{NiCo}_2\text{O}_4$  electrodes was detected.

The parameter of the lattice when it corresponds to the closest packing principle is equal to 8 Å [13]. The cell parameter of spinels is usually greater than that predicted by the packing density principle. The reported unit cell dimension of  $\text{NiCo}_2\text{O}_4$  can be situated in the range of 8.10 to 8.12 Å [7,8,14,15]. The lattice parameter or unit cell dimension  $a_0$  was simply determined from the

Table 6.4.: The values of the interplanar d-spacing ( $\text{\AA}$ ), the Miller indices and the relative intensities of the  $\text{NiCo}_2\text{O}_4$  electrodes as function of  $T_p$  and  $t_p$ .

hkl		111		220		311		111		222		200		400		422		511,333		220		440	
$T_p(^{\circ}\text{C})-t_p(\text{h})$		d	$I/I_1$	d	$I/I_1$	d	$I/I_1$	d	$I/I_1$	d	$I/I_1$	d	$I/I_1$	d	$I/I_1$	d	$I/I_1$	d	$I/I_1$	d	$I/I_1$	d	$I/I_1$
250	10	4.68	24	2.88	37	2.45	100			2.34	24			2.03	85	1.66	14	1.56	35			1.43	38
300	1	4.70	19	2.87	32	2.45	100			2.34	22			2.03	68	1.65	16	1.56	36			1.43	50
300	10	4.66	15	2.87	33	2.45	100			2.35	19			2.03	54	1.66	16	1.56	32			1.43	48
350	1	4.66	19	2.86	30	2.45	100			2.34	27			2.03	60	1.65	19	1.56	40			1.43	54
400	1	4.68	15	2.87	28	2.45	100			2.35	14			2.03	41	1.66	14	1.56	33			1.43	44
400	10	4.69	13	2.87	32	2.45	100			2.35	20			2.03	48	1.66	15	1.56	35			1.43	44
500	1	4.68	14	2.87	31	2.45	100	2.41	10	2.35	14	2.09	10	2.03	55	1.66	10	1.56	34	1.48	9	1.43	47
600	1	4.66	12	2.86	36	2.44	100	2.41	33	2.34	12	2.09	40	2.03	45	1.65	11	1.56	22	1.48	24	1.43	40
								(83)				(100)								(60)			
$\text{NiCo}_2\text{O}_4$	ASTM 20-781	4.69	14	2.87	25	2.45	100			2.34	10			2.03	25	1.66	8	1.56	30			1.43	45
NiO	ASTM 4-0835							2.41	91			2.09	100							1.48	57		

observed d-spacings for the planes (311) and (440) by making use of the cubic formula for the interplanar spacing d,

$$a_o = d \cdot \sqrt{h^2 + k^2 + l^2} \quad (6.2)$$

where h, k and l represent the Miller indices.

The unit cell dimension determined from the Debye-Scherrer powder samples shows the tendency to increase slightly (8.08 to 8.10 Å) in the  $T_F$ -range of 250 to 400°C. Above 400°C a decrease in  $a_o$  was noticed. No appreciable variation in the lattice constant as function of  $t_F$  was observed.

The lattice parameter of the coatings showed somewhat higher values, i.e. 8.10 to 8.12 Å, and more discrepancies in the temperature range below 400°C. The decrease in  $a_o$  above 400°C was more clearly observed.

The observation of the decrease in  $a_o$ -values above 400°C in both cases, i.e. powder or coatings, might be related to the spinel decomposition. The difference in  $a_o$ -values in the  $T_F$ -range of the spinel only phase is suggested to be a result of a difference in measuring technique.

## 6.5 Temperature programmed reduction

### 6.5.1 Introduction

Temperature programmed reduction (TPR) is applied to investigate the reduction behaviour of the oxide catalyst  $\text{NiCo}_2\text{O}_4$ . In TPR hydrogen is continuously led over the catalyst, while the temperature is raised linearly with time. By measuring the consumption of hydrogen, due to the reduction of species in the catalyst, as a function of the applied temperature a so-called reduction profile is obtained. The total hydrogen consumption during the reduction makes it possible to determine the stoichiometric composition of the oxide. The ratio  $\text{H}_2/\text{M}$  is a measure for the total hydrogen consumption, and expresses the average number of dihydrogen molecules required for the reduction of a metal ion (M) in the oxide. So, TPR allows the determination of the mean valency state of the metal ions in the oxide and, therefore, is of great value in the characterization of the catalyst.

### 6.5.2 Experimental

The TPR apparatus we used has recently been described in detail by Boer et al. [16]. A schematic drawing of the apparatus is presented in figure 6.4. The hydrogen consumption is measured with a thermal conductivity detector (TCD) of the diffusion type. TCD is very sensitive in detecting small changes in the concentration of  $H_2$  in Ar because of the differences in thermal conductivity between the active phase,  $H_2$ , and the inert phase Ar. The heating rate during all TPR experiments is  $5^\circ C \text{ min}^{-1}$ .

The TPR experiments were carried out by the group of Prof. R. Prins at the Department of Inorganic Chemistry, Eindhoven University of Technology.

TPR experiments of supported and unsupported catalysts were carried out.  $NiCo_2O_4$  and  $Co_3O_4$  spinel oxides were prepared by thermal decomposition. The supports used were  $TiO_2$  (Anatase, Tioxide CLDD 1367,  $19 \text{ m}^2/\text{g}$ ), and Grace  $SiO_2$  (SP 2-324-382,  $290 \text{ m}^2/\text{g}$ ). The  $NiCo_2O_4$  catalyst was deposited on the supports by means of a standard, pore volume impregnation method: a known amount of an aqueous solution of  $Ni(NO_3)_2 \cdot 6H_2O$  and  $Co(NO_3)_2 \cdot 6H_2O$ , mixed in stoichiometric amounts of 1:2, was added to the support. The samples were dried at moderate temperature, and finally cured at  $T_F$  °C for 24 hours to form the spinel oxide.

### 6.5.3 Results and discussion

The TPR profiles of the unsupported  $NiCo_2O_4$  (curve a) and  $Co_3O_4$  (curve b and c) are shown in figure 6.5. Curve c is the TPR profile of commercial  $Co_3O_4$  (Merck). The  $H_2/M$  values are given in the curves. The reduction profiles of  $NiCo_2O_4$  and  $Co_3O_4$  are similar. The reduction peaks are asymmetric and broad, indicating that various reducible species are present. It appears that the TPR of  $NiCo_2O_4$  (curve a) takes place at lower temperatures than the reduction of  $Co_3O_4$  (curve b), for both catalysts prepared under identical conditions.

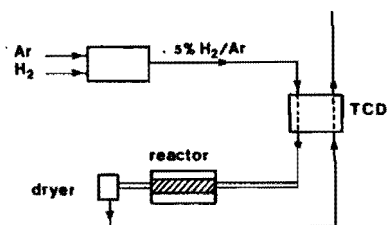


Fig. 6.4. Schematic drawing of the TPR apparatus:

- 1: pneumatic gas dosage system for preparing 5%  $H_2$  in Ar,
- 2: thermal conductivity cell,
- 3: reactor section = quartz tube placed in a silver block oven.

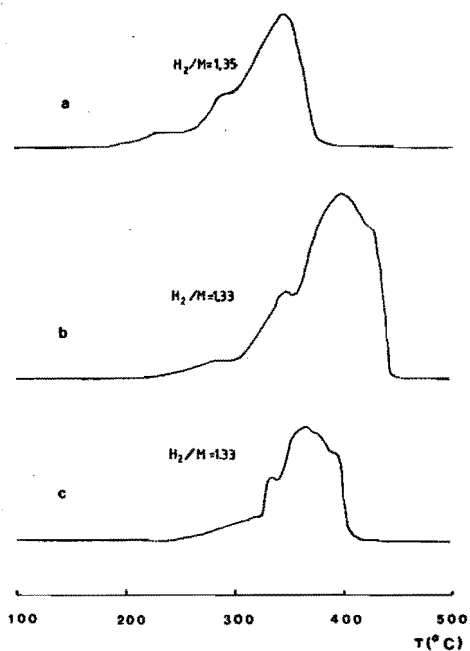


Fig. 6.5. TPR profiles of unsupported  $NiCo_2O_4$  and  $Co_3O_4$  catalysts.

a/  $NiCo_2O_4$  : 400°C - 1 h

b/  $Co_3O_4$  : 400°C - 1 h

c/  $Co_3O_4$  (Merck).

Most probably, this is due to a difference in stability of the spinel oxides. It has been reported [8,17] that  $\text{NiCo}_2\text{O}_4$  forms a 'metastable' spinel structure, which already breaks down above  $400^\circ\text{C}$ , while  $\text{Co}_3\text{O}_4$  is stable up to  $900^\circ\text{C}$ , as shown in the TGA-curves in section 6.2.

Two peak maxima are observed for both spinel oxides and suggest a two stage process. Also the same stoichiometry is observed. The  $\text{H}_2/\text{M}$ -value indicates that the average oxidation state of the metal cation before reduction is 2.67+. Table 6.5 shows a comparison of the TPR characteristic features of the literature data and this work. Paryjczak et al. [18] has performed a TPR study on  $\text{Co}_3\text{O}_4$  prepared by coprecipitation and Martens et al. [19] on  $\text{Co}_3\text{O}_4$  supported on  $\text{TiO}_2$ . Our results are in agreement with the literature data.

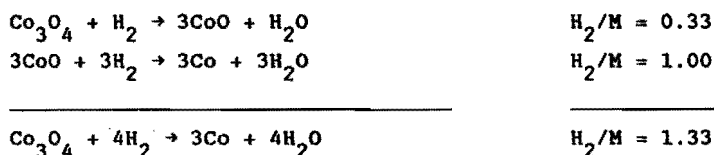
Table 6.5.: TPR characteristic features of  $\text{Co}_3\text{O}_4$  and  $\text{NiCo}_2\text{O}_4$

Sample	Peak maxima ( $^\circ\text{C}$ )	Peak area ratio	$\text{H}_2/\text{M}$	Ref	
$\text{Co}_3\text{O}_4$ <sup>1</sup> ( $T_F = 400^\circ\text{C} - t_F = 1 \text{ h}$ )	347	402	1 : 3	1.33	this work
$\text{Co}_3\text{O}_4$ (Merck) <sup>1</sup>	336	371	1 : 3	1.33	this work
$\text{Co}_3\text{O}_4$ (coprecip.) <sup>1</sup>	320	390	1 : 3	1.33	[17]
$\text{Co}_3\text{O}_4/\text{TiO}_2$ <sup>2</sup>	315	413	1 : 3	1.33	[18]
$\text{NiCo}_2\text{O}_4$ <sup>1</sup> ( $T_F = 400^\circ\text{C} - t_F = 1 \text{ h}$ )	288	348	1 : 3	1.35	this work

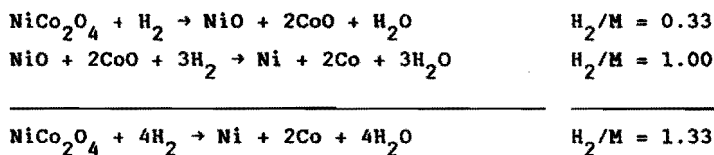
1 : unsupported; 2 : supported

The first step in the TPR of  $\text{Co}_3\text{O}_4$ , i.e.  $\text{Co}^{2+}[\text{Co}^{3+}]_2\text{O}_4$ , is the reduction of  $\text{Co}_3\text{O}_4$  to  $\text{CoO}$  and the second step is the reduction of  $\text{CoO}$  to metallic  $\text{Co}$ , as follows.





From the observed peak ratio and the  $\text{H}_2/\text{M}$  ratio a similar course of the TPR of  $\text{NiCo}_2\text{O}_4$  can be proposed.



The reduction of the unsupported  $\text{Co}_3\text{O}_4$  and  $\text{NiCo}_2\text{O}_4$  takes place in two not clearly separated peaks. However, in the case of  $\text{Co}_3\text{O}_4$  supported on  $\text{TiO}_2$  [19], two clearly separated peaks were observed with  $\text{H}_2/\text{M}$  ratios of 0.33 versus 1.00, which led to the two steps reduction model. Figure 6.6 presents the TPR profile of 7.15 wt.%  $\text{NiCo}_2\text{O}_4/\text{TiO}_2$  for different calcination temperatures  $T_F$ , i.e. 300 and 400°C.

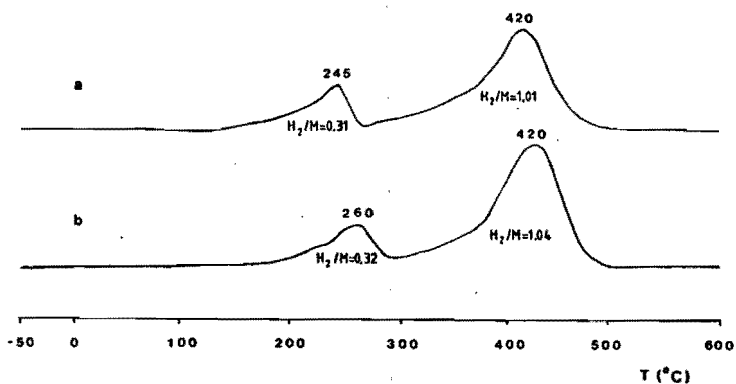


Fig. 6.6. TPR profiles of  $\text{NiCo}_2\text{O}_4/\text{TiO}_2$  catalysts  
 a/ 7.15 wt.%  $\text{NiCo}_2\text{O}_4$  : 300°C  
 b/ 7.15 wt.%  $\text{NiCo}_2\text{O}_4$  : 400°C

The two reduction peaks are now completely separated, and the start of the reduction, i.e. the first reduction maximum, takes place at lower temperatures than in the case of the unsupported catalyst. This can be explained as a consequence of the particle size and distribution. It can be assumed from the properties of the supporting material that the  $\text{NiCo}_2\text{O}_4$  particles of the supported catalyst are smaller, and more uniform in size, whereas the unsupported particles are greater and have a less uniform particle size distribution. Smaller particles have a relative higher surface area, and thus relatively more surface defects where the reduction can start. The reduction of  $\text{NiCo}_2\text{O}_4$  supported on  $\text{SiO}_2$  also takes place in two separated peaks, and at lower temperatures than for  $\text{NiCo}_2\text{O}_4/\text{TiO}_2$ . This is in accordance with the line of reasoning described above. The expected particle size on  $\text{SiO}_2$  ( $290 \text{ m}^2 \text{ g}^{-1}$ ) will be smaller than on  $\text{TiO}_2$  ( $19 \text{ m}^2 \text{ g}^{-1}$ ). However, it was reported [18] that for  $\text{Co}_3\text{O}_4$  supported on silica or alumina, the reduction takes place at higher temperatures. This was ascribed to an interaction between the active phase, the oxide, and the support material. Our results indicate that there is no interaction between the  $\text{NiCo}_2\text{O}_4$  catalyst, and  $\text{SiO}_2$  or  $\text{TiO}_2$ . The compounds, i.e. nickel and cobalt titanates or silicates, responsible for the interaction are probably only formed at higher temperatures ( $T_F$  was maximum  $400^\circ\text{C}$ ). However, the complete reduction of the supported  $\text{NiCo}_2\text{O}_4$  takes place at higher temperatures than the unsupported  $\text{NiCo}_2\text{O}_4$  powders. It can be assumed that the second stage in the reduction of the unsupported sample is faster because of an earlier presence of a metallic phase.

The total hydrogen consumption of the first versus the second reduction peak is in the ratio of 1 to 3. The  $\text{H}_2/\text{M}$  value of 1.33 indicates that the stoichiometric oxide  $\text{NiCo}_2\text{O}_4$  is formed and thus can be presented by the general formula  $\text{M}^{2+}\text{M}_2^{3+}\text{O}_4$ . If instead of  $\text{NiCo}_2\text{O}_4$ ,  $\text{NiO}$  and  $\text{Co}_3\text{O}_4$  were formed on the support, the  $\text{H}_2/\text{M}$  value should have been 1.22, which is substantially different from the observed value. It is, however, not possible to determine the individual oxidation states of Ni and Co in  $\text{NiCo}_2\text{O}_4$ .

The ratios of the  $H_2/M$  values of both the reduction peaks indicates a two stage reduction. This mechanism assumes no metallic phase to be formed in the first reduction peak. This supposition is investigated in the next experiment.  $NiCo_2O_4/TiO_2$  is reduced in a first TPR (figure 6.7 curve b) until the temperature of this first TPR is  $280^\circ C$ , which is the minimum in the hydrogen consumption between the two peaks (cf. figure 6.7 curve a). At this temperature the reactor is flushed with argon and quickly cooled down to  $25^\circ C$ . The partly reduced oxide is then reduced in a second TPR run to  $600^\circ C$  (curve c). The reduction peak in the second TPR coincides with the second peak of a TPR profile without interruption (curve a). It is known that in the presence of a metallic phase the reduction already starts at lower temperature, when the metallic phase is able to absorb hydrogen dissociatively. However, no shift towards lower temperatures of the second peak is observed. This experiment was also carried out for  $Co_3O_4$  by Paryjczak et al. [18], who found that in the first TPR peak practically no metallic phase was formed (4% metal).

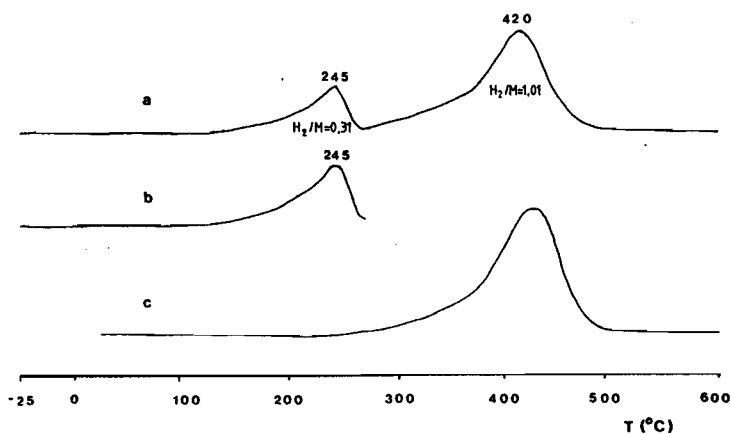


Fig. 6.7. TPR profiles of  $NiCo_2O_4/TiO_2$  catalysts:  
 7.15 wt.%  $NiCo_2O_4$  :  $300^\circ C$   
 a/ TPR-curve in the T-range of  $-50$  to  $600^\circ C$   
 b/ First TPR-curve in the T-range of  $-50$  to  $280^\circ C$   
 c/ Second TPR-curve in the T-range of  $25$  to  $600^\circ C$ .

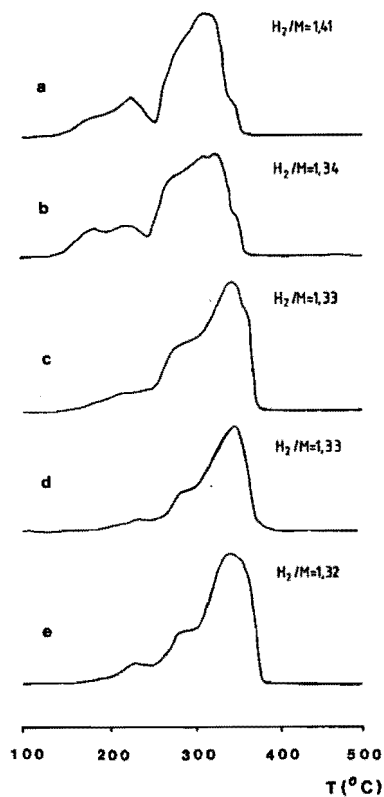


Fig. 6.8. TPR profiles of  $\text{NiCo}_2\text{O}_4$  catalysts

Heat treatment		BET-surface area
$T_F$ ( $^{\circ}\text{C}$ )	$t_F$ (h)	( $\text{m}^2 \text{g}^{-1}$ )
a/ 250	10	39.9
b/ 300	1	32.0
c/ 300	24	17.7
d/ 400	1	22.5
e/ 400	24	13.3

The influence of the temperature  $T_F$ , and the duration time  $t_F$  of the final heat treatment of  $\text{NiCo}_2\text{O}_4$  on the TPR profile is shown in figure 6.8. A shift of the reduction peaks towards higher temperatures as a function of increasing  $T_F$  and  $t_F$  is observed.

For  $T_F \geq 300^\circ\text{C}$ , the  $\text{H}_2/\text{M}$  ratio approaches the value of 1.33. The stoichiometric composition of  $\text{M}^{2+}\text{M}^{3+}_2\text{O}_4$  is reached for  $\text{NiCo}_2\text{O}_4$  with a mean cation valency of 2.67+. The increase of the  $\text{H}_2/\text{M}$  ratio at lower  $T_F$  is due to the increase in non-stoichiometry of  $\text{NiCo}_2\text{O}_4$ , as indicated by TGA in section 6.2. Although, the oxidation state of  $\text{NiCo}_2\text{O}_4$  oxide is approximately the same above  $300^\circ\text{C}$  ( $T_F$ ), the reducibility is different, as shown by the TPR profiles. The TPR curve appears to depend on the heat treatment. The reduction peaks are less separated at higher  $T_F$  and  $t_F$ . The changes in the TPR profiles are attributed to the changes in particle size and stability. The influence of the particle size was discussed above. The temperature at which the reduction starts, increases with increasing  $T_F$  and  $t_F$ , and thus with decreasing in surface area. This is corroborated by the BET surface area data, as reported in figure 6.2. On the other hand, it can be assumed that the stability of the  $\text{NiCo}_2\text{O}_4$  phase increases with  $T_F$ , resulting in a decrease in the reducibility. So the reducibility of  $\text{NiCo}_2\text{O}_4$  decreases with increasing  $T_F$  and  $t_F$ .

## 6.6. X-ray and Auger photoelectron spectroscopy.

### 6.6.1. Introduction.

X-ray photoelectron spectroscopy (XPS), also referred to as electron spectroscopy for chemical analysis (ESCA), and Auger electron spectroscopy (AES) were used to characterize and determine the composition of the surface of  $\text{NiCo}_2\text{O}_4$  anodes as a function of the temperature of the final heat treatment ( $T_F$ ).

One of the major problems in the crystal chemistry of the mixed oxide spinels is the determination of the valence state and the distribution of the cations among the octahedral and tetrahedral sublattices of the spinel structure, in particular, if two different metals are present,

each of which can adapt more than one valence state. The binding energies and the satellite structure of the XPS photoelectron lines are indicative for the Ni and Co valence states in the charge distribution of  $\text{NiCo}_2\text{O}_4$ .

#### 6.6.2. Experimental.

Auger electron and X-ray photoelectron spectra were recorded on a PHI 550 XPS/AES spectrometer equipped with a magnesium anode ( $h\nu = 1253.6$  eV), an electron gun and a double pass cylindrical mirror analyzer. A PDP 11-04 computer interfaced with the spectrometer enabled signal handling to be carried out. Figure 6.9 shows the sample holder in its experimental set-up during XPS and Auger measurements. The sample is transported via a gate valve to the work chamber. The total pressure during the measurements in the spectrometer did not exceed  $1.10^{-9}$  Torr. The XPS analyzer was frequently and carefully calibrated with a gold sample (Au 4f 7/2 at 83.8 eV). The C 1s binding energy of contamination carbon was used as internal calibration. No shift of the C 1s line (284.6 eV) was observed, which indicates that no sample charging occurs. The reproducibility of the binding energy values was within 0.25 eV.

The analyzed  $\text{NiCo}_2\text{O}_4$  electrodes were prepared as reported in chapter 3.

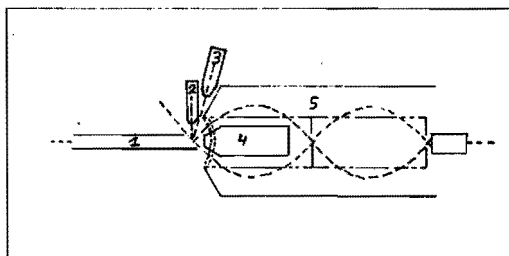


Fig. 6.9. Schematic representation of the experimental set-up during the XPS and Auger measurements.

1 = sample holder; 2 = Mg X-ray source; 3 = ion gun; 4 = electron gun; 5 = analyzer.

### 6.6.3. Results and discussion.

The XPS survey scan for a freshly prepared  $\text{NiCo}_2\text{O}_4$  electrode is shown in figure 6.10. The survey scan is sufficient for the identification of all detectable elements present. Of course, predominantly the Ni 2p, Co 2p and O 1s photoelectron lines are observed in this wide range spectrum. Also, the carbon contamination C 1s-line is observed.

The XPS concentrations of the various constituents were determined by measuring the peak area of the main photoelectron lines and by utilizing the atomic sensitivity factors, as presented by Wagner et al. [20]. This approach is satisfactory for quantitative work, except in the case of transition metal spectra with prominent shake-up lines. Therefore, the entire 2p region of nickel and cobalt, i.e.  $2p^{3/2}$  and  $2p^{1/2}$ , was used when measuring peak areas. A generalized expression for the determination of the atom fraction of any constituent in a sample  $C_x$ , can be written as

$$C_x = \frac{n_x}{\sum_i n_i} = \frac{I_x/S_x}{\sum_i I_i/S_i} \quad (6.3)$$

where  $n$  is the number of atoms of the element per  $\text{cm}^3$  of sample.  $I$  is the number of photoelectrons per second in a specific spectral peak and  $S$  is defined as the atomic sensitivity factor. The use of atomic sensitivity factors will normally furnish semiquantitative results (within 10-20%).

The surface composition of  $\text{NiCo}_2\text{O}_4$  electrodes, determined by XPS measurements as described above, is given in table 6.6 for electrodes freshly prepared at the temperatures  $T_p = 300$  and  $400^\circ\text{C}$ , and for an electrode prepared at  $T_p = 300^\circ\text{C}$ , which is aged by previously subjecting to oxygen evolution.

For freshly prepared  $\text{NiCo}_2\text{O}_4$  electrodes, it appears that with lowering  $T_p$ , the Ni:Co ratio changes: the nickel concentration decreases while the cobalt content increases. Generally, it was found

that the measured Ni:Co ratio (versus nickel) for  $T_F$  equal to 400°C varied between the ratios 1.0 : 1.0 and 1.0 : 1.4, whereas for  $T_F$  equal to 300°C the ratio varied between 1.0 : 2.0 and 1.0 : 2.6. The surface composition of a  $\text{NiCo}_2\text{O}_4$  electrode has changed after oxygen evolution at  $0.5 \text{ A cm}^{-2}$  during 24 h, as seen in table 6.6: the nickel and cobalt concentrations decrease and the oxygen content increases. From this experiment it is not clear whether the change is due to nickel or cobalt dissolution or has to be attributed to an increase in oxygen species on the surface.

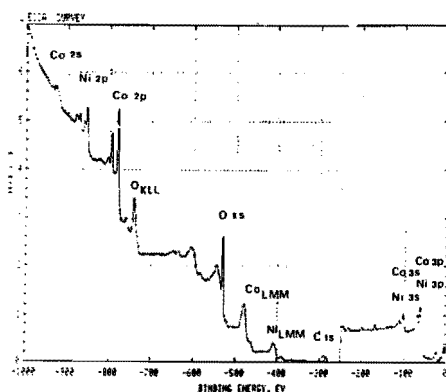


Fig. 6.10. XPS spectrum of a freshly prepared  $\text{NiCo}_2\text{O}_4$  electrode.  
 $T_F = 300^\circ\text{C}$  and  $t_F = 1 \text{ h}$ .

Table 6.6: XPS composition of  $\text{NiCo}_2\text{O}_4$  electrodes.

Materials	Elements (% in atom)			
	Ni	Co	O	C
$\text{NiCo}_2\text{O}_4$ (theor.)	14.3	28.6	57.1	-
$\text{NiCo}_2\text{O}_4$ 400°C-1 h	21.4	22.1	48.1	8.4
$\text{NiCo}_2\text{O}_4$ 300°C-1 h	12.3	32.1	47.0	8.6
$\text{NiCo}_2\text{O}_4$ 300°C-1 h (after 24 h $0.5 \text{ A cm}^{-2}$ )	8.8	28.0	52.2	11.0



Summarizing, a considerable variation in the composition of the surface of freshly prepared  $\text{NiCo}_2\text{O}_4$  electrodes was observed. Also, it was found that with increasing  $T_F$ , the surface composition deviates more from the theoretically expected one.

However, one must be aware that the experimental conditions of the XPS analysis can influence the quantitative results. Since XPS is a surface sensitive method, which is performed under vacuum, in situ redox processes and hence surface decomposition of the  $\text{NiCo}_2\text{O}_4$  sample can be induced by the X-ray radiation and the low partial oxygen pressure in the spectrometer, resulting in a change of the surface composition. On the one hand, a surface-enrichment or -depletion of certain metal ions can take place, and on the other hand, a reduction of the sample would change the valence state of the metal ions. A study of the influence of the variation of the oxygen pressure in the spectrometer, and of the power of the X-ray source would give more evidence about these phenomena.

In view of the accuracy of the XPS analysis, it is not possible to make accurate quantitative analyses. Therefore, in case of this study, the approach is useful in obtaining results in terms of orders of magnitudes. As a tendency, it can be concluded that lowering  $T_F$ , leads to Co-enrichment and Ni-depletion of the surface. Furthermore, it confirms that the surface composition is influenced by the temperature  $T_F$ , as earlier indicated by the voltammetric behaviour in chapter 5.

Auger spectroscopy was used to investigate the depth profile of the elements in the  $\text{NiCo}_2\text{O}_4$  layer. Depth profiling was accomplished by sputtering the surface with argon ions. The distribution of the elements as a function of depth into the specimen (sputtering time) is shown in figure 6.11 for  $\text{NiCo}_2\text{O}_4$ , prepared at  $T_F = 300^\circ\text{C}$ . It appears that the nickel content increases with increasing sputtering time, whereas the cobalt and oxygen concentrations slightly decrease. However, one must be conscious because the experimental conditions can influence the AES analysis in a similar way, as earlier mentioned.

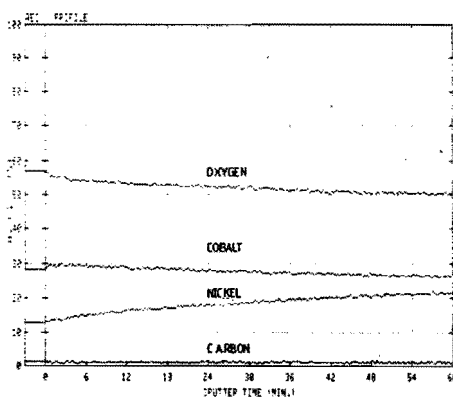


Fig. 6.11. The Auger profile distribution of the elements in a fresh  $\text{NiCo}_2\text{O}_4$  layer, prepared at  $300^\circ\text{C}$  ( $T_F$ ) for 1 h ( $t_F$ ).

The detected carbon contamination in figure 6.11 is negligible compared to the values in table 6.6. In the XPS experiments the detected carbon content varied significantly for  $\text{NiCo}_2\text{O}_4$  electrodes, prepared under similar conditions. Since, the samples exhibit the carbon 1s peak in different quantities, we are inclined to believe that it is due to experimental conditions, i.e. C-contamination in the spectrometer, and not due to the  $\text{NiCo}_2\text{O}_4$  oxide sample preparation.

Some detailed spectra of the metal photoelectron lines are given in figure 6.12 and the binding energies (BE) for the  $\text{Co } 2p^{3/2}$ ,  $\text{Co } 3p^{3/2}$ ,  $\text{Co } 3s$ ,  $\text{Ni } 2p^{3/2}$ ,  $\text{Ni } 3p^{3/2}$ ,  $\text{Ni } 3s$  and  $\text{O } 1s$  are given in table 6.7. No influence of the temperature  $T_F$ , i.e.  $300^\circ$  vs.  $400^\circ\text{C}$ , on the spectral characteristics is observed. The  $\text{Ni } 2p$  spectrum (curve a) of  $\text{NiCo}_2\text{O}_4$  shows a prominent satellite structure and the  $\text{Co } 2p$  spectrum (curve b) shows a weak satellite band. No satellite lines are observed in the  $\text{Ni } 3s$  spectrum (curve c). The  $\text{Ni } 3p$  spectrum (curve d), consisting of  $3p^{3/2}$  and  $3p^{1/2}$  shows an asymmetrical line with a weak satellite band. No satellite bands can be distinguished in the  $\text{Co } 3s$  (curve c) and  $\text{Co } 3p$  spectrum (curve d); the adjacent  $\text{Ni } 3s$  and  $\text{Ni } 3p$  lines can mask them, respectively.

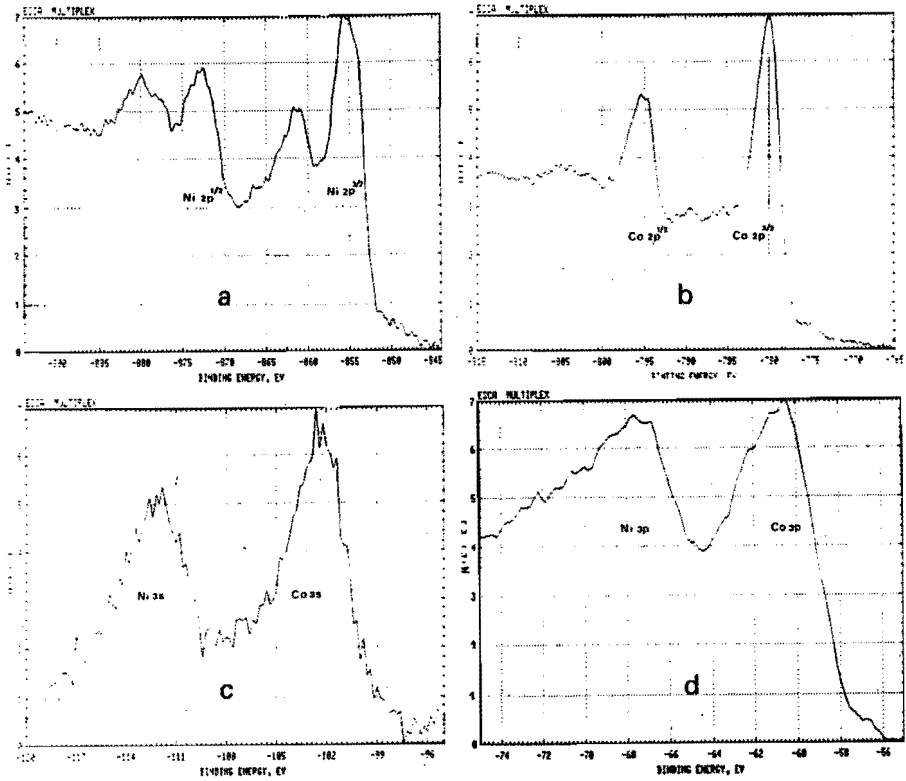


Fig. 6.12. Detailed scan of the XPS spectrum of  $\text{NiCo}_2\text{O}_4$  electrode.

$T_F = 400^\circ\text{C}$  and  $t_F = 1$  h.

a/ Ni 2p spectrum; b/ Co 2p spectrum; c/ Ni 3s and Co 3s spectra; d/ Ni 3p and Co 3p spectra.

XPS provides the ability to obtain information on chemical states from the variation in binding energy or chemical shifts of the photoelectron lines. Since the core levels of atoms may shift because of valence changes and different crystallographic sites, the splitting of core levels is a direct proof of the presence of inequivalent atoms [21]. Unfortunately, it is not always possible to find separate peaks if the

Table 6.7: Electron binding energies for  $\text{NiCo}_2\text{O}_4$  (eV).

Ni $2p^{3/2}$	$\Delta^*$	Ni $3p^{3/2}$	Ni 3s	O 1s
855.2	17.35	67.5	111.8	529.3 530.7
Co $2p^{3/2}$	$\Delta^*$	Co $3p^{3/2}$	Co 3s	C 1s
779.85	15	60.75	102.6	284.6

\*:  $\Delta$  = difference in BE of the ( $2p^{1/2} - 2p^{3/2}$ ) lines, gives the position of the  $2p^{1/2}$  line.

Table 6.8: Core level energies of nickel. (eV)

	$\text{Ni}^{2+}$ [23]	$\text{Ni}^{3+}$ [23]	$\text{NiCo}_2\text{O}_4$
Ni $2p^{3/2}$	854.9	857.1	855.2
Ni $2p^{3/2}$ sat.	862.1	863.0	861.3

Table 6.9: Ni  $2p^{3/2}$  and  $3p^{3/2}$  levels and FWHM for nickel spinels (eV).

Compound	$2p^{3/2}$	FWHM	$3p^{3/2}$	FWHM of 3p	Ref.
$\text{Ni}_{0.1}^{2+}\text{Mn}_{0.9}^{2+}[\text{Ni}_{0.9}^{2+}\text{Mn}_{0.2}^{3+}\text{Mn}_{0.9}^{4+}]_4\text{O}_4$	855.0	2.0	67.1	2.5	[37]
$\text{Zn}^{2+}[\text{Ni}^{2+}\text{Mn}^{4+}]_4\text{O}_4$	855.1	2.0	66.9	2.0	[37]
$\text{NiCo}_2\text{O}_4$	855.2	3.6	67.5	4.0	this work

shifts are too small, as seen for example for  $\text{Co}^{2+}$  and  $\text{Co}^{3+}$  states in  $\text{Co}_3\text{O}_4$  [22]. In general, the binding energy of core levels shift about 1 eV, through a change of the ionic charge of an atom by one unit, under the assumption that no other effects, such as covalency, are interfering. As the ligands are oxygen atoms for both lattice sites, covalency effects are supposed to have only a minor effect, and the core levels  $\text{M}^{2+}$  and  $\text{M}^{3+}$  ( $\text{M} = \text{Ni}$  or  $\text{Co}$ ) must be distinguishable. A comparison of the Ni  $2p^{3/2}$  of  $\text{NiCo}_2\text{O}_4$  with those for  $\text{Ni}^{2+}$  or  $\text{Ni}^{3+}$  in other oxides [23], as given in table 6.8, provide an indication that in  $\text{NiCo}_2\text{O}_4$  nickel is present as divalent ion. The Ni  $2p^{3/2}$  and  $3p$  spectrum shows a broadening of the lines as indicated by the full width at half maximum (FWHM) values given in table 6.9, compared to that of other spinel oxides. This may be caused by the presence of another valence state. However, the formal oxidation state of cobalt appears to have little influence on the metal binding energies of Co compounds. The absence of any obvious relationship between the formal oxidation state of the Co metal, and the metal binding energy has already been noted for Co oxides by McIntyre and Cook [24].

Figure 6.13 shows the O 1s spectrum of a freshly prepared  $\text{NiCo}_2\text{O}_4$  electrode and after oxygen evolution. The O 1s spectrum for  $\text{NiCo}_2\text{O}_4$  exhibits two peaks, one at 529.3 eV, and a shoulder at about 530.7 eV. Contradictory opinions have been reported as to the interpretation of the various O 1s peaks which, for example, appear in the Ni-O [25-29] and Co-O [28-31] systems. It may be expected that not only lattice oxygen ions  $\text{O}^{2-}$ , but also chemisorbed species  $\text{O}_2$ ,  $\text{O}_2^-$ ,  $\text{O}^-$  oxygen in other chemisorbed molecules such as  $\text{H}_2\text{O}$ ,  $\text{CO}$ ,  $\text{CO}_2$  etc..., as well as surface and bulk hydroxides could appear in the form of separate peaks.

The peak corresponding to the smaller binding energy, i.e. 529.3 eV, can be assigned to lattice oxygen ions  $\text{O}^{2-}$ . It was reported [24] that, in general, oxides of related metals which have identical crystallographic structures have very similar O 1s binding energies. It appears that the lattice oxygen O 1s binding energy of  $\text{NiCo}_2\text{O}_4$  is about 0.6 eV lower with respect to that of the inverse spinel oxides  $\text{NiFe}_2\text{O}_4$  and  $\text{CoFe}_2\text{O}_4$  [24] and about 0.2 eV lower with respect to

that of the normal spinel  $\text{Co}_3\text{O}_4$  [29]. An empirical relationship between the O 1s binding energy of the lattice oxygen and the valence state of the cation in oxides of the first transition metal series has been proposed by Haber et al. [29]. They reported that the O 1s binding energy of  $\text{Co}_3\text{O}_4$  pointed to the mean valence state of the cations 2.66+. However, it does not predict the expected mean valence state 2.66+ when we apply it to other mixed inverse spinels, like  $\text{NiFe}_2\text{O}_4$ ,  $\text{CoFe}_2\text{O}_4$  and  $\text{NiCo}_2\text{O}_4$ . Thus, no simple relationship exists between the binding energy of the O 1s photoelectron line and the chemical state.

The peak at higher binding energy is probably due to surface hydroxyl groups. Figure 6.13 shows the influence of oxygen evolution at a current density of  $0.5 \text{ A cm}^{-2}$  for 24 h in 5 M KOH on the O 1s photoelectron line. An increase of the O 1s peak at higher binding energy is observed, which points to hydroxyl oxygen. Also, some potassium was detected on the surface by the appearance of the  $\text{K } 2p^{3/2}$  photoelectron line.

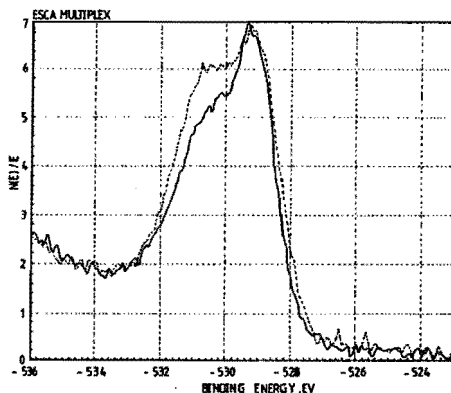


Fig. 6.13. O 1s spectrum of  $\text{NiCo}_2\text{O}_4$ , prepared at  $T_F = 300^\circ\text{C}$  and  $t_F = 1 \text{ h}$ . Solid curve: freshly prepared  $\text{NiCo}_2\text{O}_4$ ; dashed curve: after oxygen evolution at  $0.5 \text{ A cm}^{-2}$  for 24 h in 5 M KOH.

Sometimes, evidence for certain valencies can be obtained from the presence of satellites, or multiplet splitting in the spectra. In the Ni 2p region of  $\text{NiCo}_2\text{O}_4$  a prominent satellite band was observed, as shown in figure 6.12a, like in NiO,  $\text{Ni(OH)}_2$  and  $\text{NiFe}_2\text{O}_4$  [24]. The satellite shoulder on the  $2p^{3/2}$  line, as seen for NiO,

does not occur. The prominent satellite structure in the Ni 3s spectral region, as has been observed for NiO and Ni(OH)<sub>2</sub>, is not seen for NiCo<sub>2</sub>O<sub>4</sub>, like for NiFe<sub>2</sub>O<sub>4</sub> [24]. Only weak satellite lines are seen next to the 2p<sup>3/2</sup> line in the Co 2p spectrum.

The appearance of shake-up satellite lines near the M 2p core lines (M = Ni or Co) was shown to depend on the para- or diamagnetism of the compound [32-34]. Frost et al. [32,33] have shown that high-spin Co<sup>2+</sup>-compounds have intense satellite bands associated with the 3s and 2p lines, while satellite lines for the low-spin Co<sup>3+</sup>-compounds are weak or missing.

The Co 2p spectrum of NiCo<sub>2</sub>O<sub>4</sub> shows an intermediate case. The intensity of the satellite structure points to a mixture of Co<sup>2+</sup> and mainly Co<sup>3+</sup>. Because of the absence of a strong shake-up satellite in the 2p spectrum, the cobalt is mainly present as diamagnetic Co<sup>3+</sup>-ions in a low-spin state [35,36]. Furthermore, the Co 2p spectrum reveals a weak shake-up satellite due to paramagnetic, divalent high-spin cobalt. This is comparable with the mixed valence cobalt spinel oxide, i.e. Co<sup>2+</sup>[Co<sup>3+</sup>]<sub>2</sub>O<sub>4</sub>, which also shows only weak satellite lines in the Co 2p spectrum [29]. Thus, it is possible to identify the presence of low-spin Co<sup>3+</sup> and high-spin Co<sup>2+</sup> on the basis of the satellite structure. The appearance of Co<sup>2+</sup> may be caused by the reduction of Co<sup>3+</sup>-ions under the experimental conditions in the spectrometer.

#### 6.6.4. Conclusions.

The XPS spectral characteristics of NiCo<sub>2</sub>O<sub>4</sub>, i.e. the binding energy and satellite structure, are described. It was noticed that the NiCo<sub>2</sub>O<sub>4</sub> spectra can be distinguished from the individual nickel and cobalt oxides and that they show some resemblance with those of similar mixed valence spinel oxides, i.e. Co<sub>3</sub>O<sub>4</sub>, CoFe<sub>2</sub>O<sub>4</sub>, and NiFe<sub>2</sub>O<sub>4</sub>. Furthermore, the influence of the temperature T<sub>F</sub> on the surface composition has been demonstrated.

The presence of divalent nickel has been proposed on the basis of the binding energy of the Ni 2p<sup>3/2</sup> photoelectron line, and of Co as mainly diamagnetic Co<sup>3+</sup> in a low-spin state and paramagnetic divalent high-spin cobalt, based on the satellite structure.

## 6.7. Literature.

- [1] C. Duval, *Inorganic Thermogravimetric Analysis*, Elsevier Scientific Publishing Company, Amsterdam (1963).
- [2] D. Pope, D.S. Walker and R.L. Moss, *J. Colloid Interface Sci.* 60, 216 (1977).
- [3] R. Gararaglia, C.M. Mari and S. Trasatti, *Surf. Tech.* 19, 197 (1983).
- [4] V.V. Shalaginov, I.D. Belova, Yu. E. Roginskaya and D.M. Shub, *Sov. Electrochem.* 14, 1708 (1978).
- [5] D.L. Caldwell and M.J. Hazelrigg in M.O. Coulter (Ed.), *Modern Chlor-alkali Technology*, Ellis Horwood, Chichester, 221 (1980).
- [6] S. Angelov, E. Zhechera and D. Mehandjiev, *Bulg. Acad. Sci. Commun. Dept. Chem.* 13, 369 (1980).
- [7] O. Knop, K.I.G. Reid, Sutarno and Y. Nakagawa, *Can. J. Chem.* 46, 3463 (1968).
- [8] J. Robin and C. Bénard, *C.R. Acad. Sci. Paris* 235, 1301 (1952).
- [9] W.J. King and A.C.C. Tseung, *Electrochim. Acta* 19, 485 (1974).
- [10] M.R. Tarasevich, G.I. Zakharkin, A.M. Khutornoi, F.V. Markardei and V.I. Nikitin, *J. Appl. Chem. USSR* 49, 1001 (1976).
- [11] Surface area determination, Proc. of the International symposium on surface area determination, D.H. Everett and R.H. Otterwell (Eds.), Bristol U.K., 63 (1969).
- [12] Powder diffraction file of inorganic phases, W.F. McClune (Ed.), International centre for diffraction data, Swarthmore, PA 19081.
- [13] M.R. Tarasevich and B.N. Efremov in S. Trasatti (Ed.), *Electrodes of conductive metallic oxides Part A*, Elsevier scientific publishing company, Amsterdam, 221 (1980).
- [14] F.K. Lotgering, *Philips Res. Rep.* 11, 337 (1956).
- [15] P.D. Battle and A.K. Cheetham, *Mat. Res. Bull.* 14, 1013 (1979).
- [16] H. Boer, W.J. Boersma and N. Wagstaff, *Rev. Sci. Instr.* 53, 349 (1982).
- [17] W.J. King and A.C.C. Tseung, *Electrochim. Acta* 19, 492 (1974).
- [18] T. Paryjczak, J. Rynkowski and S. Karski, *J. Chromatogr.* 188, 254 (1980).



- [19] J. Martens. To be published in *J. Catalysis*.
- [20] C.D. Wagner, W.M. Riggs, J.F. Moulder and G.E. Muilenberg, *Handbook of X-ray Photoelectron Spectroscopy*, Perkin Elmer Corporation (1979).
- [21] M. Oku and K. Hirogawa, *J. Solid State Chem.* 30, 45 (1979).
- [22] M. Oku and K. Hirokawa, *J. Electron Spectrosc. Relat. Phenom.* 8, 475 (1976).
- [23] K.T. Ng and D.M. Hercules, *J. Phys. Chem.* 80, 2094 (1976).
- [24] N.S. Mc.Intyre and M.G. Cook, *Anal. Chem.* 47, 2208 (1975).
- [25] K.S. Kim and N. Winograd, *Surf. Sci.* 43, 625 (1974).
- [26] K.S. Kim, R.E. Davis, *J. Electron Spectrosc. Relat. Phenom.* 1, 251 (1972).
- [27] C.R. Brundle and A.F. Carley, *Chem. Phys. Lett.* 31, 423 (1975).
- [28] W. Dianis and J.E. Lester, *Surf. Sc.* 43, 602 (1974).
- [29] J. Haber, J. Stoch and L. Ungier, *J. Electron. Spectrosc. Relat. Phenom.* 9, 459 (1976).
- [30] K. Hirokawa, F. Honda and M. Oku, *J. Electron. Spectrosc. Relat. Phenom.* 6, 333 (1975).
- [31] J.P. Bonnelle, J. Grimblot and A. D'Huyser, *J. Electron. Spectrosc. Relat. Phenom.* 7, 151 (1975).
- [32] D.C. Frost, C.A. McDowell and I.S. Woolsey, *Chem. Phys. Lett.* 17, 320 (1972).
- [33] D.C. Frost, C.A. McDowell and I.S. Woolsey, *Mol. Phys.* 27 (1974).
- [34] L. Yin, I. Adler, T. Tsang, L. Matienzo and S.O. Grim, *Chem. Phys. Lett.* 24, 81 (1974).
- [35] B. Boucher, R. Buhl, R. Di Bella and M. Perrin, *J. Physique* 31, 113 (1970).
- [36] D. Scheerlinck and S. Houtecler, *Phys. Status Solidi b*, 73, 223 (1976).
- [37] V.A.M. Brabers, F.M. van Setten and P.S. Knapen, *J. Solid State Chem.* 49, 93 (1983).

## 7. NICKEL COBALT ALLOYS.

### 7.1. Introduction.

$\text{NiCo}_2\text{O}_4$  was investigated thoroughly in the previous chapters, and was found to have a very high activity towards oxygen evolution. In addition, we have investigated the electrochemical behaviour of two nickel-cobalt alloys in alkaline solution. Already in 1939 Grube [1] investigated nickel-cobalt alloys as electrodes for oxygen evolution in alkaline solutions. It is known that, prior to oxygen evolution on a metal electrode, an oxide layer is formed. Therefore, the electrochemical formation of oxides on nickel-cobalt alloys, with emphasis on the  $\text{Ni}_1\text{Co}_2$  composition, was investigated with cyclic voltammetry, and ellipsometry. Steady-state polarization curves were measured to examine the electrocatalytic activity for oxygen evolution.

### 7.2. Experimental.

#### 7.2.1. Electrode preparation.

Nickel and cobalt are known to exhibit substantial mutual solid solutions [2]. Alloys were made starting from a mixture of nickel (Riedel De Haën 99.8%), and cobalt powder (Ventron 99.99%). Two different compositions were prepared, i.e.  $\text{Ni}_1\text{Co}_1$ , and  $\text{Ni}_1\text{Co}_2$  alloys. The samples were pressed into pellets and molten in a flame arc in argon atmosphere. The resulting buttons were machined into small electrode pieces, which were embedded in perspex in conical matrices. The electrodes were polished on carborundum 220 and 600 in order to obtain flat electrodes. The electrodes were etched in a solution of  $\text{HNO}_3$ ,  $\text{HCl}$ ,  $\text{CH}_3\text{COOH}$  and, water before use.

#### 7.2.2. Electrochemical characterization.

All experiments were carried out in a conventional three-compartment cell, as given in figure 5.3, and the temperature was kept at 25°C. The potentials were measured against the RHE or the  $\text{Hg}/\text{HgO}$  (0.926 V vs. RHE,  $\text{KOH}$  25°C) via a Luggin capillary close to the working elec-

trode, a platinum foil ( $10 \text{ cm}^2$ ) was used as the counter electrode. All potentials are given against the RHE, and the current densities refer to the geometrical surface area ( $0.40 \text{ cm}^2$ ). The electrolyte solution, 5 M KOH, was prepared from analytical grade chemicals (Merck p.a.) and doubly distilled water.

Cyclic voltammetry was performed with the set-up as described in section 5.2.

Steady-state galvanostatic measurements were carried out as follows: the NiCo-alloys were firstly subjected to anodic polarization for 30 minutes at the highest current density, thereafter, the potentials were measured with decreasing current density. The time between each reading was 5 minutes. The ohmic potential drop between the tip of the Luggin capillary, and the working electrode was measured with the current interruptor technique [3];  $iR$ -corrected potential data are given.

### 7.2.3. Ellipsometry.

Simultaneous electrochemical and ellipsometric measurements were made in a Teflon cylindrical vessel with quartz windows, fixed for an angle of incidence of  $70^\circ$  at the mounted working electrode. The optical cell contains a platinum counter electrode ( $1 \text{ cm}^2$ ), and a Luggin capillary placed close to the working electrode and connected to the Hg/HgO reference electrode. All potentials are referred to the RHE. The optical measurements were conducted with a Rudolph automatic ellipsometer model RR 2200, equipped with a tungsten iodine light source and a monochromatic filter for  $5461 \text{ \AA}$ . In some experiments also intensity measurements were carried out with the polarizer at  $0$  and  $90^\circ$ , in order to obtain the reflection coefficients  $R_p$  and  $R_s$ . Before each experiment, the electrodes were carefully polished with alumina, down to finally  $0.3 \text{ }\mu\text{m}$ .

## 7.3. Results and discussion.

### 7.3.1. Electrochemical characterization.

Figure 7.1 presents the initial cyclic voltammetric behaviour of a

$\text{Ni}_1\text{Co}_2$ -alloy recorded in  $\text{N}_2$ -saturated 5 M KOH at a potential scan rate of  $20 \text{ mV s}^{-1}$ . Before cycling, the  $\text{Ni}_1\text{Co}_2$ -electrode was maintained at  $-0.5 \text{ V}$  for 10 minutes, and the voltammogram was recorded in the E-range  $-0.1$  to  $1.55 \text{ V}$ , starting from the lower limit potential. The voltammogram exhibits in the first scan an anodic doublet peak with the peak potentials at  $0.11$  and  $0.33 \text{ V}$ , where the latter appears to be most pronounced. This doublet peak decreases fast with further scanning. In addition to these peaks, initially a broad anodic peak is observed in the E-range  $1.05$  to  $1.30 \text{ V}$ . The following anodic potential scans exhibit a decreasing peak at about  $1.1 \text{ V}$ , and an increasing sharp anodic peak at about  $1.38 \text{ V}$ , which slightly shifts to more cathodic values. The reverse cathodic sweep shows three peaks: two increasing with scanning, at about  $1.30$  and  $1.175 \text{ V}$ , and a decreasing peak at about  $0.15 \text{ V}$ .

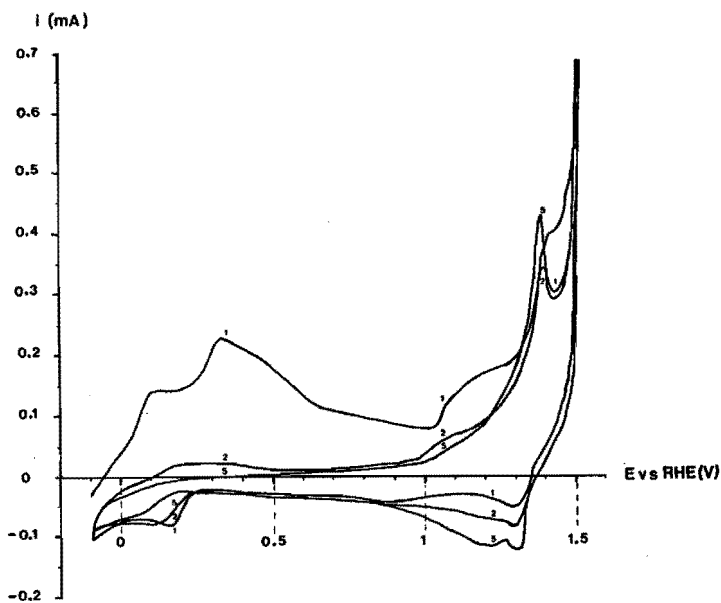


Fig. 7.1. Initial cyclic voltammetric behaviour of a  $\text{Ni}_1\text{Co}_2$ -alloy in  $\text{O}_2$ -free 5 M KOH,  $25^\circ\text{C}$  at a scan rate of  $20 \text{ mV s}^{-1}$ .

Figure 7.2 shows the initial voltammetric behaviour of the  $\text{Ni}_1\text{Co}_1$ -alloy recorded in  $\text{N}_2$ -saturated 5 M KOH at scan rate of  $20 \text{ mV s}^{-1}$ . The  $\text{Ni}_1\text{Co}_1$ -electrode was prereduced at  $-0.5 \text{ V}$  for 30 minutes, and

recorded in the E-range  $-0.275$  to  $1.525$  V. Similarly, an anodic doublet peak is initially observed with peak potentials  $0.115$  and  $0.295$  V, but in contrast to  $\text{Ni}_1\text{Co}_2$ , the first peak appears to be more pronounced. Further, another doublet peak is observed with peak potentials  $1.39$  and  $1.435$  V, which increases with cycling. These peaks are preceded by very weak peaks at about  $0.9$  and  $1.1$  V. The reverse cathodic sweep shows an increasing asymmetrical peak (probably a shoulder) at  $1.285$  V, and also a broad decreasing peak at about  $0.1$  V. It appears that the cyclic voltammograms of the two nickel-cobalt alloys are very similar, and the successive E-i recordings indicate a drastic change of the electrode surface. These initial voltammograms can be compared with the ones of pure nickel and cobalt. Both the voltammograms of Ni [4-5] (prereduced at vigorous hydrogen evolution potential), and Co [6-8] are characterized by two anodic peaks in the E-range  $0.05$  to  $0.40$  V in alkaline solution.

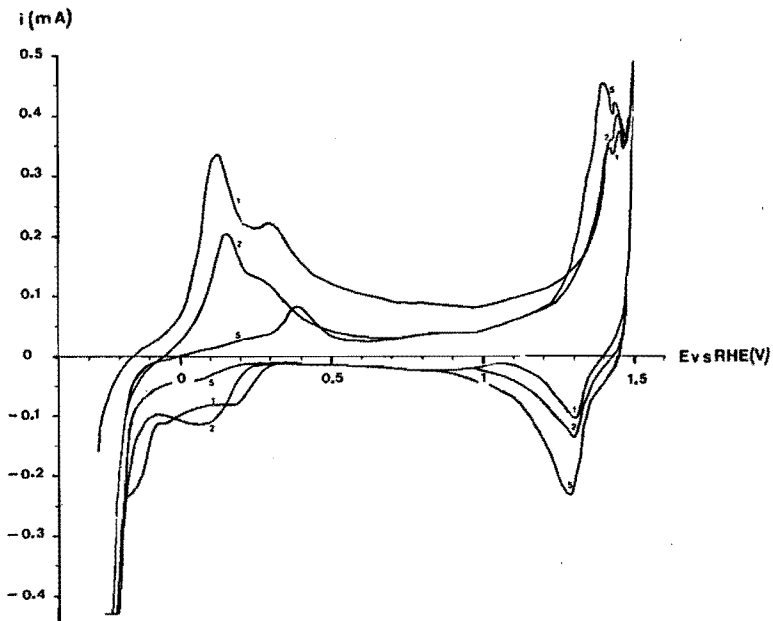


Fig. 7.2. Initial cyclic voltammetric behaviour of a  $\text{Ni}_1\text{Co}_1$ -alloy in  $\text{O}_2$ -free  $5$  M  $\text{KOH}$ ,  $25^\circ\text{C}$  at a scan rate of  $20$   $\text{mV s}^{-1}$ .

From the comparison of the voltammetric behaviour of the nickel-cobalt alloys and of the individual metals, it follows that the initial anodic doublet peak of the alloys, observed below 0.5 V can be correlated to the  $M^{0/2+}$  conversion (M is either Ni or Co): the peak at about 0.11 V can be due to the oxidation of absorbed hydrogen [4,9] or to  $Co(OH)_2$  formation [6-8], whereas the peak at about 0.30 V can be correlated with the  $Co^{2+}$  oxide formation [5-7] or the  $Ni^{2+}$  hydroxide or oxide formation [4-5, 10-12]. The stronger presence of the peak at 0.11 V on  $Ni_1Co_1$  versus  $Ni_1Co_2$  indicates that it is mainly due to nickel oxidation. The appearance of the anodic peak at about 1.1 V, more distinctly noticed in the  $Ni_1Co_2$ -alloy, is also observed on pure Co [6,7], but not on Ni [4,5,9], therefore it can be attributed to a  $Co^{2+/3+}$  conversion.

When the cathodic switching potential for  $Ni_1Co_2$  is also taken -0.1 V, as for  $Ni_1Co_2$  in figure 7.1, the anodic and cathodic peak profile, close to oxygen evolution, show a similar profile as obtained for  $Ni_1Co_2$ , figure 7.1. The shape and position of the sharp anodic peak profile and related reduction on both alloys, strongly resembles to the  $Ni^{2+/3+}$  oxidation, although other higher oxidation state transitions of Ni and Co cannot be excluded. The cathodic peak at about 0.15 V is characteristic for a reduction to Co metal [6-8]. From the voltammograms of Figure 7.1 and 7.2, it can be concluded that initially the nickel cobalt-alloys electrochemically behave as the summation of the two individual metals.

#### Influence of preanodization.

Since the oxygen evolution reaction takes place at an oxide layer, the  $Ni_1Co_2$ -alloy was previously subjected to prolonged anodization. Cyclic voltammetry is used to examine the electrochemical formed oxide layer.

Figure 7.3 shows the voltammogram of an aged  $Ni_1Co_2$  alloy, which was previously subjected to oxygen evolution at 1.8 V for 18 h, as a function of the potential scan rate,  $v$ , in the E-range 0.9 to 1.5 V. From this figure, it can be seen that after severe oxygen evolution only one large anodic peak remains at about 1.40 V. This was typical for both nickel-cobalt alloys. The position of the anodic peak appears

not to depend on the potential scan rate  $v$ , which points to a surface redox reaction. The change at 1.8 V was also investigated as a function of time, and it appeared that after oxygen evolution for 1 h at 1.8 V, no further change in peak profile or -current took place. Furthermore, the ageing was also studied as a function of the potential in the oxygen evolution range of 1.50 to 1.80 V, and in time the same stable voltammogram was obtained.

In order to study the effect of the oxide layer on the electrocatalytic activity for oxygen evolution, the  $E$ -log  $i$  curve is determined on a preanodized  $\text{Ni}_1\text{Co}_2$ -alloy (curve a), as shown in figure 7.4, and compared with the Tafel line taken immediately at a freshly polished  $\text{Ni}_1\text{Co}_2$ -alloy (curve b). It appears that an increase in the overpotential with ageing takes place, and a shift of the Tafel slope of about 50 mV for a freshly polished  $\text{Ni}_1\text{Co}_2$ -alloy to a slope of 59 mV after preanodization did not alter the Tafel line, nor the voltammetric behaviour.

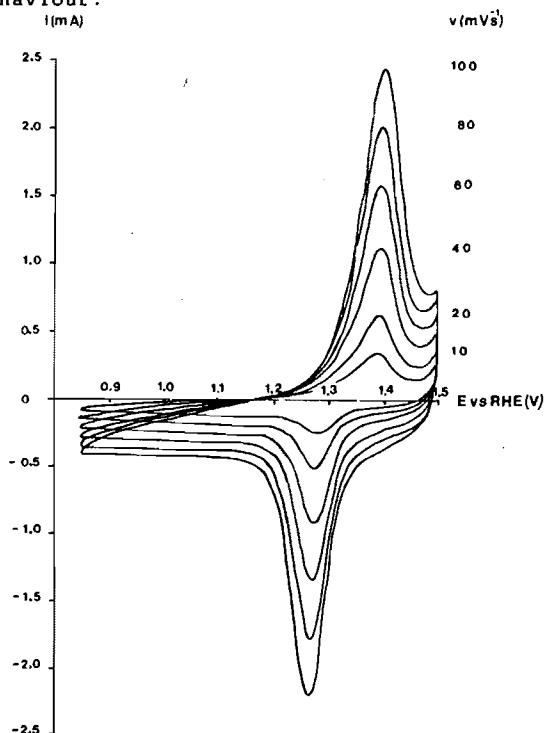


Fig. 7.3. Cyclic voltammetric behaviour of a  $\text{Ni}_1\text{Co}_2$ -alloy, previously subjected to oxygen evolution at 1.8 V for 18 h, as a function of the potential scan rate  $v$  in 5 M KOH, 25°C.

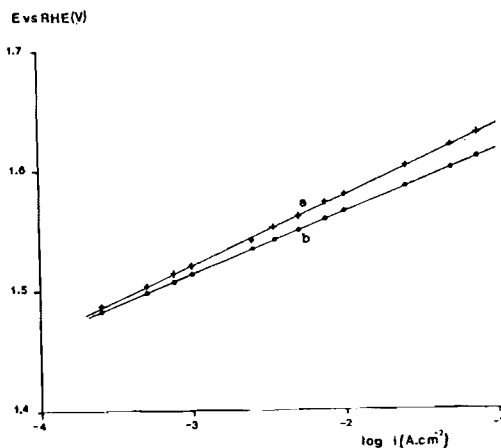


Fig. 7.4. Tafel lines on a  $\text{Ni}_1\text{Co}_2$ -alloy in 5 M KOH, 25°C as a function of the pretreatment.  
 curve a = preanodized  $\text{Ni}_1\text{Co}_2$ -alloy at 1.8 V for 1 h;  
 curve b = measurements taken immediately at a freshly polished  $\text{Ni}_1\text{Co}_2$ -alloy.

#### The influence of cycling.

The cyclic voltammetric behaviour of the nickel-cobalt alloy changes with continuous potentiodynamic cycling.

Figure 7.5 shows the change in the response of the aged  $\text{Ni}_1\text{Co}_2$ -alloy (see figure 7.3) during the first 2 h cycling at a potential scan rate of  $20 \text{ mV s}^{-1}$  in the E-range  $-0.2$  to  $1.475 \text{ V}$ . The anodic switching potential of  $1.5 \text{ V}$  was chosen in order to minimize the oxygen evolution reaction. Previously, it was noticed that with continuous cycling, and with decreasing the cathodic switching potential to at least  $0.45 \text{ V}$ , a new anodic peak at about  $1.28 \text{ V}$  is clearly observed as a shoulder on the cathodic side of the large anodic peak, just before oxygen evolution. At first, the anodic peak profile with shoulder increases with cycling, and evolves to a distinct double peak profile, as seen in figure 7.5. At the same time, both the peak potentials shift to more cathodic values. Cathodically, the related double peak profile is less distinct, and consists of a sharp peak at  $1.27 \text{ V}$  with a shoulder at about  $1.15 \text{ V}$ , which also increases and shifts in



cathodic direction, with cycling. Furthermore, a weak broad reduction peak is observed at about 0.55 V. The total voltammetric charge increases continuously with cycling, which indicates that the surface area increases. With further scanning, the doublet peak profile, close to the oxygen evolution potential range, evolves into a single asymmetrical peak, as shown in figure 7.6. This  $\text{Ni}_1\text{Co}_2$ -alloy was cycled for 22 h in the E-range  $-0.05$  to  $1.475$  V at a scan rate of  $20 \text{ mV s}^{-1}$ . The increase in the peak current, as measured for the voltammetric charge, increases linearly with the cycling time.

It can be concluded that prolonged cycling alters the potentiodynamic behaviour, and that a low cathodic switching potential is essential. Curve a shows the Tafel line of a  $\text{Ni}_1\text{Co}_2$ -electrode, on which the measurements were taken immediately after polishing, with a slope of  $48 \text{ mV}$ . After prolonged cycling (22 h), the Tafel line shifts to lower  $\eta$ , and the slope decreases to  $42 \text{ mV}$ , curve b. However, after ageing in the oxygen evolution range at  $1.8 \text{ V}$  for  $10 \text{ h}$ , the Tafel line shifts to higher overpotentials, and the slope increases to  $60 \text{ mV}$  (curve c). (Fig.7.7)

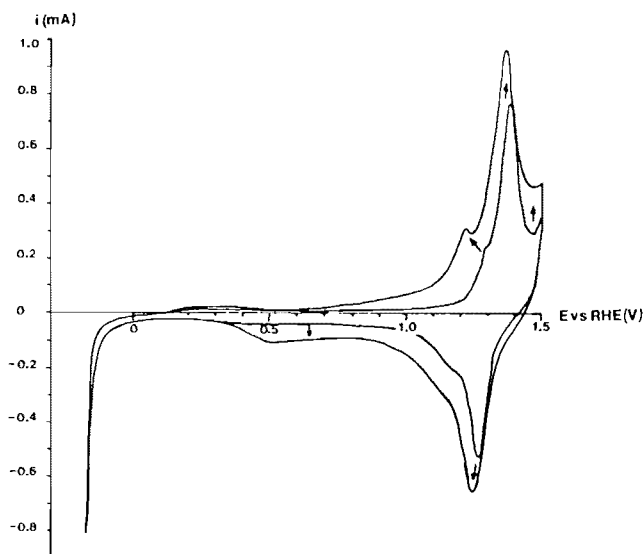


Fig. 7.5. Change in the voltammetric response of the aged  $\text{Ni}_1\text{Co}_2$ -alloy during the first 2 h cycling in the E-range  $-0.02$  to  $1.50$  V at a scan rate of  $20 \text{ mV s}^{-1}$

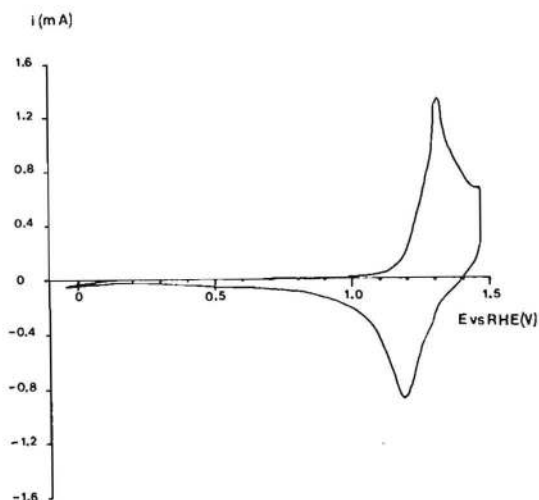


Fig. 7.6. Cyclic voltammogram of the  $\text{Ni}_1\text{Co}_2$ -alloy after 22 h cycling in the E-range  $-0.050$  V to  $1.475$  V at a scan rate of  $20 \text{ mV s}^{-1}$  in  $5 \text{ M KOH}$ ,  $25^\circ\text{C}$ .

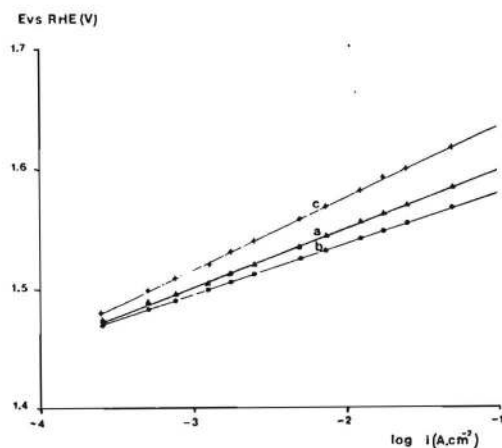


Fig. 7.7. Tafel lines on a  $\text{Ni}_1\text{Co}_2$ -alloy in  $5 \text{ M KOH}$ ,  $25^\circ\text{C}$  as a function of the pretreatment.  
 curve a = measurements taken immediately at a freshly polished  $\text{Ni}_1\text{Co}_2$ -alloy; curve b = after prolonged cycling in the E-range.

Summarizing, it is shown that the electrocatalytic behaviour of the  $\text{Ni}_1\text{Co}_2$ -alloy changes with the pretreatment. At a freshly polished  $\text{Ni}_1\text{Co}_2$ -alloy, a Tafel slope of about 40 mV and a decrease of the overpotential is found after potentiodynamic cycling, whereas after preanodization a slope of 60 mV and an increase in overpotential is observed. Furthermore, it appears that the Tafel line with a slope of 40 mV changes to a Tafel line with a slope of 60 mV after prolonged oxygen evolution. When the electrode is thereafter continuously cycled for about 20 h, the slope of 40 mV is again obtained. The difference in catalytic performance must be due to the different nature of the electrochemically formed oxides on the  $\text{Ni}_1\text{Co}_2$ -alloy. This can be explained either by assuming that spinel-like oxides are formed on the  $\text{Ni}_1\text{Co}_2$ -alloy or that, depending on the pretreatment, the alloy electrode behaves predominantly as a nickel or as a cobalt electrode. A slope of 40 mV is also observed for the  $\text{NiCo}_2\text{O}_4$  oxide electrode, as reported in chapter 4, whereas a slope of 60 mV is found for a  $\text{Co}_3\text{O}_4$  oxide electrode [13], both spinel oxides prepared by thermal decomposition. Therefore, it seems likely that with the multi-cycling procedure an oxide layer with the spinel structure of  $\text{NiCo}_2\text{O}_4$  is formed, while prolonged oxygen evolution leads to the formation of a  $\text{Co}_3\text{O}_4$  spinel type oxide. Likewise, the change in the voltammogram with cycling resembles that of the  $\text{NiCo}_2\text{O}_4$  electrode, as seen in section 5.4, where the voltammogram of a freshly prepared electrode shows two anodic peaks, prior to oxygen evolution, and changes to a single peak profile. However, the voltammogram of a preanodized  $\text{Ni}_1\text{Co}_2$ -alloy as given in figure 7.3 shows also some resemblance with the single peak profile of an aged  $\text{NiCo}_2\text{O}_4$  oxide electrode. It must be realized that in case of thermally prepared oxides, the spinel is already present, whereas on the  $\text{Ni}_1\text{Co}_2$ -alloy it still must be formed.

However, the behaviour of a cycled  $\text{Ni}_1\text{Co}_2$ -alloy can also be compared with that of a Ni electrode [9], which also shows a 40 mV slope; even so the preanodized  $\text{Ni}_1\text{Co}_2$ -alloy with that of a Co electrode [7], which exhibits a 60 mV slope. Then it must be assumed that cycling of a freshly polished  $\text{Ni}_1\text{Co}_2$ -alloy with a sufficient low cathodic switching potential should give rise mainly to the formation of a  $\text{Ni}(\text{OH})_2$  layer, and that Co disappears selectively by dis-

solution from the surface. The dissolution of  $\text{Co(OH)}_2$ , formed on Co in alkaline solution during cycling up to a potential of 1.0 V, has been reported by Behl et al. [6].

Furthermore, it seems that after subjecting a freshly polished  $\text{Ni}_1\text{Co}_2$ -alloy to prolonged oxygen evolution, the alloy behaves like a Co electrode. Bagotzky et al. [14] reported that, subjecting a cobalt electrode to anodic potentials  $\geq 1.45$  V, this results in the formation of a pure  $\text{Co}_3\text{O}_4$  spinel oxide layer. Behl et al. [6] also reported that about 1.0 V a new outside film, i.e. a  $\text{Co}_3\text{O}_4$  spinel is formed. They suggested that this film more or less acts as a filter, which blocks the dissolution of  $\text{Co(OH)}_2$  and yet allows the transport of  $\text{OH}^-$  ions for the growth of the  $\text{Co(OH)}_2$  film underneath and its subsequent oxidation. Thus, with prolonged oxidation at high anodic potentials (where no Co dissolution can take place), it can be assumed that the  $\text{Ni}_1\text{Co}_2$ -alloy behaves as a Co electrode. When such a preanodized  $\text{Ni}_1\text{Co}_2$ -electrode is again continuously cycled, Co dissolution will take place again, and consequently the Ni behaviour is again obtained (the behaviour of the  $\text{Ni}_1\text{Co}_2$ -alloy shifts to a Ni one).

However, it is not clear why a cycled  $\text{Ni}_1\text{Co}_2$ -alloy electrode, which shows a Ni behaviour, is not stable to prolonged oxygen evolution and changes to a Co behaviour.

Therefore, it seems likely that a metastable  $\text{NiCo}_2\text{O}_4$  spinel type oxide is formed with cycling, which is not stable to prolonged oxidation and subsequently decomposes, whereafter the  $\text{Ni}_1\text{Co}_2$ -alloy behaves as a  $\text{Co}_3\text{O}_4$  electrode. If this electrode is cycled to cathodic return potentials  $\leq 0.45$  V, the  $\text{NiCo}_2\text{O}_4$  spinel oxide layer is re-established.

Whether or not a  $\text{NiCo}_2\text{O}_4$  spinel-like oxide is formed on the cycled electrode, it is less suitable for water electrolysis than thermally prepared  $\text{NiCo}_2\text{O}_4$  oxide electrodes, because the initial catalytic activity decreases with prolonged oxygen evolution: the Tafel slope shifts from 40 to 60 mV and an increase in  $\eta$  takes place.

### 7.3.2. Ellipsometry.

Because electrochemical measurements and ellipsometry can be applied

simultaneously, it is expected to get more information about the difference in the oxide layers formed on  $\text{Ni}_1\text{Co}_2$ -alloy.

#### Substrate.

In order to establish the value of the refractive index of the  $\text{Ni}_1\text{Co}_2$ -substrate different pretreatments were carried out:

- 1° Polishing with alumina down to finally  $0.3 \mu\text{m}$ .
- 2° Polishing as in 1°, followed by reduction under vigorous hydrogen evolution.
- 3° Polishing as in 1°, then dipping into  $1 \text{ M H}_2\text{SO}_4$  under vigorous hydrogen evolution, rinsing with distilled  $\text{H}_2\text{O}$  and immediately transferred thereafter to the cell.

In the cell the potential was held at  $-0.075 \text{ V vs. RHE}$ , where no hydrogen evolution was observed. Table 7.1 shows the ellipsometric parameters  $\Delta$  and  $\psi$ , and refractive index ( $n-ik$ ) taken at this potential for the pretreatments 1°, 3° and 4°.

With method 2° an anodic current was observed, when the potential was brought to  $-0.075 \text{ V}$  after the vigorous hydrogen evolution, which points to anodic film formation. Method 3° gives poor reproducible results, although the lower value of the optical parameter  $\Delta$  seems to point to a cleaner surface. Pretreatment 4° gave rise to an extra, inexplicable peak, both in the voltammogram as in the optical curve. Therefore, the ellipsometric readings taken at the potential  $-0.075 \text{ V}$  after pretreatment 1° were assumed to represent the bare substrate of the  $\text{Ni}_1\text{Co}_2$  alloy electrode. The refractive index of the  $\text{Ni}_1\text{Co}_2$ -alloy, as calculated from  $\Delta$  and  $\psi$  values at  $E = -0.075 \text{ V}$ , appears to resemble more that of cobalt than that of nickel metal, as follows from a comparison with the literature data, compiled in table 7.2.

Table 7.1: The ellipsometric parameters  $\Delta$  and  $\psi$  and refractive index ( $n-ik$ ) for the different pretreatments ( $\lambda = 5461 \text{ \AA}$ ).

Pretreatment (see text)	$\Delta$	$\psi$	$n$	$k$
1°	$115.5 \pm 0.5$	$32 \pm 0.5$	$2.6 \pm 0.1$	$4.5 \pm 0.1$
3°	$110.5 \pm 2.5$	$32 \pm 0.5$	$2.3 \pm 0.2$	$4.2 \pm 0.2$
4°	$115.5 \pm 0.5$	$33 \pm 0.5$	$2.4 \pm 0.1$	$4.7 \pm 0.1$

Table 7.2: Refractive index ( $n-ik$ ) for nickel and cobalt ( $\lambda = 5461 \text{ \AA}$ )

Species	n	k	medium	Ref
Ni	1.68	3.63	Phosphate buffer	14
Ni	1.73	3.47	NaOH	11
Ni	1.889	3.449	KOH	4
Co	2.83	3.86	Borate buffer	12
Co	2.39	3.95	Borate buffer	13
$\text{Ni}_1\text{Co}_2$	2.6	4.5	KOH	this work

First cycle.

Firstly, the optical behaviour of a  $\text{Ni}_1\text{Co}_2$ -alloy during the first applied potential scan from  $-0.075$  to  $1.425$  V is investigated. The limit potentials were chosen in order to minimize the influence of the hydrogen or oxygen evolution. Figure 7.8 shows the changes in  $\Delta$  and  $\psi$ , and the corresponding cyclic voltammogram (first cycle). The results can be divided into four regions, as indicated in the figure with A, B, C and D. With increasing anodic potential, initially  $\Delta$  and  $\psi$  remain about constant. At about  $0.25$  V,  $\Delta$  begins to decrease while  $\psi$  increases (part B), and beyond about  $1.05$  V,  $\Delta$  decreases fast and  $\psi$  increases further (part C). Finally in part D,  $\psi$  starts to decrease and  $\Delta$  decreases faster. These changes in  $\Delta$  and  $\psi$  correlate with the appearance of different oxidation peaks in the corresponding voltammogram.

The results of figure 7.8 are replotted in figure 7.9 in a  $\Delta$ - $\psi$  graph. With increasing anodic potential, up to about  $1.25$  V, the change of  $\Delta$  and  $\psi$  is such that a linear  $\Delta$ - $\psi$  relation is obtained, i.e. over part B and C. This implies that in the potential range up to  $1.25$  V, an oxide layer is formed, which grows with a constant refraction index  $N$ . At the maximum in the  $\Delta$ - $\psi$  curve, the optical properties change: the decrease in  $\psi$  coincides with the onset of a further oxidation process.

From the ellipsometric data and curve fitting using the McCrackin program [15], it appears that in part a of figure 7.9 (which corresponds to part B and C of figure 7.8), one film is formed. In the

figure, several curve fittings (dashed lines) are presented for different  $n$ - and  $k$ -values; the best fit corresponds to a layer with a refractive index  $N = 2.3 - 0.1 i$ . At 1.25 V a thickness of 34 Å (film 1) is reached. The low value of the imaginary part of the refractive index,  $k$ , points to a poor conductivity.

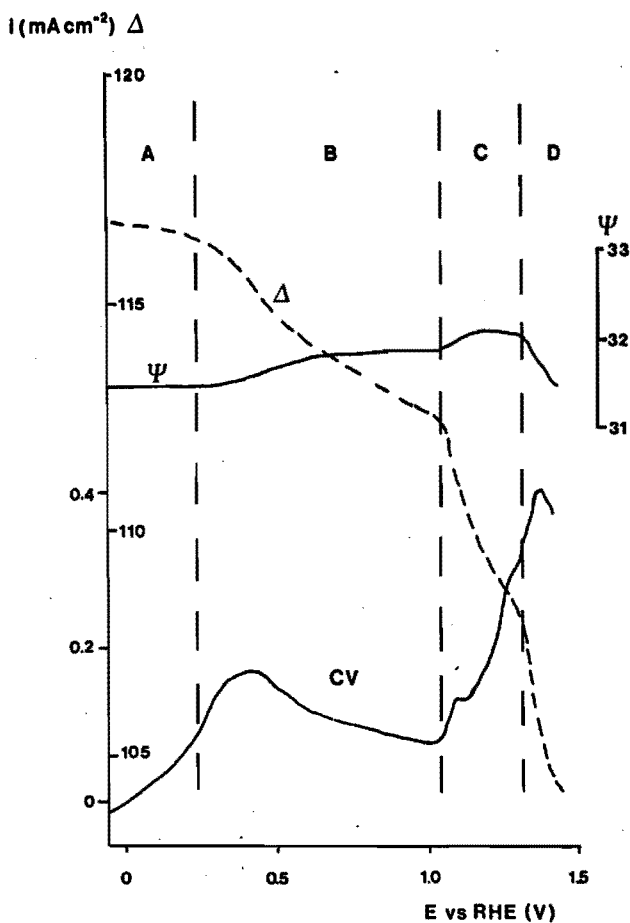


Fig. 7.8. Plot of the changes in  $\Delta$  and  $\psi$  of a  $\text{Ni}_1\text{Co}_2$ -alloy during the first potential sweep in the E-range  $-0.075$  V to 1.425 V in 5 M KOH, 25°C; scan rate  $20 \text{ mV s}^{-1}$ . CV = corresponding cyclic voltammogram.

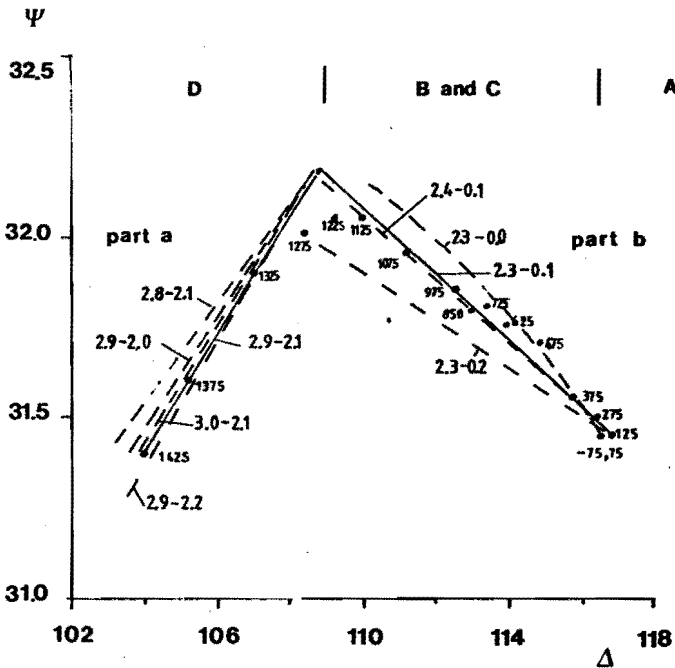


Fig. 7.9. Graph of  $\Psi$  versus  $\Delta$  for the results of figure 7.8, numbers along the curve refer to potential values. Solid and dashed curves: fitting curves.

Beyond the potential of 1.25 V the optical properties change, as seen in figure 7.9. The experimental results in part b (which corresponds to part D of figure 7.8) were fitted according to several models:

1° Conversion of film 1 ( $N = 2.3 - 0.1 i$ ) to another film, which starts either

- a/ at the film 1 - electrolyte interface
- b/ or at the substrate - film 1 interface.

2° Formation of a new film, either

- a/ on top of film 1
- b/ or on the substrate.

By curve fitting of the ellipsometric data, it appears that at higher potentials ( $> 1.25$  V) a conductive oxide (high  $k$ -value) is formed on top of the first layer. The figure presents some curve fittings for different  $n$ - and  $k$ -values (dashed lines), and the best fit (solid curve) corresponds to a layer with a refraction index  $N = 2.9 - 2.1 i$ .



This layer reaches a final thickness of  $24 \text{ \AA}$  at  $E = 1.425 \text{ V}$ . The calculated perpendicular  $R_s$  and parallel  $R_p$  values are in agreement with the measured one at  $1.425 \text{ V}$ . Summarizing, a two layer film model can be proposed with refraction indices and thicknesses, as schematic presented in figure 7.10.

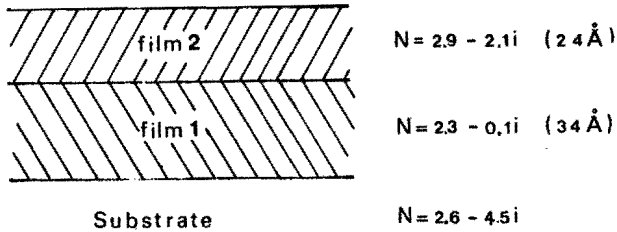


Fig. 7.10. Schematic representation of the two-layer film model.

#### Influence of cycling.

Figure 7.11 shows the changes of  $\Delta$  and  $\psi$  in a  $\Delta$ - $\psi$  plot, when the  $\text{Ni}_1\text{Co}_2$ -alloy is continuously cycled for 80 cycles (about 3.5 h) in the E-range  $-0.075 \text{ V}$  to  $1.425 \text{ V}$  at a scan rate of  $20 \text{ mV s}^{-1}$ . The first cycle is presented for the complete anodic potential range (part I). Thereafter, the values of  $\Delta$  and  $\psi$  are given at a potential of  $1.425 \text{ V}$  during successively cycling (part II), indicated with the symbol [•].

The increase in  $\psi$  in part II with cycling, points to a continuous growth of an oxide layer. It is certainly not the growth of film 2. The best fitting [15] of the experimental curve is obtained with the assumption that the first layer, i.e. film 1 (with  $N = 2.3 - 0.1 i$ ), increases in thickness whereas the upper layer, i.e. film 2 (with  $N = 2.9 - 2.1 i$ ) remains constant ( $d = 24 \text{ \AA}$ ). The solid curve in part II shows the calculated increase in thickness  $d$  of film 1, up to  $175 \text{ \AA}$ , which corresponds to 80 cycles. The accuracy of the fitting is demonstrated by the effect of the change in the value of the real part of

the refraction index,  $n$ , from 2.2 to 2.4, and of the imaginary part,  $k$ , from 0.0 to 0.2, for  $d = 100 \text{ \AA}$ , indicated in figure 7.11 with the symbol [\*]. It appears that the value of  $N = 2.3 - 0.1 i$  gives the best fit with the experimental results up to  $175 \text{ \AA}$ .

Moreover, a further confirmation is given by the measured  $R_p$  and  $R_s$  values at these points ( $d = 100 \text{ \AA}$ ), which are in agreement with the experimental ones.

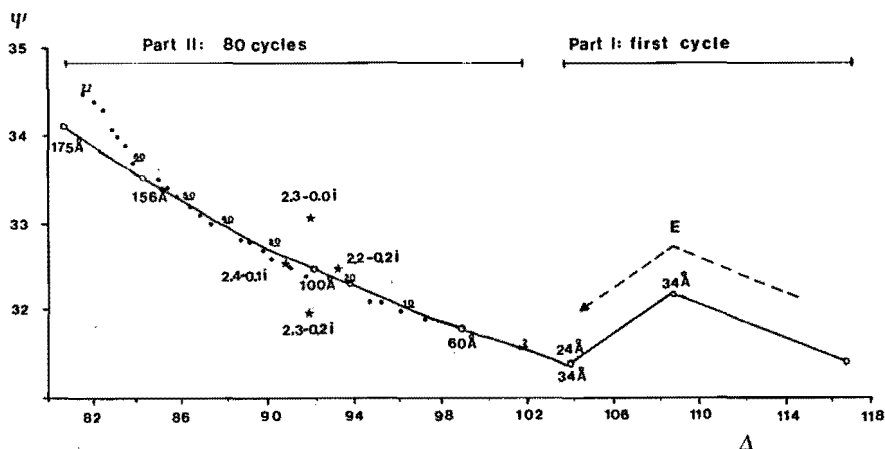


Fig. 7.11. Plot of the changes in  $\Delta$  and  $\psi$  of a  $\text{Ni}_1\text{Co}_2$ -alloy continuously cycled in the E-range  $-0.075 \text{ V}$  to  $1.425 \text{ V}$  at a scan rate of  $20 \text{ mV s}^{-1}$ .

Part I : first cycle for the complete anodic potential range.

Part II: with cycling, measured at  $E = 1.425 \text{ V}$  [\*]; solid line = fitting curve for the growth of film 1 with  $N = 2.3 - 0.1 i$ ; calculated values of  $\Delta$  and  $\psi$  for different refraction indices at a thickness of  $100 \text{ \AA}$  [\*]; underlined numbers along the curve refer to cycle numbers, the other to thicknesses [o].

#### Influence of preanodization.

The changes in  $\Delta$  and  $\psi$  as function of the polarization time at  $1.8 \text{ V}$  for  $\text{Ni}_1\text{Co}_2$ -alloy are shown in figure 7.12. The first cycle

(part I) is again completely presented for the anodic potential range. Thereafter, the changes in the ellipsometric parameters  $\Delta$  and  $\psi$  are measured at a potential of 1.425 V (no disturbance by oxygen evolution) with intervals of 30 minutes oxygen evolution at 1.8 V (part II).

It appears that there is virtually no further change in the optical parameters  $\Delta$  and  $\psi$  after 2 h preanodization. The solid curve in part II shows the best fit with the assumption of the two-layer film model with a growing underlayer (with  $N = 2.3 - 0.1 i$ ), whereas the upperlayer (with  $N = 2.9 - 2.1 i$ ) remains constant in thickness, i.e.  $d = 24 \text{ \AA}$ .

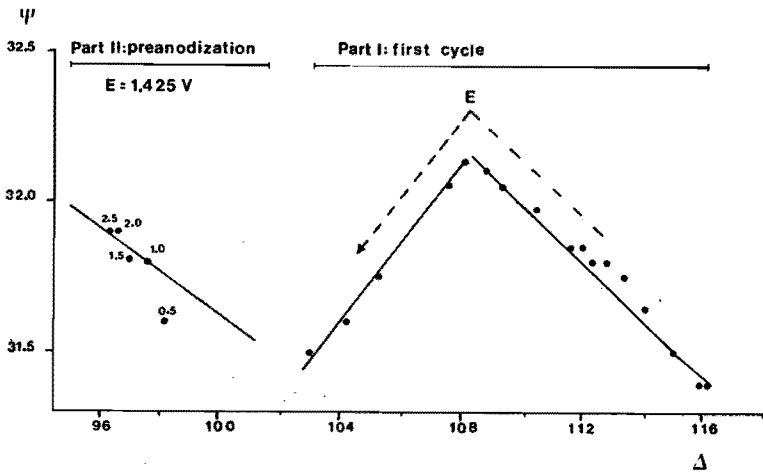


Fig. 7.12. Plot of the changes in  $\Delta$  and  $\psi$  of a  $\text{Ni}_1\text{Co}_2$ -alloy preanodized at 1.8 V.

Part I : the first cycle for the complete anodic potential range.

Part II: after preanodization, measured at  $E = 1.425 \text{ V}$ , numbers along the curve refer to the polarization time in hours.

The calculated thickness of this film 1 is plotted against the polarization time in figure 7.13. It clearly shows that the underlayer grows to a limit of about  $75 \text{ \AA}$  thickness, which is already reached after about 2 h preanodization. This is in contrast with cycling where this underlayer continuously grows.

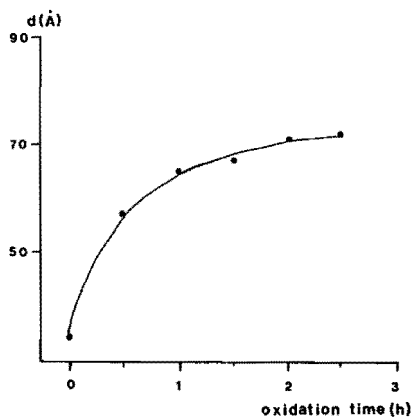


Fig. 7.13. Plot of the calculated thickness of film 1 with  $N = 2.3 - 0.1i$  against the polarization time.

Table 7.3: Refraction index ( $n-ik$ ) for nickel and cobalt compounds ( $\lambda = 5461 \text{ \AA}$ )

Species	$n$	$k$	medium	Ref.
NiO	2.23			[18]
NiO	1.52	0	KOH	[ 5]
$\alpha$ -Ni(OH) <sub>2</sub>	1.41	0	Ni(NO <sub>3</sub> ) <sub>2</sub>	[16]
$\beta$ -Ni(OH) <sub>2</sub>	1.46	0	Ni(NO <sub>3</sub> ) <sub>2</sub> , KOH	[16]
$\gamma$ -NiOOH	1.54	0.39	KOH	[16]
CoO	2.3	0.1	NaOH	[17]
Co(OH) <sub>2</sub>	1.4	0	NaOH	[19]
Co <sub>3</sub> O <sub>4</sub>	3.2	0.5	NaOH	[19]
Co <sub>2</sub> O <sub>3</sub>	3.2	0.95	NaOH	[19]

The refraction index of NiCo<sub>2</sub>O<sub>4</sub> spinel is not known. In table 7.3 some literature data of nickel and cobalt hydroxides and oxides are

compiled. A comparison of the refraction index of the two layer film with the published data of table 7.3 might suggest that film 1, with  $N = 2.3 - 0.1 i$ , is probably not a Ni or Co hydroxide, but resembles that of CoO, whereas the refraction index of film 2 with  $N = 2.9 - 2.1 i$  shows some resemblance with that of  $\text{Co}_3\text{O}_4$  or  $\text{Co}_2\text{O}_3$ . However, one must bear in mind that this can only give an indication. If indeed a  $\text{NiCo}_2\text{O}_4$  spinel type oxide is formed indeed on the  $\text{Ni}_1\text{Co}_2$ -alloy, a large  $k$ -value (as observed for film 2) is expected, since the conductivity of  $\text{NiCo}_2\text{O}_4$  is higher than that of  $\text{Co}_3\text{O}_4$ : a resistivity was reported of approximately  $10 \Omega\text{cm}$  for  $\text{NiCo}_2\text{O}_4$  and of  $10^4 \Omega\text{cm}$  for  $\text{Co}_3\text{O}_4$  [20].

#### Transient measurements.

The cyclic voltammogram (figure 7.8) shows that during the first scan in part B-C two oxidation steps are observed. However, it is not clear whether this is an oxidation of two different species or of a further oxidation of one species. From figure 7.9, it appears that part B and C are optically identical.

It was tried to distinguish between these two oxidation steps by using a transient technique: a potential step was applied at  $-0.075 \text{ V}$  to a potential in the B-C range, and the resulting changes in the ellipsometric parameters  $\Delta$  and  $\psi$  are recorded as a function of time  $t$ . Figure 7.14 shows the changes in  $\Delta$  and  $\psi$  after a potential pulse to  $0.425 \text{ V}$  (curve a),  $0.725 \text{ V}$  (curve b) and to  $1.025 \text{ V}$  (curve c), respectively, and the time is given along the curves. The changes in  $\Delta$  and  $\psi$  are given with respect to their initial value at  $t = 0$ . If there is a difference in the rate of the growth between the different layers (part B and C), this might be noticeable in the  $\Delta$ - $\psi$  curve.

In figure 7.14 several calculated curves are presented for different  $n$ - and  $k$ -values, with a thickness which increases with time, up to  $50 \text{ \AA}$ . It appears that curve c (potential step to  $1.025 \text{ V}$ ) can be fitted by a single layer with a refraction index in the range  $2.3 - 0.1 i$  to  $2.6 - 0.0 i$ , which is in reasonable agreement with the earlier findings for the first layer. The best fitting of the experimental curve b is obtained with a layer with a refraction index in the range

1.4 - 0.0 i to 1.8 - 0.0 i. A comparison of this refraction index (range ) with the published data of table 7.3 might suggest that this film (potential step up to 0.725 V) is probable a Ni or Co hydroxide. No fitting curve was found for curve a in the investigated range of refraction indices.

Thus, it can be concluded that in the B-C range indeed more than one oxide is formed.

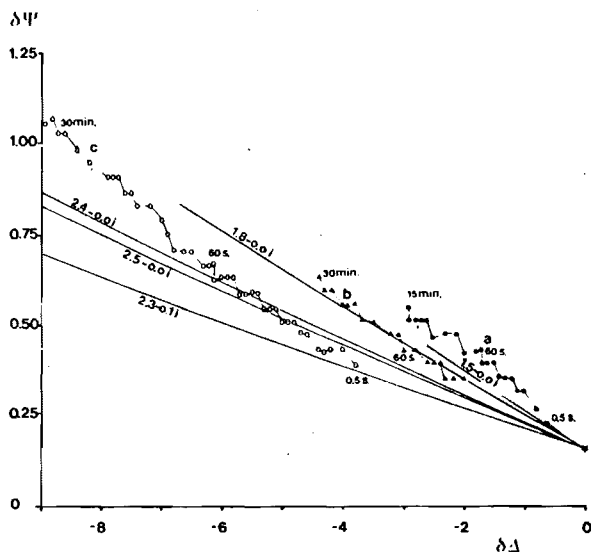


Fig. 7.14. Plot of the changes in  $\Delta$  and  $\psi$  after a potential step from  $-0.075$  V to  $0.425$  V (curve a), to  $0.725$  V (curve b) and to  $1.025$  V (curve c), respectively, and the time is given along the curves. The changes in  $\Delta$  and  $\psi$  are given with respect to their initial value at  $t = 0$ , represented as  $\delta\Delta$  and  $\delta\psi$ .

Finally, it is attempted to correlate the electrochemical (section 7.3.1) and ellipsometric results (section 7.3.2). The two different pretreatments lead optically to the same two-layer film model: only it appeared that, with cycling, film 1 continuously grows, whereas with preanodization a maximum thickness of about  $75 \text{ \AA}$  is reached.

Firstly, one can try to correlate the ellipsometric two-layer film with the above mentioned assumption that spinel-like oxides are formed on the  $\text{Ni}_1\text{Co}_2$ -alloy. It is then assumed that film 2 with  $N = 2.9 - 2.1 i$  is a spinel type oxide: it is unlikely that film 1 is a spinel-like oxide because of its low  $k$ -value. However, in order to explain the difference in kinetic behaviour of a cycled ( $\text{NiCo}_2\text{O}_4$ -like behaviour) or an oxidized  $\text{Ni}_1\text{Co}_2$ -alloy ( $\text{Co}_3\text{O}_4$ -like behaviour), it is necessary to introduce two forms of film 2, which are optically identical. It must be noticed that the ellipsometric measurements were taken at  $E = 1.425 \text{ V}$ , prior to oxygen evolution, whereas the kinetic analysis is carried out at potentials  $\geq 1.45 \text{ V}$ , i.e. in the oxygen evolution potential range. A schematic representation is given in figure 7.15, where film 2', formed by cycling, is a  $\text{NiCo}_2\text{O}_4$  spinel type oxide and film 2'' is a  $\text{Co}_3\text{O}_4$  spinel type oxide formed by oxidation. A cycled  $\text{Ni}_1\text{Co}_2$ -alloy, film 2', converts to film 2'' by oxidation. When it is thereafter continuously cycled, it is again converted to film 2'. In both cases, oxygen evolution takes place at the outer film layer, i.e. film 2' or 2''.

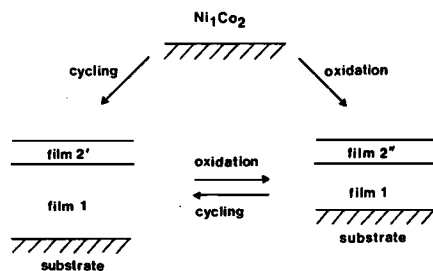


Fig. 7.15. Schematic representation with assumption of the formation of spinel type oxides on the  $\text{Ni}_1\text{Co}_2$ -alloy.

The alternative explanation for the kinetic behaviour was that, depending on the pretreatment, the  $\text{Ni}_1\text{Co}_2$ -alloy behaves predominantly as a Ni or as a Co electrode. The introduction of two forms of film 2, which are optically identical ( $N = 2.9 - 2.1 i$ ), is again required to obtain a correlation between the electrochemical and ellipsometric characterization (figure 7.16). Here, film 2' exhibits an island

structure which permits the growth of film 1 with cycling; cobalt disappears selectively by dissolution out of film 1.

Consequently, film 1 predominantly exists of nickel-oxide and oxygen evolution is supposed to take place at this film. On the other hand, oxidation of the  $\text{Ni}_1\text{Co}_2$ -alloy gives rise to the formation of a compact film 2", as earlier mentioned blocking the dissolution. This film prevents the continuous growth of film 1; the evolution of oxygen takes place at film 2" which shows mainly a cobalt behaviour. Film 2" is again converted to film 2' by cycling to low cathodic potentials. However, on basis of these results, it is difficult to discriminate between these two models.

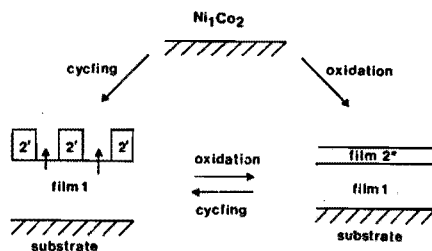


Fig. 7.16. Schematic representation with the assumption that the  $\text{Ni}_1\text{Co}_2$ -alloy behaves predominantly as a Ni or as a Co electrode.



## 7.4. Literature

- [1] G. Grube and W. Gaupp, *Z. Elektrochem.* 45, 290 (1939).
- [2] M. Hansen, *Contribution of binary alloys*, 2nd edition, NY-Toronto, London (1958).
- [3] K.R. Willems, *An introduction to fuel cells*, Elsevier, Amsterdam, 58 (1966).
- [4] W. Visscher and E. Barendrecht, *Electrochim. Acta* 25, 651 (1980).
- [5] W. Visscher and E. Barendrecht, *Surface Sc.* 135, 436 (1983).
- [6] W.K. Behl and J.E. Toni, *J. Electroanal. Chem.* 31, 63 (1971).
- [7] L.D. Burke, M.E. Lyons and O.J. Murphy, *J. Electroanal. Chem.* 132, 247 (1982).
- [8] H. Gomez Meier, J.R. Vilehe and A.J. Arvia, *J. Electroanal. Chem.* 134, 251 (1982).
- [9] P.W.T. Lu and S. Srinivasan, *J. Electrochem. Soc.* 125, 265 (1978).
- [10] Ku Ling Ying, N.A. Shumilova and V.S. Bagotskii, *Sov. Electrochem.* 3, 460 (1967).
- [11] N.A. Shumilova and V.S. Bagotskii, *Electrochim. Acta* 18, 285 (1968).
- [12] W. Paik and Z. Szklarska-Smialowska, *Surface Sci.*, 96, 401 (1980).
- [13] C. Iwakura, A. Honjii and H. Tamura, *Electrochim. Acta* 26, 1319 (1981).
- [14] V.S. Bagotzky, N.A. Shumilova and E.I. Khrushcheva, *Electrochim. Acta* 21, 919 (1976).
- [15] F.L. McCrackin, *Natl. Bur. Std. (US) Tech. Note* 479 (1969).
- [16] W. Visscher and E. Barendrecht, *J. Electroanal. Chem.* 154, 69 (1983).
- [17] K. Kudo, N. Sato and T. Ohtsuka in R.P. Frankenthal and J. Kruger (Eds.), *Passivity of Metals*, The Electrochemical Society, Proceedings Series, Princeton, 918 (1978).
- [18] Landolt Börnstein, 6. Auflage, Teil 8 (Springer Berlin, 1962) p.2-198.
- [19] T. Ohtsuka and N. Sato, *J. Electroanal. Chem.* 147, 167 (1983).
- [20] W.J. King and A.C.C. Tseung, *Electrochim. Acta* 19, 485 (1974).

## 8. GENERAL CONCLUSIONS

In this chapter, a correlation of the different results of the preceding chapters is undertaken.

$\text{NiCo}_2\text{O}_4$  electrodes, prepared by thermal decomposition, are very active for oxygen evolution. It was found that the variation of the catalyst loading has virtually no influence on the anodic performance (chapter 3), nor on the magnitude of the voltammetric charge of freshly prepared  $\text{NiCo}_2\text{O}_4$  electrodes (chapter 5). The results of chapters 3 and 5 clearly indicate that, mainly the top surface layer of the  $\text{NiCo}_2\text{O}_4$  electrode is electrochemically active for the oxygen evolution, independent of the electrode structure.

The surface morphology, and composition of the  $\text{NiCo}_2\text{O}_4$  layer was found to be dependent on the heat treatment, particularly on the temperature  $T_F$  of the final heat treatment. The correlation between the increase in activity (chapter 3 and 4), and the increase in the cyclic voltammetric charge (chapter 5) with decreasing  $T_F$  indicates that these effects can be related to a change in the surface area. Therefore, the voltammetric charge of freshly prepared  $\text{NiCo}_2\text{O}_4$  electrodes can be taken as a measure for the surface concentration of the metal ions participating in the electrochemical processes. These results indicate their number to be 5% at maximum. An apparent electrochemical roughness factor of 500 to 2000, and an electrochemical surface area of 3 to  $10 \text{ m}^2 \text{ g}^{-1}$  can be calculated in the  $T_F$ -range where only the spinel phase exists. Similarly, the BET-surface areas of  $\text{NiCo}_2\text{O}_4$  powders show a tendency to increase with decreasing  $T_F$  (chapter 6).

However, the variation in the ratio of the voltammetric charge of the anodic oxidation peaks as a function of  $T_F$  implies that, the effect of the heat treatment is not only reflected in an increase of surface area. Both anodic voltammetric peak charges,  $Q_{a1}$  and  $Q_{a2}$ , increase with decreasing  $T_F$ , but also the ratio  $Q_{a2}$  vs.  $Q_{a1}$  increases. Therefore, it is conceivable that the difference in anodic performance is not only a result of the change in surface composition. The XPS measurements (chapter 6) revealed for lower  $T_F$  an increase of the Co

content, and a decrease of the Ni content in the  $\text{NiCo}_2\text{O}_4$  surface layer with respect to the theoretical  $\text{NiCo}_2\text{O}_4$  spinel composition. This confirms that the surface composition is indeed influenced by  $T_F$ , as earlier reported in chapters 3 and 5. From a correlation between the charge ratio, and the XPS analysis data, it is conceivable that the increase of the second peak,  $E_{a2}$ , compared to the first anodic peak,  $E_{a1}$ , with decreasing  $T_F$  is probably due to a higher Co content in the surface region. Thus, irrespective of the increase in surface area, the increase in anodic performance with lowering  $T_F$  must apparently be attributed to the increased Co concentration, supposed that Co is the active site. The duration time of the final heat treatment  $t_F$  gives no significant changes in activity (chapter 3), nor in the magnitude, nor in the ratio of the voltammetric charge (chapter 5) of the anodic peaks.

Summarizing, it can be concluded that the surface composition of the  $\text{NiCo}_2\text{O}_4$  spinel oxide is affected by the temperature  $T_F$ , but not by the duration time  $t_F$  of the thermal treatment.

The performance of a  $\text{NiCo}_2\text{O}_4$  electrode depends on the valence states of the ions in the surface region in the potential range, where the desired reaction takes place. The cyclic voltammogram of a fresh  $\text{NiCo}_2\text{O}_4$  electrode represents a surface layer with ions in higher valence states. Both anodic oxidation peaks in the voltammogram point to one-electron surface-redox reactions, and it was shown that the highest oxidation state up to 1.55 V, was 4+. Furthermore, it was found that the hydroxyl ion plays an important role in the electrochemical reactions prior to oxygen evolution (chapter 5).

On the basis of the cyclic voltammetric behaviour, three different models have been suggested for the conjugated electrochemical processes, before oxygen evolution takes place on the freshly prepared  $\text{NiCo}_2\text{O}_4$  electrode. From a correlation of the observed peak potentials with the standard potentials of the individual oxides, and the voltammetric behaviour of  $\text{Co}_3\text{O}_4$ , the assignment of the first transition  $E_{a1}$  to  $\text{Co}^{2+/3+}$  is justified, whereas the second anodic peak  $E_{a2}$  could be a  $\text{M}^{3+/4+}$  transition, where M is either Ni or Co. However, on the basis of the magnitude of the photoelectron binding energy, it was suggested that nickel in  $\text{NiCo}_2\text{O}_4$  is present as

divalent ion, and from the satellite structure, that Co is mainly present in the diamagnetic, low-spin  $\text{Co}^{3+}$ -state, and to a lesser extent as paramagnetic, divalent high-spin cobalt.

Therefore, the presence of  $\text{Co}^{2+}$ , from cyclic voltammetry, as well as  $\text{Ni}^{2+}$ , from XPS, has been demonstrated. Both are surface techniques, whereby the cyclic voltammetry gives information of the surface features as a function of the potential (whereas XPS of a  $\text{NiCo}_2\text{O}_4$  electrode is measured at its rest potential). It is most likely that the voltammetric response reflects the influence of the potential on the valence state of the metal cations already present.

Therefore, it is to be expected that also the  $\text{Ni}^{2+/3+}$  transition is manifest in the cyclic voltammogram. This must be in  $E_{a1}$  or  $E_{a2}$ , since no other oxidation peaks were observed. In chapter 5,  $E_{a1}$  was solely attributed to the  $\text{Co}^{2+/3+}$  transition, this could explain the difference between the peak potentials of the first transition ( $E_{a1}$ ) on  $\text{NiCo}_2\text{O}_4$ , i.e. at 1.20 V, and on  $\text{Co}_3\text{O}_4$ , i.e. at 1.15 V. In this context, it is conceivable that the first anodic peak on  $\text{NiCo}_2\text{O}_4$  reflects a  $\text{M}^{2+/3+}$  conversion, with  $\text{M} = \text{Ni}$  or  $\text{Co}$ . The other possibility is that the  $\text{Ni}^{2+/3+}$  transition is masked by processes occurring at  $E_{a2}$ . In chapter 5, a more complex nature of  $E_{a2}$  has already been discussed.

One of the major problems of the mixed oxide spinels is the cation distribution. The determination of the valencies, and the distribution of the cation among the tetrahedral and octahedral sites of the spinel structure, is tedious, particularly, if two different metals are present, each of which can adapt more than one valence state.

A number of different site and charge distributions for  $\text{NiCo}_2\text{O}_4$ , based on magnetization, X-ray- and neutron diffraction and scattering studies, have been proposed in the literature [1-7]. Since many 'ferromagnetic' spinels are collinear-spin, Néel ferrimagnets, the spontaneous magnetization at  $T = 0$  K can generally provide a good indication of the cation distribution, and valence states if a localized electron, crystal field model gives the appropriate description of the d-electron manifold. More correctly,  $\text{NiCo}_2\text{O}_4$  is a ferrimagnetic spinel [6]. Holgersson and Karlsson [1] were the first to report a 'ferromagnetic' cubic spinel phase in the system Ni-Co-O, and assigned to it the formula  $(\text{Ni},\text{Co})\text{O}(\text{Ni},\text{Co})_2\text{O}_3$ , to represent the

likely presence of two oxidation states for each cation. Lotgering [2] found a magnetization  $[M = (B-H)/4\pi]$  of approximately  $1.5 \mu_B$  per formula unit. Blasse [3], interpreting Lotgering's magnetization data, proposed a structural formula  $\text{Co}^{2+}[\text{Co}^{3+}\text{Ni}^{3+}]_4\text{O}_4^{2-}$ . However, the spin-only ferrimagnetic magnetization predicted from this model is  $2 \mu_B$  per formula unit, which is not in agreement with the experimental magnetization data. Knop et al. [4] used X-ray, and neutron diffraction, and combined it with magnetization data. Their results show that  $\text{NiCo}_2\text{O}_4$  is an inverse spinel. But no reliable determination of the degree of inversion in  $\text{NiCo}_2\text{O}_4$  could be made. The authors were unable to distinguish between the magnetic structure proposed by Blasse, and the one with the structural formula  $\text{Co}^{3+}[\text{Ni}^{2+}\text{Co}^{3+}]_4\text{O}_4^{2-}$ . The net magnetic moment derived from the magnetization measurements was only  $1.25 \mu_B$ , which is lower than the value of  $2 \mu_B$ , expected from either model. Boussart et al. [5] attempted to clarify the ambiguity of the valency assignment by a study of the variation in paramagnetic moment  $\mu_{\text{eff}}$  with composition in the spinel system  $\text{Ni}_{1-x}\text{Co}_{2+x}\text{O}_4$  (with  $x < 1$ ). They concluded that the more probable valency distribution is  $\text{Co}_{1-x}^{2+}\text{Co}_x^{3+}[\text{Ni}_x^{2+}\text{Co}_{2-x}^{3+}]_4\text{O}_4^{2-}$ , which extrapolates to  $\text{Co}^{3+}[\text{Ni}^{2+}\text{Co}^{3+}]_4\text{O}_4^{2-}$ . However, it predicts a spontaneous magnetization at  $T = 0 \text{ K}$  of  $2 \mu_B$  per formula unit, as seen before, which is significantly larger than the observed value. King and Tseung [6] investigated the ferrimagnetic ordering of  $\text{NiCo}_2\text{O}_4$  by progressive substitution of foreign ions of precisely known charge and site preference. These authors have rejected Boussart's model on the basis of the strong octahedral site preference of  $\text{Co}^{3+}$  ions and suggested the cation distribution  $\text{Co}_{0.9}^{2+}\text{Co}_{0.1}^{3+}[\text{Ni}_{0.9}^{2+}\text{Ni}_{0.1}^{3+}\text{Co}_{3.2}^{3+}]_4\text{O}_{3.2}^{2-}$ . The considerable concentration of holes in the non-magnetic oxygen 2p bands was adjusted to give the appropriate reduction in spontaneous magnetization. However, Battle et al. [7] rejected such a complex cation distribution, as mentioned in chapter 4, because it implies metallic conductivity, which is not in agreement with the conductivity measurements on polycrystalline  $\text{NiCo}_2\text{O}_4$  materials [8]. The authors [7] have made a refinement of the nickel atom distribution on the ferrimagnetic  $\text{NiCo}_2\text{O}_4$ , using neutron diffraction. They

suggested the possibility of an inhomogeneous distribution of the nickel and cobalt, and introduced A-site  $\text{Ni}^{3+}$  (tetrahedral site). The results of the electrochemical (chapter 5), and the non-electrochemical techniques (chapter 6) might be indicative for the site and charge distribution within the spinel lattice. This is a rough approximation because it is simply assumed that the results of the surface techniques are indicative for the bulk cation distribution. In chapter 6, the presence of  $\text{Ni}^{2+}$ , high-spin paramagnetic  $\text{Co}^{2+}$ , and low-spin, diamagnetic  $\text{Co}^{3+}$  was observed by XPS analysis. Since,  $\text{NiCo}_2\text{O}_4$  is an inverse spinel [4], and low-spin  $\text{Co}^{3+}$  has a strong octahedral site preference [9-11] (and  $\text{Ni}^{2+}$ ), this leads to the preliminary distribution:  $\text{Co}^{2+}[\text{Ni}^{2+}\text{Co}^{3+}]$ . The TPR measurements in chapter 6 have shown that  $\text{NiCo}_2\text{O}_4$  is formed with the average oxidation state of the metal ions equal to 2.67+ (total valency 8+), and that it can be presented by the general formula  $\text{M}^{2+}_2\text{M}^{3+}_2\text{O}_4^{2-}$ , indicating the presence of di- and trivalent metal ions (Ni or Co) in the ratio 1:2, respectively. The cyclic voltammetric characterization in chapter 5 suggested the presence of  $\text{Co}^{2+}$ , and possibly  $\text{Co}^{3+}$  and  $\text{Ni}^{3+}$ . Therefore, with this correlation exercise the following general distribution can be proposed:

$$\text{Co}^{2+}_{1-x}\text{Co}^{3+}_x[\text{Ni}^{2+}_y\text{Ni}^{3+}_{1-y}\text{Co}^{3+}_{1.0}]_2\text{O}_{4+z}^{2-}$$

with two valence states on the sublattices, and the possibility of excess oxygen to maintain the electroneutrality, and x, y and z are related through  $z = (x-y/2)$ .

## 8.1. Literature

- [1] S. Holgerson and A. Karlsson, *Z. Anorg. Allgem. Chem.* 183, 384 (1929)
- [2] F.K. Lotgering, *Philips Res. Rept.* 11, 337 (1956).
- [3] G. Blasse, *Philips Acs. Rept.* 18, 383 (1963).
- [4] O. Knop, K.I.G. Reid, Sutarno and Y. Nakagawa, *Can. J. Chem.* 46, 3463 (1968).
- [5] H. Baussart, M. Le Bras and J.M. Leroy, *C.R. Acad. Sc. Paris Serie C* 276, 69 (1973).
- [6] W.J. King and A.C.C. Tseung, *Electrochim. Acta* 19, 493 (1974).
- [7] P.D. Battle, A.K. Cheetham and J.B. Goodenough, *Mat. Res. Bull.* 14, 1013 (1979).
- [8] G. Feuillade, R. Coffre and G. Outhier, *Annales de radioelectricite* 21, 105 (1966).
- [9] D.S. McClure, *J. Phys. Chem. Solids* 3, 391 (1957).
- [10] J.D. Dunitz and L.E. Orgel, *ibid.* 3, 318 (1957).
- [11] W.J. Schuele and V.D. Deetscreek in W.E. Khun (Ed.), *Ultra fine particles*, John Wiley, New York, 224 (1963).

**ACKNOWLEDGEMENTS**

The author is grateful to ir. J. Martens of the Eindhoven University of Technology (THE), for recording the TPR spectra and useful discussions, and to dr.ir. V.A.M. Brabers (THE) for the discussions on the interpretation of the XPS and Auger results.



## LIST OF SYMBOLS

a	activity [mole dm <sup>-3</sup> ]
a <sub>o</sub>	lattice parameter [Å]
A	surface area [cm <sup>2</sup> ]
b	Tafel slope [mV]
c	concentration [mol l <sup>-1</sup> ]
C	capacitance [F cm <sup>-2</sup> ]
d	interplanar spacing [Å]; thickness [Å]
D	diffusion coefficient [cm <sup>2</sup> s <sup>-1</sup> ]; divalent
E	potential [V]; binding energy [eV]
F	Faraday constant [C.eq <sup>-1</sup> ]
h <sup>+</sup>	electron hole
ΔH	activation enthalpy [kJ mol <sup>-1</sup> ]
i	current density [A cm <sup>-2</sup> ]
i <sub>o</sub>	exchange current density [A cm <sup>-2</sup> ]
I	current [A]; number of photoelectron per second [s <sup>-1</sup> ]
K	reaction rate constant [cm s <sup>-1</sup> ]
M	molecular weight [g mol <sup>-1</sup> ]
n	number of electrons; number of atoms per volume unit [cm <sup>-3</sup> ]
N	collection efficiency; index of refraction
p	reaction order; pressure [torr]
Q	charge amount [mC cm <sup>-2</sup> ]
R	resistance [Ω]; gas constant [kJ mol <sup>-1</sup> ]; reflection coefficient
r	radius
S	atomic sensitivity factor
t	time [s]
T	temperature [K]; trivalent
v	potential scan rate [mV s <sup>-1</sup> ]
wt %	weight percent

## Subscripts

a	anodic
c	cathodic; capacitive
D	disk
dl	double layer
f	faradaic
F	final thermal treatment
l	limiting
O	oxidized form
p	peak; parallel
R	ring; reduced form
s	surface; perpendicular
t	total
u	uncompensated

$\alpha$	transfer coefficient
$\beta$	overall transfer coefficient
$\Delta$	ellipsometric parameter
$\eta$	overpotential [V]
$\Theta$	surface coverage
$\nu$	kinematic viscosity [ $\text{cm}^2 \text{s}^{-1}$ ]
$\lambda$	wavelength [ $\text{\AA}$ ]
$\psi$	ellipsometric parameter
$\omega$	rotation frequency [ $\text{s}^{-1}$ ]

## Superscripts

o	in standard state
*	in bulk

## Abbreviations

AES	Auger Electron Spectroscopy
BE	Binding Energy
BET	Brunauer-Emmet-Teller
DHE	Dynamic Hydrogen Electrode
ESCA	Electron Spectroscopy for Chemical Analysis
NHE	Normal Hydrogen Electrode
OCV	Open Circuit Voltage
rds	rate determining step
RRDS	Rotating Ring-Disc Electrode
RHE	Reversible Hydrogen Electrode
ROE	Reversible Oxygen Electrode
SCE	Saturated Calomel Electrode
SEM	Scanning Electron Microscopy
TGA	Thermogravimetric Analysis
TPR	Temperature Programmed Reduction
XPS	X-ray Photoelectron Spectroscopy

## SUMMARY

In the last decade, a growing interest in the electrolysis of water can be noticed in the framework of the Hydrogen Economy and the necessity for an energy storage medium. However, a number of problems hinder the breakthrough. The high anodic overpotential for the oxygen evolution reaction is the main cause of the energy loss in water electrolyzers (chapter 1).

In this thesis an extensive investigation of  $\text{NiCo}_2\text{O}_4$  spinel oxide, as anode material in alkaline solution was carried out.  $\text{NiCo}_2\text{O}_4$  is a very promising anode, as shown from the comparison of the possible electrocatalysts for oxygen evolution in the literature review (chapter 2).

The electrocatalyst was prepared by thermal decomposition of metal salts. A systematic study of the preparation parameters such as the temperature  $T_F$ , and the duration time  $t_F$  of the thermal treatment, and catalyst loading was executed to establish the optimum deposition conditions, with respect to its electrocatalytic activity (chapter 3). It was concluded that mainly the top surface of the  $\text{NiCo}_2\text{O}_4$  electrode is electrochemically active. Furthermore, it was clearly shown that Teflon incorporation gives about the same activity (chapter 3 and 4).

The kinetics of the oxygen evolution reaction were examined with galvanostatic steady-state measurements in the temperature range of 10 to  $80^\circ\text{C}$ , and in the electrolyte concentration range of 0.1 to 7 M KOH (chapter 4). The Tafel plots can be divided in two regions: one with a Tafel slope of about 40 mV, i.e.  $2 RT/3 F$ , for  $\eta < 280$  mV and a range of Tafel slope values from 70 to 100 mV at higher overpotentials, i.e.  $\eta > 280$  mV, which is assumed to be  $2 RT/F$ . The change in the Tafel slope ( $\eta_c$ -value) does not depend on the temperature  $T_F$ . The activation enthalpy confirms the electrocatalytic behaviour of  $\text{NiCo}_2\text{O}_4$  and reflects the influence of the temperature  $T_F$ . Oxygen evolution is suggested to take place via the formation of higher oxides. For the different potential regions, the kinetic behaviour can be explained by a reaction mechanism, by which either a shift in active site takes place from di- to trivalent sites, or by

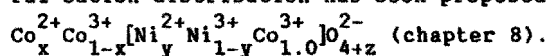
which the valence state (trivalent) does not change, but a shift from low coverages, i.e.  $\Theta_{\text{TOH}} \rightarrow 0$ , to high coverages, i.e.  $\Theta_{\text{TOH}} \rightarrow 1$ , occurs.

In order to correlate the electrocatalytic activity and spinel structure, the  $\text{NiCo}_2\text{O}_4$  catalyst has been characterized in chapter 5, using electrochemical techniques, such as cyclic voltammetry, the galvanostatic charging method and the rotating ring-disc electrode, and in chapter 6, using non-electrochemical techniques such as X-ray diffraction, temperature programmed reduction, XPS and Auger.

The surface morphology and composition of the freshly prepared  $\text{NiCo}_2\text{O}_4$  layer are found to depend on the thermal treatment, particularly on  $T_F$ : the increase in activity with decreasing  $T_F$  has been correlated with the increase in surface area and the change in surface composition.

The voltammogram of a fresh  $\text{NiCo}_2\text{O}_4$  electrode exhibits two anodic oxidation peaks, representing one-electron transfer surface redox reactions. Three different models have been suggested for the conjugated electrochemical processes, before oxygen evolution takes place. The voltammetric response of a fresh  $\text{NiCo}_2\text{O}_4$  electrode is not only influenced by the lower and upper switching potential of the scan range, but also in a different way by potentiostatic or potentiodynamic treatment. This is considered to be an ageing phenomenon which has been interpreted in terms of partial decomposition of the  $\text{NiCo}_2\text{O}_4$  surface layer.

On the basis of the voltammetric curves (chapter 5), and the results of the non-electrochemical techniques (chapter 6), the following general cation distribution has been proposed



The electrochemical formation of oxides on nickel cobalt alloys has been investigated in chapter 7. The oxide formation was examined with cyclic voltammetry, kinetic analyses and ellipsometry. The kinetic behaviour has been explained either by assuming that spinel-like oxides are formed on the  $\text{Ni}_1\text{Co}_2$ -alloy, or that, depending on the pretreatment, the alloy electrode behaves predominantly as a nickel or as a cobalt electrode.

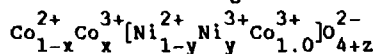
**CURRICULUM VITAE**

Johan Haenen werd geboren op 23 april 1957 te Hasselt. Na het behalen van het diploma middelbaar onderwijs, richting wetenschappelijke B, aan het St. Jan Berchmansinstituut te Zonhoven, begon hij in oktober 1976 met de studie kandidaat Scheikunde aan het Limburgs Universitair Centrum te Diepenbeek. Na het afstudeeronderzoek, dat onder leiding van Prof. F. Alderweireldt en Prof. P. de Bièvre werd uitgevoerd, behaalde hij in 1980 het licentiaatsdiploma aan de Universitaire Instelling Antwerpen te Wilrijk. In februari 1981 begon hij bij de vakgroep Elektrochemie aan de Technische Hogeschool Eindhoven, onder begeleiding van Prof. E. Barendrecht, aan het in dit proefschrift beschreven onderzoek.

De elektrokatalytische aktiviteit en de spinel-oxydestructuur zijn aan elkaar gerelateerd door de karakterisering van de  $\text{NiCo}_2\text{O}_4$ -elektrode met behulp van elektrochemische technieken (hoofdstuk 5), zoals cyclovoltammetrie, coulometrie en de roterende ring-schijfelektrode, en niet-elektrochemische technieken (hoofdstuk 6), zoals Röntgen-diffractie, temperatuur geprogrammeerde reductie, XPS en Auger. De oppervlaktemorfologie en -samenstelling van een vers bereide elektrode is afhankelijk van de thermische behandeling, in het bijzonder van de temperatuur  $T_F$ : de toename in de aktiviteit met afnemende temperatuur  $T_F$  kan gecorreleerd worden aan de toename in de grootte van het oppervlak en aan de verandering in de oppervlaktesamenstelling. Het voltammogram van een vers bereide  $\text{NiCo}_2\text{O}_4$ -elektrode vertoont twee anodische oxydatiepieken, tengevolge van één-elektronoverdrachts-reakties. De elektrochemische oxydatie- en reductieprocessen, voorafgaand aan de zuurstofontwikkeling, zijn met elkaar gekombineerd via drie verschillende modellen.

Het voltammetrisch gedrag van een vers bereide  $\text{NiCo}_2\text{O}_4$  elektrode wordt niet alleen beïnvloed door de kathodische en anodische omkeerpotentialen van het potentiaaltrajekt, maar ook op een verschillende wijze als gevolg van een potentiostatische of een potentiodynamische behandeling. Dit verouderingsfenomeen wordt toegeschreven aan een partiële ontleding van de  $\text{NiCo}_2\text{O}_4$  oppervlaktelaag.

De kationverdeling



(hoofdstuk 8) is gebaseerd op de elektrochemische en niet-elektrochemische karakterisering.

Tenslotte is de elektrochemische vorming van oxydes aan nikkel-kobalt legeringen onderzocht (hoofdstuk 7) met behulp van cyclovoltammetrie, kinetiekstudie en ellipsometrie. In een poging om het waargenomen kinetisch gedrag te verklaren, wordt enerzijds verondersteld dat spinel-type oxydes gevormd worden, en anderzijds, dat afhankelijk van de elektrochemische voorbehandeling, de legeringselektrode zich voornamelijk gedraagt als een nikkel of als een kobalt elektrode.

## CURRICULUM VITAE

Johan Haenen werd geboren op 23 april 1957 te Hasselt. Na het behalen van het diploma middelbaar onderwijs, richting wetenschappelijke B, aan het St. Jan Berchmansinstituut te Zonhoven, begon hij in oktober 1976 met de studie kandidaat Scheikunde aan het Limburgs Universitair Centrum te Diepenbeek. Na het afstudeeronderzoek, dat onder leiding van Prof. F. Alderweireldt en Prof. P. de Bièvre werd uitgevoerd, behaalde hij in 1980 het licentiaatsdiploma aan de Universitaire Instelling Antwerpen te Wilrijk. In februari 1981 begon hij bij de vakgroep Elektrochemie aan de Technische Hogeschool Eindhoven, onder begeleiding van Prof. E. Barendrecht, aan het in dit proefschrift beschreven onderzoek.

## DANKWOORD

Tenslotte wens ik al degenen, die aan de totstandkoming van dit proefschrift hebben bijgedragen te bedanken, met name:

Prof. E. Barendrecht voor de mogelijkheid om elektrochemie te bedrijven, en de voortdurende steun en waardevolle werkbeprekingen tijdens het promoterschap van dit onderzoek.

Prof. J. Schoonman voor de bereidheid om als promotor op te treden en voor de kritische en konstruktieve opmerkingen.

Wil Visscher voor haar immer stimulerend enthousiasme in de dagelijkse, elektrochemische realiteit, in periodes van 'ups' en 'downs' die een promotie-onderzoek vergezellen en voor de wetenschappelijke begeleiding.

Prof. J. van Hooff en Prof. R. Metselaar voor hun bereidwilligheid om het manuscript door te nemen.

Harry Zeilmaker voor de XPS en Auger metingen.

Anton Cox voor de vele experimenten, die hij ten behoeve van dit onderzoek verricht heeft.

Toine Kuiper voor de ellipsometrische metingen en Toku-Software.

Marléne Blijlevens voor de SEM opnamen en de dagelijkse koffie.

Nettie Rijpkema voor het zorgvuldig 'tekstverwerken' en het duo Fred & Fred voor de tekeningen, die samen de vormgeving van het proefschrift in hoge mate bepaalden.

Alle (ex)-kamergenoten en andere leden van de vakgroep Elektrochemie voor hun bijdrage, in welke vorm dan ook, tot het uiteindelijke resultaat en voor de aangename werksfeer.

Het thuisfront, Sonja en Freddy, voor al die jaren van sympathie.

In het bijzonder, Inge, voor het vele geduld en steun in de voorbije vier jaar.



## STELLINGEN

1. De bewering van Tseung et al., dat Teflon-inbouw in  $\text{NiCo}_2\text{O}_4$ -elektroden de activiteit voor zuurstofontwikkeling sterk verhoogt, is onjuist.

A.C.C. Tseung, S. Jasem, and M.N. Mahmood; in Hydrogen Energy Systems, T.N. Veziroglu and W. Seifritz (Eds.), Pergamon Press, Vol. I, 215 (1978).

Dit proefschrift, hoofdstuk 3.

2. De aanname van Willems et al., dat voor de verklaring van de gevonden reaktieorden van zuurstofontwikkeling aan Co-elektroden, de activiteit van water constant is in het onderzochte KOH-concentratiegebied, is onjuist.

H. Willems, A.G.C. Kobussen, J.H.W. de Wit, and G.H.J. Broers; J. Electroanal. Chem., 110, 227 (1984).

3. Het verdient aanbeveling om bij de vergelijking van elektrokatalysatoren voor zuurstofontwikkeling gebruik te maken van het produkt van de Tafelhelling en de uitwisselingsstroombichtheid, uitgedrukt in  $b \cdot \log i_0$ .
4. De door Hsueh et al. geïntroduceerde werkwijze voor de bepaling van de snelheidsconstanten voor de elektroreduktie van zuurstof, is geen verbetering van de eerder door Pleskov en Filinovskii ontwikkelde methode.

K.L. Hsueh, and D.T. Chin, J. Electroanal. Chem., 153, 79 (1983).  
Yu.V. Pleskov, and V.Yu. Filinovskii, The Rotating Disc Electrode, Consultants bureau, New York-London (1976).

5. De definitie van een oxydatiepotentiaal door Skoog en West is fundamenteel onjuist.

D.A. Skoog and D.M. West, Fundamentals of Analytical Chemistry, CBS College Publishing (1982).

6. De algemene opvatting dat het oog licht waarneemt, is ogenschijnlijk juist, maar in werkelijkheid oogverblindend.

T. Tomita, Cold Spring Harb. Symp. Quant. Biol. 30, 559 (1965).

D.A. Baylor and M.G.F. Fuortes, J. Physiol. 207, 77 (1970).

7. Het gebruik van literatuurreferenties met de verwijzing "... to be submitted, private communication, unpublished results, etc...." is frustrerend voor een 'jong' onderzoeker.

8. De Belgische opvatting dat Nederlanders zuinig zijn, is, met de kosten gemaakt voor dit proefschrift op rekening van de Nederlandse belastingbetaler, weerlegd.

9. Innovatief onderzoek, dat pas voor een volgende generatie van wezenlijk belang is, moet mogelijk zijn en blijven aan de Universiteiten en Hogescholen.

Eindhoven, 28 juni 1985

Johan Haenen